Synthesis, Structure and Reactivity Studies of Nickel Pincer Complexes and Evaluating Redox Non-innocence of the Ligand.

Debashis Adhikari

Submitted to the faculty of the University Graduate School in Partial Fulfillment of the
Requirements for the Degree of Doctor of Philosophy in the Department of Chemistry

Indiana University, Bloomington, Indiana

August, 2009

Acceptance

Accepted by the Graduate Faculty, Indiana University, in partial fulfillment of the requirements for the degree of Doctor of Philosophy.

Associate Professor Daniel J. Mindiola

Associate Professor Mu-Hyun Baik

Doctoral Committee

Distinguished Professor Kenneth G. Caulton

Professor Krishnan Raghavachari

May 11, 2009

Dedication

To my parents

Acknowledgements

This is a thrilling moment and I wish to look back five years ago when I started this voyage in a graduate school. The endeavor would not been ever completed without unrelenting support and constant inspiration from my mother. So at the first point I like to thank her for being so inspirational, patient and supportive for my whole graduate life. I was trained as a master student in IIT Kanpur, India and like to thank the faculties in my old alma mater for inculcating the zeal to pursue science as my future career.

Spending five years with Prof. Mindiola was a great experience. He is a person who truly nurtures the passion for chemistry in his heart and tries to pass on the quality to his protégés. From him I learnt the basic disciplines of a chemical laboratory as well as how to shape ideas driven towards a specific direction. I am very thankful my other committee members, Prof. Caulton, Prof. Raghavachari and Prof. Baik for being kind to provide me several helpful suggestions throughout my journey. Attending a computational course from Prof. Raghavachari and Baik was a bit challenging at the earlier stage but I can feel how I'm paid off from those endeavors I took.

The work presented in the third and fourth chapter is a fruit of successful collaboration with Prof. Robert K Szilagyi in Montana State University. I feel myself very fortunate to get chance to work with such an amazing spectroscopist and theoretician like him. I could not unravel the mystery of ligand non-innocence without my sojourn in Stanford Synchrotron Research Laboratory (SSRL) and Montana State University with him. Also I am very thankful to Prof. Karsten Mayer and Dr. Susanne Mossin in the University of Erlangen, Germany for their help in other spectroscopic measurements. Specially Dr. Mossin was very enthusiastic in collecting long time data for my samples in SQUID and Mossbauer spectrometers.

I have had the real joy with my all past and present colleagues in Mindiola laboratory. Post doctoral fellow Dr. Basuli and former grad student Brad Bailey were very generous to share their knowledge and skill in chemistry. I also thank Alison Fout, Uriah Kilgore, Justin Orlando for being such a good friend and help me out. Ba Tran is a literature freak and wants to share his knowledge with me. Help from Dr. Maren Pink in the crystallography lab, Dr. Gao from NMR lab was also very crucial and timely to shape my research. Occasional chatting with Richard and Soumya in Baik group sparked lot of new ideas. Thanks to all of them for their valuable time they spent for me.

Last but not the least, so many friends in Bloomington who made my life so enjoyable. At the early phase, I could not imagine life without sharing food and chat with Dr. Basuli. At the later phase so many other Indian friends who accompanied me beyond lab and help me accomplishing such a great achievement. My wife Moitree is a true epitome of patience and she is perfectly tolerant with my extended laboratory hours. Without her encouraging words and co-operation I could not see myself finishing this degree successfully.

ABSTRACT

Debashis Adhikari

Synthesis, Structure and Reactivity Studies of Nickel Pincer Complexes and Evaluating Redox Non-innocence of the Ligand

Bimetallic cores are ubiquitous in natural enzymes and presently being used in several important chemical transformations such as epoxidation of olefins or stereoselective polymerization of oxiranes. To understand the nature of interaction between two metal centers in a bimetallic core we synthesized the diamond core, $[\mathrm{Ni}(\mu_2\text{-PNP})]_2$ ($\mathrm{PNP}^- = \mathrm{N}[2\text{-P}(\mathrm{CHMe}_2)_2\text{-}4\text{-MeC}_6\mathrm{H}_3]_2$) and observed that the two Ni(I) metal centers are feebly interacting, particularly in an antiferromagnetic manner, despite an extremely short distance (2.3288(7) Å) between them. The molecule behaves as a masked Ni(I) synthon and can perform the cleavage of a plethora of homonuclear or heteronuclear bonds to incorporate rare functionalities onto nickel.

A current interest has been surged in group transfer reactions employing nickel reagents since its higher congeners, namely Pd and Pt are too expensive. Transition metal mediated transfer of boryls to aromatic and aliphatic hydrocarbons to engender corresponding aryl boronic esters appears to be very promising given the widespread utility of the ester in C−C bond coupling reactions. In the attempt of nickel mediated borylation we discovered a simple route to engender formation of a stable, square planar nickel boryl complex, (PNP)NiBcat, (cat = $\mathrm{O_2C_6H_4}$) hitherto unknown in literature. Theoretical calculations (DFT) suggested the single bond nature of the Ni−B bond and quite gratifyingly the boryl moiety was successfully transferred to bromobenzene in a cyclic manner. A mild protocol for the synthesis of relatively rare nickel silyl complexes has also been developed.

An important discovery along these investigations was the conclusive proof of redox non-innocence behavior of the pincer PNP backbone. Prior to our work, the PNP ligand was believed to be a redox inactive ancillary, but through extensive spectroscopies including multi-edge X-ray absorption spectroscopy we were able to show unequivocally its redox non-innocence. First, the redox non-innocence was manifested through a ligand based oxidation of (PNP)NiCl. Later we extend this study over other 3d transition metals to prove that the redox non-innocence of the ligand behaves as a function of metal.

Associate Professor Daniel J. Mindiola

Associate Professor Mu-Hyun Baik

Distinguished Professor Kenneth G. Caulton

Professor Krishnan Raghavachari

Table of Contents

4 Evaluation of The Non-innocence of PNP Ligand as a Function of Metal Centers

Chapter 1

Synthesis and Reactivity Study of a Ni_2N_2 Diamond Core: A Masked Three Coordinate $Ni^{(I)}$ Synthon

1.1 Introduction

1.1.1 Background of nickel chemistry and importance of bimetallic core

Nickel is a versatile metal in organometallic chemistry and is used in a variety of industrial processes such as hydrodesulfurization of crude oil or as a catalyst in homogeneous processes such as C-C bond coupling reactions.[1-3] In addition to these synthetic applications, a plethora of examples are also present in the realm of bioinorganic chemistry where nickel and organonickel intermediates play a crucial role in biological transformations. The ubiquity of nickel is evident from the five classes of nickel containing enzymes which are urease, hydrogenase, methyl-CoM reductase, Ni-dependent SOD and CO dehydrogenase.[4-11] Nickel +II is the most common among the possible oxidation states ranging from 0-IV. Several review articles discuss the more unusual oxidation state of nickel such as +I, since this oxidation state might introduce a new regime of chemistry. [12,13] It is important to mention in this context that +III and +IV oxidation states of nickel are also extremely rare.[14] The scarcity of $Ni^{(I)}$[15-32] is due to its proneness for dissociation or disproportionation, particularly in solution phase. Though the involvement of $Ni^{(I)}$ as an intermediate is conceived in the biological transformations involving nickel containing enzymes, isolable examples of such oxidation states are still scant. Due to the paucity of the $Ni^{(I)}$ species, its chemistry is still esoteric and provides an opportunity to study the reactivity associated with such unusual oxidation state.

Bimetallic complexes are ubiquitous in nature since they offer distinct advantages over their monometallic counterparts. For example, charge delocalization over two centers versus one metal facilitates two electron redox reactions that would demand a large thermodynamic driving force in a mononuclear center. Moreover, activation barriers arising from nuclear reorganization of the solvent and the surrounding medium can be less of a problem in binuclear versus the mononuclear centers possessing the same net charge. Another salient feature of a bimetallic core lies in polyatomic substrate binding where the binding event is facilitated by multi atomic site at a binuclear center. Similarly, electrostatic activation of a substrate is more facile when the responsible complex in question is $[M_2]^{2n+}$ compared to its mononucler counterpart, i.e., M^{n+} owing to higher charge contained in the former. Such distinctions between monometallic and bimetallic centers become really important when bioinorganic transformations are performed in a cooperative fashion utilizing two or more metal centers. Consequently, chemistry performed in a cooperative manner becomes one of the nature's quintessential strategies to finely carry catalytic processes in the active site of the enzymes. The bimetallic and more precisely the diamond cores of Cu_A site, methane monoxygenase, Fe−Ni hydrogenase are few to name among the numerous examples available in natural systems, that can overcome difficult hurdles in the binding, activation, and functionalization of "kinetically and thermodynamically inert" substrates. In all these given examples, the presence of a second metal atom either behaves as an electron donor/ acceptor, or can stabilize the incipient structure, or shuttle the electron density to stabilize the system as a whole. Bimetallic systems also show enormous promise beyond natural enzymes and are profusely used to perform organic transformations. It has long been postulated that some metal catalyzed epoxide polymerization take place via a bimetallic core where one metal center coordinates the epoxide and other delivers the polymer alkoxide. Several recent studies on homogeneous systems have consolidated this postulation.[33-35] Furthermore, an elegant study by Jacobsen and coworkers have delineated the bimetallic nature of enantioselective epoxide hydrolysis using chiral cobalt salen (salen = N, N'-bis(3,5-di-tert-butylsalicylidene)1,2-cyclohexane-(1R, 2R)-diamine).[36] Following this strategy, Coates *et al.* designed a cobalt bimetallic catalyst which smoothly can perform stereoregular and enantioselective polymerization of epoxides.[37]

Bimetallic cores consisting of the most accessible oxidation state of Ni, namely $Ni^{(II)}$ centers have been scrutinized in depth to address the electronic interaction between metal ions, more specifically the mechanism of the communication among the two metal centers via superexchange through spin delocalization or spin polarization.[38] Although $Ni^{(II)}$ centers have been studied, their reduced forms, $Ni^{(I)}$, remain unexplored. As a result, investigating the electronic and magnetic interactions between two $Ni^{(I)}$ centers should provide clear clues to how these systems, if any, cooperatively perform important chemical transformations relating to bond breaking and forming reactions. In general, understanding the interaction between two metal centers represents an important paradigm in coordination chemistry since it can lead to predictions on how dinuclear moieties operate, in concert, and along the way to performing unusual transformations such as bond activation.

In a bimetallic motif consisting of two d^9 metal centers, one can categorize three different type of electronic states that depend greatly on the strength of metal-metal interaction.[39] In one case, the two metal centers in question can be virtually non-interactive, essentially displaying properties amenable to an isolated d^9 unit and more consistent with a paramagnetic monomer. In a second case scenario, whereby there is a weak interaction, the metal centers can be communicating weakly, thus leading to ferromagnetic and antiferromagnetic ground states depending on whether the high spin or low spin state can be attained. In such a case of weak interaction, it is expected that the triplet excited state should be close in energy to the singlet ground state, and that such a low-lying excited state should be populated thermally. In the third case scenario, the two metal centers could be interacting strongly thereby forming a metal-metal bond which eventually would display diamagnetic behavior. Deciphering these types of interactions can be challenging, given the interplay between metal-metal bonds, ferro- and antiferromagnetic coupling through space or the bridging ligands, as well as a possible caveat involving a monomer-dimer equilibrium scenario in solution. In order to understand the interaction between two $Ni^{(I)}$ centers in a bimetallic core we synthesized a bimetallic diamond core $[(\mu_2\text{-PNP})_2Ni_2]$, (PNP = $[N(2\text{-}P(CHMe_2)_2\text{-}4\text{-}MeC_6H_3)_2]^-$) [40] and studied how the nature of interaction between two nickel centers dictate the core's reactivity pattern.

1.1.2 Background of the ligand system

Pincer type ligands, more specifically a PCP type scaffold was first used as a supporting ancillary platform to conduct novel chemical transformations by Shaw in the late 1970's (Scheme 1).[41] Following his seminal work, pincer ligands have drawn immense popularity in different areas of chemistry, such as, a specific bond activation, small molecule activation and group transfer. [42]After Shaw's initial design of the pincer, Fryzuk modified the backbone by changing the PCP platform to PNP platform which combined soft phosphines with a hard π-base such as amido group.[43-48] The major advantage of replacing the carbon by a nitrogen is to generate a more flexible system which prefers the facial arrangement unlike the meridional geometry preferred by the former. Despite the enhanced flexibility of Fryzuk's system, the N-Si linkages in the backbone are susceptible towards hydrolysis or nucleophilic displacement reactions. Another potential drawback to the Fryzuk's PNP is the presence of β-hydrogens in the backbone. To circumvent these issues Liang and Kaska introduced a new ligand where *o*-arylene bridges connect the amido and phosphine residues.[49,50]Furthermore, Ozerov and co-workers modified the aforementioned ligand by introducing the alkyl substituents instead of aryl substituents on the phosphine.[51] The potential problem of ortho-PPh metalation was resolved by this strategic incorporation as well as the ^{1}H NMR spectrum was greatly simplified.[51] The latter ligand prefers to bind a metal in meridional fashion due to the rigidity of the aryl backbone. Interestingly, *para*-tolyl groups were incorporated as the ligand backbone by Ozerov and coworkers which could be used as spectroscopic handle to monitor the progress of a reaction. An analogous tridentate ligand was synthesized by Schrock and co-workers which possessed a chelating diamido functionality bridged by oxygen.[52,53] This dianionic ligand is flexible to bind a metal center in either meridional or facial geometry. However, this system is dianionic, making it too electron rich for the late transition metals.

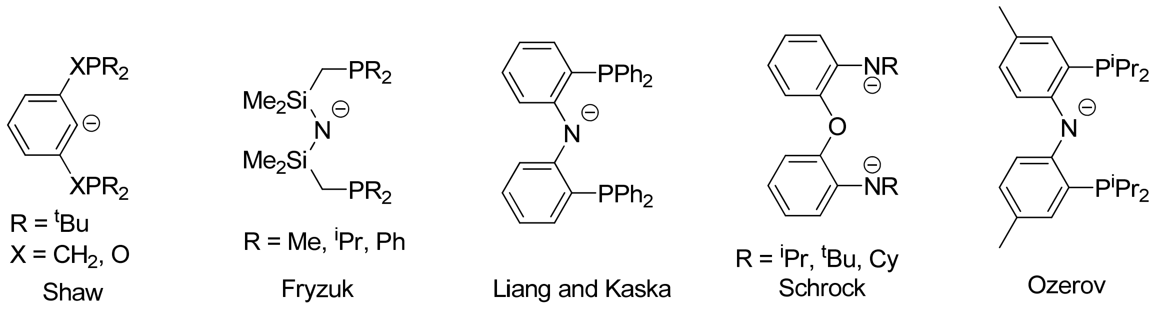

Scheme 1: Development of pincer type ligands.

1.2 Results and Discussion

1.2.1 Synthesis of (PNP)NiCl

Reaction of a toluene solution of (PNP)Li with $NiCl_2(THF)_{1.5}$[54] affords the diamagnetic (PNP)NiCl (**1**) complex as bright green crystals in 94% isolated yield (Scheme 2). The compound can also be prepared from $NiCl_2$ but the yield is highly improved by the use of the more soluble THF adduct of $NiCl_2$. Ozerov and co-workers have reported an alternative way of preparing **1** treating (PNP)H with $NiCl_2$ in the presence of triethyl amine.[55]

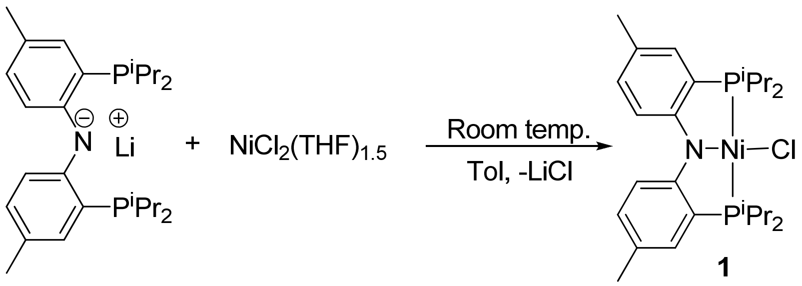

Scheme 2: Synthesis of **1.**

To elucidate the metrical parameters of **1** we analyzed the structure by X-ray diffraction studies. The solid state structure (Figure 1) shows the geometry around the $Ni^{(II)}$ center to be square planar, clearly consistent with a d^8 electronic configuration. In the solution state ^1H NMR spectrum of complex **1**, a single resonance for the tolyl group is observed which is the result of the ligand having a C_2 rotational axis through the N11-Ni1-Cl2 bond (*vide infra*) as well as a plane of symmetry. The plane of symmetry is the outcome of rapid skewing motion of the aryl motifs around $N-C_{aromatic}$ bond in solution state despite the solid state structure exhibiting the aryl motifs to be tilted slightly from strict planarity. The Ni1-P3 and Ni1-P19 distances are 2.2012(6) Å and 2.2025(6) Å, respectively, which are shorter due to significant backbonding from nickel to phosphorus compared to the Ti-P bonds (2.626(3) and 2.638(3) Å respectively) in $(PNP)Ti(CH_2PMe_3)_2$ reported earlier from our group.[56] These shorter Ni-P bonds pull the aromatic rings towards the respective P's, thus avoiding the hindered rotation posed by two confronting ortho hydrogen atoms in the aromatic rings of the pincer ligand.

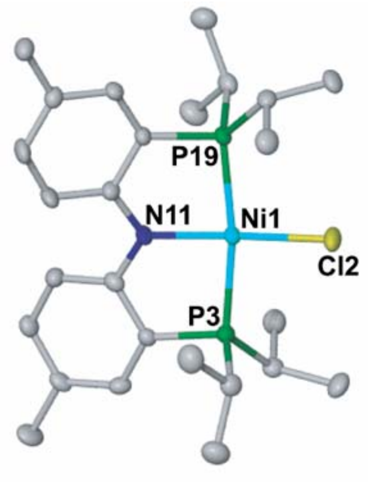

Figure 1: Molecular structure of **1** with thermal ellipsoids at the 50% probability level. Solvent, Hydrogen atoms and methyls of the isopropyls have been omitted for clarity.

Selected metrical parameters (lengths in Å, angles in degrees): Ni1-Cl2, 2.1568(6); Ni1-P3, 2.2012(6); Ni1-P19, 2.2025(6); Ni1-N11, 1.8980(15); N11-Ni1-P3, 84.68(5); N11-Ni1-P19, 84.86(5); Cl2-Ni1-P3, 94.78; Cl2-Ni1-P19, 95.82(2); N11-Ni1-Cl2, 177.51(6).

1.2.2 Electrochemistry of 1

To probe the electrochemical behavior of **1,** a cyclic voltammogram was recorded in THF solutions containing 0.30 M $[N(^nBu)_4]PF_6$ as supporting electrolyte and using a Pt-working electrode and silver wire reference electrode in a one-compartment cell. Ferrocene (Fc) was used as an internal standard and all potentials were referenced versus the ferrocene/ferrocenium redox couple (Fc/Fc^+) fixed at 0 V. Accordingly, complex **1** displays a reversible anodic wave at −0.058 V and an irreversible cathodic wave at −2.48 V (Figure 2). The high reduction potential supposedly stems from the electron donation of a hard amide which makes the species very electron rich.

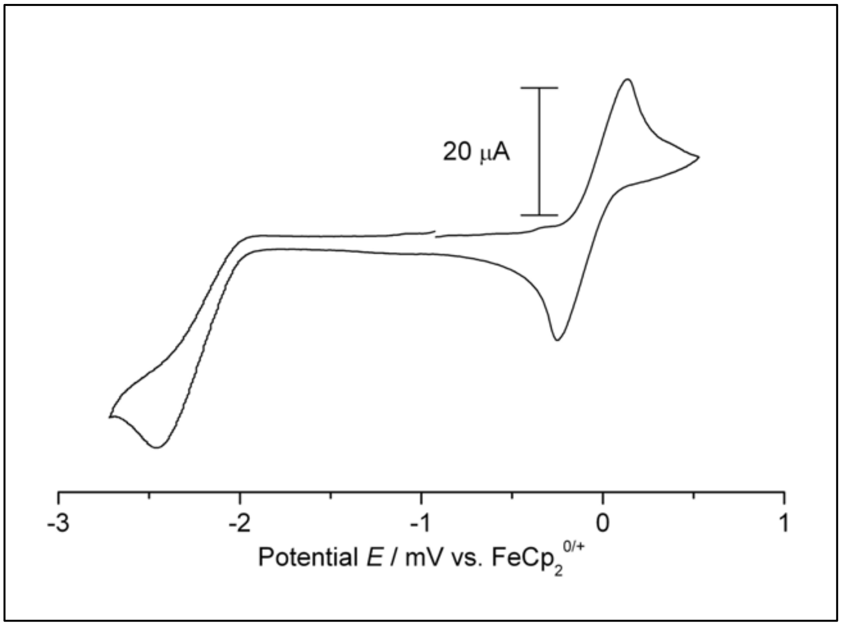

Figure 2: Cyclic voltammogram of **1** in THF using 0.30 M $[N(^nBu)_4]PF_6]$ as an electrolyte. Scan rate for the experiment was 100 mV/sec

1.2.3 Chemical reduction of 1 to afford 2

The cyclic voltammetry experiment provides clear evidence for using a strong reductant to convert **1** into a hypothetical Ni$^{(I)}$ species.[57] This is especially true since chemical treatment of **1** with 1% Na/Hg resulted in no detectable reaction when assayed by ^{1}H NMR spectroscopy. However, chemical reduction of **1** was accomplished with a more powerful reductant like KC_8 in THF over 1 hour, which afforded brown crystals of $[(\mu_2\text{-PNP})_2Ni_2]$ (**2**) a complex bearing a Ni_2N_2 diamond-core resting state on the basis of single crystal X-ray diffraction analysis (Scheme 3).[58] A similar type of Co_2N_2 diamond core has been reported earlier by our group,[59] while a Cu_2N_2 core has also been reported by the Peters' group with a $[SNS]^-$ (SNS = bis(2-tert-butylsulfanylphenyl)amido) ligand.[60]

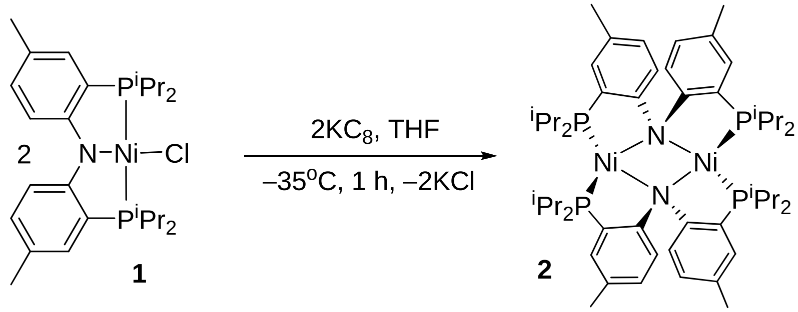

Scheme 3: Synthesis of **2** via the reduction of **1** with KC_8.

Complex **2** is isolated in moderate yield (62%) from the hexane solution and we presume the reason behind moderate yield is the high solubility of **2** in hexane along with the production of another byproduct, (PNP)NiH, **3**. Complex **3** has been reported earlier by Ozerov and coworkers and can be identified by its distinct resonance at −18.4 ppm ($J_{H\text{-}P}$ = 20 Hz) in the ^{1}H NMR spectrum. In our attempts to obtain pure **2** we discovered that pure and freshly made KC_8 can lead to complete conversion of **1** to **2** without any contamination of **3**. Through different independent studies we observed that treatment of **2** with excess KC_8 in THF did not produce **3** (no reaction), suggesting that over-reduction was not a competing pathway. Notably, the origin of the hydride ligand in **3** was not the solvent medium, THF, since treatment of **2** with 1 equivalent of KC_8 in THF-d_8 did not yield the expected isotopologue (PNP)NiD, **3**-d_1. Therefore these results convey that **2** is not a precursor to **3** and that the hydride must originate from ligand degradation of the pincer ancillary in **1** or possibly, from an impurity present in KC_8.

Complex **2** is soluble in most common organic solvents such as benzene, hexane, THF, Et_2O. It exhibits reasonable thermal stability both in solution and in solid state under inert atmosphere, but upon exposure to oxidants (e.g. O_2) or halogenated solvents (CH_2Cl_2), it rapidly decomposes to a mixture of intractable products. The ^1H NMR spectrum of **2** in C_6D_6 reveals broad resonances in the range of 16.68 to 0.89 ppm, which is consistent with a paramagnetic species. To probe the molecularity of the complex in solid state and the geometry around Ni-center we obtained single crystal X-ray diffraction data. Our structural diagram for **2** clearly reveals that the ligand geometry rearranges significantly to afford a dimer in the solid state, whereby a reorganization of the pincer backbone changes from meridional configuration to the bridging configuration. The structure of the dimeric $Ni^{(I)}$ diamond core has been shown in Figure 3. Among the salient features, distortion from planarity is observed for both Ni(1) and Ni(2) centers, where the sum of angles around the Ni centers are 327.05^o and 328.03^o respectively.

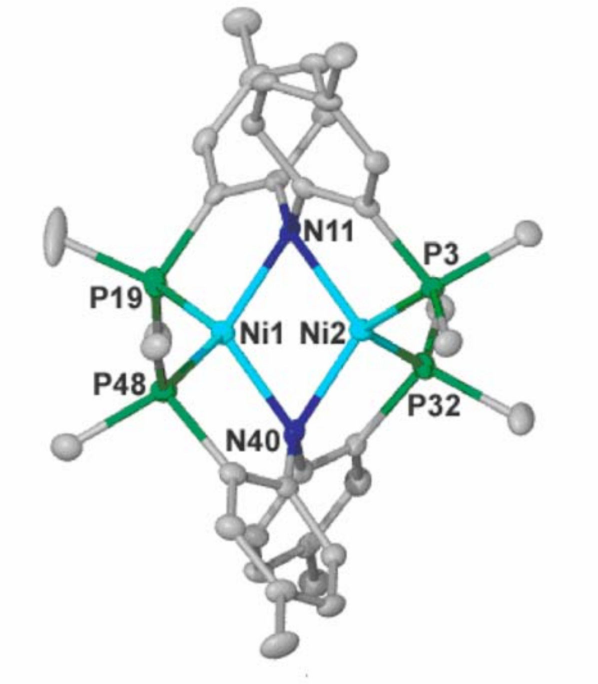

Figure 3: Molecular structure of **2** depicting thermal ellipsoids at the 50% probability level. Solvent, hydrogen atoms and methyls of the isopropyl groups have been omitted for clarity. Selected metrical parameters (lengths in Å, angles in degree): Ni1-P48, 2.2138(10); Ni1-P19, 2.2195(10); Ni2-P32, 2.2287(10); Ni2-P3, 2.2344(10); Ni1-N40, 2.084(3); Ni2-N40, 2.070(3); Ni1-N11, 2.050(3); N12-N11, 2.062(3); Ni1-Ni2, 2.3288(7); Ni1-N40-Ni2, 68.19(9); Ni1-N11-Ni2, 68.99(9). P19-Ni1-P48, 122.17(4); P32-Ni2-P3, 119.30(4); N11−Ni1−N40, 111.33(11); N11−Ni2−N40, 111.43(11); N11−Ni1−P19, 89.64(8); N11−Ni1−P48, 126.00(8); N11−Ni2−P3, 89.09(8); N11−Ni2−P32, 124.66(8); N40−Ni1−P19, 120.72(8); N40−Ni1−P48, 89.72(8); N40−Ni2−P3, 127.51(8); N40)−Ni2−P32, 88.63(8).

From the crystal structure the P-Ni-P angles are found to be 119.30° and 122.17°, which are slightly distorted from ideal tetrahedral geometry. These values more closely approximate a cis-divacant octahedron at each nickel site with [P, Ni, P] and [N, Ni, N] planes being nearly orthogonal. N11-Ni2 and N11-Ni1 bond lengths are 2.062(3) Å and 2.050(3) Å, which are far elongated compared to the N11-Ni1 distance of 1.8980(15) in **1** as depicted in Figure 3. The Shakal diagram shown in Figure 4 focuses on the first coordination sphere in the solid state structure of **2**. Congruently, the phosphorus atoms composing a PNP ligand extend across each metal center. This expansion of the phosphine pendant arm adds some strain to the aryl framework, which is reflected by the dihedral angles N-C-C-P (1.4(4), 1.8(4), 6.2(4), and 6.8(4)^{o}). This difference in the dihedral angles creates some deviation of the two halves of the molecule. As a result, one PNP ligand in **2** is undergoing more tension than the other. Therefore, each half of the molecule is not strictly equivalent. Figure **2** displays a Ni···Ni distance of 2.3288(7) Å, which is marginally close to the sum of covalent radii of two Ni$^{(I)}$ centers, 2.32 Å.[61] Thus, intuitively it appears that two Ni$^{(I)}$ centers in complex **2** will be interacting and forming a strong metal-metal bond.[62] Through a series of EPR and SQuID experiments we will be addressing the nature of the metal-metal interaction (*vide infra*).

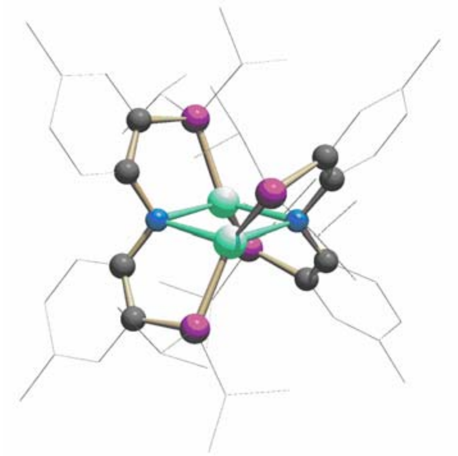

Figure 4: Shakal diagram for **2** to describe specifically the Ni_2N_2 core. This figure also specifies different amount of torsion experienced by different ligand fragments.

1.2.4 Magnetism of complex 2

In a bimetallic core such as **2** it is very important to evaluate the nature of interaction between two centers. Intuitively, two d^9 centers closely spaced to each other (Ni···Ni distance is 2.3288(7) Å) should be strongly coupled to render the system $S = 0$, therefore making it diamagnetic. In our case, however, the complex exhibits paramagnetic behavior over a wide range of temperatures (300 K to 4 K). Solution state magnetic moment of **2** (calculated for the monomer) measured by Evans method is 1.78(1) μ_B in toluene at 25 °C. The magnetic moment is slightly temperature dependent, varying from 1.45 μ_B at 218 K to 1.74 μ_B at 348 K, suggesting that **2** might exist as a mixture of monomers "(PNP)Ni, or (PNP)Ni(solvent)$_x$ (X = 1 or 2)", or even a dinuclear compound. In a non-coordinating solvent such as cyclohexane, some change in magnetic moment is observed, but in a coordinating solvent such as pyridine the magnetic moment does not appear to decrease with temperature (see experimental section). These findings hint towards an equilibrium being present in solution whereby the monomeric component of the equilibrium can be stabilized by coordination of the solvent. Though we have some distinct evidence for the monomer being present in solution phase, the presence of equilibrium of monomer↔dimer is still questionable and lacks unambiguous evidence. A similar equilibrium scenario has been proposed for the Co$^{(I)}$ analogue, [Co(μ_2-PNP)]$_2$.[59] Since solution state magnetic moment measurements were coupled with the molecularity of the complex in solution, we attempted to scrutinize the solid state magnetic behavior of complex **2**. Accordingly, the magnetization data of crystalline sample of **2** were recorded over a temperature range of 300 K to 2 K by SQuID magnetometry. The data has been corrected for underlying diamagnetism using tabulated pascals constants[63,64] and plotted as the effective magnetic moment versus temperature (Figure 5)

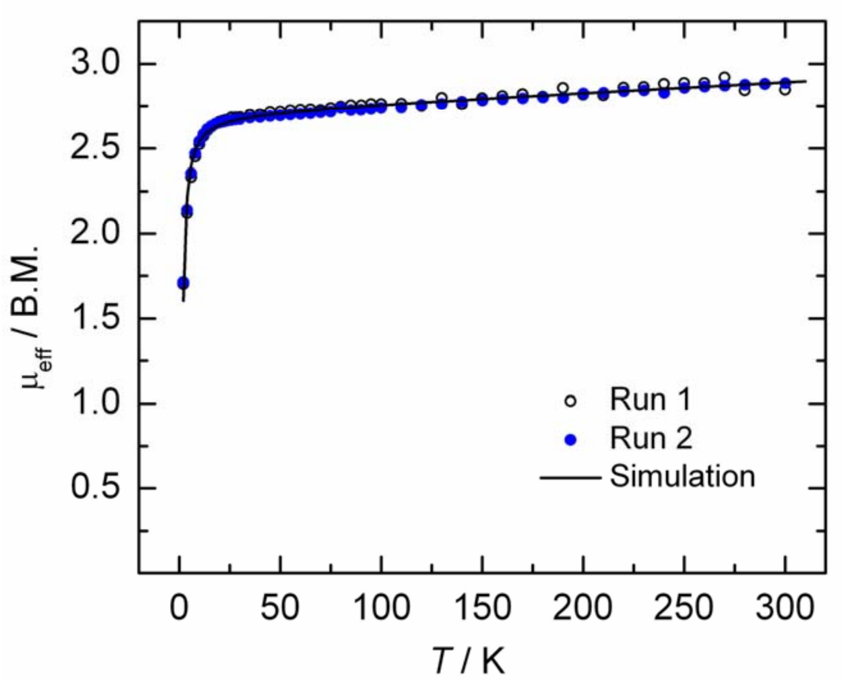

Figure 5: Plot of μ_{eff} as a function of temperature shown for **2** in temperature interval 2–300 K. Open spheres and blue spheres represent runs performed on two independently prepared samples. The line shows the fit using the dimer model and the parameter described in the text.

The effective magnetic moment measured by SQuID magnetometry varies from 1.6 μ_{B} at 2 K to 2.9 μ_{B} at 300K (assuming dimer). Disregarding a temperature-independent paramagnetism (TIP) of 450 x 10^{-6} $\mathrm{cm^3.mol^{-1}}$ per dimer molecule, the susceptibility is fairly constant over a wide range of temperature, 50–300 K. This data is reproducible taking another batch of independently synthesized pure sample and has been plotted as run 2 in Figure 5. Shortly, the nature of the curve, particularly the drop of magnetic moment in the range of 2–50 K will be explained.

Qualitatively, this magnetization data of **2** could correspond to three different spin state situations. We already discarded the strong coupling case where two electrons are placed in the same spatial orbital, hence leading towards diamagnetic behavior of the complex. Keeping in mind that the complex is paramagnetic, we must consider three different situations. Case 1 is a very strong ferromagnetic coupling between the S = ½ nickel centers with a triplet (S = 1) ground state and very high lying singlet state (S = 0). The energy difference between triplet and singlet state is high enough to prohibit even any partial population at room temperature (> 500 cm^{-1} higher in energy). Case 2 corresponds to magnetically isolated S = ½ centers where no communication can be invoked between these two centers. Case 3 gives rise to a weakly antiferromagnetically coupled dimer with a singlet ground state and an excited triplet state only several cm^{-1} higher in energy.

We like to pinpoint the correct ground state and the corresponding case depending on our SQuID data in conjunction with EPR (*vide infra*). Our best fit of the SQuID measurements have been shown in Figure 5 as a black solid line. For this simulation we invoke a dimer model using the usual spin Hamiltonian $H = -2J(S_1 \times S_2) + g\mu_B B(S_1 + S_2)$ with $S_1 = S_2 = ½$. When the simulation is performed in order to match the data for case 1, i.e. the strongly ferromagnetic coupling case, a g-value of 1.95 is obtained from the fit. Since the experimental g value (g_{iso} = 2.205 in solution state) deviates significantly, we discard this possibility being operational in our system. It is also very unlikely to observe such an extremely strong ferromagnetic coupling regardless of the Ni···Ni distance. Using the dimer model as the starting point, our fitting was performed for all three cases where a gradual decrease in magnetic moment had been observed at very low temperatures. When cases 1 and 2 are considered, the latter feature will be due to intermolecular interactions with neighboring nickel centers and is expressed as a Weiss temperature, while for case 3, this lowering in effective magnetic moment is mainly due to the intramolecular antiferromagnetic interaction in the dimer. For case 3, proper fitting provided an extremely small coupling constant value, $J = 1.52(5)\ \text{cm}^{-1}$, an isotropic g value of 2.21(1), a TIP of $450 \times 10^{-6}\ \text{cm}^3.\text{mol}^{-1}$ and a Weiss temperature of $\theta = -0.4$ K. The g value is in excellent agreement with the g value obtained from the solution and solid state EPR data (2.205 and 2.214 in solution and solid state, respectively, *vide infra*). From these data we conclusively believe that S = 0 as the ground state in **2** with very closely lying S = 1 excited state. Case 2 is disproved solely on the basis of low temperature EPR data in the solid state, which will be discussed herein.

1.2.5 X-Band EPR spectroscopy of complex 2

Complex **2** is paramagnetic and two metalloradicals are present within their close proximity. To examine the nature of the radical involved in this molecule, X-band EPR spectroscopy experiments were performed. Solution state EPR spectroscopy experiments at room temperature in toluene displays a virtually featureless resonance line that can be simulated with an isotropic g value of 2.205(5) (Figure 6, top). The value clearly tells us that the electron is metal based. Expectedly, the X-band EPR in the solid state at 298 K evolves an anisotropic rhombic signal and gives rise to three different g values of 2.393(4), 2.238(4) and 1.992(4) after simulation (Figure 6, bottom). An average of these three values exactly matches very well with the isotropic g value from the solution state experiment substantiating the fact that the same radical is yielding both signals. The non-axiality of the nickel environment in the solid state is clearly observed from the rhombic anisotropy of the experimental g-values. The g-values observed for complex **2** are analogous to the values observed by others.[65]

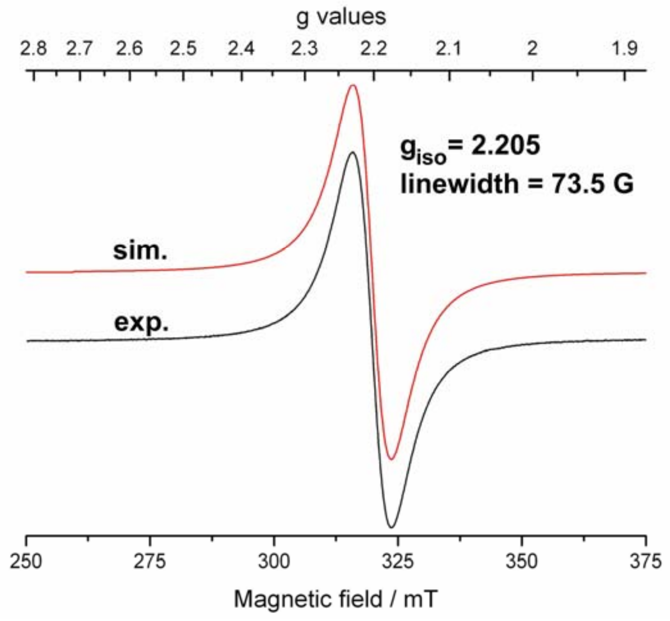

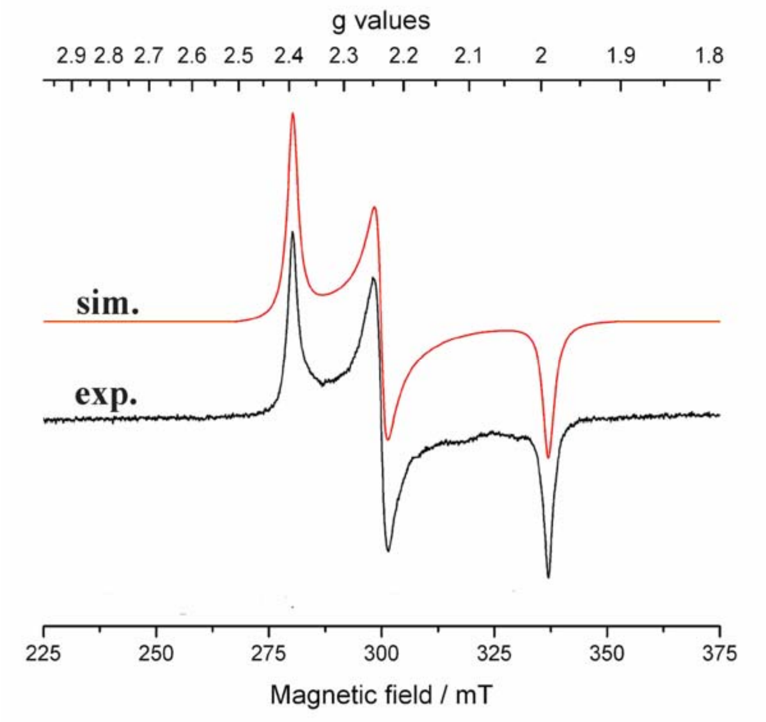

Figure 6: Solution (top) and solid state (bottom) X-band EPR spectra of complex **2**. Experimental lines have been shown in black and the simulated lines in red. Experimental

conditions are 298 K: microwave frequency, 9.390083 GHz; microwave power, 0.2012 mW; modulation frequency, 100 KHz; modulation amplitude, 0.8 mT.

As mentioned earlier, that the magnetization data showed that the $Ni^{(I)}$ centers in **2** were weakly antiferromagnetically coupled, and thus we were interested to corroborate the data by low-temperature EPR spectroscopy. For this purpose we collected solid state EPR data at 4 K which is shown in Figure 7. The spectroscopic features are close to the room temperature spectra, only deviating very slightly with lower g-values of 2.380(4), 2.225(4), 1.980(4). We now analyze the problem of correct spin state assignment, and must conclusively choose between case 2 and 3 (*vide supra*). The main lines in the solid-state EPR spectrum of complex **2** were simulated using both models (Figure 7, top and middle). A low intensity feature at approximately half field (positioned at g = 4.24) was observed at 4 K, and this feature should only be present in case 3: a weak interaction in a dinuclear complex. The simulation using the dimer model discloses a spin Hamiltonian with S = 1, at 4 K: S = 1, $g_x = 2.380(4)$, $g_y = 2.225(4)$, $g_z = 1.980(4)$, D = 0.001 cm^{-1}, line width = 25 G, and Lorentzian line shapes. At 25 ^{o}C: S = 1, $g_x = 2.393(4)$, $g_y = 2.238(4)$, $g_z = 1.992(4)$, D = 0.000 cm^{-1}, line width = 17 G, and Lorentzian line shapes. Similar half -field resonances in EPR spectroscopy have been authenticated as the proof of S = 1 state by Wieghardt *et al.* in a nitridochromium complex, *trans*-$[Cr(cyclam)(N_3)](ClO_4)$, (cyclam = 1,4,8,11-tetraazacyclotetradecane).[66] As discussed above, observation of half filled signal (g = 4.24) by low temperature EPR spectroscopy should be taken as an unequivocal proof of the weakly coupled $Ni^{(I)}$ centers in **2**. Usually, the presence of a small nonzero-field splitting parameter, D, in the spin Hamiltonian induces a slight mixing of the three energy levels in the triplet state (M_s = –1, 0 and +1), which relaxes the selection rules, therefore influencing the intensity in the forbidden $\Delta M_s = 2$ line (transition from $m_s = -1$ to $m_s = +1$) found at the half-field position. From the appearance of half-field (g = 4.24), the possibility of isolated centers sitting close in the molecule **2** is completely discarded. The observed experimental line for the half-filled transition is more than a magnitude intense than the simulated line, and that can be originating from the inequivalence of two $Ni^{(I)}$ centers. The observation is also supported by the crystallographic detail where a close look insinuates to inequivalence of two $Ni^{(I)}$ centers.

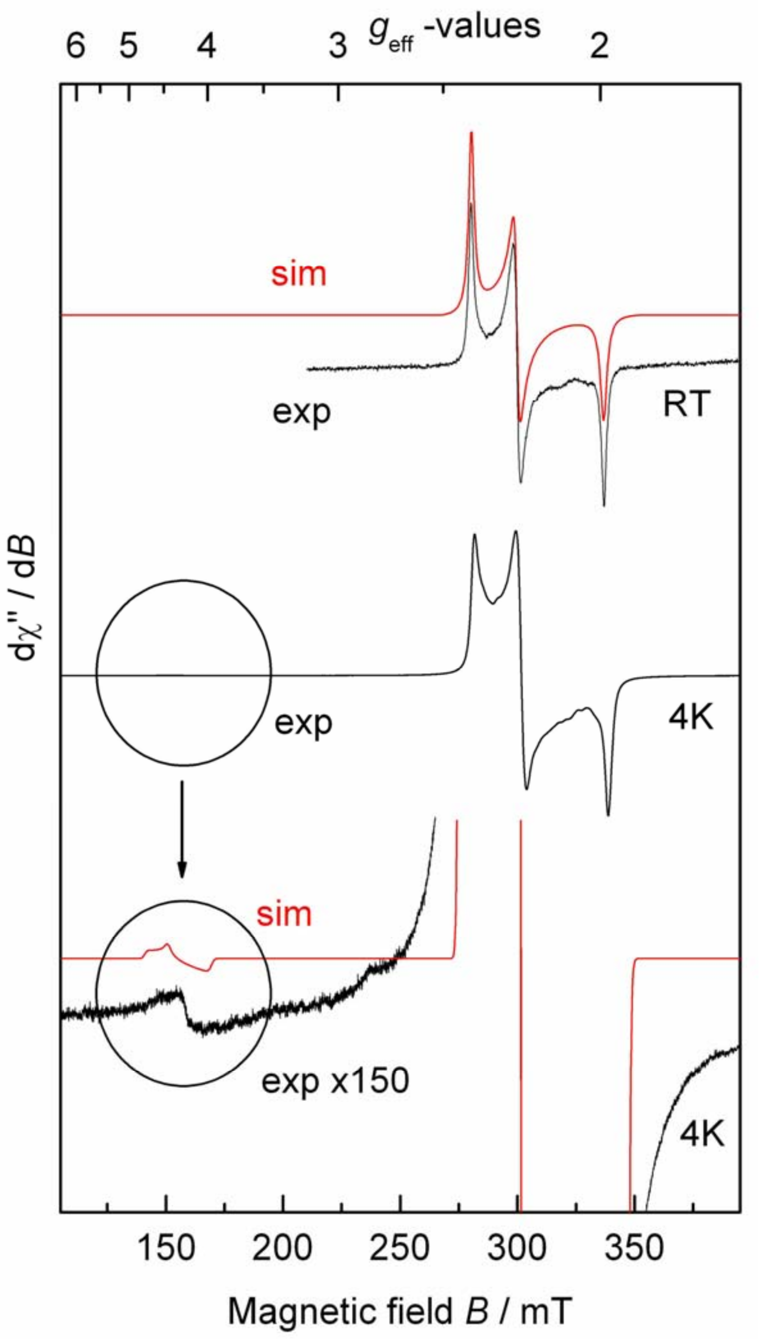

Figure 7: X-band EPR spectra of solid state **2** at room temperature (top) and 4 K (middle). At the bottom, the 4 K spectra has been expanded by a factor of 150 to show the weak line found at approximately half field (*g*-value of the position of this line is 4.24). Experimental conditions at 300 K: Microwave frequency 9.390083 GHz, microwave power 0.2012 mW, modulation frequency 100 kHz, modulation amplitude 0.8

mT. At 4 K, middle spectrum: Microwave frequency 9.016023 GHz, microwave power 0.998 mW, modulation frequency 100 kHz, modulation amplitude 1.0 mT. At 4 K, bottom spectrum: Microwave frequency 9.014827 GHz, microwave power 0.998 mW, modulation frequency 100 kHz, modulation amplitude 0.5 mT, collected over three runs. The simulations shown in red lines were performed with the spin Hamiltonian model and the parameters described in the text. The field scale of the middle and bottom spectra have been corrected for the differing frequencies compared to the top spectrum to facilitate comparisons.

It is also well known that lowering the symmetry of the system can be very effective in incrementing intensity in the forbidden line.[67] We do not have enough evidence, however to unambiguously determine the magnitude of the main axis of the zero-field splitting and can only therefore confirm this parameter to indeed be nonzero at liquid helium temperatures, and maximally at 0.0015 cm^{-1}. Otherwise, splitting in the main axis would be present, which is not observed in our case. Since the g value is anisotropic, position of the half-field line is dependent on which g value is assigned to the z-axis. Our findings point toward the lower g value being assigned to the z axis (axis of the zero-field splitting parameter D). Since the half-field signal is the key point to experimentally observe the S = 1 state, we took special care to verify its presence. The signal was highly reproducible from independently synthesized sample and no half field line was observed from the background measurement. It is unlikely that a decomposition byproduct/impurity of **2** would be responsible for this signal given our consistent magnetization data collected for two independently crystallized samples. Although an extremely small amount of iron$^{(III)}$

impurities can generate a weak signal at g = 4.3, we are confident that compound **2** is analytically pure material which is prepared under highly reducing conditions. So with all these magnetization and EPR experiments we are able to correctly assign the spin ground state of **2**, which is S = 0.

1.2.6 DFT studies to understand $Ni^{(I)}$…$Ni^{(I)}$ interaction

The geometry about the diamond core of complex **2** is extremely rare given the extremely short distance between two $Ni^{(I)}$ centers. Such a short distance between the metal centers is likely the result of ligand backbone rearrangement, which subsequently leads to a strained coordination environment. To address the geometry and the magnetic behavior of **2** we examined this system using high level DFT calculations (at the PBE/cc-pVTZ(-f) level of theory).

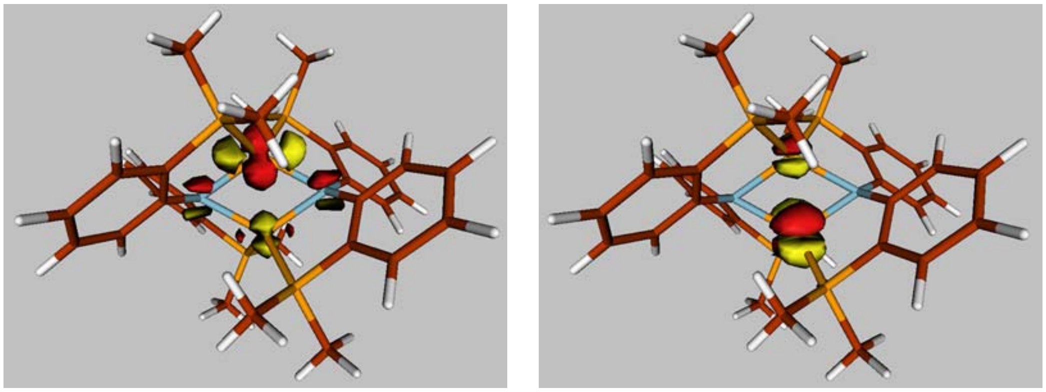

SOMO1 SOMO2

Figure 8: SOMO1 (d_{xz} on one Ni center) and SOMO2 (d_{yz} on the other Ni center) for the simplified model of **2** where the isopropyl groups have been simplified to methyl groups.

The simplified model (isopropyl groups of the phosphines have been reduced to methyl groups and methyl substitutions in the aromatic backbone have been reduced to hydrogen atoms) of **2** suggests that the two unpaired electrons are localized on the two metal centers whereby the SOMOs housing these spins do not hold the symmetry for interaction or delocalization (Figure 8). From the MO's (*vide supra*) it is quite evident that the single electrons are localized in independent $Ni^{(I)}$ centers and that such electrons are housed in antisymmetric d_{xy} and d_{xz} orbitals. Hence, there is no orbital overlap between the metal centers to suggest a metal-metal bond. In fact, the bridging nitrogens do not appear to cooperate in a Ni-N-Ni interaction, which could ultimately result in substantial antiferromagnetic coupling between the two $Ni^{(I)}$ centers. In a model experiment we observed that the short distance between two $Ni^{(I)}$ centers is mainly due to the ring constrain imposed by the two PNP ligands. Consistent with this hypothesis, computation of an analogous model complex $[Ni(PMe_3)_2(NMe_2)]_2$ using monodentate phosphines, result in much longer Ni⋯Ni distance (2.67 Å). Unfortunately we did not pursue more detailed theoretical studies as the current paradigm of DFT was not sufficient to address the spin state issues, particularly when two spin states are very closely in energy. For example, a hybrid functional B3LYP concluded the ground state of **2** to be $S = 0$, but the geometry of the complex was not reproduced well. On the other hand, a pure functional PBE reproduced the geometric features of the complex well, but did not locate $S = 0$ as the ground state. For the given problem of correct spin ground state assignment, a multi-reference method such as CASSCF can be useful, but we discarded the investigation due to the high cost associated with this type of calculation.

1.2.7 Trapping the Ni$^{(I)}$ monomer

Our data strongly suggests that **2** is a biradical species in the solid state both at room temperature and near absolute zero. After understanding the solid state behavior of **2** we attempted to understand the solution state behavior of the molecule. The results obtained by Evans magnetization measurements over a narrow temperature range do suggest an equilibrium being present but do not prove it conclusively. The possibility of monomer being formed from **2** was probed by treating a toluene solution with a strong Lewis base such as 4-N,N-dimethylaminopyridine. In that case no desired product was isolated. Fortunately, we detected the monomer in gas chromatography-mass spectrometry experiment of a hexane solution of **2** (calculated for monomer, 486.1989; found 486.1977), but this data could also imply that the dimeric core is fragile enough to be dissociated into monomer under the experimental condition of mass spectrometry. The most definitive proof for the monomer in solution was obtained by molecular weight determination using freezing point depression method of a 1.0% w/w solution of **2** in naphthalene at its melting point (Table 1).

Table 1: Molecular weight (MW) determination from melting point measurements of four samples of **2** in naphthalene.

sample	T	ΔT	MW
napthalene	80.25		
Sample1	80.08	0.17	259
Sample2	80.12	0.13	339
Sample3	80.13	0.12	367
Sample4	80.17	0.08	551

Similar cryoscopic methods have been used by others providing distinctive clue in addressing the solution state molecularity.[68,69] Four independent collection of data for **2** gives an average of 379(107) g/mol, which is clearly lower than the expected value for the monomer but within the limitation of the method. Therefore, these results advocate the presence of the monomer appears prevalent in solution at a temperature of 80 °C. We are still uncertain about the solution state behavior of **2** at room temperature or below since the cryoscopic experiment offers molecular weight value at 80 °C. However, whether the dimer is in equilibrium with the monomer is a question that remains unanswered despite our extensive spectroscopic studies. UV-Vis spectroscopy performed on toluene solution of **2** did not exhibit any significant change of the spectrum at room temperature and at 100 °C. From the above mass spectroscopic and cryoscopic experiments it is proved that complex **2** is predominantly a monomer in solution and this monomeric form (**2A**) is presumably responsible for the reactivity of the molecule (Scheme 4).

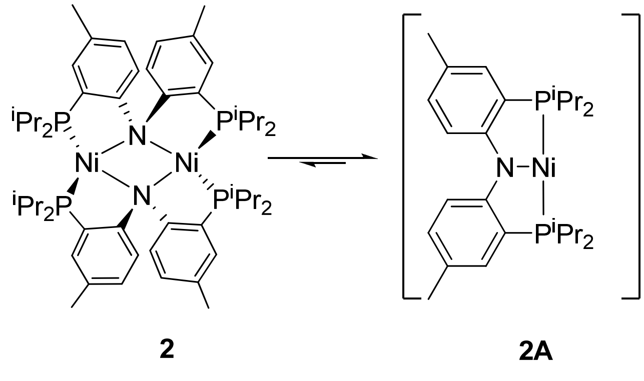

Scheme 4. Proposed equilibrium of monomer and dimer of **2** in Solution.

It is probable that the g value of a $Ni^{(I)}$ center in monomer is very similar to that of the dimer. The slight deviation of solution state isotropic g-value (2.205(5)) from solid state anisotropic g-values (average of the rhombic values is 2.214(4)) may be indicative of this kind of accidental degeneracy. Several attempts to trap the elusive monomer employing donors such as THF, PMe_3 and pyridine were unsuccessful. Gratifyingly we were able to trap the $Ni^{(I)}$ monomer by treating **2** in pentane along with 2 equivalents of N_2CPh_2. The reaction resulted in a gradual color change from dark green to brown concurrent with precipitation of the three-coordinate $Ni^{(I)}$ complex, Ni(PNP=NNCPh$_2$), **4** as a brown solid (Scheme 5). The paramagnetic material was isolated in 61% yield after crystallizing from concentrated solution of hexane. The identity of the $Ni^{(I)}$, a d^9 center, is further clarified by the solution state magnetic moment (2.22(3) μ_B) established by the method of Evans (300 K) which is consistent with a magnetic moment for a S = ½ species. The metal based nature of the radical was further proved by a broad solution X-band EPR spectrum, revealing a signal at $g_{iso} = 2.19$. The EPR signal is significantly broadened (line width, W = 55 G) due to unresolved hyperfine coupling with proximal nuclear spins such as ^{31}P (I = ½, 100% abundance) and ^{14}N (I = 1, 99.64% abundant). To unambiguously determine the degree of aggregation and geometry of paramagnetic **4** we collected single crystal X-ray diffraction data. The solid state structure unequivocally represents a three coordinate $Ni^{(I)}$ center trapped in a T-shaped geometry where one of the pendant phosphorus arms composing the PNP framework has been oxidized by the diazo unit to furnish a monosubstituted (phosphoranylidene) hydrazone group (PNP=N–NCPh$_2$) (Figure 9). The α-N of the (phosphoranylidene) hydrazone moiety is bound to the nickel center.

Examples of three coordinate $Ni^{(I)}$ centers are relatively rare and represent unprecedented reactivity pattern.[15,70-79]

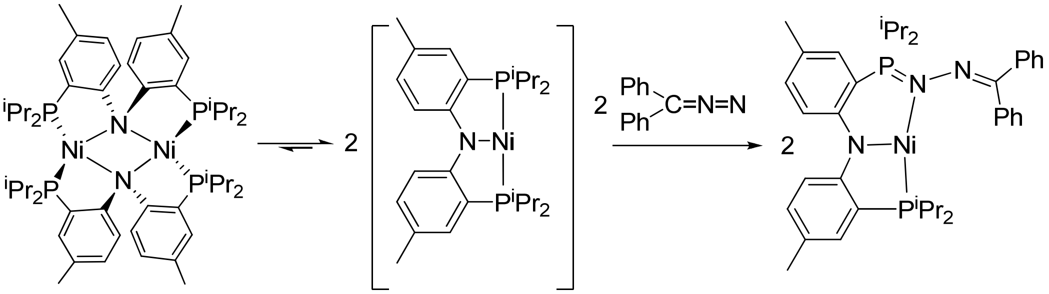

Scheme 5: Trapping the Ni(I) monomer using diphenyl diazomethane.

Ylide bond formation (N=P distance is 1.678(8) Å) results from the coordination of third nucleophilic site to the $Ni^{(I)}$ center (Ni–N, 1.913(8) Å), a parameter comparable to the Ni–N_{amide} distance of 1.979(9) Å obtained for the pincer amide group. From the crystal structure it is evident that one of the phenyl rings from the diazo fragment blocks the open site of the $Ni^{(I)}$ ion. Tantalizingly, it seems that there is some electron donation from the metal center to phenyl ring.

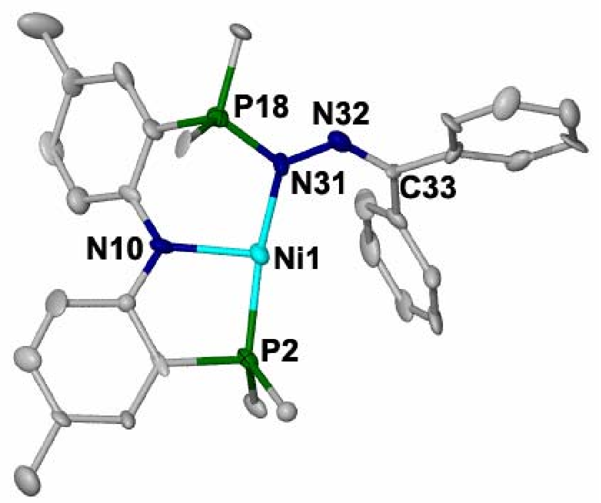

Figure 9. Molecular structure of **4** depicting thermal ellipsoids at the 50% probability level. Solvent, hydrogens and methyls in isopropyls have been omitted for clarity. Selected metrical parameters (lengths in Å, angles in degree): Ni1-N10, 1.979(9); Ni1-P2, 2.158(3); Ni1-N31, 1.923(8); N31-N32, 1.408(10); C33-N32, 1.311(12); P18-N31, 1.678(8), N10-Ni1-P2, 88.4(3); N31-Ni1-N10, 98.5(3); P18-N31-Ni1, 115.2(4); N32-N31-Ni1, 125.8(7); C33-N32-N31, 114.4(9).

However, the distance between the metal center and the centroid of the ring is > 2.92 Å, which is longer than the distance observed for a legitimate interaction. A Cambridge structural data analysis revealed a value 2.3-2.4 Å to be the limit of such distance invoking any significant interaction. Although complex **4** represents a trapped version of the $Ni^{(I)}$ monomer in **2**, it still casts some doubt as to whether this species was generated from the monomer or the dimer. Given the sterically congested environment in **2** it is not unreasonable to consider that complex **4** originates from the reaction of N_2CPh_2 with a putative (PNP)Ni monomer in solution. Other attempts to trap the $Ni^{(I)}$ radical using TEMPO (2,2,6,6-tetramethyl-1-piperidine-N-oxyl) unfortunately led to a myriad of non characterizable products. In addition, single electron oxidation of **2** using $Fc^*B(C_6F_5)_4$ failed to provide a mixed valent $Ni_2^{(I,II)}$ diamond core. This result implies that the Ni_2N_2 core in **2** is not robust enough to oxidation by ultimately retaining its original core structure. Peters and coworkers have reported an amido bridged Cu_2N_2 core that undergoes single electron oxidation to generate a class III delocalized $Cu^{1.5}Cu^{1.5}$ species with minimal structural reorganization in the core.[49] The failure of the single electron oxidation in **2** indirectly suggests the fragility of the Ni_2N_2 diamond core.

1.3.1 Biradical type reactivity of 2

Considering **2** as a dimer in the solid state, this species behaves as a biradical where the two unpaired electrons in each $Ni^{(I)}$ center appears to interact independently. From this standpoint, complex **2** behaves as a masked three coordinate $Ni^{(I)}$ synthon. To address the hypothesis of biradical type nature in **2**, we attempted to reductively cleave a variety of bonds, since $Ni^{(I)}$ centers are generally good reducing agents. As shown in Scheme 6, treatment of **2** with 2 equivalents of trityl chloride in ether affords green blocks of **1** with concurrent formation of Gomberg's dimer,[80-82]quantitatively. Gomberg's dimer is separated by washing the crude mixture several times with pentane and **1** is isolated in pure form in 76% yield (Scheme 6).

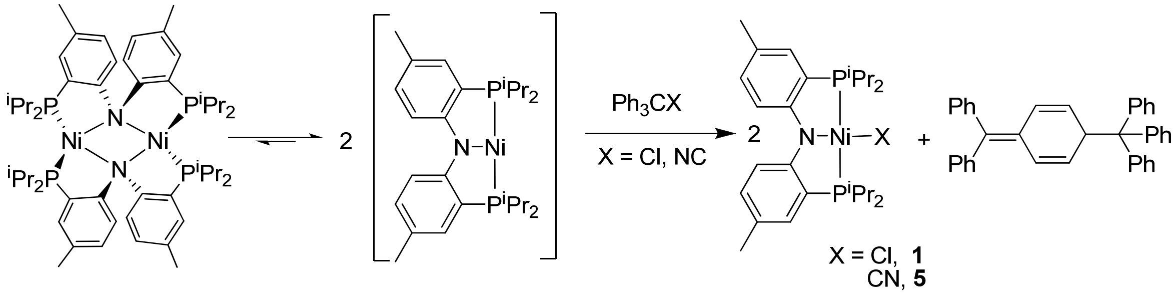

Scheme 6: Biradical type reactivity of **2** to cleave C-Cl and C-N bonds

Gomberg's dimer forms through radical recombination of •CPh_3 after reduction of the trityl cation by the $Ni^{(I)}$ center. Similarly, treatment of **2** with 2 equivalents of trityl isocyanide also results in redox chemistry to generate (PNP)Ni(CN) (**5**) along with the formation of Gomberg's dimer. Complex **5** has been characterized by its diagnostic peak in ^{13}C NMR spectrum at 119.5 ppm which is a triplet due to the splitting by attached nitrogen (I = 1, 100% abundant). The C-N stretch is also clearly observed at 2243 cm^{-1} in the IR spectrum (in nujol) and consistent with our claim for the identity of **5**. Since the diamond core in **2** was fragile in solution, we were interested to examine whether it could exchange with other $[(\mu_2\text{-PNP})Co]_2$ diamond core reported from our group.[59] No reaction was observed when **2** was mixed with $[(\mu_2\text{-PNP})Co]_2$ in THF and heated to 60 °C. In contrast Pd-dimers reported by Ozerov and co-workers exchanged between themselves to form a mixed dimer upon heating at 75 °C (Scheme 7).[83]

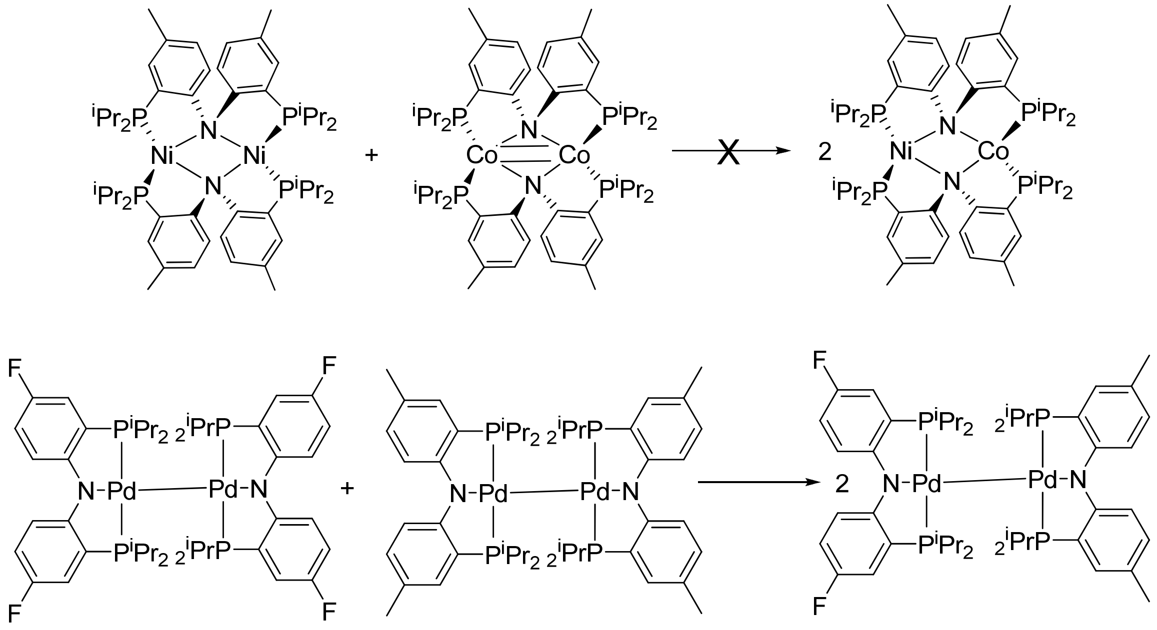

Scheme 7: Exchange reaction does not take place between **2** and [(μ_2-PNP)$_2$Co$_2$] but does take place in Pd-dimers reported by Ozerov *et al.*

The biradical nature of the Ni$_2$N$_2$ diamond core is also manifested by its ability to reduce the S–S and Se–Se bonds, presumably via a homolytic bond reduction process (Scheme 8). When **2** is treated with an equal molar amount of PhS–SPh in cold hexane, a dark brown color results after 1 hour of reaction to yield (PNP)NiSPh (**6**) quantitatively (by ^{31}P NMR spectroscopy). Complex **6** is diamagnetic which the anticipated electronic state for a square planar geometry around Ni$^{(II)}$. Furthermore, the ^{31}P NMR spectrum of **6** displays a single resonance at 33.65 ppm consistent with a C$_{2v}$ symmetric system. Likewise, compound (PNP)NiSePh (**7**) is obtained in quantitative yield (by ^{31}P NMR spectroscopy) when **2** is treated with PhSe–SePh and reacted for 1 hour. Structurally, complex **7** should be very similar to **6**, which is evident from similar ^{1}H NMR spectrum. Most notably, a single resonance at 36.44 ppm in ^{31}P NMR spectrum and two sets of isopropyl methyl resonances in ^{1}H NMR spectrum substantiates the fact of a C_{2v} symmetric system in solution.

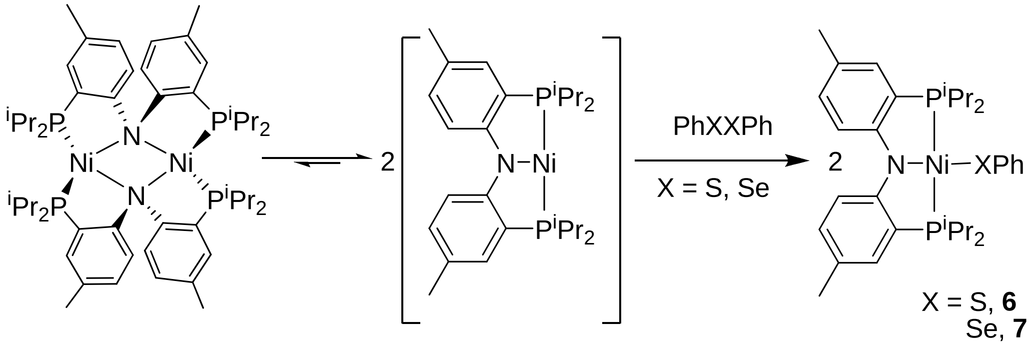

Scheme 8: X-X Type bond cleavage reactions promoted by **2**.

Riordan *et al.* have reported S–S bond cleavage reactions of elemental sulfur by a Ni$^{(I)}$ center in [PhTt^{tBu}]Ni(CO)[84] [PhTt^{tBu} = phenyl{tris[tert-butylmethyl)thio]-methyl}borate]. In their case the product possesses a μ-η^2: η^2- S_2 ligand fostering antiferromagnetic exchange coupling between two Ni$^{(II)}$ ions. Furthermore, Hillhouse *et al.* reported a similar reaction to ours: reductive cleavage of the S–S bond in PhSSPh by a dimeric Ni$^{(I)}$ complex, [(dtbpe)NiCl]$_2$, (dtbpe = 1,2-bis(di-tert-butylphosphino)ethane).[85] It is worthy to note that nickel sulfides are effective catalysts for hydrogenation,[86] hydrodesulfurization[87] and have been explored as cathode material for rechargeable batteries.[88] From this viewpoint, **6** could be potentially used as a catalyst for hydrogenation or hydrosulfurization.

1.3.2 Reactivity of 2 to cleave H-X bonds

Complex **2** is amenable to two electron chemistry by splitting a wide variety of other homo and heterobonds. In addition to the X–X bonds (S–S and Se–Se), it is also capable of cleaving H−X bonds (X = H, OH, OMe, PHPh), which results the formation of a four coordinate (PNP)NiH (**3**) and the corresponding (PNP)Ni–X counterpart (X = H, **3**; OMe, **9**; PHPh, **10**; Bcat, **11**) (Scheme 9).

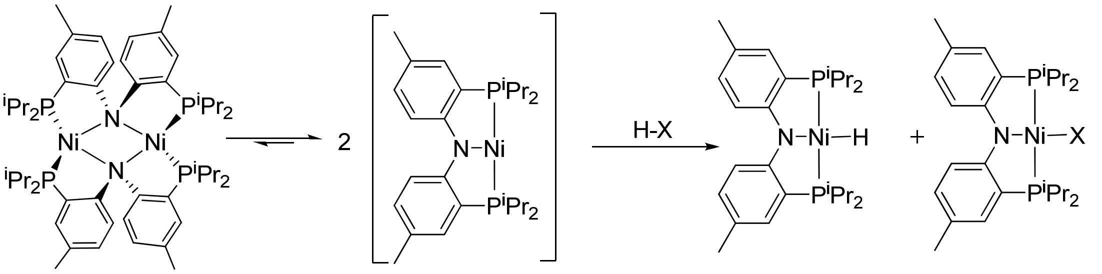

X = H, **3;** OH, **8**; OMe, **9**
PHPh, **10**; Bcat, **11**

Scheme 9. H−X type bond cleavage reactions promoted by **2** or its monomer **2A.**

Dimer **2** acts as a masked three-coordinate $Ni^{(I)}$ synthon, and Scheme 9 demonstrates very elegantly the reducing power of the $Ni^{(I)}$ complex supported by electron rich phosphine ligands. When a J-Young tube containing **2** is charged with H_2 in deuterated benzene, formation of **3** is instantaneous, which is revealed by the compound's characteristic ^1H and ^{31}P NMR resonances (*vide supra*). When the mixture is assayed by ^1H NMR spectroscopy, formation of **3** is cleanly manifested by hydride resonance at an upfield −18.4 ppm ($^2J_{P\text{-}H}$ = 60 Hz). Identity of **3** was also verified to the sample prepared independently following Ozerov's method of treating **1** with $NaBH_4$.[55] We discovered that **3** can also be prepared in moderate yield (57%) by treating **1** with Li^tBu. Furthermore, treatment of **2** with water results in the splitting of the O–H bond concurrent with the formation of diamagnetic, four-coordinate nickel hydroxo complex, (PNP)NiOH (**8**) and **3** in equal molar amounts. The most distinctive spectroscopic signature of the hydroxo ligand of **8** is its resonance appearing as a triplet at −5.06 ppm ($^3J_{P\text{-}H}$ = 6 Hz) in the ^{1}H NMR spectrum. Interestingly, there are only few structurally characterized examples of bridging and terminal hydroxo complexes of Ni in the literature.[89-93] In order to confirm the mode of hydroxo coordination we resorted to single crystal X-ray diffraction studies (Figure 10).

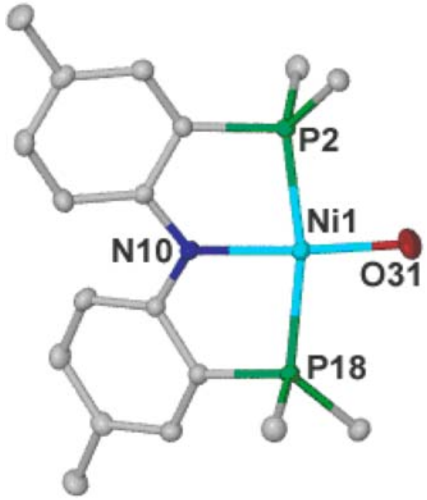

Figure 10: Molecular structure of **8** depicting thermal ellipsoids at the 50% probability level. Hydrogens and methyls of isopropyl groups have been omitted for clarity. Selected bond lengths (Å) and angles (degrees): Ni1-O31, 1.8634(9); Ni1-P2, 2.1883(4); Ni1-P18, 2.2025(4); Ni1-N10, 1.9125(8); N10-Ni1-O31, 176.52; N10-Ni1-P2, 84.13(3); N10-Ni1-P18, 83.98; O31-Ni1-P2, 92.39(3); O31-Ni1-P18, 99.50(3).

The X-ray structure of **8** displays a rare example of a mononuclear and terminal hydroxo complex of Ni$^{(II)}$ with the Ni$^{(II)}$ center possessing a square planar geometry. The most salient feature of the structure includes the Ni−O bond length of 1.8634(9) Å. The latter value seems shorter when compared to 1.955(2) Å observed in [Ni(tmc)(OH)](OTf) (tmc = 1,4,8,11-tetramethyl-1,4,8,11-tetraazadodecane) reported by Riordan group.[94] The terminal Ni−O bond length in our case is expectedly shorter than the bridging Ni−O bond lengths, 2.006(1) Å and 2.023(1) Å as reported in $[Ni_2(OH)_2(Me_2\text{-tpa})_2]^{2+}$ (Me_2-tpa = bis {(6-methyl-2-pyridyl)methyl}{(2-pyridyl)methyl}amine by Suzuki *et al.*[95] Unfortunately, the hydrogen atom of the hydroxide ligand is not found in the difference Fourier map (*vide supra*) due to the poor quality of the crystal. Gratifyingly the presence of hydroxyl hydrogen is evident from high level DFT calculations. Assuming the full model of **8** as the starting point geometry, geometrical optimization was performed at B3LYP/LACVP** level. The O–H bond length appears to be 0.97 Å from these calculations. Likewise, the proton of the hydroxide ligand can be unambiguously assigned since it readily exchanges with D_2O, confirmed by ^2H spectroscopy. Upon treating **2** with anhydrous MeOH, (PNP)NiOMe (**9**) along with **3** are formed but unfortunately the reaction is slightly contaminated with **8** given the problem of incomplete dehydration of MeOH. Complex **9** has been characterized by multinuclear NMR (^1H, ^{31}P, ^{13}C) and mass spectroscopy (MS-CI). The given complex displays a diagnostic ^1H NMR resonance at 3.30 ppm and ^{13}C NMR resonance at 57.37 ppm for the methoxy group. Complex **2** can also split P−H bonds as observed with treatment of 1 equivalent of PH_2Ph with **2** which after two hours affords (PNP)NiPHPh (**10**) along with equimolar formation of **3**. Notably, four coordinate terminal nickel phosphide complexes are extremely rare[96,97] and generating such a motif through P−H bond cleavage is unprecedented. This happens when phosphine binds to form adduct rather than further cleavage of P−H bond. Stephan and coworkers isolated such type of adducts, (nacnac)Ni(PH_2Ph) (nacnac = HC[C(Me)NC_6H_3(^{i}pr)$_2$]$_2$) and (nacnac)Ni($PHPh_2$) by simple adduct formation with Ni$^{(I)}$ precursor, [(nacnac)Ni]$_2$(μ-η^3:η^3-$CH_3C_6H_5$.[98] Since no P−H bond activation is observed, indirectly it proves the biradical nature of **2** is likely playing a role in P−H activation reaction. This contrasting feature with our complex **2**, i.e. adduct formation vs complete cleavage may largely derive from the different amount of electron donation to the P−H σ* orbital. We surmise more number of coordinating atoms to the Ni$^{(I)}$ center in PNP ligand makes the metal more electron rich compared to less number of coordinating atoms in nacnac, henceforth augmenting the Ni$^{(I)}$ center to promote more electron to the targeted antibonding orbital of the substrate. However, the influence of the electronic nature of the diamond core could play important role behind this transformation and should not be refuted as a possibility. In related work of P−H activation, several reports of catalytic oligomerization of PRH_2 (R = Ph, Cy, C_6H_2-2,4,6-Me_3) using a zirconium hydride catalyst has been reported by Stephan *et al.* [99,100]Our success in cleaving several H–X type bonds prompted us to cleave B–H bond to install a novel boryl moiety onto nickel which is hitherto unknown in literature. Gratifyingly, the strategy was successful as treatment of **2** with a THF solution of HBcat (cat = $O_2C_6H_4$) resulted equimolar formation of **3** and (PNP)NiBcat, **11**. Complex **11** was carefully characterized by multinuclear NMR spectroscopies, high resolution mass spectroscopy as well as solid state crystallographic analysis. The detailed characteristics of the molecule and chemistry performed by it will be discussed in Chapter 2. We speculate at this point that ammonia can also be cleaved by **2** to result nickel amido complex along with the formation of **3**. Unfortunately, attempt to engender (PNP)NiNH_2, (**12**) by cleaving NH_3

remained unsuccessful since the reaction of **2** with NH_3 resulted equal molar formation of **3** and **8**. The problem appears to originate from adventitious water present in the ammonia used and repeated trials to dry it were frustrated with failure. Complex **12** can be prepared independently from treating **1** with $LiNH_2$ (*vide infra*) and is exceptionally susceptible to moisture and as a consequence of which **12** may be converted into **8** in presence of even slight amount of moisture (*vide infra*). A $Pd^{(I)}$ system having pincer type ligands, $[(PNP)Pd]_2$, (PNP = $[N(2\text{-}P(CHMe_2)_2\text{-}4\text{-}RC_6H_3)_2]^-$, R = Me, F), has been recently shown to cleave NH_3 but the resulting product out of this cleavage reaction, $(PNP)PdNH_2$, is not as susceptible to moisture as **12** is.[83] Thermal cleavage of the molecule $[(PNP)Pd]_2$ in the solid state has been investigated by EPR spectroscopy which proves the notion that monomeric (PNP)Pd might be responsible behind the reaction. In addition to cooperative bimetallic cleavage few examples of cleaving NH_3 via a single metal center have been also documented in literature (Scheme 10).[101,102]

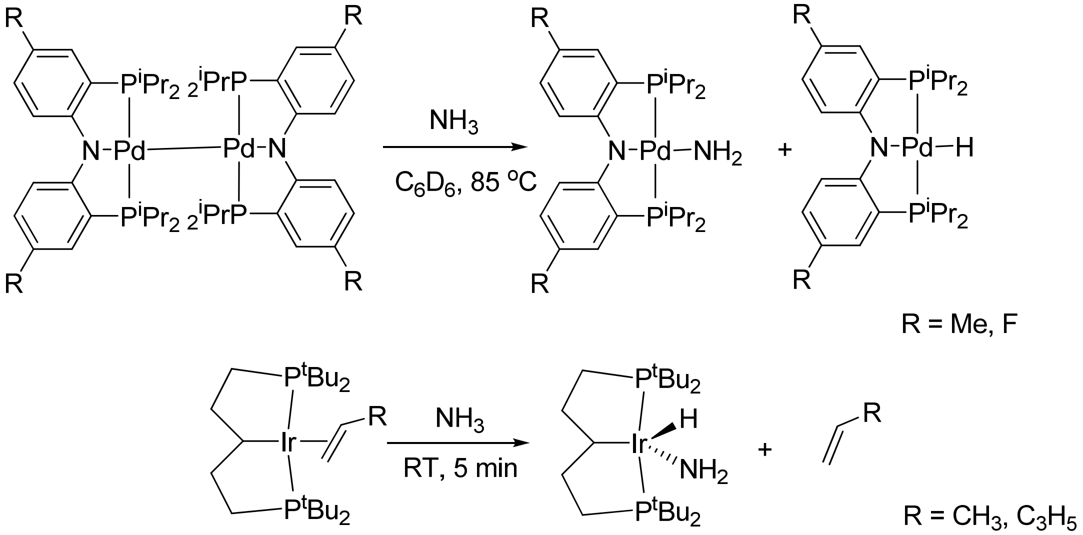

Scheme 10: Ammonia cleavage by dimer(top) and monomer (bottom).

So far we have been able to show a wide array of bond splitting reactions promoted by complex **2**. We were very intrigued by what the mechanistic pathway the molecule was following to smoothly perform these splitting reactions. Several plausible mechanistic pathways might be operational, and are discussed in Scheme 11.

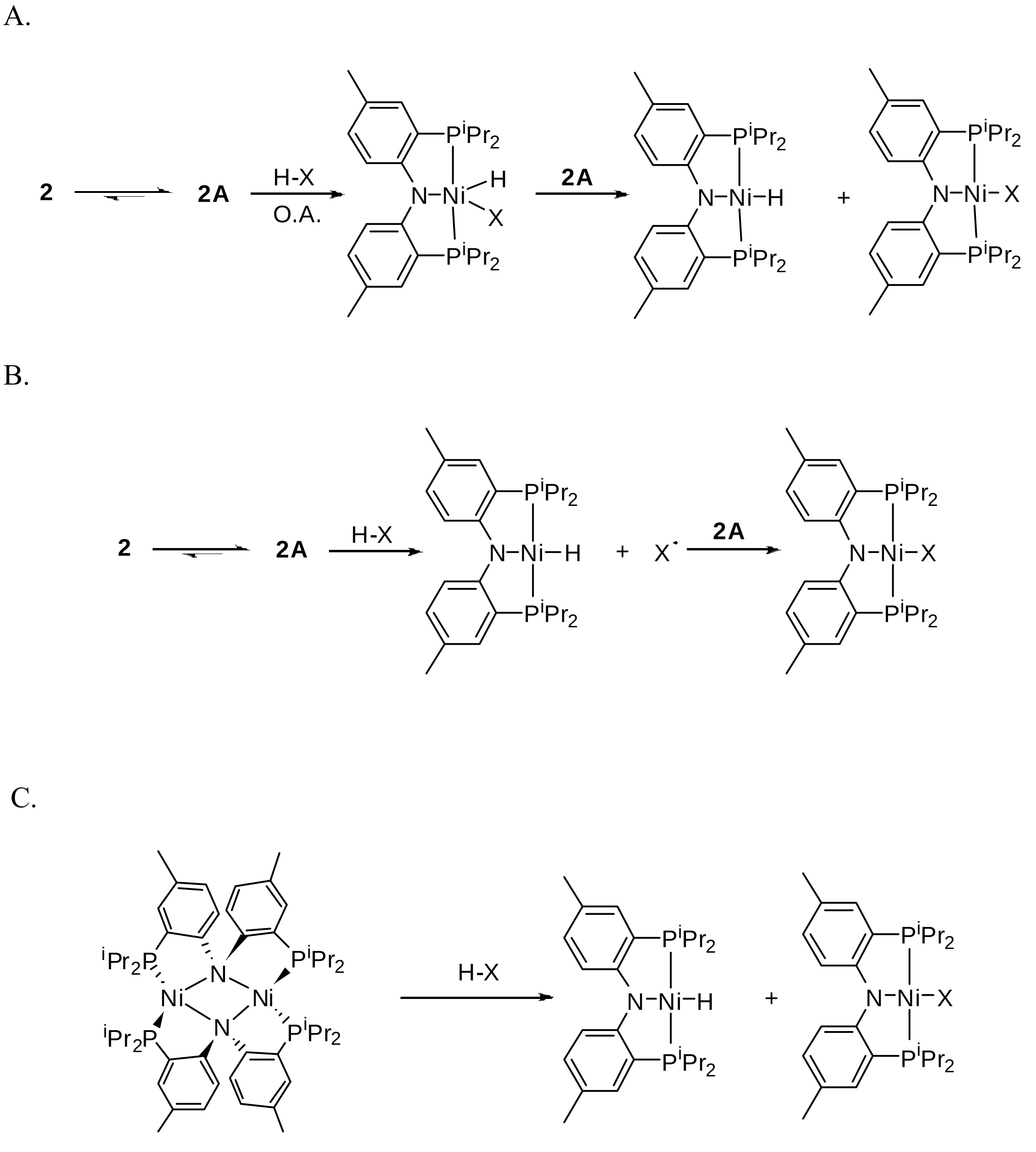

Scheme 11: Plausible mechanisms of H-X type bond cleavage reactions.

As shown by pathway A in Scheme 9, a Ni$^{(I)}$ monomer can oxidatively add a H−X bond to form a transient five coordinate intermediate. Comproportionation with the monomer **2A**, could generate **3** and an equimolar amount of the corresponding (PNP)NiX species. Alternatively, a radical chain reaction pathway is also feasible in which atom transfer radical (ATR) generates a X$^{\cdot}$ or H$^{\cdot}$ radical along with the formation of **3** or corresponding (PNP)NiX product (pathway B). A completely separate mechanism from the above mentioned ones will be the involvement of the dimer to carry out H−X bond cleavage in a concerted fashion, instead of using its monomeric counterparts. In such a scenario, the dissociation of the H−X bond can happen through binuclear oxidative cleavage in a cooperative manner (pathway C).[103-105] Throughout the course of H−X type bond cleavage reactions, no H_2 was detected, hence supporting the notion that a binuclear oxidative cleavage could be operative. At this point we prefer the first two pathways given the fact that **2** is mostly solvated or naked monomer in solution. However, we can not refute the possibility of forming a metal-metal bonded species, (PNP)Ni−Ni(PNP) along the pathway, analogously to that observed by Ozerov and co-workers.[83] Overall, the simple association of the H−X bond to the dimeric core and cooperative bond cleavage is not very likely given the steric congestion offered by the isopropyl groups surrounding the Ni_2N_2 diamond core. Since several substrates of our bond cleavage reactions are quite bulky, it is not probable to fit those across the two Ni$^{(I)}$ centers composing the core. Although, the labile nature of the phosphine arms may open up the coordination without perturbing the diamond core and consequently substrate binding may be facilitated.

1.3.3 Independent syntheses of 8−12

With the aid of **2** we have shown that a wide array of bonds can be cleaved, and thus we are able to assemble novel functionalities onto nickel$^{(II)}$. To unambiguously characterize the newly synthesized complexes **8−12,** we prepared these newly synthesized complexes without contamination of **3** by adopting an alternative synthetic method. Synthesis of these complexes, **8-10** and **12** has been achieved by applying salt metathesis of **1** with the corresponding Li or Na-salts (Scheme 12).

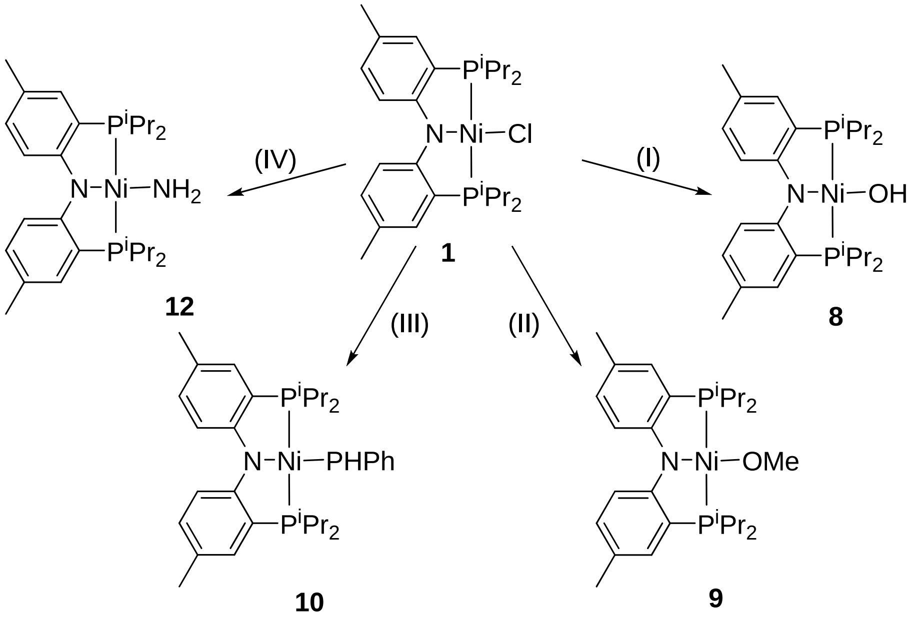

Scheme 12^b: Synthesis of terminal Ni-X bond (X = H, OH, OMe, PHPh, NH$_2$) by salt metathesis with **1.**^{b} Reagents and conditions used in the scheme are (i) KOH in H_2O, THF, −KCl (ii) KOH in MeOH, THF, −KCl (iii) LiPHPh, ether, −LiCl (iv) NaNH$_2$, Et$_2$O, −NaCl.

The terminal nickel hydroxo complex, **8**, can be synthesized by salt metathesis of **1** with KOH in water. The byproduct KCl, is partially soluble in water, hence complete formation of **8** never occurs given the equilibrium to regenerate **1**. As a result, a large excess of KOH can be used, and this does improve the extent of conversion, but isolation of **8** is always marred with content of **1**. Further we figured out that **8** can be prepared cleanly by treating degassed water with **12**. Independent synthesis of **9** was accomplished by treating **1** with KOH in methanol. Similarly, independent synthesis of **10** follows treatment of LiPHPh with **1** in ether resulting a rapid color change of the reaction mixture from green to red. The reaction was completed after 1 hour after which the byproduct LiCl was discarded by filtration. Filtered ethereal solution was concentrated and cooled at −35 ^{o}C to afford red crystals of **10** in 71% yield. The ^{1}H NMR spectrum of **10** displays the characteristic resonance for phosphido α-hydrogen at 3.64 ppm ($^{1}J_{\text{P-H}}$ = 179 Hz, $^{3}J_{\text{P-H}}$ = 20 Hz). The proton of the phosphine ligand is resolved into a doublet of triplets ratifying the presence of two inequivalent phosphorus nuclei in the complex. The other interesting feature of the salt metathesis reaction to prepare rare functional groups on nickel is the clean preparation of terminal parent nickel amide complex, (PNP)NiNH$_2$, **12**, synthesized from (PNP)NiCl and NaNH$_2$. Terminal amides of nickel are rare possibly due to contrasting combination of a soft late transition metal with a hard donor ligand such as an amide.[106] Lone pair repulsion between the electronegative atom with d-electron rich metal center also decreases the stability of such complexes.[107]In general, late metal alkoxide and amides are very prone to β-hydride elimination leading to metal hydride since weak M−O and M−N bonds lower the intrinsic barrier to β-hydride elimination. To the best of our knowledge, only one structurally characterized mononuclear nickel amido has been reported so far.[108] Complex **12** is soluble in most of organic solvents and ^{1}H NMR spectrum reveals a broad triplet at −2.30 ppm ($^3J_{P\text{-}H}$ = 8 Hz). The triplet nature of the resonance originates from the coupling with the two equivalent phosphorus atoms of the PNP, and not the nitrogen, since the ^{1}H{^{31}P} NMR spectroscopic experiment displays a singlet. The earlier assignment of amide protons is also substantiated by the IR absorptions associated with γ_{as} and γ_s stretching modes at 3359 and 3289 cm^{-1} respectively. To know the connectivity and nuclearity of complex **12** we evaluated its structure by single crystal X-ray diffraction analysis. Although crystals were found to be badly split and twinned, the molecular structure unambiguously proves a terminal amido motif as well as the square planar geometry around nickel. (Figure 11).

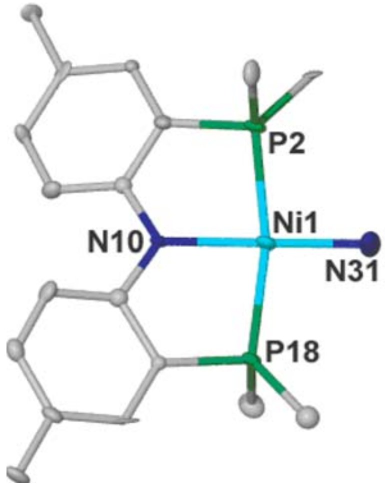

Figure 11: Molecular structure of **12** depicting thermal ellipsoids at the 50% probability level. Hydrogen atoms and methyls of isopropyl groups have been omitted for clarity. Selected bond lengths (Å) and angles (degrees): Ni1- N3, 1.884(9); Ni1-P18, 2.195(4); Ni1-P2, 2.192(4); Ni1-N10, 1.931(7); N10-Ni1-N31, 179.3(6); N10-Ni1-P2, 84.0(3); N10-Ni1-P18, 95.9(4); N31-Ni1-P2, 96.1(4).

The hydrogens in molecular structure of **12** are not located in the difference Fourier map due to the badly twinned nature of the crystal. The Ni1−N31 bond distance in complex **12** is found to be 1.884(9) Å (Figure 11), which is very similar to the first reported Ni−N bond length as 1.872(2) Å in (PCP)Ni−NH_2 (PCP^- = 2,6-bis((diisopropylphosphino)methyl)phenyl). [108] The Ni−N bond is appreciably longer than the reported Ni=N bond length of 1.702(2) Å by Hillhouse *et al.* for the three coordinate nickel-imido complex, Ni(=NC_6H_3-2,5-$^iPr_2$)(dtbpe) (dtbpe = 1,2 bis(di-tertbutylphosphino)ethane).[73] Complex **12** reacts vigorously with water to afford **8** very cleanly along with liberation of ammonia as monitored by ^1H NMR spectroscopy. Complex **11** can be synthesized independently by treating **3** with catecholborane at room temperature. The detail of the synthesis as well as the full characterization has been described in Chapter 2.

1.4 Conclusions

To summarize, we have synthesized a $Ni^{(I)}$ complex, **2**, having a Ni_2N_2 diamond core inferred by its single crystal X-ray structure. The $Ni^{(I)}$ species was prepared by single electron reduction of **1** in THF. The diamond core in **2** is formed after significant rearrangement of the ligand backbone which transforms from a terminal chelating mode to a bridging mode via the amide N. This Ni_2N_2 diamond core exhibits interesting magnetic properties whereby the two $Ni^{(I)}$ metal centers are extremely weakly coupled to each other despite the very short distance between them. A series of magnetization and spectroscopy studies provide strong proof of the S = 0 being the ground state of the molecule, and having a S = 1 state extremely close in energy (J = 1.52(50 cm^{-1}). Due to such low lying S = 1 excited state, we observe the triplet state behavior of the molecule at ambient temperatures. Although the solid state structure appears to be a dimer, we have credible evidence to suggest a monomer-dimer equilibrium scenario appears to dominate the solution state, predominantly populated by the monomer. Fortunately, we can trap the three coordinate $Ni^{(I)}$ species by reacting **2** with Ph_2CN_2. Our results present compelling evidence to suggest that a dinuclear $Ni^{(I)}$ radical based system engages in H−X splitting reactions. The two $Ni^{(I)}$ centers in **2** appear to be reducing the substrates in a bimetallic oxidative cleavage pathway, since no hydrogen has been detected for the aforementioned reactions. Alternatively, the fragile core of the dimer is transformed into monomers in solution and the monomer is responsible for the discussed reactivity. Although we can not refute the possibility of PNP framework in **2** rearranging, in the presence of substrates, to a metal−metal bonded species (PNP)Ni−Ni(PNP) which further dissociates into a monomer and react with the substrate. A recent report from Ozerov and coworkers documents the cleavage of small molecules (H_2, H_2O, NH_3) via a $(PNP^R)Pd{-}Pd(PNP^R)$ (R = F, Me).[83] Their study suggests that monomer is formed in solution since it forms a mixed dimer with the form $(PNP^{Me})Pd{-}Pd(PNP^F)$. In our case such an exchange reaction did not take place when **2** was treated with $[(\mu_2\text{-PNP})_2Co_2]$. However, similar reactivity pattern of **2** might be transpiring from the same kind of intermediate species as observed by Ozerov *et al*. In addition, the monomer (PNP)Ni can promote a radical chain reaction analogous to the well documented examples such as $[Co(CN)_5]^{3-}$, and other metal radicals such as $Rh^{(II)}$ and mixed valent Ir_2 cores.[103,104,109] Interestingly, H-H bond cleavage (bond enthalpy 104.05 kcal mol^{-1}) by **2** takes place almost instantaneously whereas S-S bond cleavage (bond enthalpy 101.50 kcal mol^{-1}) is completed in an hour.

Such a different time of reaction is indicative of two different mechanisms, bimetallic oxidative cleavage and reaction promoted by the monomer might be taking place. Indirectly that also proves the presence of equilibrium between monomer and dimer of **2** in solution. The variety of bonds which can be cleaved by **2** encompasses H-H, H-OH, H-OMe, H-PPh, S-S, Se-Se, C-Cl, C-NC. With the facilitated H-X bond cleavage performed by **2**, this route may be amenable to incorporate varieties of important functionalities onto nickel such as hydroxo, parent amido, boryl etc.

1.5 Experimental Section

General Procedures. Unless otherwise stated, all operations were performed in a M. Braun Lab Master double-dry box under an atmosphere of purified nitrogen or using high vacuum standard Schlenk techniques under an argon or dinitrogen atmosphere. Anhydrous *n*-hexane, pentane, toluene, and benzene were purchased from Aldrich in sure-sealed reservoirs (18 L) and dried by passage through two columns of activated alumina and a Q-5 column.[110] Diethylether was dried by passage through a column of activated alumina.[110] THF was distilled, under nitrogen, from purple sodium benzophenone ketyl and stored over sodium metal. Distilled THF was transferred under vacuum into thick walled reaction vessels before being carried into a dry box. Deuterobenzene was purchased from Cambridge Isotope Laboratory (CIL), degassed and vacuum transferred to a storage vessel where it was kept over 4 Å molecular sieves. All other deuteron solvents were stored under sodium metal. Celite, alumina, and 4 Å molecular sieves were activated under vacuum overnight at 200 ºC. $NiCl_2(THF)_{1.5}$[54] (PNP)H,[51] Li(PNP),[51] KC_8,[111] Ph_2CN_2,[112] and LiPHPh[113] were prepared according to the literature methods. All other chemicals were purchased from Strem Chemicals or Aldrich and used as received. CHN analyses were performed by Desert Analytics, Tucson, AZ. ^1H, ^{13}C, ^{11}B and ^{31}P NMR spectra were recorded on Varian 500, 400 or 300 MHz NMR spectrometers. ^1H and ^{13}C NMR are reported with reference to residual solvent resonances. ^{31}P NMR chemical shifts are reported with respect to external H_3PO_4 (0.0 ppm). ^{11}B NMR chemical shifts are reported with respect to external $BF_3.OEt_2$ (0.0 ppm). Magnetic moments were obtained by the method of Evans.[114,115]UV-visible spectra were recorded on a Cary 5000 UV-vis-NIR spectrophotometer. For the variable temperature UV-vis experiment, the sample in the cuvette was cooled and heated by an external cooler regulated by Peltier effect. Magnetization measurements were performed on a Quantum Design SQuID susceptometer at 0–5 T and 2–300 K. Susceptibility data was fitted using the program JulX version 1.3 written by Dr. Eckhard Bill, Max-Planck-Institut für Bioanorganische Chemie, Mühlheim an der Ruhr, Germany. X-ray diffraction data were collected on a SMART6000 (Bruker) system under a stream of N_2 (g) at low temperatures. The EPR measurements were performed in quartz tubes equipped with J-young valves. EPR spectra were recorded on a JEOL continuous wave spectrometer JES-FA200 equipped with an X-band Gunn diode oscillator, a cylindrical mode cavity and a helium cryostat. EPR data for **4** were recorded in a Bruker EMX EPR instrument. EPR data was simulated using the full matrix diagonalization program ESRSIM written by Høgni Weihe, University of Copenhagen, Denmark.[116]

Cyclic Voltammetry (CV) Details. In a typical CV experiment, 0.3 M $[N(^nBu)_4]PF_6$ in THF was used as a supporting electrolyte where 15–20 mg of crystalline **1** was dissolved in ~ 5 mL of TBAH solution in THF at 25 °C. A platinum disk (2.0 mm diameter, Bioanalytical Systems), a platinum wire, and silver wire were employed as the working electrode, the auxiliary, and the reference electrode, respectively. A one compartment cell was used in the CV measurement. The electrochemical response was collected with the assistance of an E2 Epsilon (BAS) autolab potentiostat/galvanostat with the BAS software. All the potentials were reported against ferrocenium/ferrocene ($Fc^{+/0}$) couple (0.0 V) measured as an internal standard, and spectra were recorded under a N_2 atmosphere.

Molecular Weight Determination

This procedure follows an earlier protocol reported by Holland *et al.*[68] A mixture of **2** (1.8 mg) and naphthalene (sublimed, 185 mg) was heated until the brown solution formed. After cooling, an aliquot of the brown solid was placed in a capillary, which was plugged with silicon grease and flame-sealed. Melting point depressions, compared to that of authentic naphthalene (average of two sample runs which were sublimed prior to usage), were measured on a Thomas-Hoover melting point apparatus, using a VWR precision 0.01 Thermometer equipped with a Pt-100Ω sensor. Molecular weights were determined using the formula molecular weight = K.w.1000/ΔT.W, where K = 4.9 for the naphthalene, w = mass of complex **2,** W = mass of naphthalene and ΔT = temperature depression. The obtained data has been presented in Table 1 (see text).

Synthesis of Complex (PNP)NiCl (1). Complex **1** was prepared by a modified procedure to the literature and the identity of the product was confirmed by ^1H and ^{31}P

NMR spectra to independently prepared samples.[55] In a 500 mL round-bottom flask $NiCl_2(THF)_{1.5}$ (500 mg, 2.10 mmol) was suspended in toluene (250 mL) and Li(PNP) (915.50 mg, 2.10 mmol) in 10 mL of toluene was added dropwise to the suspension. The mixture was stirred for 12 hours at room temperature after which the volatiles were evaporated completely in vacuo. The residue was extracted with toluene, filtered and the filtrate concentrated and cooled to −35 ^oC to afford green crystals of (PNP)NiCl (**1**) (1.05 g, 2.02 mmol, 96 % yield). Anal. Calcd for $C_{26}H_{40}NP_2NiCl$: C, 59.74; H, 7.71; N 2.68. Found: C, 60.92; H, 7.69, N, 2.46. M.p. 178(2) ^oC.

Synthesis of Complex $[Ni(\mu_2\text{-}PNP)]_2$ (2). Compound **1** (200 mg, 0.38 mmol) was taken in a vial with ~ 5 mL of THF and the solution cooled to −35 ^oC. An analogously cold suspension of KC_8 in THF (56 mg, 0.42 mmol) was added to the nickel solution. The reaction mixture was stirred for 1 hour and the dark suspension was then dried under reduced pressure. The dried mass was extracted with hexane, filtered and the filtrate kept cold (−35 ^oC) for two days to isolate brown crystals of $[Ni(\mu_2\text{-}PNP)]_2$ (**2**) (115 mg, 0.12 mmol, 62 % yield). ^1H NMR (25 ^oC, 399.8 MHz, C_6D_6): δ 16.68 (br, $\nu_{1/2}$ = 279 Hz) , 8.41 (br, $\nu_{1/2}$ = 96 Hz), 4.53 (br, $\nu_{1/2}$ = 53 Hz), 2.85 (br, $\nu_{1/2}$ = 347 Hz), 1.25 (br, $\nu_{1/2}$ = 22 Hz), 0.89 (br, $\nu_{1/2}$ = 6 Hz). μ_{eff} : 2.84 (1) μ_B (C_6D_6, 25 ^oC, Evans method). Anal. Calcd for $C_{52}H_{80}N_2P_4Ni$: C, 64.08; H, 8.23; N 2.87. Found: C, 64.36; H, 8.17, N, 2.86. UV-Vis (hexane, λ in nm, ε in $mol^{-1}cm^{-1}$): 616 (826), shoulder at 475 (2521), shoulder at 438 (4526), shoulder at 390 (8383). M.p. 148(2) ^oC.

Bond Splitting Reaction of 2 with H_2. Synthesis of Complex (PNP)NiH (3). In a J-Young tube complex **2** (40 mg, 0.041 mmol) was dissolved in C_6D_6 and degassed by standard freeze-pump-thaw technique. Excess amount of dihydrogen gas was passed through the solution during which the brown color changed to yellowish after 10 min. Examination by ^{1}H and ^{31}P NMR spectra confirmed quantitative formation of compound **3**.

Synthesis of Complex Ni(PNP=NNCPh$_2$) (4). In a vial **2** (75 mg, 0.08 mmol) was dissolved in ~5 mL of hexane and cooled to −35 °C. In a separate vial Ph_2CN_2 (29.9 mg, 0.15 mmol) was taken in hexane and cooled to −35 °C. Ph_2CN_2 solution was added dropwise to **2** and stirred for 2 hours. During the course of the reaction (~20 minutes) a brown colored precipitate appears. After completion of the reaction the reaction mixture was filtered and the brown colored residue was collected and washed with 10 mL of hexane. The product was dried, redissolved in a minimum of toluene (~2 mL) and then added two drops of hexane in the toluene solution from which brown colored crystals were obtained at −35 °C (63.8 mg, 0.09 mmol, 61% yield). ^{1}H NMR (25 °C, 399.8 MHz, C_6D_6): δ 8.21 (br, $\nu_{1/2}$ = 36 Hz), 7.69 (m, aryl), 7.35 (m, aryl), 7.02 (m, aryl), 2.11−1.99 (br, *Me*Ar and C*H*Me$_2$ resonances overlapped), 1.23 (br, CH*Me*$_2$), 0.89 (br, CH*Me*$_2$). μ_{eff}: 2.22(3) μ_B (C_6D_6, 25 °C, Evans method). M.p. 118(2) °C. Multiple attempts to obtain a satisfactory combustion analysis data failed given the thermal instability of the complex.

Synthesis of (PNP)NiCN, (5)

In a vial **2** (75 mg, 0.07 mmol) was dissolved in 3 mL of diethyl ether and cooled to −35 ^{o}C . An analogously cooled solution of trytil isocyanide (39.6 mg, 0.15 mmol) was added dropwise to the solution of **2**. After 10 hours the reaction mixture was evaporated in vacuo, extracted with pentane and filtered. The filtrate solution was cooled to −35^{o}C to afford green crystals of **5** (48 mg, 0.09 mmol, 60.8% yield). ^{1}H NMR (25 ^{o}C , 399.8 MHz, C_6D_6): δ 7.41(d, C_6H_3, 2H), 6.82 (s, C_6H_3, 2H), 6.68(d, C_6H_3, 2H), 2.22-1.98(br, C*H*Me$_2$, 4H), 2.09(s, *Me*Ar, 6H), 1.41 (dd, CH*Me*$_2$, 12H), 1.15 (dd, CH*Me*$_2$, 12H). ^{13}C NMR (25 ^{o}C, 100.6 MHz, C_6D_6):162.31(aryl), 132.56 (aryl), 131.92 (aryl), 129.97 (aryl), 125.51(aryl), 119.47(*C*N), 116.74 (aryl), 23.78 (*C*HMe$_2$), 20.37 (MeAr), 18.45 (CH*M*e$_2$), 17.67 (CH*M*e$_2$). ^{31}P NMR (25 ^{o}C, 121.5MHz, C_6D_6) δ 38.8.

Synthesis of Complex (PNP)Ni(SPh) (6).

Complex **2** (20 mg, 0.021 mmol) and diphenyldisulfide (4.6 mg, 0.021 mmol) were loaded into a J-Young tube in hexane. No immediate color change was observed after the loading. The reaction mixture was stirred for an hour and the brown color of the solution was intensified during the course of the reaction. The mixture was monitored by ^{31}P NMR spectroscopy until complete (1 hour). After this time the reaction mixture was dried in vacuo and the ^{1}H NMR spectrum showed quantitative formation of the product, **6**. ^{1}H NMR (25 ^{o}C, 399.8 MHz, C_6D_6): δ 8.04 (d, SC_6H_5, 2H), 7.54 (d, C_6H_3, 2H), 7.02 (t, SC_6H_5, 1H), 6.89 (m, overlapped resonances of aryl protons, 4H), 6.77 (d, C_6H_3, 2H), 2.22-2.08 (br, C*H*Me$_2$, 4H), 2.14 (s, *Me*Ar, 6H), 1.40 (dd, CH*Me*$_2$, 12H), 1.17 (dd, CHMe_2, 12H). ^{13}C NMR (25 ^{o}C, 100.6 MHz, C_6D_6): δ162.04 (aryl), 133.33 (aryl), 132.47 (aryl), 131.81 (aryl), 129.33 (aryl), 127.66 (aryl), 125.02 (aryl), 122.02 (aryl), 121.41 (aryl), 116.15 (aryl), 24.54 (CHMe$_2$), 20.53 (MeAr), 18.53 (CHMe_2), 17.65 (CHMe_2). ^{31}P NMR (25 ^{o}C, 121.5 MHz, C_6D_6): δ 33.65.

Synthesis of Complex (PNP)Ni(SePh) (7). Complex **2** (20 mg, 0.021 mmol) and diphenyldiselenide (6.6 mg, 0.021 mmol) were loaded into a J-Young tube along with hexane. The reaction mixture was stirred for an hour, and monitored by ^{31}P NMR spectroscopy, and during the course of the reaction brown color of the solution was intensified. After 1 hour the reaction mixture was dried in vacuo and the ^{1}H NMR spectrum showed quantitative formation of product, **7**. ^{1}H NMR (25 ^{o}C, 399.8 MHz, C_6D_6): δ 8.07 (d, SC$_6H_5$, 1H), 7.54 (m, overlapped resonances of aryl protons, 2H), 6.95 (m, overlapped resonances of aryl protons, 6H), 6.79 (d, C$_6H_3$, 2H), 2.21-2.06 (br, CHMe$_2$, 4H), 2.15 (s, MeAr, 6H), 1.41 (dd, CHMe_2, 12H), 1.18 (dd, CHMe_2, 12H). ^{13}C NMR (25 ^{o}C, 100.6 MHz, C_6D_6): δ161.70 (aryl), 136.28 (aryl), 132.39 (aryl), 131.90 (aryl), 131.73 (aryl), 129.40 (aryl), 124.94 (aryl), 124.00 (aryl), 121.86 (aryl), 116.13 (aryl), 24.83 (CHMe$_2$), 20.54 (MeAr), 18.94 (CHMe_2), 17.84 (CHMe_2). ^{31}P NMR (25 ^{o}C, 121.5 MHz, C_6D_6): δ 36.44.

Bond Splitting Reaction of 2 with H_2O. Synthesis of Complex (PNP)Ni(OH) (8) and 3. In a Schlenk flask complex **2** was dissolved (60 mg, 0.062 mmol) in 20 mL of THF. To the solution was added degassed water (purged with argon over 10 minutes, 0.04 mL, 1.24 mmol) by means of a syringe. The solution was stirred for 2 hours upon which the color of the reaction mixture rapidly changed from brown to green. Within an hour the solution was dried under reduced pressure. ^1H and ^{31}P NMR spectra of the reaction mixture revealed an equimolar formation of **3** and **8**.

Bond Splitting Reaction of 2 with CH_3OH. Synthesis of Complex (PNP)Ni(OCH_3) (9) and 3. CH_3OH (10 mL) was stirred over a few pieces of thin sodium film (~500 mg) for 16 hours and the solution filtered through alumina to obtain anhydrous reagent. Complex **2** (60 mg, 0.062 mmol) was taken in a vial and dissolved in THF (5 mL). To the brown solution was added via syringe anhydrous CH_3OH (1.98 mg, 0.062 mol) and the mixture stirred. During the course of 2 hours the reaction gradually changed from brown to reddish brown. After 2 hours of stirring the reaction mixture was dried under vacuo. ^1H and ^{31}P NMR spectra confirmed formation of **3** and **9** in an equimolar amount.

Bond Splitting Reaction of 2 with H_2PPh. Synthesis of Complex (PNP)Ni(PHPh) (10) and 3. In a vial was dissolved **2** (40 mg, 0.041 mmol) in 5 mL of THF and the solution cooled to −35 °C. An analogously cooled solution of phenylphosphine (4.52 mg, 0.041 mmol) in 2 mL of hexane was added dropwise to the cooled solution of **2**. The reaction mixture was stirred for 2 hours during which the color of the solution changed immediately from brown to red. The solution was then dried under reduced pressure and ^1H and ^{31}P NMR spectra confirmed an equimolar formation of compounds **3** and **10**.

Bond Splitting Reaction of 2 with HB(catechol). Synthesis of Complex (PNP)Ni[B(catechol)]) (11) and 3. In a vial compound **2** (50 mg, 0.053 mmol) was dissolved in 5 mL of hexane and the solution cooled to −35 °C. In a separate vial an analogously cooled solution of catecholborane (6.28 mg, 0.053 mmol) in hexane was added dropwise to the solution of **2**. The solution was stirred for 3 hours during which the color gradually changed from brown to yellowish. The solution was evaporated to dryness and ^{1}H and ^{31}P NMR spectra of the mixture confirmed an equalmolar formation of **11** and **3** as the only two products.

Attempted Bond Splitting Reaction of 2 with NH_3. Complex **2** (60 mg, 0.062 mol) was taken in Schlenk flask in ~ 5 mL of THF and in situ generated NH_3 [generated from $LiNH_2$ (7.02 mg, 0.31 mmol) and 2,6-diisopropylphenol (22.05 mg, 0.31 mmol) in ~ 10 mL THF) was passed through a vacuum adapter. The solution was stirred for 1 hour during the course of which the color of the nickel solution changed from brown to green. ^{1}H and ^{31}P NMR spectra of the reaction revealed the formation of an equalmolar of **3** and **8**. Note: Anhydrous NH_3 gas was generated *in situ* via the reaction of $LiNH_2$ and 2,6-diisopropyl phenol using two Schlenk flasks joined by a vacuum transfer bridge. Attempts to generate dry NH_3 from Na/NH_3 electride solution also resulted in quantitative formation of **3** and **8** from **2**.

Synthesis of Complex (PNP)Ni(NH_2) (12). Complex **1** (150 mg, 0.29 mmol) was dissolved in diethyl ether (~5 mL), cooled to –35 °C and a suspended amount of $NaNH_2$ (11.5 mg, 0.29 mmol) in diethyl ether was added dropwise. After stirring the reaction mixture for 8 hours the mixture was filtered and concentrated to ~2 mL. The concentrated solution was cooled to –35 °C for 48 hours to yield green crystals of **9**. (99 mg, 0.20 mmol, 69 % yield). ^{1}H NMR (25 °C, 399.8 MHz, C_6D_6): δ 7.58 (d, 2H, C_6H_3), 6.97 (s, 2H, C_6H_3), 6.77(d, 2H, C_6H_3), 2.16−2.02(br, 4H, C*H*Me$_2$), 2.12(s, 6H, *Me*Ar), 1.40 (dd, 12H, CH*Me*$_2$), 1.26(dd, 12H, CH*Me*$_2$), –2.30(t, 2H, N*H*$_2$). ^{13}C NMR (25 °C, 100.6 MHz, C_6D_6): δ 162.05 (aryl), 132.06 (aryl), 131.86 (aryl), 123.87 (aryl), 120.64 (aryl), 116.07 (aryl), 23.86 (*C*HMe$_2$), 20.56 (M*e*Ar), 18.74 (CH*Me*$_2$), 17.99 (CH*Me*$_2$). ^{31}P NMR (25 °C, 121.5 MHz, C_6D_6) δ 30.77. MS-CI, $[M+H]^+$, calcd 502.217, found 502. 189. M.p. 166(3) °C.

Independent Synthesis of Complex 8. Method A: Complex **1** (120 mg, 0.24 mmol) was dissolved in 50 mL of THF in a Schlenk flask. In a separate Schlenk flask KOH (752 mmolar solution, large excess) in water (1.92 mL, 1.44 mmol) was deareated by standard freeze-pump-thaw technique. To the cold (−78 °C) solution of nickel, the KOH solution in water was transferred via cannula and the reaction mixture was slowly allowed to warm up to the room temperature. After 4 hours of stirring the reaction mixture was dried under reduced pressure and extracted with pentane. The green color extract was filtered and cooled to isolate the desired product, **5** (53.2 mg, 0.106 mmol, 46% yield). The low yield was due to the unachieved completion of the reaction, supposedly stemming from the solubility of byproduct KCl which can drive the reaction in the backward direction. Crude product was always isolated along with the contamination of **1**. Method B: In a Schlenk flask complex **12** (100 mg, 0.20 mmol) was dissolved in 10 mL of hexane. Excess amount of deoxygenated water was added dropwise under a positive pressure of N_2 and the solution stirred for 10 minutes. After this time, the solution was dried under vacuo and green color product was collected (96 mg, 0.19 mmol, 96 % yield). ^{1}H NMR (25 °C, 399.8 MHz, C_6D_6): δ 7.52 (d, 2H, C_6H_3), 6.92 (s, 2H, C_6H_3), 6.70 (d, 2H, C_6H_3), 2.28-2.10 (br, C*H*Me$_2$, 4H), 2.16 (s, 6H, *Me*Ar), 1.51 (dd, 12H, CH*Me*$_2$), 1.29 (dd, 12H, CH*Me*$_2$), –5.06 (t, 1H, O*H*). ^{13}C NMR (25 °C, 100.6 MHz, C_6D_6): δ 162.26 (aryl), 132.10 (aryl), 131.94 (aryl), 124.16 (aryl), 120.78 (aryl), 116.94 (aryl), 23.46 (*C*HMe$_2$), 20.49 (*Me*Ar), 18.62 (CH*Me*$_2$), 17.87 (CH*Me*$_2$). ^{31}P NMR (25 °C, 121.5 MHz, C_6D_6) δ 26.89. MS-CI, $[M+H]^+$, calcd 502.217, found 502. 189 along with 486.2 corresponding to $(PNP)Ni^+$. M.p. 82(2) °C.

Independent Synthesis of Complex 9. In a Schlenk flask complex **1** (300 mg, 0.60 mmol) was dissolved in 50 mL THF. In a separate Schlenk flask was charged with KOH in methanol (0.58 mL, 0.60 mmol) and deareated by standard freeze-pump-thaw technique. To the cold solution (−78 °C) of nickel, the KOH in methanol was transferred via cannula and the reaction mixture was allowed to warm up to room temperature. After 3 hours of stirring the reaction mixture was dried in vacuo, extracted with pentane and filtered. From the filtrate brown colored crystals of $(PNP)Ni(OCH_3)$ (**9**) were isolated after cooling the solution −35 °C for 48 hours (234 mg, 0.45 mmol, 79% yield). ^{1}H NMR (25 °C , 399.8 MHz, C_6D_6): δ 7.43 (d, 2H, C_6H_3), 6.92 (s, 2H, C_6H_3), 6.71(d, 2H, C_6H_3), 3.30 (s, 3H, O*C*H$_3$), 2.28-2.12 (br, 4H, C*H*Me$_2$), 2.15 (s, 6H, *Me*Ar), 1.54 (dd, 12H, CH*Me*$_2$), 1.32 (dd, 12H, CH*Me*$_2$). ^{13}C NMR (25 °C, 100.6 MHz, C_6D_6): δ 162.26 (aryl), 132.12 (aryl), 131.95 (aryl), 124.52 (aryl), 120.03 (aryl), 116.61 (aryl), 57.37 (O*C*H$_3$), 23.63 (*C*HMe$_2$), 20.50 (*Me*Ar), 18.52 (CH*Me*$_2$), 17.78 (CH*Me*$_2$). ^{31}P NMR (25 °C, 121.5 MHz, C_6D_6): δ 24.61. MS-CI, $[M+H]^+$, calcd. 517.217, found 517.215. M.p. 128(2) °C.

Independent Synthesis of Complex 10. Complex **1** (100 mg, 0.19 mmol) was dissolved in 5 mL of diethyl ether and cooled to −35 °C. In a separate vial LiPHPh (22.2 mg, 0.19 mmol) was dissolved in 2 mL of diethyl ether and the solution cooled to –35 °C. LiPHPh solution was added dropwise to the nickel solution upon which the color changed to reddish brown after 5 minutes. After allowing the mixture to stir for 2 hours, the volatiles were removed under reduced pressure, the solid extracted with pentane, and the solution filtered. The filtrate was then concentrated and cooled to –35 °C over 4 days to afford red crystals of (PNP)Ni(PHPh) (**10**) (81 mg, 0.14 mmol, 71% yield). ^{1}H NMR (25 °C , 399.8 MHz, C_6D_6): δ 8.01 (t, 1H, PHAr), 7.68 (d, C_6H_3, 2H), 7.09- 6.98 (br, 4H, C_6H_3), 6.94 (d, 2H, PHAr), 6.84 (d, 2H, PHAr), 3.64 (doublet of triplets) 1H, NiP*H*Ph), 2.23-2.11 (br, 4H, C*H*Me$_2$), 2.18 (s, 6H, *Me*Ar), 1.26 (dd, 12H, CH*Me*$_2$), 1.11 (dd, 12H, CH*Me*$_2$). ^{13}C NMR (25 °C, 100.6 MHz, C_6D_6): δ161.24 (aryl), 136.67 (aryl), 132.44 (aryl), 132.04 (aryl), 129.33 (aryl), 127.50 (aryl), 126.00 (aryl), 124.33 (aryl), 121.02 (aryl), 115.53 (aryl), 24.70 (*C*HMe$_2$), 20.64 (*Me*Ar), 19.02 (CH*M*e$_2$), 17.83 (CH*M*e$_2$). ^{31}P NMR (25 °C, 121.5 MHz, C_6D_6) δ –59.33 (*P*HAr, $^{1}J_{P–H}$ = 179 Hz), 38.36 (Ar*P*^{i}Pr$_2$, $^{3}J_{P–H}$ = 20 Hz). Anal. Calcd for formula $C_{32}H_{46}NP_3Ni$: C, 64.45; H, 7.77; N 2.35. Found: C, 64.59; H, 7.92, N, 2.39. M.p. 72(2) °C.

Crystallographic Details. Single crystals of **2**·Et$_2$O (Et$_2$O), **4**·Et$_2$O (Et$_2$O)**, 8** (pentane), and **12** (Et$_2$O) were grown at −35 °C from concentrated solutions. Inert-atmosphere techniques were used to place the crystal onto the tip of a diameter glass capillary (0.05 mm) mounted on a SMART6000 (Bruker) at 113−137(2) K. A preliminary set of cell constants was calculated from reflections obtained from three nearly orthogonal sets of

10−30 frames. The data collection was carried out using graphite-monochromated Mo Kα radiation with a frame time of 10s and a detector distance of 5.0 cm. A randomly oriented region of a sphere in reciprocal space was surveyed. In general, three sections of 606 frames were collected with 0.30° steps in ω at different ϕ settings with the detector set at −43° in 2θ. Final cell constants were calculated from the *xyz* centroids of strong reflections from the actual data collection after integration (SAINT).[117] The structure was solved using SHELXS-97 and refined with SHELXL-97.[118]

Crystallographic Details for **2**·Et_2O. The crystals occurred as very small dark needles that appeared to have a red or green tinge. Several crystals were examined and found to be twinned, and the structure was initially solved using a twinned crystal. Further examination of the sample finally revealed a single crystal of approximate dimensions 0.20 × 0.05 × 0.04 mm which was used as sample. Intensity statistics and systematic absences suggested the centrosymmetric space group $P2_1/c$ and subsequent solution and refinement confirmed this choice. A direct-methods solution was calculated which provided most non-hydrogen atoms from the E-map. Full-matrix least squares / difference Fourier cycles were performed which located the remaining non-hydrogen atoms. A slight disorder occurs in one isopropyl group, and a diethyl ether solvent is present. All non-hydrogen atoms were refined with anisotropic displacement parameters. With the exception of those associated with the disordered atoms, all hydrogen atoms were located in subsequent Fourier maps and included as isotropic contributors in the final cycles of refinement. All hydrogen atoms associated with the disorder were placed in ideal positions and refined as riding atoms with relative isotropic displacement parameters.

Crystallographic Details for **4**·Et_2O. The sample consisted of extremely small red needles of maximum diameter only a few microns. Inert atmosphere techniques were used to place a typical crystal of dimensions 0.20 × 0.03 × 0.03 mm onto the tip of a 0.02 mm diameter glass fiber. Intensity statistics and systematic absences suggested the centrosymmetric space group $P2_1/c$ and subsequent solution and refinement confirmed this choice. A direct-methods solution was calculated which provided most non-hydrogen atoms from the E-map. Full-matrix least squares / difference Fourier cycles were performed which located the remaining non-hydrogen atoms. Non-hydrogen atoms were refined with anisotropic displacement parameters except for two carbon atoms that converged to non-positive values. The latter were refined isotropically. All hydrogen atoms were placed in ideal positions and refined as riding atoms with relative isotropic displacement parameters.

Crystallographic Details for **8**. Crystals were typically elongated parallelogram shaped prisms of varying sizes. Inert atmosphere techniques were used to place a typical crystal of approximate dimensions 0.30 × 0.13 × 0.05 mm. Intensity statistics and systematic absences suggested the centrosymmetric space group $P2_1/n$ and subsequent solution and refinement confirmed this choice. A direct-methods solution was calculated which provided most non-hydrogen atoms from the E-map. Full-matrix least squares / difference Fourier cycles were performed which located the remaining non-hydrogen atoms. All non-hydrogen atoms were refined with anisotropic displacement parameters. After the conclusion of the initial refinement it was recognized that there was a “ghost” image of the molecule translated by 0.5 along the *a*-axis. Using the SAME command in SHELX it was possible to refine to a suitable model with a relative occupancy of 0.958 :

0.42. Examination of the packing reveals that the molecules are stacked in channels parallel to the a-axis. Two additional crystals were examined and the same translational disorder was located, differing only in the occupancy. All hydrogen atoms were placed in ideal positions and refined as riding atoms with relative isotropic displacement parameters.

Crystallographic Details for **12**. Inert atmosphere techniques were used to place a green crystal of approximate dimensions 0.15 × 0.10 × 0.03 mm. Several other crystals were examined and all were badly split or twinned. During data collection, two major components were identified using George Sheldrick's CELL_NOW program. The Bruker-AXS SAINT program was used to generate an HKL5 file that was used in the refinement. The intensity data were corrected for absorption (TWINABS). Intensity statistics and systematic absences suggested the centrosymmetric space group P−1 and subsequent solution and refinement confirmed this choice. A direct-methods solution was calculated which provided most non-hydrogen atoms from the E-map. Full-matrix least squares / difference Fourier cycles were performed which located the remaining non-hydrogen atoms. It was necessary to use isotropic thermal parameters for several of the atoms, and examination of the ORTEP drawings shows that the model is not 100% agreeable. All hydrogen atoms were placed in ideal positions and refined as riding atoms with relative isotropic displacement parameters. It was not possible to locate the two hydrogens on the N atom.

Solution state Magnetic moment study in different solvents

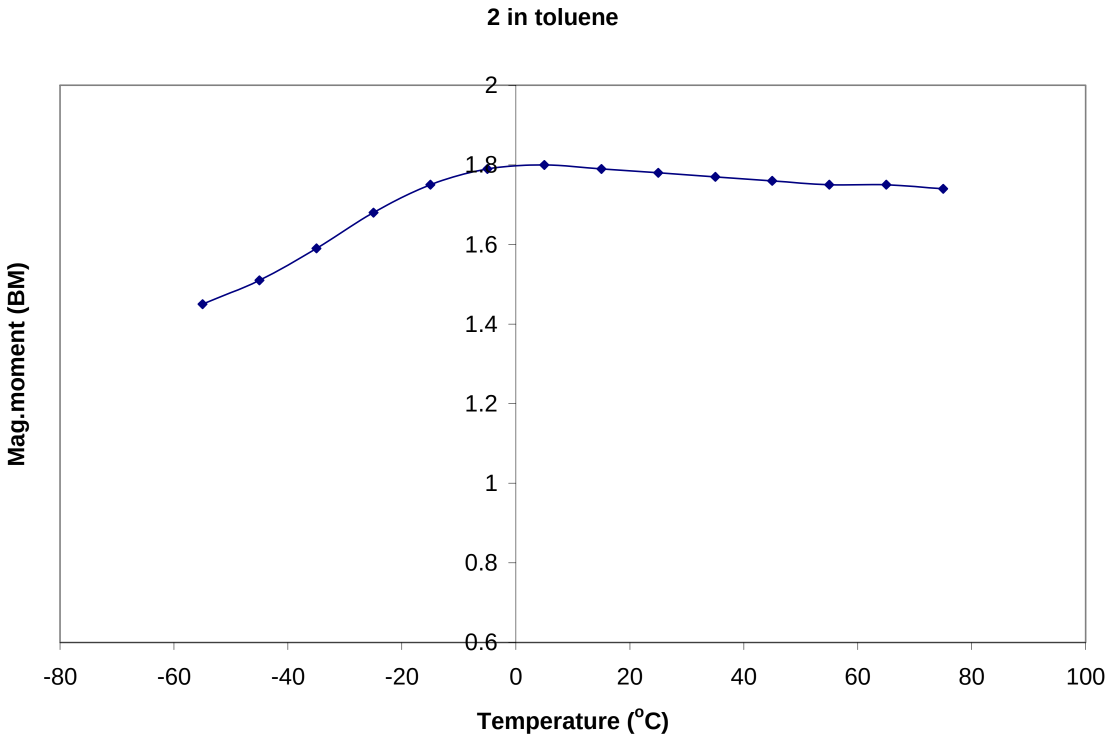

Figure S1. Variable temperature magnetic moment data of **2** (per Ni center) in toluene.

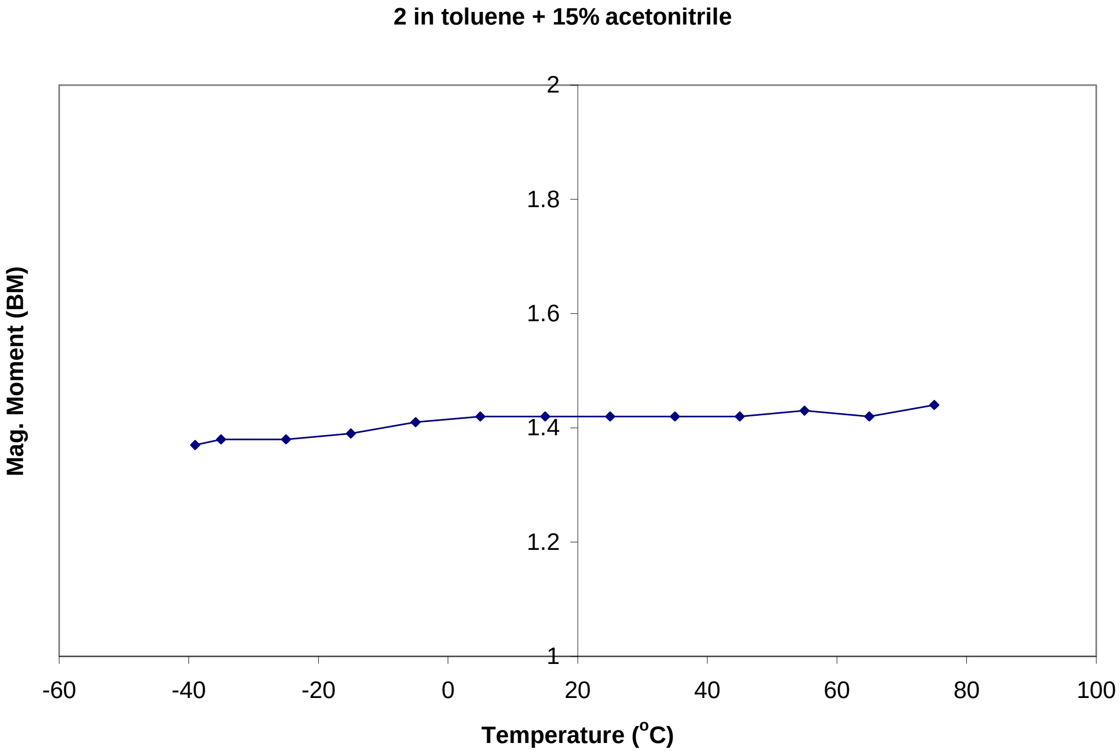

Figure S2. Variable temperature magnetic moment data of **2** (per Ni center) in toluene mixed with 15% acetonitrile.

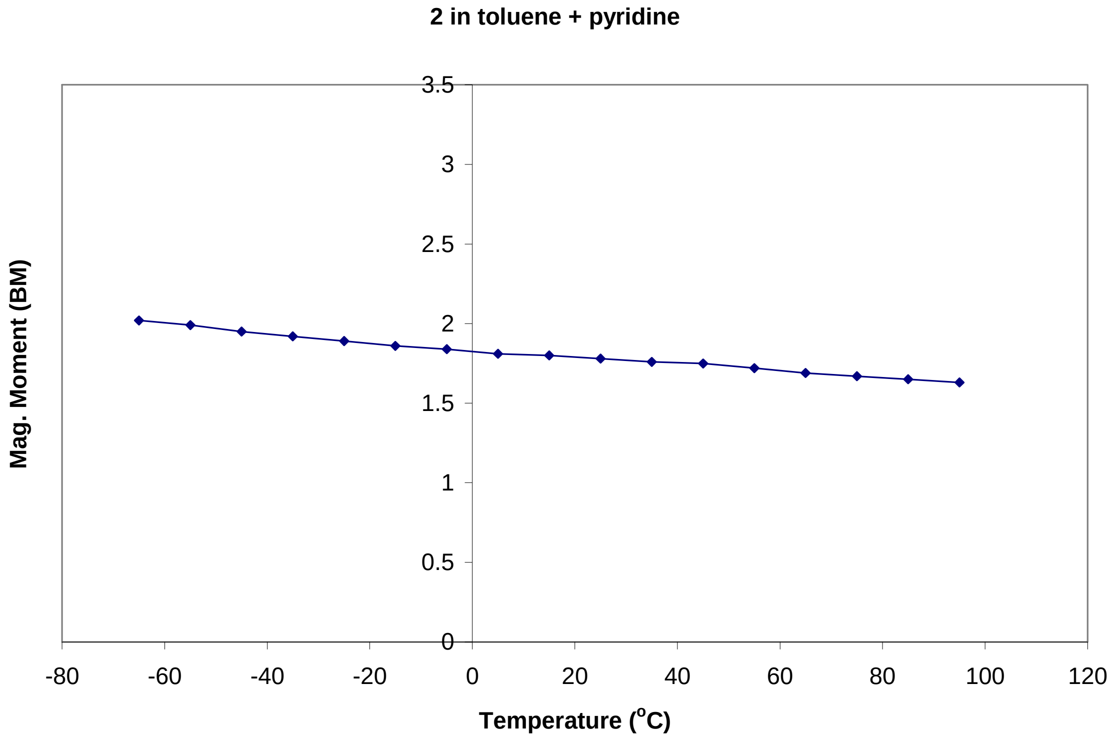

Figure S3. Variable temperature magnetic moment data of **2** (per Ni center) in toluene mixed with pyridine.

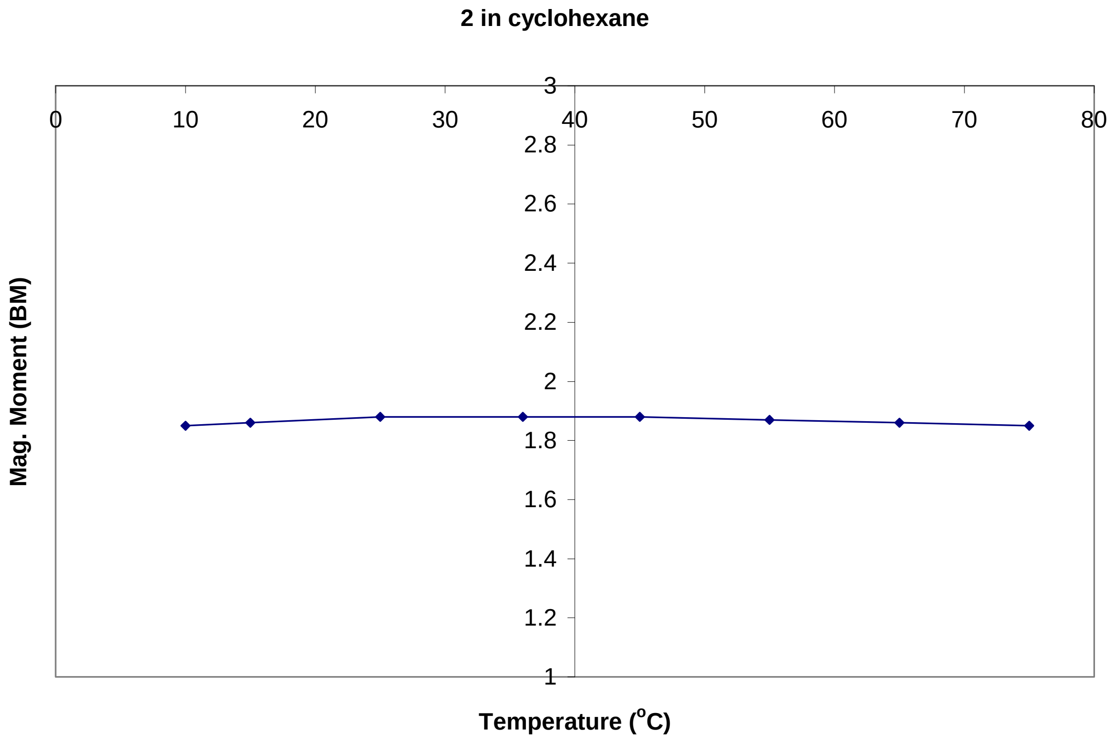

Figure S4. Variable temperature magnetic moment data of **2** (per Ni center) in cyclohexane.

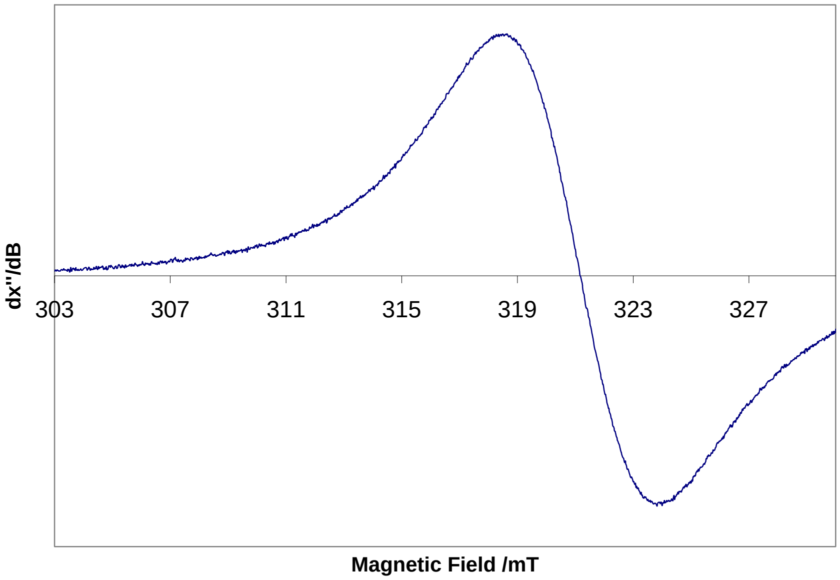

Figure S5. X-band room temperature EPR spectrum of **4** in toluene.

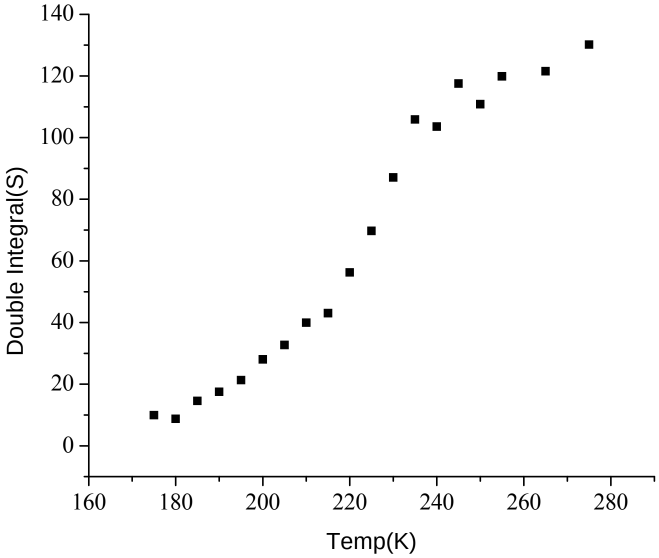

Figure S6. Plot of the X-band EPR signal intensity vs temperature of the signal at g = 2.205 of **2** in toluene solution at 175−280K.

1.6 References

(1) Tolman, C. A.; McKinney, R. J.; Seidel, W. C.; Druliner, J. D.; Stevens, W. R. *Adv. Catal.* **1985**, *33*, 1.

(2) Seidel, W. C.; Tolman, C. A. *Ann. N. Y. Acad. Sci.* **1983**, *415*, 201.

(3) Startsev, A. N. *Catal. Rev. - Sci. Eng.* **1995**, *37*, 353.

(4) Mulrooney, S. B.; Hausinger, R. P. *FEMS Microbiol. Rev.* **2003**, *27*, 239.

(5) Svetlitchnyi, V.; Dobbek, H.; Meyer-Klaucke, W.; Meins, T.; Thiele, B.; Roemer, P.; Huber, R.; Meyer, O. *Proc. Natl. Acad. Sci. U. S. A.* **2004**, *101*, 446.

(6) Dobbek, H.; Svetlitchnyi, V.; Gremer, L.; Huber, R.; Meyer, O. *Science* **2001**, *293*, 1281.

(7) Drennan, C. L.; Heo, J.; Sintchak, M. D.; Schreiter, E.; Ludden, P. W. *Proc. Natl. Acad. Sci. U.S.A.* **2001**, *98*, 11973.

(8) Hausinger, R. P. *Nat. Strut. Biol.* **2003**, *10*, 234.

(9) Webster, C. E.; Darensbourg, M. Y.; Lindahl, P. A.; Hall, M. B. *J. Am. Chem. Soc.* **2004**, *126*, 3410.

(10) Ermler, U.; Grabarse, W.; Shima, S.; Goubeaud, M.; Thauer, R. K. *Science* **1997**, *278*, 1457.

(11) Craft, J. L.; Horng, Y.-C.; Ragsdale, S. W.; Brunold, T. C. *J. Am. Chem. Soc.* **2004**, *126*, 4068-4069.

(12) Haines, R. I.; McAuley, A. *Coord. Chem. Rev.* **1981**, *39*, 77.

(13) Nag, K.; Chakravorty, A. *Coord. Chem. Rev.* **1980**, *33*, 87.

(14) Aldridge, S. *Angew. Chem. Int. Ed.* **2008**, *47*, 2348.

(15) Bradley, D. C.; Hursthouse, M. B.; Smallwood, R. J.; Welch, A. J. *Chem. Commun.* **1972**, 872.

(16) Bencini, A.; Benelli, C.; Gatteschi, D.; Sacconi, L. *Inorg. Chim. Acta* **1979**, *37*, 195.

(17) Bianchini, C.; Mealli, C.; Midollini, S.; Sacconi, L. *Inorg. Chim. Acta* **1978**, *31*, L433-L434.

(18) Dapporto, P.; Sacconi, L. *Inorg. Chim. Acta* **1980**, *39*, 61.

(19) Cecconi, F.; Midollini, S.; Orlandini, A. *Dalton Trans.* **1983**, 2263.

(20) Schaefer, H.; Binder, D.; Deppisch, B.; Mattern, G. *Anorg. Allg. Chem.***1987**, *546*, 79.

(21) Stavropoulos, P.; Muetterties, M. C.; Carrie, M.; Holm, R. H. *J. Am. Chem. Soc.* **1991**, *113*, 8485.

(22) Vicic, D. A.; Jones, W. D. *J. Am. Chem. Soc.* **1999**, *121*, 4070.

(23) Scott, F.; Krueger, C.; Betz, P. *J. Organomet. Chem.* **1990**, *387*, 113.

(24) Mandimutsira, B. S.; Yamarik, J. L.; Brunold, T. C.; Gu, W.; Cramer, S. P.; Riordan, C. G. *J. Am. Chem. Soc.* **2001**, *123*, 9194.

(25) Mindiola, D. J.; Hillhouse, G. L. *J. Am. Chem. Soc.* **2002**, *124*, 9976.

(26) Melenkivitz, R.; Mindiola, D. J.; Hillhouse, G. L. *J. Am. Chem. Soc.* **2002**, *124*, 3846.

(27) Bach, I.; Goddard, R.; Kopiske, C.; Seevogel, K.; Poerschke, K.-R. *Organometallics* **1999**, *18*, 10.

(28) Bakac, A.; Espenson, J. H. *J. Am. Chem. Soc.* **1986**, *108*, 713.

(29) Sadler, N.; Scott, S. L.; Bakac, A.; Espenson, J. H.; Ram, M. S. *Inorg. Chem.* **1989**, *28*, 3951.

(30) Barefield, E. K.; Krost, D. A.; Edwards, D. S.; Van Derveer, D. G.; Trytko, R. L.; O'Rear, S. P.; Williamson, A. N. *J. Am. Chem. Soc.* **1981**, *103*, 6219.

(31) D'Aniello, M. J., Jr.; Barefield, E. K. *J. Am. Chem. Soc.* **1978**, *100*, 1474.

(32) DeLaet, D. L.; Powell, D. R.; Kubiak, C. P. *Organometallics* **1985**, *4*, 954.

(33) Braune, W.; Okuda, J. *Angew. Chem., Int. Ed.* **2003**, *42*, 64-68.

(34) Moore, D. R.; Cheng, M.; Lobkovsky, E. B.; Coates, G. W. *J. Am. Chem. Soc.* **2003**, *125*, 11911.

(35) Lee, B. Y.; Kwon, H. Y.; Lee, S. Y.; Na, S. J.; Han, S.-i.; Yun, H.; Lee, H.; Park, Y.-W. *J. Am. Chem. Soc.* **2005**, *127*, 3031.

(36) *Catalytic, Asymmetric Epoxide Ring-Opening Chemistry in Aziridines and Epoxides in Organic Synthesis*; Nielsen, L. P. C.; Jacobsen, E. N., Eds.; Wiley: New York, 2006.

(37) Hirahata, W.; Thomas, R. M.; Lobkovsky, E. B.; Coates, G. W. *J. Am. Chem. Soc.* **2008**, *130*, 17658.

(38) Arriortua, M. I.; Cortes, A. R.; Lezam, L.; Rojo, T.; Solans, X.; Font-Bordia, M. *Inorg. Chim. Acta* **1990**, *174*, 263.

(39) Hay, P. J.; Thibeault, J. C.; Hoffmann, R. *J. Am. Chem. Soc.* **1975**, *97*, 4884.

(40) Ozerov, O. V.; Guo, C.; Papkov, V. A.; Foxman, B. M. *J. Am. Chem. Soc.* **2004**, *126*, 4792.

(41) Moulton, C. J.; Shaw, B. L. *Dalton Trans.* **1976**, 1020.

(42) D. Morales-Morales; Jensen, C. M. *The Chemistry of Pincer Compounds*; 1 st Ed. ed.; Elsevier:Oxford, 2007.

(43) Fryzuk, M. D. *Can. J. Chem.* **1992**, *70*, 2839.

(44) Fryzuk, M. D.; Haddad, T. S.; Berg, D. J. *Coord. Chem. Rev.* **1990**, *99*, 137.

(45) Fryzuk, M. D.; Haddad, T. S.; Rettig, S. J. *Organometallics* **1991**, *10*, 2026.

(46) Fryzuk, M. D.; MacNeil, P. A. *J. Am. Chem. Soc.* **1984**, *106*, 6993.

(47) Fryzuk, M. D.; MacNeil, P. A.; Rettig, S. J.; Secco, A. S.; Trotter, J. *Organometallics* **1982**, *1*, 918.

(48) Fryzuk, M. D.; Montgomery, C. D. *Coord. Chem. Rev.* **1989**, *95*, 1.

(49) Liang, L.-C.; Lin, J.-M.; Hung, C.-H. *Organometallics* **2003**, *22*, 3007.

(50) Winter, A. M.; Eichele, K.; Mack, H.-G.; Potuznik, S.; Mayer, H. A.; Kaska, W. C. *J. Organomet. Chem.* **2003**, *682*, 149.

(51) Fan, L.; Yang, L.; Guo, C.; Foxman, B. M.; Ozerov, O. V. *Organometallics* **2004**, *23*, 4778.

(52) Baumann, R.; Davis, W. M.; Schrock, R. R. *J. Am. Chem. Soc.* **1997**, *119*, 3830.

(53) Baumann, R.; Stumpf, R.; Davis, W. M.; Liang, L.-C.; Schrock, R. R. *J. Am. Chem. Soc.* **1999**, *121*, 7822.

(54) Eckert, N. A.; Bones, E. M.; Lachicotte, R. J.; Holland, P. L. *Inorg. Chem.* **2003**, *42*, 1720.

(55) Ozerov, O. V.; Guo, C.; Fan, L.; Foxman, B. M. *Organometallics* **2004**, *23*, 5573.
(56) Bailey, B. C.; Fan, H.; Baum, E. W.; Huffman, J. C.; Baik, M.-H.; Mindiola, D. J. *J. Am. Chem. Soc.* **2005**, *127*, 16016.
(57) Connelly, N. G.; Geiger, W. E. *Chem. Rev.* **1996**, *96*, 877.
(58) Adhikari, D.; Mossin, S.; Basuli, F.; Dible, B. R.; Chipara, M.; Fan, H.; Huffman, J. C.; Meyer, K.; Mindiola, D. J. *Inorg. Chem.* **2008**, *47*, 10479.
(59) Fout, A. R.; Basuli, F.; Fan, H.; Tomaszewski, J.; Huffman, J. C.; Baik, M.-H.; Mindiola, D. J. *Angew. Chem., Int. Ed.* **2006**, *45*, 3291.
(60) Harkins, S. B.; Peters, J. C. *J. Am. Chem. Soc.* **2004**, *126*, 2885.
(61) Pauling, L. *The Nature of the Chemical Bond*; 3rd ed.; Cornell University Press: Ithaca, NY, 1960.
(62) Oster, S. S.; Lachicotte, R. J.; Jones, W. D. *Inorg. Chim. Acta* **2002**, *330*, 118.
(63) O'Connor, C. J. *Prog. Inorg. Chem.* **1982**, *29*, 203.
(64) David, R. L. *CRC Handbook of Chemistry and Physics*; 60th ed.; CRC Press: Boca raton, Fl, 1979.
(65) Muresan, N.; Weyhermuller, T.; wieghardt, K. *Dalton Trans.* **2007**, 4390.
(66) Meyer, K.; Bendix, J.; Bill, E.; Weyhermueller, T.; Wieghardt, K. *Inorg. Chem.* **1998**, *37*, 5180.
(67) Abragam, A.; Bleaney, B. *Electron Paramagnetic Resonance of Transition Ions*; Clarendon press: Oxford, U.K., 1970.
(68) Smith, J. M.; Lachicotte, R. J.; Holland, P. L. *J. Am. Chem. Soc.* **2003**, *125*, 15752.
(69) Keefe, M. H.; O'Donnell, J. L.; Bailey, R. C.; Nguyen, S. T.; Hupp, J. T. *Adv. Mater.* **2003**, *15*, 1936.
(70) Nilges, M. J.; Barefield, E. K.; Belford, R. L.; Davis, P. H. *J. Am. Chem. Soc.* **1977**, *99*, 755.
(71) Ellis, D. D.; Spek, A. L. *Acta Crystallogr., Sect. C: Cryst. Struct. Commun.* **2000**, *C56*, 1067.
(72) Eaborn, C.; Hill, M. S.; Hitchcock, P. B.; Smith, J. D. *Chem. Commun.* **2000**, 691.
(73) Mindiola, D. J.; Hillhouse, G. L. *J. Am. Chem. Soc.* **2001**, *123*, 4623.
(74) Kitiachvili Kristina, D.; Mindiola Daniel, J.; Hillhouse Gregory, L. *J Am Chem Soc.* **2004**, *126*, 10554.
(75) Kogut, E.; Wiencko, H. L.; Zhang, L.; Cordeau, D. E.; Warren, T. H. *J. Am. Chem. Soc.* **2005**, *127*, 11248.
(76) Eckert, N. A.; Dinescu, A.; Cundari, T. R.; Holland, P. L. *Inorg. Chem.* **2005**, *44*, 7702.
(77) Holland, P. L.; Cundari, T. R.; Perez, L. L.; Eckert, N. A.; Lachicotte, R. J. *J. Am. Chem. Soc.* **2002**, *124*, 14416.
(78) Bai, G.; Wei, P.; Stephan, D. W. *Organometallics* **2005**, *24*, 5901.
(79) Hu, X.; Castro-Rodriguez, I.; Meyer, K. *Chem. Commun.* **2004**, 2164.
(80) Gomberg, M. *J. Am. Chem. Soc.* **1900**, *22*, 757.
(81) Lankamp, H.; Nauta, W. T.; MacLean, C. *Tetrahedron Lett.* **1968**, 249.
(82) McBride, J. M. *Tetrahedron* **1974**, *30*, 2009.

(83) Fafard, C. M.; Adhikari, D.; Foxman, B. M.; Mindiola, D. J.; Ozerov, O. V. *J. Am. Chem. Soc.* **2007**, *129*, 10318.

(84) Cho, J.; Van Heuvelen, K. M.; Yap, G. P. A.; Brunold, T. C.; Riordan, C. G. *Inorg. Chem.* **2008**, *47*, 3931.

(85) Mindiola, D. J.; Waterman, R.; Jenkins, D. M.; Hillhouse, G. L. *Inorg. Chim. Acta* **2003**, *345*, 299.

(86) Olivas, A.; Cruz-Reyes, J.; Petranovskii, V.; Avalos, M.; Fuentes, S. *J. Vac. Sci. Technol., A* **1998**, *16*, 3515.

(87) Vicic, D. A.; Jones, W. D. *J. Am. Chem. Soc.* **1999**, *121*, 7606.

(88) Han, S.-C.; Kim, H.-S.; Song, M.-S.; Kim, J.-H.; Ahn, H.-J.; Lee, J.-Y. *J. Alloys Compd.* **2003**, *351*, 273.

(89) Lopez, G.; Garcia, G.; Sanchez, G.; Garcia, J.; Ruiz, J.; Hermoso, J. A.; Vegas, A.; Martinez-Ripoll, M. *Inorg. Chem.* **1992**, *31*, 1518.

(90) Hikichi, S.; Yoshizawa, M.; Sasakura, Y.; Akita, M.; Moro-oka, Y. *J. Am. Chem. Soc.* **1998**, *120*, 10567.

(91) Shiren, K.; Ogo, S.; Fujinami, S.; Hayashi, H.; Suzuki, M.; Uehara, A.; Watanabe, Y.; Moro-oka, Y. *J. Am. Chem. Soc.* **2000**, *122*, 254.

(92) Itoh, S.; Bandoh, H.; Nakagawa, M.; Nagatomo, S.; Kitagawa, T.; Karlin, K. D.; Fukuzumi, S. *J. Am. Chem. Soc.* **2001**, *123*, 11168.

(93) Dible Benjamin, R.; Sigman Matthew, S. *J. Am. Chem. Soc.* **2003**, *125*, 872.

(94) Kieber-Emmons, M. T.; Schenker, R.; Yap, G. P. A.; Brunold, T. C.; Riordan, C. G. *Angew. Chem., Int. Ed.* **2004**, *43*, 6716.

(95) Cho, J.; Furutachi, H.; Fujinami, S.; Suzuki, M. *Angew. Chem., Int. Ed.* **2004**, *43*, 3300.

(96) Kourkine, I. V.; Maslennikov, S. V.; Ditchfield, R.; Glueck, D. S.; Yap, G. P. A.; Liable-Sands, L. M.; Rheingold, A. L. *Inorg. Chem.* **1996**, *35*, 6708.

(97) Langer, J.; Goerls, H.; Fischer, R.; Walther, D. *Organometallics* **2005**, *24*, 272.

(98) Bai, G.; Wei, P.; Das, A. K.; Stephan, D. W. *Dalton Trans.* **2006**, 1141.

(99) Fermin, M. C.; Stephan, D. W. *J. Am. Chem. Soc.* **1995**, *117*, 12645.

(100) Stephan, D. W. *Angew. Chem., Int. Ed.* **2000**, *39*, 315.

(101) Jana, A.; Objartel, I.; Roesky, H. W.; Stalke, D. *Inorg. Chem.* **2009**, *48*, 798.

(102) Zhao, J.; Goldman, A. S.; Hartwig, J. F. *Science* **2005**, *307*, 1080.

(103) Cui, W.; Zhang, P. X.; Wayland, B. B. *J. Am. Chem. Soc.* **2003**, *125*, 4994.

(104) Jamali, S.; Nabavizadeh, S. M.; Rashidi, M. *Inorg. Chem.* **2005**, *44*, 8594.

(105) Crabtree, R. H. *The Organometallic Chemistry of the Transition Metals*; Wiley Interscience: New York, 2001.

(106) Holland, P. L.; Andersen, R. A.; Bergman, R. G. *Comments Inorg. Chem.* **1999**, *21*, 115.

(107) Miskowski, V. M.; Gray, H. B.; Hopkins, M. D. *Adv. Transition Met. Coord. Chem.* **1996**, *1*, 159.

(108) Campora, J.; Palma, P.; del Rio, D.; Mar Conejo, M.; Alvarez, E. *Organometallics* **2004**, *23*, 5653.

(109) Jimenez, M. V.; Sola, E.; Lopez, J. A.; Lahoz, F. J.; Oro, L. A. *Chem.- A Eur. J.* **1998**, *4*, 1398.
(110) Pangborn, A. B.; Giardello, M. A.; Grubbs, R. H.; Rosen, R. K.; Timmers, F. J. *Organometallics* **1996**, *15*, 1518.
(111) Schwindt, M. A.; Lejon, T.; Hegedus, L. S. *Organometallics* **1990**, *9*, 2814.
(112) Miller, J. B. *J. Org. Chem.* **1959**, *24*, 560.
(113) Dias, H. V. R.; Power, P. P. *J. Am. Chem. Soc.* **1989**, *111*, 144.
(114) Sur, S. K. *J. Magn. Reson.* **1989**, *82*, 169.
(115) Evans, D. F. *J. Chem. soc.* **1959**, 2003.
(116) Jacobsen, C. J. H.; Pedersen, E.; Villadsen, J.; Weihe, H. *Inorg. Chem.* **1993**, *32*, 1216.
(117) SAINT; 6.1 Ed ed.; Bruker Analytical X-ray System: Madison, WI, 1991-2003.
(118) SHELEXL-plus; 5.10 Ed. ed.; Bruker Analytical X-ray systems: Madison, WI, 1999.

Chapter 2

A Mild Protocol for the Synthesis of a Nickel Boryl and Nickel Silyl Complexes and Attempted Group-Transfer Reactions

2.1 Introduction

Synthesizing organic molecules by metal catalyzed reactions has seen tremendous success for the last two decades. From this perspective organoborane compounds are among the most commonly used reagents necessary for various organic transformations. Multifarious use of the carbon-boron bonds for installing wide varieties of functionalities has become the major goal in this field. For example, synthetic methodology for carbon-carbon bond formation reaction employs Suzuki-Miyaura palladium catalyzed cross-coupling reaction between aryl boronate and vinyl boronate esters.[1] In addition to this, organoboranes can be converted to alcohols, peroxides, amines, halocarbons, aldehydes and alkylarenes very conveniently while in most cases keeping the regiochemistry of the functionality preserved. Moreover, particular organoboranes such as arylboronic acids and esters are not only extensively used for C−C bond formation reactions, they also find utility in other bond coupling reactions such as C−O, C−N.[2,3] Beyond being just a component of a fabric, i.e bond formation reaction, organoboranes also display biological activity and promising molecular recognition properties.[4] Thus the widespread utility of these class of organoborane compounds has created the demand to discover new avenues for the synthesis of the boronate esters.

In the context of important chemical transformations such as borylation, transition metals play a pivotal role. Whenever transition metal facilitates the process of borylation, it is usually considered that the transition metal boryl is the intermediate along the pathway. Transition metal boryl compounds are generally regarded as a class of compound in which a two-center, two-electron bond exists between the metal center and a three-coordinate sp^2-hybridized boron atom ($M{-}BR_2$). Other classes of compounds containing transition metal boron bond includes borane, bridging and terminal borylenes.

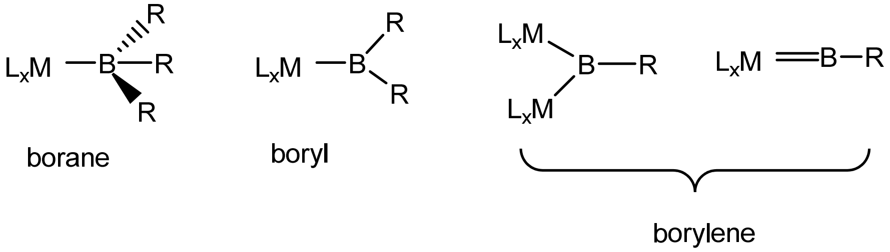

Scheme 1: Pictorial description of several transition metal boron compounds possessing 2c-2e bonds.

In $M{-}BR_3$ type borane-transition metal complexes, the interaction between boron and the transition metal is purely Lewis acid-base adduct type, where the metal acts as a Lewis base. In contrast, boryl transition metal complexes contain a terminal σ-bonded boryl group BR_2, where the boryl group is a strong σ-donor, comparable to a hydride. In borylene complexes a borylene ligand, BR**:** coordinates to metal either through terminal or bridging mode depending on the coordination number. Among these classes of compounds, transition metal boryls are of enormous promise owing to their utility in hydroboration and diboration of carbon-carbon multiple bonds.[5] The addition of boranes to alkenes is usually a very slow process at room temperature, but the rate is dramatically enhanced once a transition metal is used in catalytic amounts.[6] There are innumerable instances of such 'catalyzed hydroboration' in organic synthesis.[6,7] When hydroboration of the multifunctional substrate becomes the target, catalysis by a metal may play a colossal role in specific determination of chemoselectivity, regioselectivity and stereoselectivity.

In recent years transition metal boryl complexes have shown their prodigious utility in both stoichiometric and catalytic C−H bond activation chemistry. In the realm of organometallic chemistry, activation of thermodynamically inert C−H bonds is one of the holy grails in catalysis.[8-10] Traditional methods to functionalize C−H bonds of hydrocarbons sometimes involve radical or superacid reagents which prohibit the desired selectivity. Enzymatic activation also sometime engenders a product of poor selectivity in the case of linear alkanes. In light of these limitations, homogeneous transition metal systems offer better selectivity and preferential activation of primary C−H bonds. Hartwig and coworkers have discovered such selective activation using boron based transition metal systems such as $(CO)_5MnBcat$, $(CO)_5ReBcat$, $CpFe(CO)_2Bcat$ (cat = $O_2C_6H_4$).[11] The unusual functionalization of unreactive C−H bonds stems from the effect of boron. The boryl group's effect on the reactivity and regiochemistry of H−X bond was initially documented by the reaction of metal boryl complexes with protic reagents. A metal hydride formed along with concurrent formation of aminoborane, alkoxoborane and haloborane from reaction with amine, alcohol and mineral acid. Reaction of boryls with hydrocarbon follows the same regioselectivity and chemoselectivity to produce a metal hydride and a boryl functional group. The boryl ligand's surprising role in the chemoselectivity probably originates from the electrophilic nature of boron, due to its vacant p-orbital or the presumed σ-donating ability of the anionic boryl ligand. Notably, functionalization of hydrocarbons with boryl complexes is also augmented by a thermodynamic driving force given the fact that it results a strong boron-carbon bond.[12]

Given the quest for alkane and arene activation and functionalization, catalytic pathways in this field are most desirable. Archetypal metal catalyzed oxidations are notoriously unselective for linear alkanes, hence, catalytic functionalization of hydrocarbons represents a long-standing challenge in homogeneous and heterogeneous catalysis. To insure the catalytic viability of the process, Lewis acidic reagents are an automatic preference since the Lewis basic counterpart may poison the coordinatively unsaturated or cationic reagents responsible for C−H activation. Under this premise, boryl ligands play a gigantic role in carrying out the activation process in a fine manner. Iverson and Smith have elegantly demonstrated that Cp*Ir(PMe_3)(H)(R) (R = cy, Ph) can lead to alkylborane derivatives under thermal condition via intermolecular C−H activation and catalytic borylation.[13] Later, Hartwig and coworkers were able to show catalytic functionalization of C−H bonds by using Cp'M$(CO)_3$ (Cp' = C_5H_5, C_5H_4Me, C_5Me_5 and M = Mn, Re) and B_2Pin_2 (Pin = $OCMe_2CMe_2O$) under photolytic condition (Scheme 2).[14]

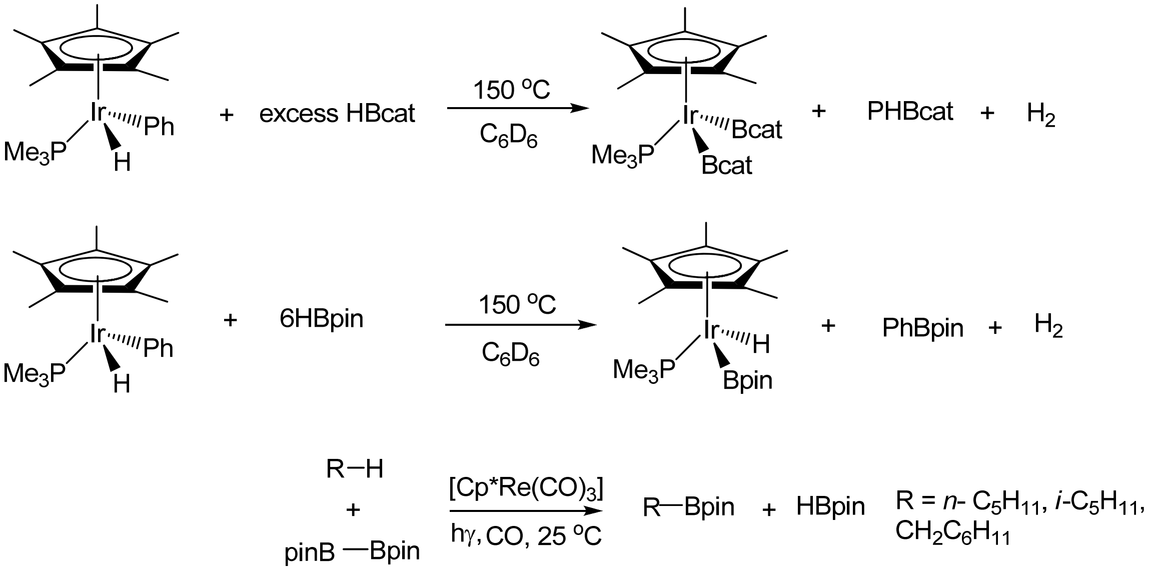

Scheme 2: Thermal and photolytic borylation as shown by Smith and Hartwig.

Thermal, catalytic, and regiospecific functionalization has been achieved for linear alkanes using Cp*Rh(C_2H_4)$_2$, in octane with B_2Pin_2, resulting in the exclusive formation of n-octylBPin. In addition, Marder and coworkers have catalytically borylated both aromatic and benzylic C−H bonds of toluene, p-xylene and mesitylene into C−B(OR)$_2$ (R = OCMe$_2$CMe$_2$O) type species using RhCl(P^{i}Pr)$_3$(N$_2$) and HBpin.[15]

Under the present paradigm of catalytic hydroboration and C−H activation processes,[16] intermediacy of the transition metal boryl complexes are often proposed. Consequently, the exact nature and role of such as intermediate is a matter of investigation. As discussed previously, efficient transition metal catalysts for these processes often includes heavy metals, but more specifically, expensive metals, e.g. Pd, Pt, Rh, Ir. Having that idea we focused our attention to designing an efficient catalyst employing a relatively cheap metal like nickel. To our surprise reported examples of borylation reactions using nickel are extremely scant.[17,18] Arguably, the scarcity of nickel mediated borylation may stem from the lack of stable and isolated systems bearing a prototypical Ni−BR$_2$ linkage. Intrigued by this we were interested in synthesizing a nickel-boryl species which can be viable to achieve the proposed catalytic role in the regime of bond activation and group-transfer chemistry. In this context it is worthy to mention that silicon shows some parallels to boron in its chemical behavior owing to the diagonal relationship in the periodic table. Hence we are also interested to extend this chemistry to form analogous nickel-silyl complexes which are described in the later part of this Chapter.

2.2 Results and discussion

2.2.1 Characterization of a nickel boryl complex, (PNP)Ni−Bcat, 2

Synthetic strategies involving the preparation of transition metal-boryl complexes consists of the following methods: (I) The nucleophilic reaction of anionic metal species with haloboranes (X−BR_2, X = Cl, Br, I), (II) the reaction of metal hydride compounds with haloboranes in presence of a base, (III) σ-bond metathesis and (IV) oxidative addition of haloboranes or hydroboranes to metal compounds. Recent investigations have demonstrated that oxidative addition of B−H of alkoxy-stabilized boranes such as HBcat (cat = catecholato, $O_2C_6H_4$) and B−B bonds of related compounds are preferred over the oxidative addition of less stable halo, alkyl or aryl boranes.[19] In the attempt of assembling a boryl moiety onto nickel, we treated (PNP)NiH, **1** with catechol borane. (PNP = N[2-$P(CHMe_2)_2$-4-$MeC_6H_3]_2^-$)[20]. The reaction between **1** and catechol borane is completed in 12 hours at room temperature and during the process liberates H_2 which has been detected by ^1H NMR spectroscopy (Scheme 3).[21]

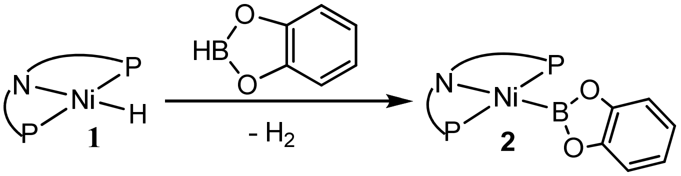

Scheme 3: Synthesis of **2** from nickel-hydride precursor, **1.** The PNP cartoon represents the ligand, N[2-$P(CHMe_2)_2$-4-$MeC_6H_3]_2^-$.

The yellow colored product, (PNP)Ni−Bcat, **2** is isolated in 81% yield upon work up and crystallization from diethyl ether at −35 °C. A similar technique for synthesizing a boryl complex, RhBcat from RhH and HBcat was documented earlier by Marder and coworkers.[22] To elucidate the structural features of **2** we scrutinized a single crystal by X-ray diffraction analysis which displayed a square planar nickel center bearing a terminal and planar catecholboryl group (Figure 1). From the solid state structure it is also apparent that the molecule possesses a C_{2v} symmetry, which will be further corroborated by solution state NMR spectroscopic data. In addition to X-ray analysis the molecule, **2**, has been thoroughly characterized by multinuclear NMR spectroscopy including ^{11}B NMR, UV-vis spectroscopy and high resolution mass spectroscopic data. To the best of our knowledge this is the first well characterized example of a Ni-boryl complex. Although Noth *et al.*, in 1971 reported an example of a nickel-boryl complex, $\{(Ph_3P)_2NiBPh_2.0.5Et_2O\}_n$, n ≥ 2, the system was not properly characterized, hence casting some doubt about the identity of the complex.[23] Structurally, the Ni−B bond length of **2** (1.9091(18) Å, Figure 1) is consistent with other crystallographically characterized boryl complexes for the 3d metals such as Co (1.970(11) Å,[24] Fe (1.973(2) Å,[25] Mn (2.018(6) Å)[11]. The plane composing the O−B−O atoms bisects the imaginary plane defined by the P−Ni−P atoms (~ 71.4 ^{o}) which exposes the empty p(y) orbital of boron along the (PNP)Ni xy-plane. Intuitively it seems that nickel would be involved in back donating electrons to the vacant p(y) orbital of boron, although theoretical calculations affirm that there is no detectable amount of backdonation from the nickel center (*vide infra*).

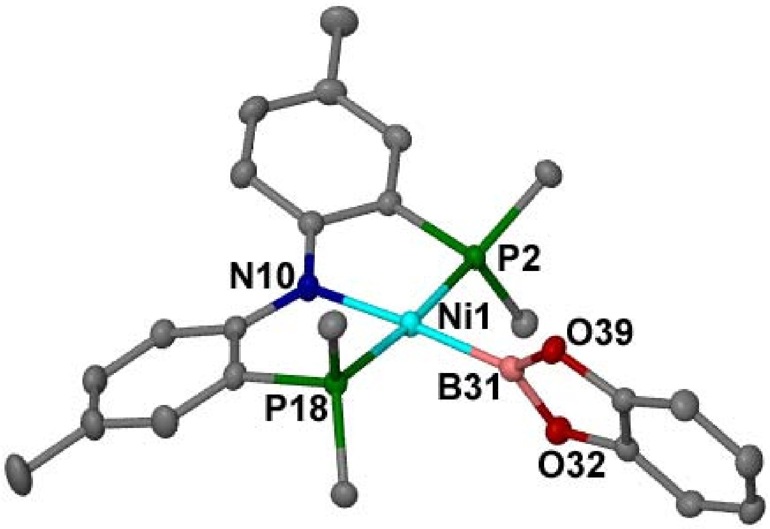

Figure 1: Molecular structure of **2** depicting thermal ellipsoids at the 50 % probability level. Hydrogens, Et_2O solvent and methyls of the isopropyl groups have been omitted for clarity selected bond lengths (Å) and angles (degree): Ni1−B31, 1.9091(18); Ni1−P2, 2.1447(4); Ni1−P18, 2.1408(4); Ni1−N10, 1.932(2); B31−O32, 1.419(2); B31−O39, 1.423(2); P2−Ni1−P18, 174.42(7); N10−Ni1−P2, 87.45(4); N10−Ni1−P18, 87.40(4); N10−Ni1−B31, 174.54(7); P2−Ni1−B31, 93.43(5); P18−Ni1−B31, 91.89(5); Ni1−B31−O32, 129.2(2); Ni1−B31−O39, 122.8(2).

Salient features of complex **2** from NMR spectroscopy include a distinct singlet at 51.2 ppm in ^{31}P NMR which suggests the species to possess C_{2v} symmetry in solution. The diamagnetic nature of the complex is unequivocal from the sharp resonances in the ^{1}H NMR spectrum, therefore in accord with a square planar environment about a $Ni^{(II)}$ center. Most importantly, ^{11}B NMR spectrum displays a broad resonance at ~ 47 ppm which is comparable to other chemical shifts reported for the other 3d transition metal boryls.[26] Intuitively, it appears that the broadness of the boryl resonance stems from the coupling associated with two equivalent phosphorus atoms, but our attempt to resolve the coupling by low temperature experiment (− 45 °C) did not unravel any $J_{B\text{-}P}$ coupling. Our observed ^{11}B δ-value corroborates a value found in the complexes where boron is trigonal planar.[27] There is precedence where ^{11}B NMR data has been used to measure the level of π-electron density and hence π-acceptance onto the boron atom from its three substituents. Hartwig and co-workers has suggested that correlating the electron density around the boron atom and NMR chemical shift can be invoked, but with caution, as the paramagnetic shielding effects of the metal exert a dominant influence on the chemical shifts of atoms bound directly to the metal atom.[28] Other than these features, the high resolution mass spectroscopy (MS-CI) of **2** discloses a peak at 605.2290 (expected monoisotopic peak at 605.2288) unequivocally proving the identity of the complex.

Usually, transition metal boryl complexes show instability towards heat leading to the decomposition of the boryl groups. For example, bisboryl compounds $[Fe(CO)_4(Bcat')_2]$, (cat' = 1,2-O_2-4-$Bu^tC_6H_3$ or 1,2-O_2-3,5-$Bu^tC_6H_2$) decompose in solution within an hour and even within a day in solid state.[28] A similar tendency towards decomposition has been observed for the complexes involving late transition metal such as $[RhCl(PPh_3)_3]$ with HBcat in THF or CH_2Cl_2 decomposes to several products including B_2cat_3 and $[RhHCl(PPh_3)_2(Bcat)]$.[29] In contrast, complex **2** is remarkably stable towards heat since solutions of **2** in benzene retain integrity at a temperature as high as 155 °C for several days. Complex **2** is even mildly stable in air (30 minutes) but decomposes to intractable products in presence of water.

2.2.2 Alternative routes to synthesize 2

In our previous chapter we described how the molecule [Ni(μ_2-PNP)]$_2$, **3** can easily cleave homo and heteronuclear bonds to assemble important and novel functionalities onto nickel$^{(II)}$.[30] After our initial success in cleanly synthesizing **2** we turned our attention to cleaving B−B bond promoted by **3** as a viable synthetic method. Accordingly, treatment of **3** with biscatecholato diborane (B_2cat_2) results in smooth formation of the desired complex, **2**, in 80% isolated yield (Scheme 4). The brown colored hexane solution of **3** gradually changes to yellow upon stirring for 3 hrs. As speculated earlier, this transformation may undergo a cooperative bimetallic cleavage or a B−B bond cleavage reaction promoted by the three coordinate Ni$^{(I)}$ monomer (Chapter 1).

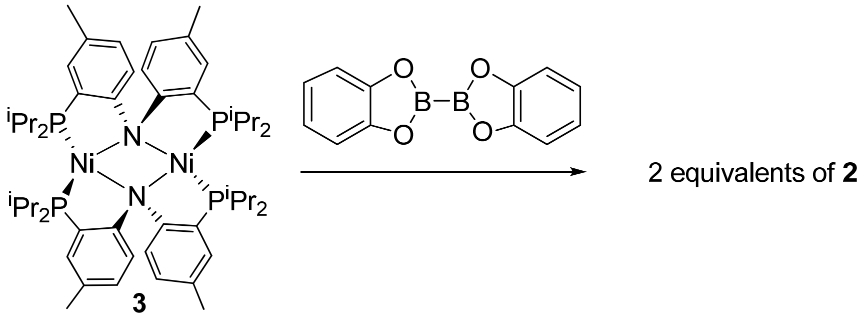

Scheme 4: Alternative synthesis of **2** through a B−B bond splitting reaction mediated by [Ni(μ_2-PNP)]$_2$, **3.**

Alternatively, **3** can also promote the cleavage of heteronuclear bonds such as B−H, inasmuch as treating **3** with catechol borane yields an equimolar mixture of **1** and **2** within 3 hours. Furthermore, we found that **2** can be accomplished via a sigma-bond metathesis reaction by a late transition metal alkoxide, namely (PNP)NiO^{t}Bu, **4. 4** was prepared by salt metathesis of (PNP)NiCl with KO^{t}Bu and the blue colored product was isolated in 79% yield. The diamagnetic product was well characterized by multinuclear NMR spectroscopy as well as mass spectroscopy. Very recently Sadighi and coworkers successfully employed late transition metal alkoxides to cleanly isolate the (IPr)CuBpin species (IPr = 1,3-bis(2',6'-diisopropylphenyl)imidazol-2-ylidene).[31] Anticipating that the same strategy can be useful to install boryl fragment onto nickel we attempted to cleave the B−B bond by **4** (Scheme 5).

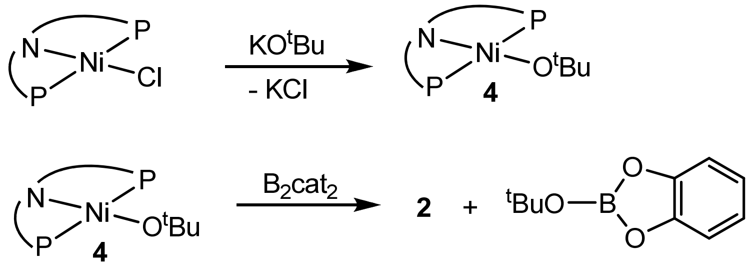

Scheme 5 : Alternative synthesis of **2** by late transition metal alkoxide mediated cleavage of B−B bonds.

To our surprise, during the course of the reaction of **4** and biscatecholdiborane we observed an intermediate forming *en route* to splitting of the B−B bond. The color of the reaction changed sharply from green to red immediately after B_2Cat_2 was mixed with **4**. The progress of the reaction was monitored by ^{31}P NMR spectroscopy and the decay of the resonance corresponding to **4** (17.6 ppm) was evident along with a growing resonance at 29.8 ppm (Figure 2a). A new resonance in ^{11}B NMR spectroscopy also appeared at ~ 18 ppm (broad) validating the intermediate formation.

a.

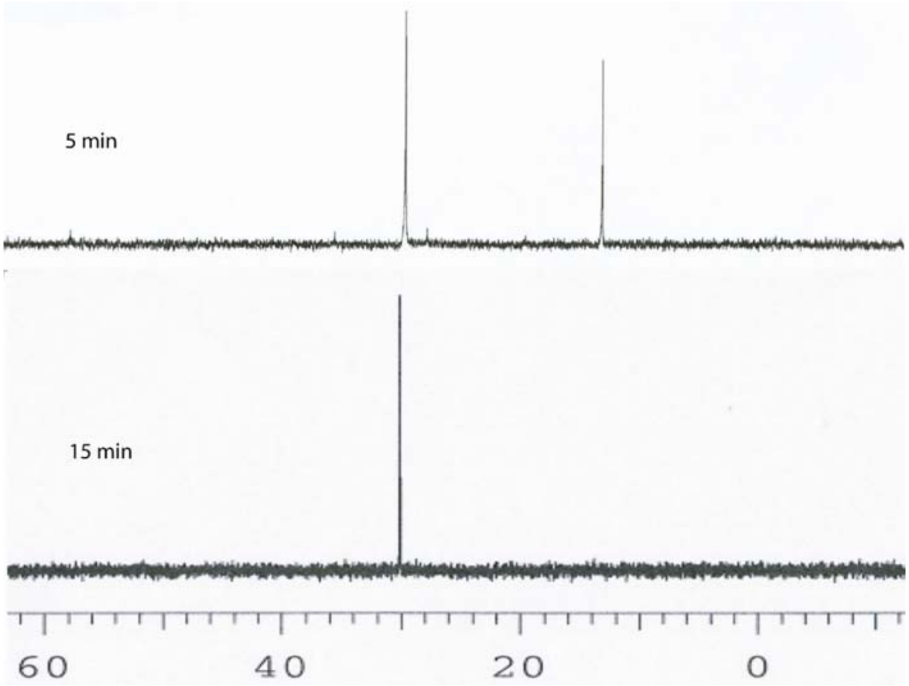

b.

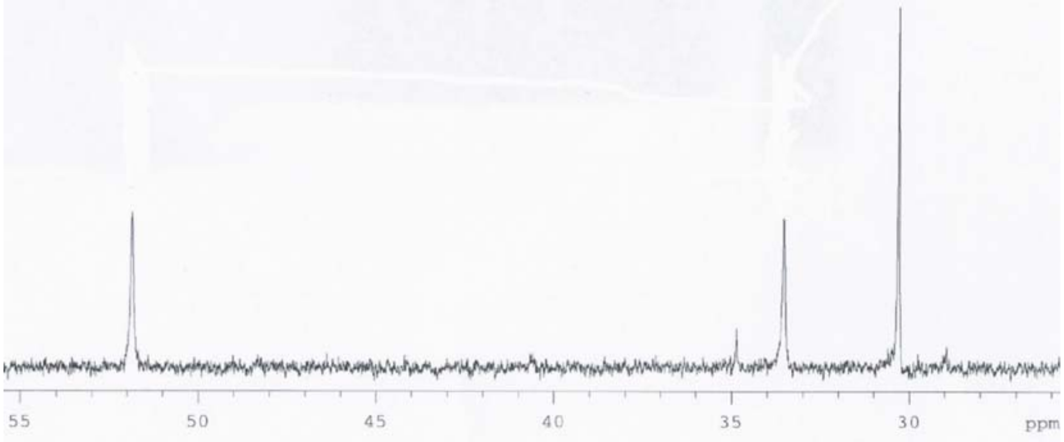

Figure 2: Intermediate formation (at 29.8 ppm in ^{31}P NMR) along the B−B splitting pathway by **4** (2a). After 20 minutes the intermediate start decaying to produce **2** (at 51.2 ppm) along with some other uncharacterized products (2b).

After the complete consumption of **4,** the resonance corresponding to the intermediate started decaying to engender **2**, judged by formation of a yellow solution. Recent theoretical work by Marder *et al.* disclosed the presence of such an intermediate during the B−B bond cleavage, but so far the intermediate has not been confirmed experimentally.[32,33] Unfortunately, our attempts to trap the intermediate failed and prohibited further characterization of such a complex. Hence, to investigate the nature of the intermediate we resorted to high level DFT calculations using B3LYP/6-31G** level of theory. Results from the calculations are very consistent with the proposed intermediate suggested by Marder and coworkers explaining the mechanism of the diboration of aldehydes catalyzed by a copper-boryl complex. According to their calculations, the diboron species coordinates across the Cu−O bond of the copper alkoxide species to form an intermediate which then performs the consequent cleavage.[32] A similar bound diboron adduct species to the metal-alkoxide has also been proposed by Ito and coworkers.[34] In our case, the intermediate is a σ-complex, whereby a σ-bond metathesis follows the binding event (Scheme 6).

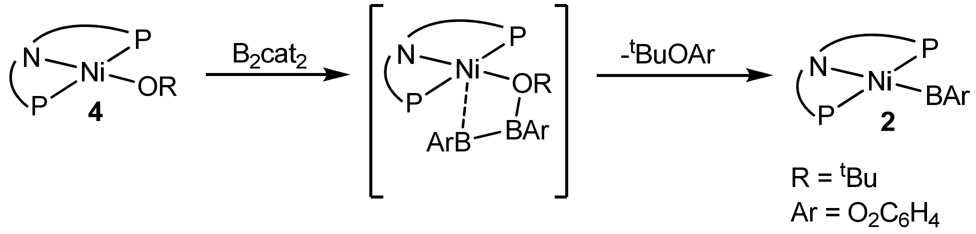

Scheme 6: Formation of the intermediate en route to formation of **2** from **4.**

From theoretical calculations, as observed the nature of intermediate in 3B (Figure 3), one boron atom is directly connected to the oxygen atom of the O^{t}Bu ligand while the other boron atom is likely forming a weak interaction with the nickel center. The computed Ni**…**B2 distance is 2.741 Å which is quite longer than a true Ni−B bond

(1.9091(8) Å). B1−O bond length is 1.52 Å which is slightly longer than our observed B−O bond length of 1.42 Å in **2**. The computational data clearly indicates that B−O bond forms in the intermediate with weak Ni−B interaction present.

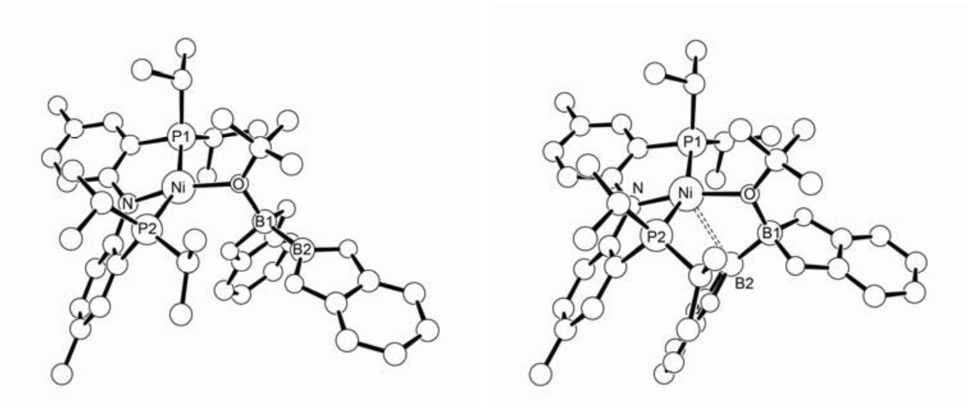

A B

Figure 3: Two intermediate geometries (DFT generated) along the pathway to cleave the B−B bond promoted by **4**.

Such a binding event between alkoxide and diborane, specially the weak Ni−B interaction definitely facilitates the σ-bond metathesis to cleave the B−B bond. In another conformation (3A), the Ni−B interaction is not possible but given the energy difference (5.17 kcal mol^{-1}, 3B is more stable than 3A by this amount of energy) between these two isomers it is very likely that the isomer B is present more predominantly than the isomer A. Alternatively a facile single bond rotation across the B−O bond in 3A can lead to the ideal intermediate for the σ-bond metathesis process to occur. While probing the reaction by ^{31}P NMR spectroscopy, we observe a single intermediate peak (δ 29.8). We can not assign which isomer corresponds to the resonance we observe, given their predicted similar shifts coupled with the large error affiliated with DFT NMR predictions (8−16 ppm). In order to detect the other intermediate isomer we performed low temperature NMR experiments. Unfortunately, no separate peak for the second isomer appeared even at −55 °C, though the peak became considerably broad. A related experimental observation was also documented by Fernandez and coworkers wherein a binding of diborane to (NHC)Cu was described as the key step.[19] The observation of the intermediate in our borylation process is the first experimental realization of this theoretically predicted σ-bond complex as an intermediate. During the formation of **2** from **4**, some uncharacterized minor products were also forming as tracked by ^{31}P NMR spectrum discouraging any kinetic experiments to be performed with this system. To prove the generality of late transition metal alkoxide promoted B−B bond cleavage, we are also currently synthesizing Co and Fe-boryl complexes supported by the pincer PNP ligand (Scheme 7).[35]

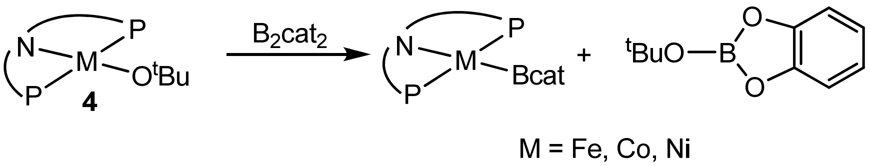

Scheme 7: Late transition alkoxide mediated splitting of B−B bond towards the synthesis of late transition metal boryls.

2.2.3 Structural elucidation of 2 by DFT

Since complex **2** is the first well characterized nickel boryl complex, we were interested in evaluating the nature of Ni−B bonding. We surmised that understanding the nature of frontier orbitals will explain why **2** was so stable unlike the other known transition metal boryls. The general description of metal-boron bonding has been depicted in Scheme 8.

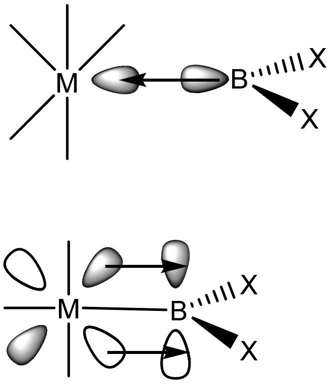

Scheme 8: Principal orbital interactions in a transition metal boryl complex.[26]

As delineated in Scheme 8, σ-bonding between the boron and the metal center can be viewed simplistically as the overlap between the filled sp^2-hydridized orbital on boron, and an empty σ-hybrid orbital of appropriate symmetry on the transition metal. Furthermore, the possibility of a π-interaction between the boron and the metal exists in the form of π-back donation from a metal based frontier orbital to the boron p-orbital. The strength of the M−B bond depends on the amount of backdonation present from the metal to the boryl fragment. To evaluate the geometric features and whether the backbonding is playing a role in governing stability of **2** we attempted to theoretically analyze it. Geometry optimizations at B3LYP/6-31G** level of theory clearly ratifies the structure of the complex characterized crystallographically. For example, DFT optimized Ni−B bond length is 1.93 Å compared to the crystallographically characterized length of 1.9091(18) Å. Similarly, B−O bond lengths are 1.419 and 1.423 Å respectively compared to 1.42 Å proposed by DFT. Considering covalent radii of B and O, B−O bond length clearly suggests that the significant shortening has been taken place in this bond which invokes multiple bond character present there. To shed light on the nature of the nickel-boron interaction, bond order of the Ni−B has been calculated by natural bond order analysis which appears to be 0.84, clearly insinuating to the single bond nature of the bond and consequent lack of back bonding interaction. Since NBO calculations do not account for the electrostatic component between Ni and B interaction, and the Ni−B linkage in **2** lacks π overlap, our predicted bond order is less than one. In earlier theoretical studies several groups have focused to address the role of σ-donation and π-backdonation in determining the metal-boryl bond strength.[36,37] From these studies, it becomes evident that the bond strength of the metal-boryl bond originates mainly from σ-donation with a small contribution from π-backdonation.[36] Intuitively it appears that changes in metal electron density for π-backdonation or its lack thereof, should be reflected by the boron chemical shift. However, caution needs to be exercised when interpreting the ^{11}B NMR spectroscopic data as a proof of backbonding since the paramagnetic shielding effects of the metal exert a dominant influence on the chemical shifts of atoms bound directly to metal (vide supra). As a mark of proof, ^{11}B NMR shifts for both titanium[38,39] and niobium[40] borane adducts are virtually identical to the structurally dissimilar boryl complexes. Most notably, when boron is connected to the heteroatoms such as in the case of Bcat, the lone pair of the heteroatom is donated to the vacant orbital of boron. Under this scenario, boron has no longer a vacant orbital present where backdonation from nickel is possible, which is our case in hand. As expected for a square planar d^8 system, complex **2** has a filled $d(z^2)$ HOMO−1 orbital and an unoccupied $d(x^2- y^2)$ LUMO orbital augmented with PNP aryl π^*. In addition to the π^* character in

HOMO orbital, it is also significantly contributed by the lone pair of PNP nitrogen (Figure 4)

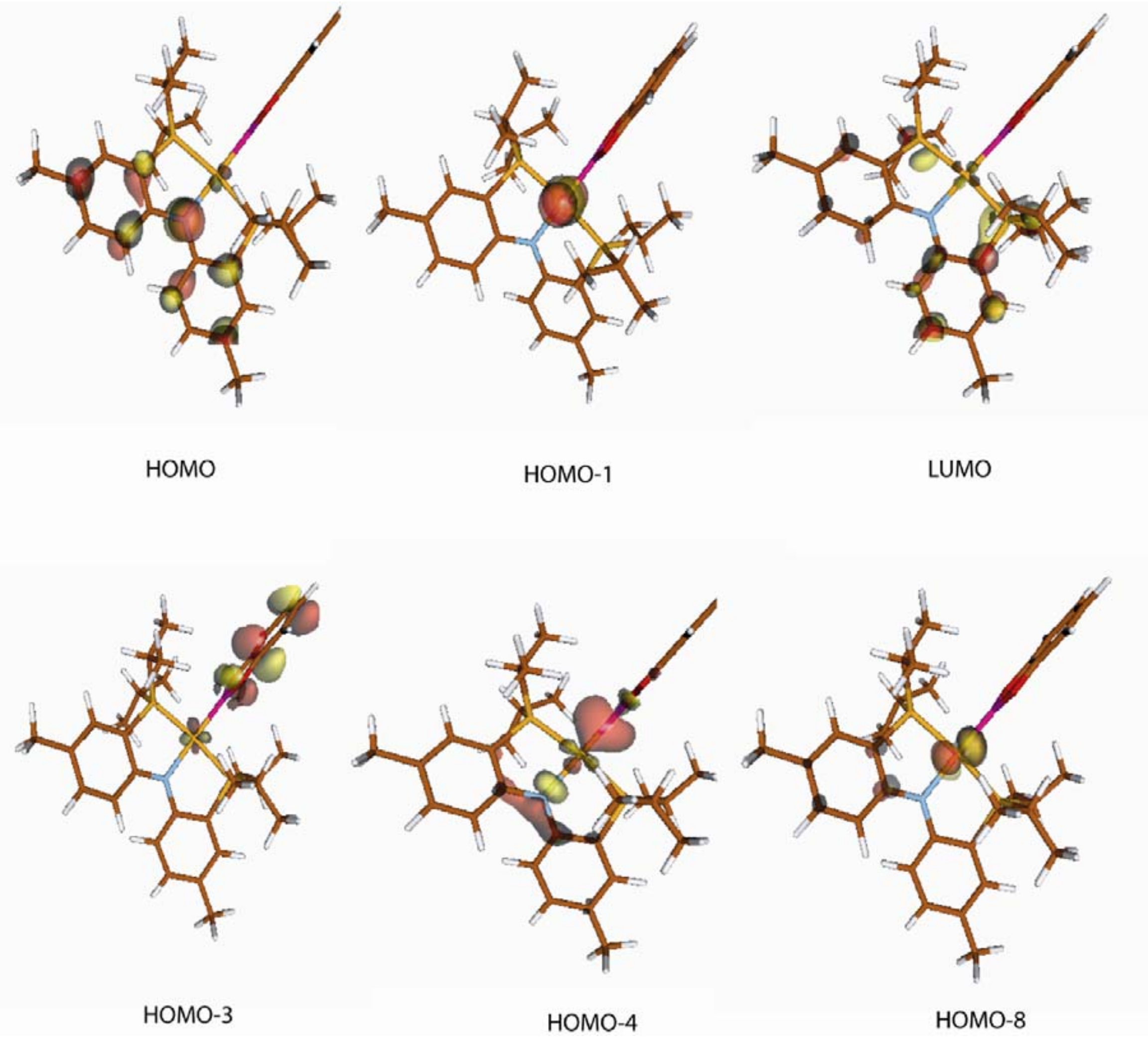

Figure 4: Important molecular orbitals of **2**. The molecular orbitals have been drawn using the full model and plots are drawn with isodensity 0.05.

Further analysis of the frontier orbitals reveals that the Ni−B σ bond is a combination of Ni *d*(x^2-y^2) and B p(x) as evident from the orbital HOMO−4. This clearly conveys the lack of multiple bond character in the Ni−B bond. On the other hand, HOMO−3 displays the multiple bond character associated with the B−O bond, while HOMO−8 depicts the *d*(y^2-z^2) as a filled orbital as expected for a square planar d^8 system. Since the boryl motif has been proved to be a strong σ-donating trans influencing ligand,[41,42] the energy of the *d*(x^2-y^2) orbital becomes lower and energetically compatible to the B p(x) orbital. From this detailed analysis of the nature of Ni−B bond it can be inferred that the boryl ancillary should be conveniently transferred to some other moiety, because of the lack of Ni−B backbonding.

2.2.4 Boryl Transfer Reactivity of 2

Since we speculated that the boryl group can be transported to other substrates owing to the single bond nature of Ni−B bond, we were interested to test such hypothesis. Theoretically, a successful group transfer reaction will engender arylboronic ester. Arylboronic esters are very valuable organic feedstock given their widespread use in organic synthesis,[1,43,44] biology[45] and molecular recognition.[46-48] Indeed, complex **2** transfers its boryl group, inasmuch as treatment with bromobenzene at 120 °C for 18 hours affords PhBcat and (PNP)NiBr, **5** quantitatively, as inferred from ^{1}H and ^{31}P NMR spectroscopy (Scheme 9). Isolation of the B−C bond coupled product, PhBcat can be easily performed via preparatory thin layer chromatography and can be obtained in 68% yield. The identity of the product PhBcat and the byproduct **5** were further authenticated by independent syntheses[11] and characterization by multinuclear NMR spectroscopy and GC-MS spectrometry.

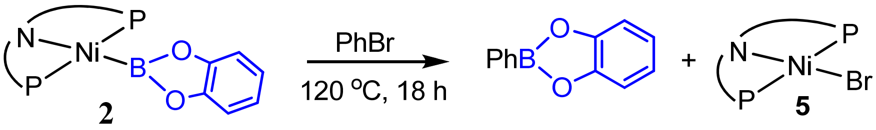

Scheme 9: Boryl transfer reactivity of **2** with bromobenzene

In the synthesis of arylboronic acids or their esters, direct borylation of aryl halides or pseudo-halides is inarguably a better pathway compared to transmetallation between arylmagnesium reagents and boron compounds with good leaving groups.[49-51] In the case of transmetallation step by Grignard, a potential problem is the susceptibility of several functional groups present in the aryl moiety to the Grignard reagent, which limits the scope of the reaction. Protection/deprotection protocols for the susceptible functional groups are also not desirable as it adds more steps (therefore costs) to the overall synthetic scheme. Transfer of the boryl moiety to 4-substituted arylbromide has been documented earlier by Marder and coworkers using a cobalt boryl complex but our borylation is an improvement over their system (*vide infra*).[52] Inspired by our success in group transferring ability of the boryl motif we attempted to transfer it to a more common feedstock such as cholorobenzene, but unfortunately, reflux of **2** with such a reagent for 3 days at 120 °C only resulted in <10% conversion of the product with formation of known (PNP)NiCl. This observation hints to the greater C−Cl bond strength in haloaromatics and the consequent higher energy barrier might be hindering the reaction. It has been documented previously that (PNP)NiCl can be easily converted to **1** by treatment with ^{t}BuLi or $NaBH_4$,[53] Hence we reasoned that if **5** can be converted to **1** in a single pot, the borylation might be elevated to a catalytic reaction. Accordingly, in a J-Young tube, 20 mol% of **2** with HB(cat) and $NaBH_4$ were mixed in neat bromobenzene and the mixture was heated at 120 °C for 18 hours. Unfortunately catalysis did not prevail despite some arylboronate ester formation. We surmise that **1** reacts with bromobenzene in a comparable rate to **2**, hence consuming the starting material leading to an undesired side reaction of benzene formation.

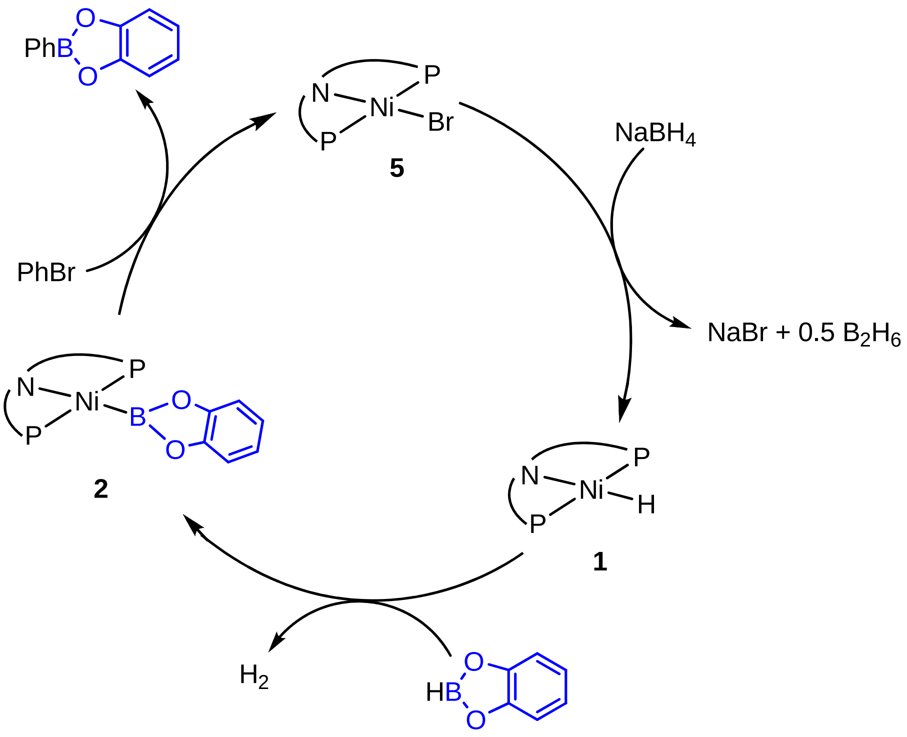

Scheme 10: Cyclic borylation to stoichiometrically transfer the boryl moiety

In addition, catechol boron has a propensity to degrade to various boron-substituted product in presence of $NaBH_4$,[29,54] especially under forcing conditions. These side reactions might be plausible reasons for such a process not being catalytic. Despite the limitation, our borylation can be performed in a cyclic manner as the by-product **5** could be recycled back to **1** and further used to generate **2** (Scheme 10). Independently, **5** was synthesized from (PNP)H and $NiBr_2$ isolated in 65% yield and the molecule was converted smoothly to (PNP)NiH upon treatment to $NaBH_4$. Moreover, **5** can be recycled from the reaction mixture via chromatographic separation in 88% yield.

Our proposed mechanism for the borylation reaction involves a $Ni^{(II)}/Ni^{(IV)}$ redox couple where $Ni^{(II)}$ promotes oxidative addition to bromobenzene. Reductive elimination follows to remove aryl boronate ester. Unfortunately, we do not observe any intermediate along the oxidative addition/reductive elimination pathway, to unambiguously determine if a nickel redox couple is involved. Masuda and coworkers have reported earlier a palladium catalyzed preparation of aryl boronate ester from alkyl halides and triflates with dialkoxyborane. In their case, the presence of a base such as Et_3N is necessary, presumably because it polarizes the B−H bond to eventually form Et_3NHX (X = halide, triflate). Our proposed mechanism certainly contrasts with the mechanistic pathway suggested by Masuda since a $Ni^{(II)}/Ni^{(IV)}$ couple is believed to be involved instead of a $Pd^{(0)}/Pd^{(II)}$ couple (Scheme 11).[55]

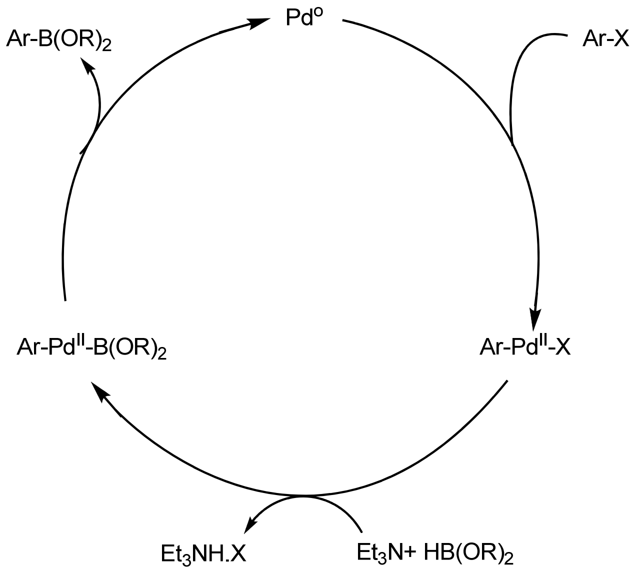

Scheme 11: Catalytic borylatyin as proposed by Masuda involving $Pd^{(0)}/Pd^{(II)}$ couple.

Alternatively, the non innocence redox properties of the PNP ligand (discussed in detail in Chapter 3) might be playing a role in the conversion since it could serve as an electron-hole reservoir along the oxidative addition/reductive elimination pathway. In the case of ligand's involvement, the associated redox couple could be $Ni^{(I)}/Ni^{(III)}$. In Masuda's case oxidative addition precedes Pd−B bond formation, though the possibility of these two processes occurring in a reverse manner has not been refuted. In our proposed case, Ni−B bond formation unambiguously precedes oxidative addition of aryl halide. Our approach to aryl boronate ester formation and the recyling diagram (Scheme 10) is attractive for the following reasons.

(i) Three key intermediates along the borylation cycle can be isolated, and characterized which includes the first synthesis of Ni-boryl complex, **2**.

(ii) Easily synthesized and readily available starting materials such as **1**, **2**, and **5** can be recycled.

(iii) This proposed borylation cycle uses a cheaper metal (Ni as opposed to the most heavy and expensive metals) as well as cheaper catecholborane as an alternative boryl source rather than expensive biscatecholborane reagent.

(iv) Our hypothesized mechanistic scheme involves a $Ni^{(II)}/Ni^{(IV)}$ redox couple whereby a $Ni^{(II)}$ boryl undergoes oxidative addition of ArBr.

2.3 Introduction to Nickel Silyl Chemistry.

Organosilicon compounds have been the major focus of several research groups owing to their wide applications in organic synthesis,[56,57] as well as their interesting physio-chemical properties.[58] In order to develop the metal catalysts which can smoothly perform the synthesis of such compounds, a detail perception of the nature of metal-silicon bond is necessary. The synthesis and structure of metal-silicon bonds have been actively pursued targeting two particular objectives: (I) Primarily it allows comparison with related systems containing metal-carbon bond and (II) provides a better understanding and insight into the elementary steps that may take place in very important metal catalyzed industrial processes such as hydrosilylation[59-61] and the dehydrogenative coupling of primary and secondary silanes.[62] [63,64] In this context, hydrosilylation is a very effective tool in chemist's arsenal to form C−Si bonds, especially if this can be performed in a catalytic manner. The C−Si bond in turn can have widespread use to incorporate multiple functionalities leading to novel organosilicon compounds, to produce fine chemicals, chemical intermediates and organosiloxane polymers.[65,66] For example, asymmetric hydrosilylation followed by oxidative cleavage of C−Si bond results in optically active alcohols, avoiding the potentially difficult and sometimes inconsistent step of asymmetric hydroboration.[67] Moreover, biaryl species can be easily furnished employing the Hiyama coupling,[68-72] in which organosilanes are coupled with aryl and alkyl halogenides or triflates. Therefore, organosilane is an important precursor and can be readily prepared by hydrosilylation. It has been proposed in a number of stoichiometric and catalytic silylation reactions that transition metal complexes having a metal-silicon bond might be playing an essential role in these processes.[73-75] Under this premise, transition metal catalyzed hydrosilylation utilizing a metal like nickel is always attractive given the low cost associated with this element when compared to its heavier congeners or precious group of coinage metals such as Pd, Pt, Re. Quite justifiably, nickel catalyzed reactions for the three component coupling of aldehydes, alkynes and silanes to produce protected allylic alcohols is also becoming an attractive field of study.[76,77]

As noted before, in the nickel catalyzed silylation reactions, it is believed that nickel silyl or even silylene complexes may be playing pivotal roles in these transformations. Our current interest in nickel mediated group transfer reactions prompted us to explore silylation chemistry using this transition metal.[21] Surprisingly, a survey of the literature reveals that silyl complexes of nickel are not very well documented and isolable examples of such functional group is relatively scarce.[78-87] Arguably, the low number of isolable and well characterized nickel silyl complexes might stem from the lack of synthetic methods to generate the silyl anion ligand. Indeed, such limitation likely involves the difficulty associated with synthesizing lithium salts of silanes which are necessary to perform salt metathesis with metal halides to prepare the corresponding silyl complexes.[88-90] Our earlier success to stabilizing a nickel-boryl complex, **2**, by the PNP ancillary ligand (*vide supra*) prompted us to use the same platform to stabilize the nickel silyl complexes. The following section discusses a mild protocol for the synthesis of nickel-silyl complexes synthesized from both primary and secondary silanes, their full characterization, and pertinent reactivity associated with the Ni−Si bond.

2.4 Results and Discussion

2.4.1 Synthesis of Nickel Silyl Complexes.

The first transition metal silyl complex was $Cp(CO)_2FeSiMe_3$, synthesized by Wilkinson et al. in 1956. From then onwards there is a growing interest in synthesizing transition metal silyl complexes for their potential use in hydrosylilation. In the earlier section of this chapter we described how we were able to synthesize a novel nickel boryl complex, **2** when **1** was stirred with catechol borane. Complex **2** is formed in room temperature along with the liberation of hydrogen gas (*vide supra*). In the pursuit of synthesizing nickel silyl complexes we speculated that the same strategy may produce an analogous set of complexes having terminal Ni−Si bonds. Unfortunately, we observed that reaction of **1** with phenyl silane requires forcing conditions (120 ^{o}C, >14 days) for at least 50−60% conversion of complex **1** to convert the corresponding silyl species (PNP)Ni(SiH_2Ph) (**6**). Though it is expected that the liberation of dihydrogen will create the entropic driving force towards product formation, the sluggishness of the reaction may stem from inherent strength of the Ni−H bond coupled with the reactivity of the Ni−Si bond. Inspired by the work of Liang and coworkers where use of a powerful Lewis acid such as $AlMe_3$ triggered the C−H activation of benzene by a similar nickel hydride species (PNP')NiH (PNP'= N[2-PR_2-C_6H_5]$_2$, R = Cy, $^{i}Pr_2$), we envisioned that an analogous Si−H activation reaction could be promoted if the Ni−H bond were to be polarized.[91]

Accordingly, complex **1** was treated with various Lewis acids to facilitate silane activation to form the desired Ni−Si bond. Gratifyingly it was found that the primary silane, $PhSiH_3$, in presence of ZnI_2 (anhydrous) could generate the nickel silyl species **6** within 14 hours (quantitatively) when the mixture was heated at 60 ^{o}C (Scheme 12). The product was isolated in good yield (82%) when crystallized from diethylether at −35 ^{o}C over 2 days. Complex **6** is stable for months when stored under a nitrogen atmosphere, or upon heating in benzene at 150 ^{o}C for prolonged periods of time (~ 4 days). Even under these forcing conditions, no decomposition products are detected by ^{31}P and ^{1}H NMR spectroscopy. In the case of secondary silane such as Ph_2SiH_2, the use of ZnI_2 was ineffective in promoting clean Si−H activation by **1**. Instead, copious amounts of (PNP)NiI were observed as a side product when the mixture was heated to 60 °C for 24 hours in hexane. Other attempts in employing MgI_2, $AlMe_3$, or $SmCl_3$ as Lewis acids also failed to generate the expected product. To our surprise, it was found that $[PhNHMe_2][B(C_6F_5)_4]$ was the most suitable reagent to accomplish formation of the desired secondary silyl complex, (PNP)Ni($SiHPh_2$) (**7**), isolated in 42% yield as a red colored material.

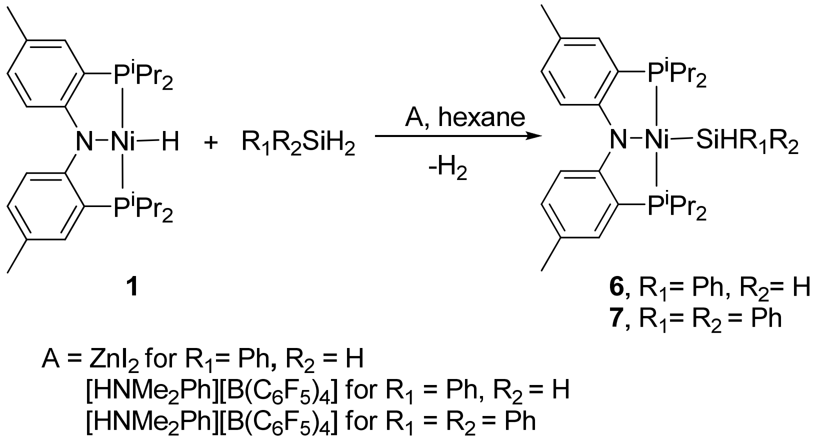

Scheme 12. General synthetic scheme for the preparation of compounds **6** and **7** from the hydride precursor **1**.

Usually, synthesis of transition metal silyls from hydrosilanes, are sensitive to the steric bulk imposed by the hydrosilane. Since in case of formation of **7**, a sterically bulky hydrosilane, Ph_2SiH_2 was involved, we surmised that the intermediate species generated from **1** with $[PhNHMe_2][B(C_6F_5)_4]$ was very reactive. Conceptually, this Brønsted acid will accelerate the reaction of **1** with $PhSiH_3$ *en route* to the formation of **6**. Indeed, the reaction was completed within 3 hours at 65 °C when $[PhNHMe_2][B(C_6F_5)_4]$ was employed as an activator. Parallel methods of treating a metal alkyl complex with free silane to liberate alkane is a known strategy, and Tilley *et al*. has reported the preparation of Cp(dmpe)VSiHPh$_2$ (Cp = cyclopentadienyl, dmpe = 1,2-bis(dimethylphosphino)ethane) from Cp(dmpe)VMe with Ph$_2$SiH$_2$.[92] But assembling the corresponding silyl complexes using Lewis acid promoted reaction has not been documented earlier. Other routes to preparing nickel silyls includes reaction of hydrosilane with a reactive Ni$^{(0)}$ precursor.[82] Given the sensitivity of the Ni$^{(0)}$ reagents and cost associated with it, starting with Ni$^{(II)}$ complexes are more advantageous. In this context it is relevant to mention that other transition metal silyls having the same pincer-PNP ligand have been explored recently by Tilley and Ozerov *et al*.[93,94]

2.4.2 Characterization of the Nickel Silyl Complexes 6 and 7

In order to unambiguously ascertain the geometry about the metal center in complex **6** we resorted to single crystal X-ray diffraction analysis. The crystal structure of **6** as depicted in Figure 5, unequivocally exposes the nickel center confined in a square planar environment, and bearing a terminal *sp*^{3} hybridized silicon atom. The phenyl ring associated with the Si atom makes an angle of 90.05° with the imaginary plane comprising the atoms Ni−P−P−N. The orthogonal orientation of the ring is probably due to avoid steric congestion imposed by the isopropyl groups on phosphorus. If one assumes local symmetry of the −SiH$_2$Ph group, the molecular structure of complex **6** grossly possesses C_{2v} symmetry which is corroborated by ^{1}H NMR spectroscopic data (*vide infra*). Diamagnetic **6** evinces a triplet at 4.63 ppm for the silyl hydrogens (^{1}H

NMR: ${}^{3}J_{\mathrm{P-H}}$ = 10 Hz) therefore proving the equivalence of the hydrogens attached to silicon.

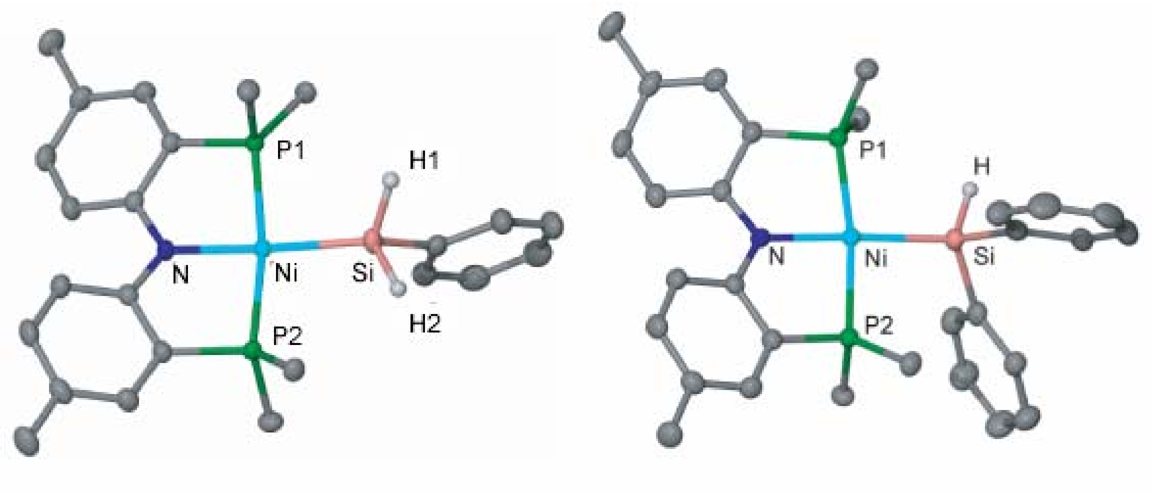

Figure 5. Solid state structures of complexes **6** (left) and **7**. All hydrogens except those on silicon, and solvents and isopropyl methyls on phosphorus have been removed for clarity. Thermal ellipsoids are displayed at the 50% probability level. Selected metrical parameters (distances in Å and angles are in °). For **6**: Ni−Si, 2.2346(5); Ni−P1, 2.1765(4); Ni−P2, 2.1776(4); Ni−N, 1.9362(12); Si−H1, 1.44(2); Si−H2, 1.40(2); N−Ni−Si, 174.24(4); P1−Ni−P2, 168.127(17); Ni−Si−H1, 113.2(9); Ni−Si−H2, 115.4(9); N−Ni1−P1, 85.13(4); N−Ni1−P2, 86.24(4); P1−Ni1−Si, 92.914(17); P2−Ni−Si, 94.882(17). For **7**: Ni−Si, 2.2607(7); Ni−P1, 2.1792(6); Ni−P2, 2.1857(6); Ni−N, 1.9375(17); Si−H, 1.42(3); N−Ni−Si, 175.06(6); P1−Ni−P2, 171.57(2); Ni−Si−H, 112.1(10); N−Ni−P1, 85.12(5); N−Ni1−P2, 86.53(5); P1−Ni−Si, 94.41(2); P2−Ni−Si, 93.81(2).

Analogously, the ^{31}P NMR spectrum displays a singlet at 44.13 ppm further being consistent with the proposed C_{2v} symmetry of the complex. In the ^{31}P NMR spectrum, satellites are observed due to coupling with ^{29}Si nucleus ($I = ½$, 4.68% abundant) with a coupling constant $^{2}J_{P-Si}$ of 54 Hz. Most notably, the ^{29}Si{^{1}H} NMR spectrum exposes a triplet at −40.45 ppm (Figure 6), while the proton coupled ^{29}Si NMR spectrum portrays a triplet of triplets due to phosphorus and hydrogen coupling ($^{2}J_{P-Si} = 54$ Hz, $^{1}J_{Si-H} = 160$ Hz, Figure 6). The combination of the ^{29}Si NMR chemical shift value and large J_{Si-H} are in accord with the sp^3 hybridized silicon nucleus, and argues against the possibility of the silylene moiety being present in solution by virtue of an 1,2-hydrogen migration.[87,94-99] This argument is further supported by the Ni−Si bond length, 2.2346(5) Å, which is slightly shorter than the value, 2.245(2) Å reported by Hillhouse *et al.* in (dtbpe)Ni(μ-H) SiH(Mes)$_2$ (dtbpe = 1,2-bis(di-tert-butyl-phosphino)ethane, Mes = mesityl) and comparable to the few structurally characterized nickel-silyl complexes reported in literature.[82] In fact, for the nickel-silyl single bond lengths, a range of 2.14−2.30 Å has been documented in the literature.[100] Notably, another mode of silyl coordination to the nickel is Si−H σ-coordination in a η^2 fashion. This bonding mode is truly important along the pathway of oxidative addition of Si−H bond to the nickel center. Logically, Ni−Si bond distances are longer in that scenario compared to the terminal case as ours. In accordance with our claim for a Ni−Si single bond length, the presence of a sp^3-hydridized silicon atom was evident from the located silyl-hydrogens in the Fourier difference map (Si−H distances were 1.44(2) and 1.40(2) Å). Other structural details regarding data collection and metrical parameters are summarized in Table 1 (see experimental section).

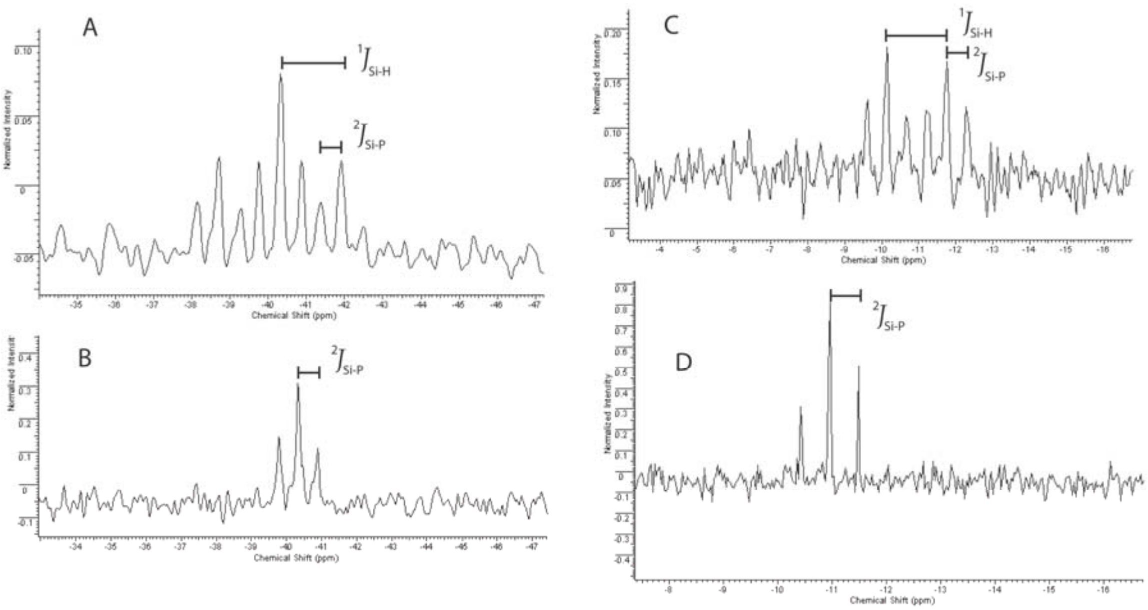

Figure 6. Expanded regions of the $^{29}Si\{^1H\}$ and ^{29}Si NMR spectra for complexes **6** (**A** and **B**) and **7** (**C** and **D**).

Likewise, the molecular structure of **7** presents grossly the same features as found in **6**. One of these features includes the formation of a square planar nickel center coordinating a terminal, and secondary silyl ligand with a Ni−Si bond distance of 2.2607(7) Å. The hydrogen atom on silicon is oriented away from the metal center thus excluding the possibility of an α-H agostic interaction taking place in the solid state.[101-103] Importantly, the agostic interaction of Si−H bond in the β-position is fairly common in the case of group 4−6 metals, and such an interaction has a considerable effect on the stability of the complex. Another noteworthy feature is the elongated Ni−N bond length of 1.9375(17) Å, due to presence of silyl group in the trans position, compared to Ni−N bond length of 1.8980(15) Å in (PNP)NiCl . Silyl groups are believed to be a strong trans influencing group as it behaves as a strong σ-donor.[104] The elongation of a bond which is located trans to the silyl ligand is vividly observed in both **6** (1.9362 Å) and **7** (1.9375 Å) when compared to other square planar nickel complex such as (PNP)NiCl (Ni−N bond length is 1.8980(5) Å). Similar elongation has been reported by Puddephatt *et al*. where Pt−I distance has been significantly increased when a $-\text{SiMe}_3$ group is present trans to the iodide ligand.[105] The ^{1}H NMR spectrum of complex **7** shows the silyl hydrogen centered at 5.42 ppm ($^3J_{\text{P–H}}$ = 13 Hz), a value which is expected for most transition metal silyl complexes. This proton resonance position is also a proof for the agostic interaction to be non-operational since in that case proton resonance of the involved hydrogen is shifted considerably upfield.[104] Equivalence of phosphorus due to $C_{2\text{v}}$ symmetry is evident from a singlet at 42.59 ppm, along with the observation of Si satellites ($^2J_{\text{Si-P}}$ = 52 Hz). To our surprise, however, the ^{29}Si{^{1}H}NMR spectrum exhibits a doublet at −11.08 ppm, that is significantly deshielded when compared to the silyl chemical shift observed in **6** (Figure 6). We surmise that the electron density around the silicon atom in **7** considerably depletes due to the presence of an additional electron withdrawing phenyl ring compared to **6**, hence shifting the resonance for **7** more downfield than the primary phenylsilyl. When the ^{1}H coupled ^{29}Si NMR spectrum is collected for **7**, the signal resolves as a doublet of triplets with a $^1J_{\text{Si–H}}$ = 161 Hz (Figure 6). The $^1J_{\text{Si–H}}$ coupling constant value clearly advocates a classic 2c-2e bond in the Ni−Si segment compared to any nonclassical 3c-2e bond involved in η^2(Si−H) interaction to the metal center.[106]

2.4.3 Alternative syntheses for 6 and 7

Alternatively, complexes **6** and **7** can also be synthesized by a metalloradical assisted reductive cleavage of the Si−H bond of the corresponding organosilane. Accordingly, the reaction of **3** with PhSiH_3 rapidly produces **1** and **6** in equal molar amounts (Scheme 13).[30] In case of the secondary silane, Ph_2SiH_2, binuclear oxidative addition of the Si−H bond also occurs to form **1** and **7**, but the reaction requires moderate heating and extended period of time (65 °C, 20 hours), presumably due to increased steric encumbrance surrounding the Si−H bond of the organosilane. This lack of reactivity for sterically crowded hydrosilanes were further evidenced as tertiary silanes such as Et_3SiH and Ph_3SiH did not render any corresponding nickel silyl complex formation even under prolonged heating of the mixture at 80 °C.

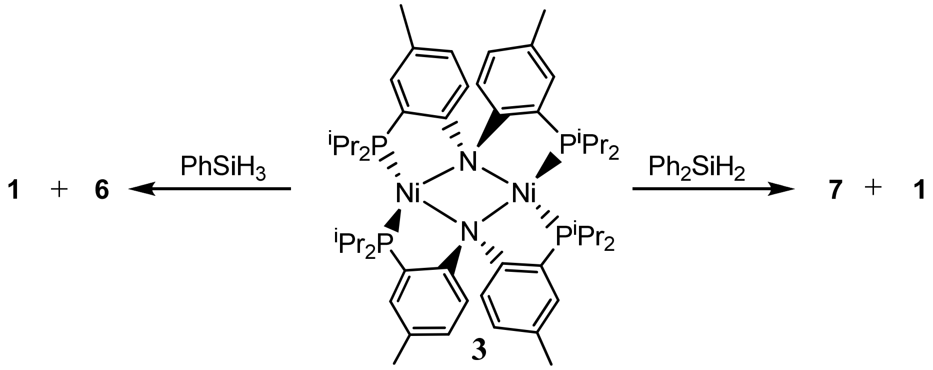

Scheme 13. Si−H bond cleavage promoted by a dimeric complex **3** to prepare equal molar mixtures of hydride **1** and silyl **6** or **7**.

2.4.4 DFT analysis for structural elucidation of 6 and 7

In order to understand the electronic structure of the nickel silyl complexes **6** and **7**, as well as the nature of the Ni−Si bond, we performed high level DFT calculations on the full model of the complexes. Structural optimization using the B3LYP/6-31G** level of theory reproduced the geometrical features of the two molecules expectedly well. The Ni−Si bond order obtained from NBO[107] calculations reveals a value of 0.91 for both **6** and **7**, thus unequivocally supporting the presence of a single Ni−Si bond. As portrayed in Figure 7, the frontier orbitals of complex **6** have a filled *d*(z^2) HOMO-1 orbital and unoccupied *d*(x^2-y^2) LUMO orbital, which is anticipated for a square planar d^8 system. The HOMO contains a great amount of the pincer amide nitrogen lone pair character as well as alternating carbons composing the PNP aryl rings.[108] Further analysis reveals that the LUMO is localized primarily on the silyl moiety with significant contribution from the Si sp^3 hybrid orbital. Not surprisingly, the DFT analysis of complex **7** reveals essentially the same features as observed for **6** (Figure 8**).** Additional calculations to obtain a quantitative understanding of the orbital composition using the ADF package[109] are also fully consistent with the above result (See experimental section).

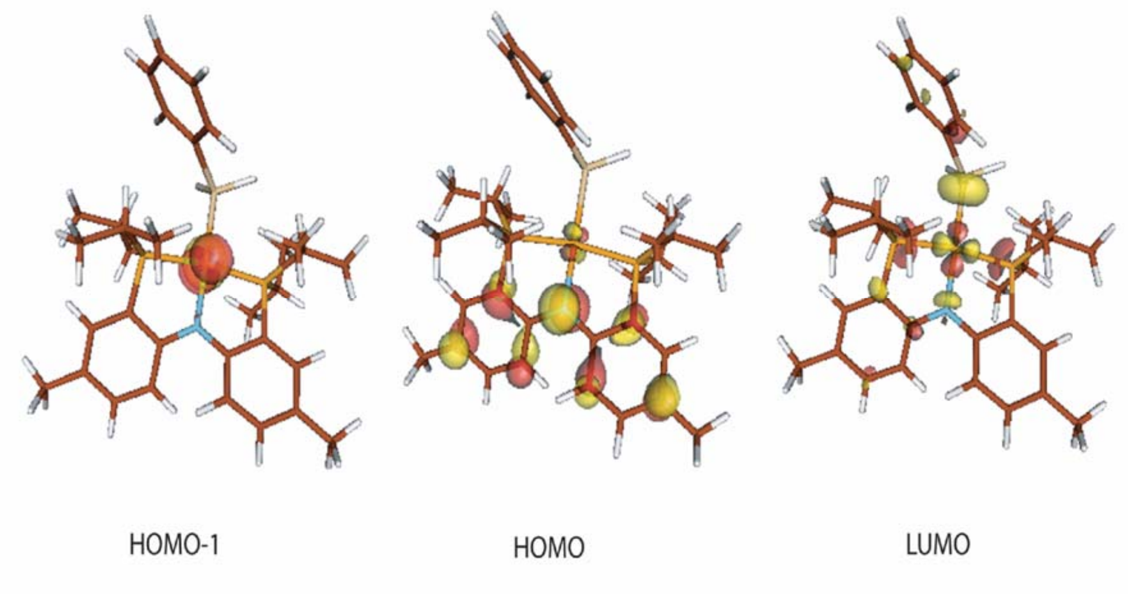

Figure 7: Most important molecular orbitals for complex **6** shown with isodensity = 0.05 au.

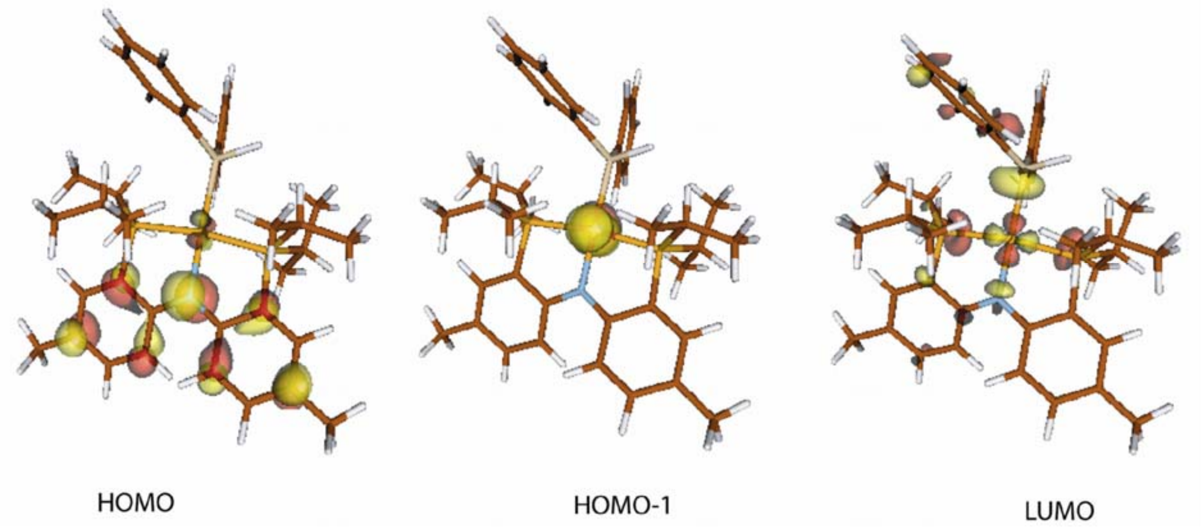

Figure 8: Most important molecular orbitals for complex **7** shown with isodensity = 0.05 au.

2.4.5 Reactivity of 6 and 7

The reactivity of compounds **6** and **7** was examined with 1-hexene. Unfortunately, no insertion was observed even upon heating the mixture at 120 °C for 24 hours. This phenomenon suggests that the square-planar $Ni^{(II)}$ environment prevents substrate from reacting at the Ni−Si bond. Likewise, treatment of **6** or **7** with benzaldehyde also failed to react even under extended periods (2 days) at 70 °C, presumably due to the same kinetic factors. Moreover, addition of 1 equivalent of Ph_2SiH_2 to a hexane solution of **6** did not result in any equilibrium mixture of **7** and $PhSiH_3$ even under thermolytic conditions (120 °C, 12 hours) therefore rendering the nickel-silyl ligand rather inert towards substitution chemistry. In agreement with the exchange behavior, complexes **6** and **7** do not show any silyl ligand dissociation even at higher temperatures as evidenced by ^{29}Si NMR spectroscopy opposed to the very rapid dissociation of silyl fragment in (dtbpe)Ni(μ-H) $SiH(Mes)_2$ reported by Hillhouse *et al.* [82] Even at room temperature, a benzene solution of the mentioned complex displays the free silane resonance and the undissociated complex is observed predominantly only at low temperature. However this proclivity of the silyl fragment to be dissociated is a function of steric encumbrance associated with the silyl moiety since less sterically congested analogues do not show such dissociation. Similarly, Cp(dmpe)$VSiHPh_2$ also exhibits rapid exchange behavior when it is exposed to the other silanes.[92] Silyl group-transfer also fails to occur with bromobenzene over a period of 3 days at 120 °C. Therefore, our ability to kinetically stabilize nickel silyl complexes in a square-planar environment compromises its reactivity, presumably at the expense of a sterically congested ligand environment about the $d(x^2-y^2)$ orbital.

2.4.3 Investigation of the Mechansim to Si−H Activation.

Work by Liang and co-workers have demonstrated that a powerful Lewis acids such as $Al(CH_3)_3$ can promote the activation of the C−H bond in benzene or toluene when combined with a nickel hydride or methyl complex (PNP')NiR (PNP'= N[2-PR'$_2$-phenyl]$_2$, R = H, Me; R' = Cy, $^iPr_2$).[91]Although not addressed, it is anticipated that hydride or methide abstraction by $Al(CH_3)_3$, binding of benzene to the electrophilic $Ni^{(II)}$ cation, and subsequent acid-base chemistry might be transpiring along this type of process. Interestingly, we observed an intermediate formation (intermediate appeared at 39.87 ppm in ^{31}P NMR spectrum) during the reaction of $Al(CH_3)_3$ with **1** employing our ligand set. For us, the use of $Al(CH_3)_3$ to promote Si−H activation resulted in formation of a myriad of uncharacterized products along with a minor amount of the expected nickel silyl complexes. However, the use of anhydrous ZnI_2 proved fortuitous since it is a much milder Lewis acid than $Al(CH_3)_3$. On the other hand, wet or crude ZnI_2 did not yield the same result therefore arguing against adventitious HI being involved for the aforementioned reaction. In fact, no HI is likely generated in this reaction since addition of a base such as Et_3N does not inhibit the formation of **6** from **1** and $PhSiH_3$. To understand the process leading to Si−H activation, we investigated the reaction of ZnI_2 with **1** in benzene and in the absence of silane. The result was considerable amount of (PNP)NiI formation under 1 hour heating at 60 ^{o}C therefore suggesting activation of the hydride by the Lewis acid. Unfortunately, we have been unable to characterize the Zn byproducts formed from this control experiment. Addition of ZnI_2 to silane resulted in no detectable reaction when the mixture was heated at 60 ^{o}C and monitored by ^{1}H NMR spectroscopy. Examination of the volatiles from the reaction mixture leading to **6** revealed formation of H_2 as a byproduct thus hinting that ZnI_2 is likely polarizing the hydride moiety in **1** to facilitate metathesis with the H−Si bond in H_3SiPh. We cannot refute, however, the possibility of ZnI_2 polarizing the hydridic Si−H bond especially since a similar reactions has been proposed and reported in the literature.[110,111] Regardless, ZnI_2 must be used as a stoichiometric reagent in order for complete conversion of **1** to **6** to take place. The latter fact suggests that ZnI_2 is likely being transformed along the Si−H activation pathway.

Unfortunately, the use of ZnI_2 failed to promote the activation of the Si−H bond in the secondary silane H_2SiPh_2. Instead, the Brønsted acid $[PhNHMe_2][B(C_6F_5)_4]$ facilitated the conversion when combined with **1** and a secondary silane. In fact, examination of the volatiles for the latter process also reveals H_2 to be produced as a by-product. The use of **1** in the Si−H activation is essential since $[PhNHMe_2][B(C_6F_5)_4]$

alone fails to show any reactivity with the secondary silane. It was found that addition of NEt_3 to **1** and $[PhNHMe_2][B(C_6F_5)_4]$/silane completely ceased formation of **7** therefore implicating that acid-base chemistry likely takes place in this type of reaction. Therefore, we propose for the latter reaction, that the nickel hydride (PNP)NiH is likely being protonated to a transient cation $[(PNP)Ni]^+$, which engages in activation of the silane, presumably via the base NMe_2Ph. Unfortunately, substoichiometric amounts of $[PhNHMe_2][B(C_6F_5)_4]$ (20 mol%) resulted in incomplete reactions, thus hinting that the salt is likely involved in another way apart from just a simple acid-base transformation. We cannot ignore the possibility of the PNP nitrogen being involved in a deprotonation step since recent studies by Caulton and co-workers have demonstrated the role of a pincer-type nitrogen in C−H activation processes.[112]

Obviously, the role of the Si−H bond is critical in these reactions, since tertiary silanes such as triphenyl silane or triethyl silane failed to react with **1** in presence of ZnI_2 or $[PhNHMe_2][B(C_6F_5)_4]$. As a result, we are presently unsure of what mechanism is governing these set of reactions, especially given the differing nature of the activators (ZnI_2 versus $[PhNHMe_2][B(C_6F_5)_4]$) and the selectivity for Si−H activation of a primary versus a secondary silane.

2.5 Conclusion

A nickel-boryl molecule which has been synthesized from **1** and catechol borane has been thoroughly characterized by multinuclear NMR spectroscopy and X-ray crystallography. This molecule is the first isolated and well characterized example of a boryl species involving nickel. No significant backdonation has been observed from nickel to boron as supported by theoretical analysis and this result prompts us to conclude the single bond nature associated with the Ni−B bond. The boryl group can be easily transferred to bromobenzene to engender an important organic feedstock aryl boronic ester under moderate condition. The byproduct of the reaction **5** can be recycled back to **2** hence making the whole process cyclic. However, complex **1** reacts with the substrate bromobenzene under the reaction condition, eliminating the possibility of catalysis. One way to improve the system to be catalytic can be replacing **1** as a means of forming **2**, thus bypassing undesired side reaction which kills the catalytic cycle. Keeping the similarity of boron and silicon in mind due to their diagonal relationship in the periodic table, same strategy was employed to synthesize nickel silyl complexes. However a Lewis promoted activation of the Ni−H bond is required to accomplish formation of the nickel-silyl species **6** and **7,** from primary and secondary silanes under mild condition. Preliminary theoretical analysis implies a bond order of one for the Ni−Si bond in both complexes. The robust coordination of the pincer ligand kinetically stabilizes these species but the reactivity of the complexes is sacrificed since the only available $d(x^2\text{-}y^2)$ orbital in a square planar environment becomes sterically protected. A ligand with low coordination number might be eliminating this reactivity problem by changing the geometry of the nickel center, hence giving access to the orbitals.

2.6 Experimental Section

General Considerations. Unless otherwise stated, all operations were performed in a M. Braun Lab Master double-dry box under an atmosphere of purified nitrogen or using high vacuum standard Schlenk techniques under an argon atmosphere.[113] Anhydrous *n*-

hexane, pentane, toluene, and benzene were purchased from Aldrich in sure-sealed reservoirs (18 L) and dried by passage through two columns of activated alumina and a Q-5 column. Diethylether was dried by passage through a column of activated alumina. THF was distilled, under nitrogen, from purple sodium benzophenone ketyl and stored under sodium metal. Distilled THF was transferred under vacuum into collection flask before being transferred into a dry box. C_6D_6 was purchased from Cambridge Isotope Laboratory (CIL), degassed and vacuum transferred to 4 Å molecular sieves. (PNP)Li (PNP = $N[2\text{-}P(CHMe_2)_2\text{-}4\text{-}MeC_6H_4]_2^-$)[20,53] was prepared according to the literature. All other chemicals were used as received. Hydrosilanes used in this manuscript were bought commercially from Aldrich and Alfa Aesar and used without further purification. $AlMe_3$ was purchased from Aldrich and used as it is (*Caution should be exercised when handling this reagent as it is highly pyrophoric and combusts spontaneously when comes in contact of air or moisture*). ^1H, ^{13}C, ^{11}B, and ^{31}P NMR spectra were recorded on Varian 400 or 300 MHz NMR spectrometers and ^{29}Si NMR spectra were recorded in a Varian 500 MHz spectrometer. ^1H and ^{13}C NMR are reported with reference to solvent resonances (residual C_6D_5H in C_6D_6, 7.16 ppm and 128.0 ppm respectively). ^{31}P NMR chemical shifts are reported with respect to external H_3PO_4 (aqueous solution, δ 0.0 ppm). ^{11}B NMR chemical shifts are reported with respect to external $BF_3.OEt_2$ (δ 0.0 ppm). ^{29}Si NMR chemical shifts are reported with respect to external $SiMe_4$ set at 0.0 ppm. UV-Vis spectra were recorded on a Cary 5000 UV-Vis-NIR spectrophotometer. X-ray diffraction data were collected on a SMART6000 (Bruker) system under a stream of N_2 (g) at low temperatures.

Synthesis of (PNP)Ni[B(catechol)] (2).

In a vial (PNP)NiH (**1**) (100 mg, 0.205 mmol) was dissolved in 5 mL of benzene and a solution of catecholborane (25 mg, 0.205 mmol) in benzene was added dropwise. The reaction mixture was stirred for 12 hours and then dried in vacuo. The yellow-brown material was extracted with diethyl ether, filtered, and the filtrate reduced in volume. The solution was then cooled to − 35 °C to afford **2** as yellow colored crystals (101 mg, 0.166 mmol, 81% yield). ^{1}H NMR (25 ^{o}C, 399.8 MHz, C_6D_6): δ 7.86 (d, 2H, C_6H_3), 7.24 (m, 2H, C_6H_4), 6.91 (br, 4H, overlap of aromatic resonances), 6.84 (m, 2H, C_6H_3), 2.28-2.21 (br, 10H, methyl and isopropyl methine resonances overlapped), 1.08 (dd, 12H, CH*Me*$_2$), 1.00 (dd, 12H, CH*Me*$_2$). ^{13}C NMR (25 ^{o}C, 100.6 MHz, C_6D_6): δ 161.3 (aryl), 150.2 (aryl), 132.7 (aryl), 132.5 (aryl), 128.4 (aryl), 124.0 (aryl), 121.6 (aryl), 114.8 (aryl), 111.4 (aryl), 23.5 (*C*HMe$_2$), 20.6 (*Me*Ar), 18.5 (CH*Me*$_2$), 17.6 (CH*Me*$_2$). ^{31}P NMR (25 ^{o}C, 121.5 MHz, C_6D_6) δ 51.2. ^{11}B NMR (25 ^{o}C, 160.6 MHz, C_6D_6) δ 46.9. MS-CI, $[M+H]^+$: calcd: 605.2288, found: 605.2290. M. p. 172 ^{o}C. UV-vis (hexane, 24 ^{o}C): 413 nm (ε = 4042 $M^{-1}\cdot cm^{-1}$).

Synthesis of (PNP)NiO^{t}Bu (4)

In a vial Ni(PNP)Cl (300 mg, 0.571 mmol) was taken in 5 ml of THF and cooled to −35 ^{o}C. An analogously cooled solution of KO^{t}Bu (64.29 mg, 0.571 mmol) was added dropwise to the cooled solution of Ni(PNP)Cl. After 30 minutes the color of the reaction mixture changed to bluish. The reaction mixture was stirred for 2 hours and then dried in vacuo. The dried mass was extracted with pentane to afford a blue color solution which upon keeping at −45 °C yield crystals (252 mg, 0.449 mmol, 79% yield).

^{1}H NMR (25 °C, 399.8 MHz, C_6D_6): δ 7.34 (d, C_6*H_3*, 2H), 7.06 (s, C_6*H_3*, 2H), 6.65(d, C_6*H_3*, 2H), 2.36(septate, C*H*Me_2, 4H), 2.14(s, *Me*Ar, 6H), 1.60 (q, CH*Me_2*, 12H), 1.35(dd, overlapped with s, CH*Me_2* and ^{t}O*Bu* resonances overlapped, 21H). ^{13}C NMR (25 °C, 100.6 MHz, C_6D_6): δ 162.26 (aryl), 131.87 (aryl), 131.74 (aryl), 124.34 (aryl), 121.28 (aryl), 117.46 (aryl), 66.83 (O*C*$(CH_3)_3$), 35.89 (OC(*C*$H_3)_3$) 24.45 (*C*HMe_2), 20.59(*Me*Ar), 19.39 (CH*Me*$_2$), 17.34 (CH*Me*$_2$). ^{31}P NMR (25 °C, 121.5 MHz, C_6D_6) 17.23. MS-CI, $[M\text{-}O^tBu]^+$: calcd: 487.247, found: 487.205

Synthesis of (PNP)NiBr (5).

In a thick wall reaction vessel anhydrous $NiBr_2$ (200 mg, 0.915 mmol) was suspended in 10 ml of benzene and a benzene solution of (PNP)H (393 mg, 0.915 mmol) was added dropwise. The reaction mixture was heated to 90 °C for 21 hours upon which 5 drops of NEt_3 was added. The mixture was filtered through a plug of celite and silica gel. The filtrate was dried under vacuo, extracted with diethyl ether and the solution was cooled to − 35 °C to afford dark green crystals of **3** (171.6 mg, 0.302 mmol, 65% yield). ^{1}H NMR (25 °C, 399.8 MHz, C_6D_6): δ 7.52 (d, 2H, C_6*H_3*), 6.92 (s, 2H C_6*H_3*), 6.73 (d, 2H, C_6*H_3*), 2.33 (m, 4H, C*H*Me_2), 2.12 (s, 6H, *Me*Ar), 1.53 (dd, 12H, CH*Me_2*), 1.24 (dd, 12H, CH*Me_2*). ^{13}C NMR (25 °C, 75.5 MHz, C_6D_6): δ 162.13 (aryl), 132.42 (aryl), 131.95 (aryl), 125.60 (aryl), 120.97 (aryl), 116.85 (aryl), 24.57 (*C*HMe_2), 20.46 (*Me*Ar), 18.84 (CH*Me*$_2$), 17.90 (CH*Me*$_2$). ^{31}P NMR (25 °C, 121.5 MHz, C_6D_6): δ 37.54. MS-CI, $[M+H]^+$: calcd: 565.1167, found: 565.1160. M.p. 168 °C.

Synthesis of (PNP)NiH (1) from 5 and $NaBH_4$.

In a vial **3** (100 mg, 0.176 mmol) was dissolved in 10 ml of THF and a suspension of $NaBH_4$ (66.7 mg, 17.6 mmol) in THF was added. The reaction mixture was stirred for 3 hours and filtered. The filtrate was then dried under vacuo, extracted with pentane and the solution cooled to −35 °C to afford brown colored crystals of **1** (53.36 mg, 0.109 mmol, 62 % yield). The characterizations of **1** was confirmed by ^1H and ^{31}P NMR spectra of independently prepared sample reported in the literature.[30]

Separation of 5 and Phenyl Boronic Ester Using preparatory Thin Layer Chromatography.

The product phenyl boronic ester was separated from **5** by a preparatory thin layer chromatography plate coated with silica. After loading the sample, the plate was eluted with 3:7 ethyl acetate, hexane solution. The phenyl boronic ester and **5** were collected in 68% and 88% respectively. Isolation of the boronic ester must be performed quickly since this product decomposes slowly in contact with silica. The phenyl boronic ester was synthesized independently by refluxing $PhB(OH)_2$ and catechol in benzene for 2 hours (in air), then removing water azeotropically by dint of a Dean-Stark apparatus.[114] The crude product was dissolved in toluene and cooled to −20 °C to afford pure ester. Although this product has been reported in the literature,[114] no ^1H NMR spectrum was documented. ^1H NMR (25 °C, 399.8 MHz, C_6D_6): δ 8.12 (m, aryl), 7.18 (m, aryl, overlapping resonances), 7.06 (m, aryl), 6.81 (m, aryl). ^{11}B NMR (25 ^{o}C, 160.6 MHz, C_6D_6) δ 32.

Crystallographic Detail of 2. OEt_2

Inert atmosphere techniques were used to place a yellow needle of approximate dimensions 0.25 × 0.25 × 0.15 mm onto the tip of a 0.1 mm diameter glass fiber. A total of 55063 reflections ($-12 \leq h \leq 12$, $-15 \leq k \leq 15$, $-20 \leq l \leq 20$) was collected at T = 132(2) K in the 2Θ range of 2.05 to 27.56^{o}, of which 6455 were observed ($R_{\text{int}} = 0.0730$). A direct-methods solution was calculated which provided most non-hydrogen atoms from the E-map. Full-matrix least squares / difference Fourier cycles were performed which located the remaining non-hydrogen atoms. All non-hydrogen atoms were refined with anisotropic displacement parameters. All hydrogen atoms were located in subsequent Fourier maps and included as isotropic contributors in the final cycles of refinement.

Synthesis of (PNP)Ni(SiH_2Ph) (6)

In a thick walled reaction vessel **1** (75 mg, 0.154 mmoml), phenylsilane (16.6 mg, 0.154 mmol) and zinc iodide (49.2 mg, 0.154 mmol) were charged in 2 mL hexane. The reaction mixture was heated at 60 ^{o}C for 14 hours and by the course of the reaction the solution color changed to orange. After the completion of the reaction, the reaction mixture was filtered, dried, dissolved in ether and kept at −45 ^{o}C. Within 2 days bright orange colored crystals of **6** were obtained (74.3mg, 0.118 mmol, 82 % yield). ^{1}H NMR (25 ^{o}C, 399.8 MHz, C_6D_6): δ 8.04 (d, 2H, C_6H_5), 7.78 (d, 2H, C_6H_3), 7.22 (m, 3H,

C_6H_5), 6.96 (s, 2H, C_6H_3), 6.88 (d, 2H, C_6H_3), 4.63 (t, 2H, SiH_2Ph) ($^3J_{\text{H-P}}$ = 10 Hz), 2.34 (septet, 4H, C*H*Me$_2$), 2.19 (s, 6H, ArCH_3), 1.21 (dd, 12H, CH*Me*$_2$), 1.06 (dd, 12H, CH*Me*$_2$). ^{13}C NMR (25 °C, 75.46 MHz, C_6D_6): δ 161.05 (aryl), 140.65 (aryl), 137.13 (aryl), 132.49 (aryl), 132.14 (aryl), 127.61 (aryl), 124.39 (aryl), 121.86 (aryl), 115.14 (aryl), 24.84 (*C*HMe$_2$), 20.66(*Me*Ar), 19.28 (CH*Me*$_2$), 17.88 (CH*Me*$_2$), one aromatic resonance was not located which might be buried under the residual solvent peak. ^{31}P NMR (25 °C, 121.5 MHz, C_6D_6) δ 44.13. ^{29}Si NMR (25 °C, 99.5 MHz, C_6D_6) δ −40.45 (triplet, $^2J_{\text{Si-P}}$ = 54 Hz). UV-vis (hexane, 25 °C): 441 nm (ε = 1471 M^{-1} cm^{-1}). MS-CI, calcd 593.230, found 593.229. M.p. 68 °C.

Synthesis of (PNP)Ni(SiHPh$_2$) (7)

In a thick walled reaction vessel **1** was taken (60 mg, 0.123 mmol) in 2 mL of hexane. Diphenyldisilane (22.65 mg, 0.123 mmol) and [HNMe$_2$Ph][B(C_6F_5)$_4$] (102.7 mg, 0.123 mmol) were added to that and heated in an oil bath at 65 °C for 12 hours. During the reaction yellow color of the solution changed to deep orange. After the completion of the reaction, the hexane solution was filtered and dried. The dried mass was redissolved in ether and kept at −45 °C to afford bright orange crystals of **7** (36.7 mg, 0.051 mmol, 42% yield). ^{1}H NMR (25 °C, 399.8 MHz, C_6D_6): δ 7.96 (m, 4H, C_6H_5), 7.78 (d, 2H, C_6H_3), 7.21 (m, 6H, C_6H_5), 6.97 (s, 2H, C_6H_3), 6.87 (d, 2H, C_6H_3), 5.42 (t, 1H, Si*H*Ph$_2$), ($^3J_{\text{H-P}}$ = 13 Hz), 2.11-2.19 (m, 10H, *Me*Ar and C*H*Me$_2$ resonances overlapped), 1.17 (dd, 12H, CH*Me*$_2$), 1.04 (dd, 12H, CH*Me*$_2$). ^{13}C NMR (25 °C, 75.46 MHz, C_6D_6): δ 160.89 (aryl), 142.92 (aryl), 137.34 (aryl), 132.38 (aryl), 132.29 (aryl), 127.47 (aryl), 124.15 (aryl), 121.96 (aryl), 121.73 (aryl), 115.33 (aryl), 24.83 (*C*HMe$_2$), 20.66 (*Me*Ar), 19.98

(CH*Me*$_2$), 18.16 (CH*Me*$_2$). ^{31}P NMR (25 ^{o}C, 121.5 MHz, C_6D_6) 42.59 ($^2J_{\text{Si-P}}$ = 52 Hz). ^{29}Si NMR (25 ^{o}C, 99.5 MHz, C_6D_6) δ −11.08 (triplet, $^2J_{\text{Si-P}}$ = 54 Hz). UV-vis (hexane, 25 ^{o}C): 427 nm (ε = 3200 M^{-1} cm^{-1}). MS-CI, calcd 669.2614, found 669.2605. M.p. 106 ^{o}C

Synthesis of (PNP)NiI

In a thick walled reaction vessel (PNP)H (50 mg, 0.116 mmol) was charged with anhydrous NiI_2 (36.4 mg, 0.116 mmol) in benzene and heated at 110 ^{o}C for 5 hours. During the course of the reaction, solution color changed to deep green. After the completion of the reaction two drops of triethyl amine was added and the reaction mixture was filtered through a pad of silica gel. The green filtrate was dried in vacuo and the solid mass was found to be spectroscopically pure (50 mg, 0.081 mmol, 70% yield).

^{1}H NMR (25 ^{o}C, 399.8 MHz, C_6D_6): δ 7.56 (d, C_6H_3, 2H), 6.94 (s, C_6H_3, 2H), 6.75 (d, C_6H_3, 2H), 2.40(m, C*H*Me$_2$, 4H), 2.13(s, *Me*Ar, 6H), 1.50 (dd, CH*Me*$_2$, 12H), 1.22(dd, CH*Me*$_2$, 12H). ^{13}C NMR (25 ^{o}C, 100.6 MHz, C_6D_6): δ 162.37 (aryl), 132.47 (aryl), 132.02 (aryl), 125.46 (aryl), 121.36 (aryl), 116.53 (aryl), 25.53 (*C*HMe$_2$), 20.47(*Me*Ar), 19.20 (CH*Me*$_2$), 18.06 (CH*Me*$_2$). ^{31}P NMR (25 ^{o}C, 121.5MHz, C_6D_6) δ 44.74. [MS-CI] calcd: 613.1029; observed: 613.1002.

Si−H bond splitting reaction with 3 to prepare 6 and 1

In a J-Young tube **3** was dissolved (30 mg, 0.031 mmol) in hexane and calculated amount of $PhSiH_3$ (3.32 mg, 0.031 mmol) was added to that. The brown color of the solution was changed to orange immediately. The reaction mixture was stirred at room temperature for

5 minutes. By ^{1}H and ^{31}P NMR spectra it was observed that **1** and **6** have been formed in equal molar amount.

Si−H bond splitting reaction with 3 to prepare 7 and 1

In a J-Young tube **3** was dissolved (30 mg, 0.031 mmol) in hexane and calculated amount of Ph_2SiH_2 (5.67 mg, 0.031 mmol) was added to that. No immediate color change was observed after the addition. The reaction mixture was stirred for 20 hours at 65 ^{o}C. By ^{1}H and ^{31}P NMR spectra it was observed that **1** and **7** have been formed in approximately equal molar amount.

Reaction of 1 with $PhSiH_3$ in presence of $AlMe_3$

In a J-Young tube **1** (30 mg, 0.06 mmol) was dissolved in 1mL hexane along with phenyl silane (3.31 mg, 0.06 mmol) and trimethyl aluminium (4.46 mg, 0.06 mmol). The reaction mixture was stirred for 30 minutes at room temperature and the solution of the color was changed to orange from yellow. ^{31}P NMR experiment showed myriad of uncharacterized products formation along with very little formation of **6**.

Reaction of 1 with Et_3SiH in presence of ZnI_2

In a J-Young tube **1** (30 mg, 0.06 mmol) was dissolved in 1mL hexane along with triethyl silane (3.57 mg, 0.06 mmol) and anhydrous zinc iodide (19.8 mg, 0.06 mmol). The reaction mixture was heated 60 ^{o}C for 12 hours to result copious amount of (PNP)NiI formation without engendering any trace of corresponding nickel silyl species.

Control experiment: Synthesis of 6 in presence of a base

In a J-Young tube **1** (30 mg, 0.06 mmol) was dissolved in 1mL hexane along with phenyl silane (3.31 mg, 0.06 mmol) and anhydrous zinc iodide (19.8 mg, 0.06 mmol). To that solution triethyl amine was added (6.07 mg, 0.06 mmol) and the resulting mixture was heated at 60 ^{o}C for 14 hours. During heating the color of the solution changed to orange and **6** was isolated quantitatively at the end of the reaction. This control reaction proves that external base does not restrict the formation of **6**.

Control experiment: Attempt to Synthesize 7 in presence of a base

In a J-Young tube **1** (30 mg, 0.06 mmol) was dissolved in 1mL hexane along with diphenyl silane (12.4 mg, 0.06 mmol) and $[NHMe_2Ph][B(C_6F_5)_4]$ (51.3 mg, 0.06 mmol). To that solution triethyl amine was added (6.07 mg, 0.06 mmol) and the resulting mixture was heated at 65 ^{o}C for 12 hours. During the addition of base effervescence was coming out of the solution mixture. No desired product formation was observed during the course of the reaction proving that external base ceases the formation of **7**.

Control experiment: Reaction of ZnI_2 with $PhSiH_3$

In a J-Young tube was mixed ZnI_2 (12.5 mg, 0.039 mmol) along with phenyl silane (4.2 mg, 0.039 mmol) in deuterated benzene and started heating at 60 ^{o}C. No shifting of Si-H resonance was observed when monitored by ^{1}H NMR hinting that Si-H bond is not polarized by the given Lewis acid.

Control experiment: Reaction of $[PhNMe_2H][B(C_6F_5)_4]$ with Ph_2SiH_2

In a J-Young tube was mixed $[PhNMe_2H][B(C_6F_5)_4]$ (56.5 mg, 0.041 mmol) along with diphenyl silane (20.1 mg, 0.041 mmol) in deuterated benzene and started heating at 60 ^{o}C. No shifting of Si-H resonance was observed when monitored by ^{1}H NMR hinting that Si-H bond is not polarized by the given Bronsted acid.

Control experiment: Reaction of $[PhNMe_2H][B(C_6F_5)_4]$ with 1

In a J-Young tube was mixed $[PhNMe_2H][B(C_6F_5)_4]$ (56.5 mg, 0.041 mmol) along with **1** (12.4 mg, 0.041 mmol) in deuterated benzene and started heating at 60 ^{o}C. The progress of the reaction was monitored by ^{31}P NMR spectroscopy. After 20 minutes it was observed that significant amount of **1** had decayed generating an unknown species corresponding to 52.5 ppm.

Synthesis of 6 without any promoter

In a J-young tube **1** (30 mg, 0.061 mmol) was charged with phenyl silane (6.58 mg, 0.061 mmol) in deuterated benzene and heated at 120 ^{o}C. The progress of the reaction was monitored by ^{1}H and ^{31}P NMR and only 50 % of the formation of **6** was realized after 14 days. The reaction was extremely slow and did not progress any more upon further heating.

Synthesis of 7 without any promoter

In a J-young tube **1** (30 mg, 0.061 mmol) was charged with diphenyl silane (11.3 mg, 0.061 mmol) in deuterated benzene and heated at 120 ^{o}C. The progress of the reaction was monitored by ^{1}H and ^{31}P NMR and only 50 % of the formation of **7** was realized after 14 days. The reaction was extremely slow and did not progress any more upon further heating.

Exchange reactions:

a) In a J-young tube **6** was loaded (20 mg, 0.034 mmol) with hexane along with diphenyl silane (6.26 mg, 0.034 mmol) and the exchange reaction was monitored by ^{31}P NMR spectroscopy. No exchange between the silyl complexes (**6** and **7**) were observed even upon heating the solution at 120 °C for 12 hours.
b) In a J-young tube **7** was loaded (20 mg, 0.030 mmol) with hexane along with phenyl silane (3.21 mg, 0.034 mmol) and the exchange reaction was monitored by ^{31}P NMR spectroscopy. No exchange between the silyl complexes (**6** and **7**) were observed even upon heating the solution at 120 °C for 12 hours

Synthesis of 6 using substoichiometric amount of promoter

In a J-Young tube **1** (30 mg, 0.061 mmol) was loaded in hexane with phenyl silane (6.58 mg, 0.061 mmol) along with 20 mol% ZnI_2 (3.90 mg, 0.012 mmol) and the reaction mixture was heated at 60 °C for 14 hours. Only substoichiometric amount of formation of **6** was realized at the end of the reaction proving the role of ZnI_2 not catalytic.

In a similar set up using identical amount of **1**, diphenyl silane and 20 mol% $[PhNMe_2H][B(C_6F_5)_4]$ it was proved that the role of $[PhNMe_2H][B(C_6F_5)_4]$ was of a promoter, not a catalyst.

Crystallographic Details for 6. 0.5 Et_2O

The sample consisted of orange crystals of the proposed complex. Inert atmosphere techniques were used to place a typical crystal of dimensions 0.21 × 0.13 × 0.11 mm onto the tip of a 0.1 mm diameter glass capillary. Intensity statistics and the lack of systematic absences suggested the space group P-1 and subsequent solution and refinement confirmed this choice. A direct-methods solution was calculated which provided most non-hydrogen atoms from the E-map. Full-matrix least squares / difference Fourier cycles were performed which located the remaining non-hydrogen atoms. The hydrogen atoms were placed in ideal positions and refined as riding atoms with relative isotropic displacement parameters with the exception of two hydrogen atoms connected to silicon, which were found in the difference map and refined for all parameters. The final full matrix least squares refinement converged to R1 = 0.0312 and wR2 = 0.0846 (F2, all data). The remaining electron density is located near the ether molecule, which is disordered over an inversion center and was refined with a set of restraints and constraints.

Crystallographic Details for 7. pentane

A red crystal (approximate dimensions 0.20 x 0.20 x 0.10 mm^3) was placed onto the tip of a 0.1 mm diameter glass capillary and mounted on a Bruker platform diffractometer equipped with an APEX II CCD detector at 130(2) K. The space group C 2/c was determined based on intensity statistics and systematic absences. The structure was solved and refined with SHELXL-97. A direct-methods solution was calculated, which provided most non-hydrogen atoms from the E-map. Full-matrix least squares / difference Fourier cycles were performed, which located the remaining non-hydrogen atoms. All non-hydrogen atoms were refined with anisotropic displacement parameters. The hydrogen atoms were placed in ideal positions and refined as riding atoms with relative isotropic displacement parameters with the exception of the hydrogen atom connected to silicon, which was found in the difference map and refined for all parameters. The final full matrix least squares refinement converged to R1 = 0.0351 and wR2 = 0.1021 (F^2, all data). The remaining electron density was located near the disordered solvent.

Table 1. Summary of Crystallographic Data and Structure Refinement Details for Complexes **6**•0.5 Et_2O and **7**•C_5H_{12}.

Complex	**6**	**7**
empirical formula	$C_{32}H_{47}NNiP_2Si$•$0.5Et_2O$	$C_{38}H_{51}NNiP_2Si$•C_5H_{12}
Fw	631.51	706.63
crystal system	Triclinic	Monoclinic
space group	*P*-1	*C*2/c
a (Å)	10.0074(7)	24.9191(13)
b (Å)	10.0249(7)	10.3235(5)
c (Å)	17.2061(12)	31.4006(16)
α (°)	84.918(1)	90.00
β (°)	77.723(1)	110.577(3)
γ (°)	83.292(1)	90.00
V ($Å^3$)	1671.5(2)	7562.5(7)
Z	2	8
D_{calc} ($g•cm^{-3}$)	1.255	1.241
crystal size (mm)	0.21 × 0.13 × 0.11	0.20 x 0.20 x 0.10
crystallization solvent,	Et_2O,	pentane,

crystal color	Orange	reddish orange
(h, k, l)	$-12 \leq h \leq 12$, $-13 \leq k \leq 13$, $-22 \leq l \leq 21$	$-31 \leq h \leq 31$, $-12 \leq k \leq 12$, $-39 \leq s \leq 39$
F(000)	678	3032
θ range	2.05 to 27.53°	2.16 to 26.42°
linear abs. coeff. (mm^{-1})	0.737	0.658
total reflections collected	24624	50579
independent reflections	7674	7751
unique reflections	6947	5952
R_{int}	0.0251	0.0811
data/parameter	7674 / 387	7751 / 403
R_1, wR_2 (for $I > 2\sigma(I)$)	0.0312, 0.0846	0.0351, 0.0964
GoF	1.050	0.860
peak/hole (e/Å^{-3})	0.698/ −0.729	0.555/ −0.525

Goodness-of-fit = $[\Sigma[w(F_o^2 - F_c^2)^2]/N_{\text{observns}} - N_{\text{params}})]^{1/2}$, all data. R1 = $\Sigma(|F_o| - |F_c|) / \Sigma |F_o|$. wR2 = $[\Sigma[w(F_o^2 - F_c^2)^2] / \Sigma [w(F_o^2)^2]]^{1/2}$.

Computational details

All calculations have been carried out using Density Functional Theory as implemented in the Jaguar 5.5 suite of ab initio quantum chemistry programs. Geometry optimizations have been performed with the B3LYP functional and 6-31G** basis set. Transition metal Ni has been represented using the Los Alamos LACVP** basis that includes relativistic effective core potentials. A modified version of the LACVP**, designated as LACV3P** has been used where the exponents are documented to match the effective core potential with the triple-ξ. The structures of the computational model were derived from their crystal structures without any modification. A full model has been used to obtain Mayer's bond order from NBO 5.0 implemented in Jaguar 5.5 suite. Orbital composition was computed with BP86 functional using the Amsterdam density functional (ADF 2006) package using a triple-ζ basis set with double polarization function (TZ2P or BSIV in ADF).

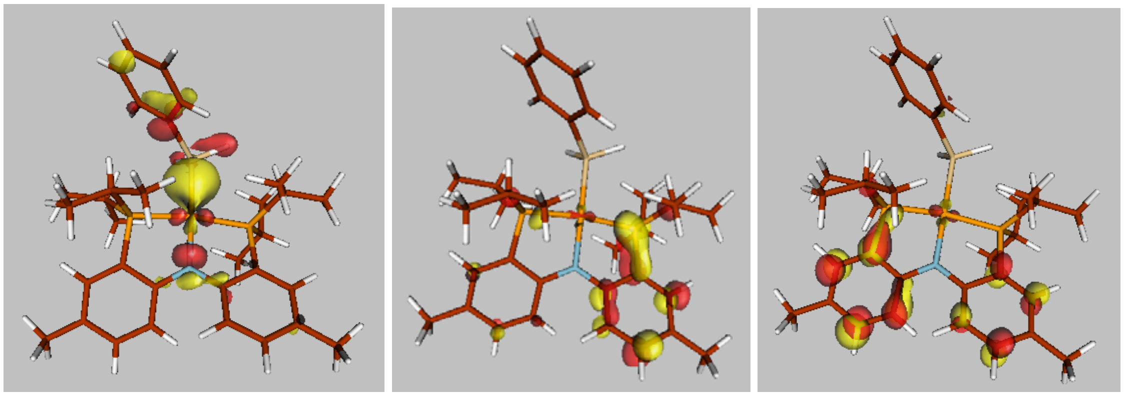

Figure S1. HOMO-2 (left), LUMO+1(middle), LUMO+2 (right) orbitals of **6**. The orbitals have been drawn with isodensity = 0.05 au.

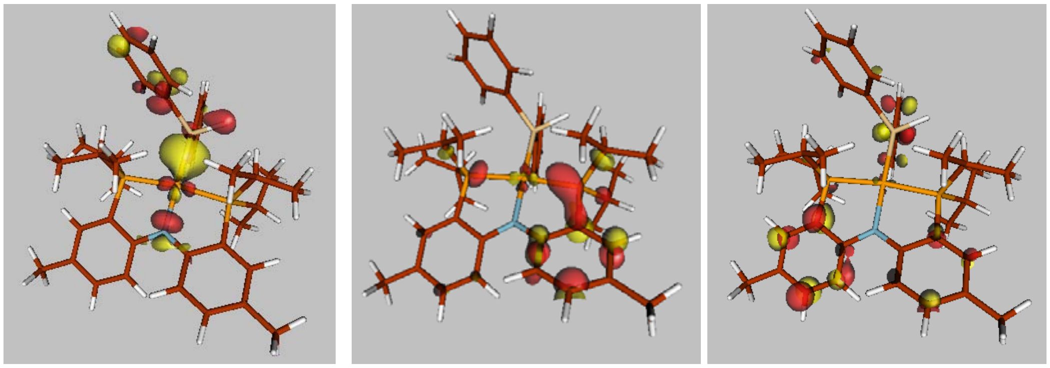

Figure S2. Important orbitals for compound **7.** From left to right HOMO-2, LUMO+1, LUMO+2. The orbitals have been drawn with isodensity = 0.05 au.

Bond order for Ni−Si bond in **6** is 0.91.

Bond order for Ni−Si bond in **7** is 0.91.

Composition of few important orbitals (from ADF calculation)

For **6**:

HOMO-1: 95.2% Ni

HOMO: 16.5% Ni + 26.8% N + 43.2% C

LUMO: 18.1% Ni + 10.2% Si + 17.2% P + 28.4% C

For **7**:

HOMO-1: 99.6% Ni

HOMO: 19.6% Ni + 25.5% N + 42.0% C

LUMO: 22.1% Ni + 17.8% Si + 16.3% P + 17.6% C + 1.7% N

2.7 References

(1) Miyaura, N.; Suzuki, A. *Chem. Rev.* **1995**, *95*, 2457.
(2) Wolfe, J. P.; Wagaw, S.; Marcoux, J.-F.; Buchwald, S. L. *Acc. Chem. Res.* **1998**, *31*, 805.
(3) Ley, S. V.; Thomas, A. W. *Angew. Chem., Int. Ed.* **2003**, *42*, 5400.
(4) Chan, D. M. T.; Monaco, K. L.; Li, R.; Bonne, D.; Clark, C. G.; Lam, P. Y. S. *Tetrahedron Lett.* **2003**, *44*, 3863.
(5) Burgess, K.; Ohlmeyer, M. J. *Chem. Rev.* **1991**, *91*, 1179.
(6) Fu, G. C. *Transition Met. Org. Synth.* **1998**, *2*, 141.
(7) Marder, T. B.; Norman, N. C. *Top. Catal.* **1998**, *5*, 63.
(8) Arndtsen, B. A. B., R. G.; Mobley, T. A.; Peterson, T. H. *Acc. Chem. Res.* **1995**, *28*, 154.
(9) Shilov, A. E.; Shul'pin, G. B. *Chem. Rev.* **1997**, *97*, 2879.
(10) Stahl, S.; Labinger, J. A.; Bercaw, J. E. *Angew. Chem., Int. Ed.* **1998**, *37*, 2181.
(11) Waltz, K. M.; He, X.; Muhoro, C.; Hartwig, J. F. *J. Am. Chem. Soc.* **1995**, *117*, 11357.

(12) Waltz, K. M.; Muhoro, C. N.; Hartwig, J. F. *Organometallics* **1999**, *18*, 3383.

(13) Iverson, C. N.; Smith, M. R., III *J. Am. Chem. Soc.* **1999**, *121*, 7696.

(14) Chen, H.; Hartwig, J. F. *Angew. Chem., Int. Ed.* **1999**, *38*, 3391.

(15) Shimada, S.; Batsanov, A. S.; Howard, J. A. K.; Marder, T. B. *Angew. Chem., Int. Ed.* **2001**, *40*, 2168.

(16) Smith, M. R., III *Prog. Inorg. Chem.* **1999**, *48*, 505.

(17) Rosen, B. M.; Huang, C.; Percec, V. *Org. Lett.* **2008**, *10*, 2597.

(18) Wilson, D. A.; Wilson, C. J.; Rosen, B. M.; Percec, V. *Org. Lett.* **2008**, *10*, 4879.

(19) Lillo, V.; Fructos, M. R.; Ramirez, J.; Braga, A. A. C.; Maseras, F.; Mar Diaz-Requejo, M.; Perez, P. J.; Fernandez, E. *Chem.-Eur. J.* **2007**, *13*, 2614.

(20) Fan, L.; Foxman, B. M.; Ozerov, O. V. *Organometallics* **2004**, *23*, 326.

(21) Adhikari, D.; Huffman, J. C.; Mindiola, D. J. *Chem. Commun.* **2007**, 4489.

(22) Burgess, K.; Van der Donk, W. A.; Westcott, S. A.; Marder, T. B.; Baker, R. T.; Calabrese, J. C. *J. Am. Chem. Soc.* **1992**, *114*, 9350.

(23) Cundy, C. S.; Noeth, H. *J. Organomet. Chem.* **1971**, *30*, 135.

(24) Dai, C.; Stringer, G.; Corrigan, J. F.; Taylor, N. J.; Marder, T. B.; Norman, N. C. *J. Organomet. Chem.* **1996**, *513*, 273.

(25) Aldridge, S.; Calder, R. J.; Rossin, A.; Dickinson, A. A.; Willock, D. J.; Jones, C.; Evans, D. J.; Steed, J. W.; Light, M. E.; Coles, S. J.; Hursthouse, M. B. *Dalton Trans.* **2002**, 2020.

(26) Irvine, G. J.; Lesley, M. J. G.; Marder, T. B.; Norman, N. C.; Rice, C. R.; Robins, E. G.; Roper, W. R.; Whittell, G. R.; Wright, L. J. *Chem. Rev.* **1998**, *98*, 2685.

(27) Noeth, H. W., B. *Nuclear Magnetic Resonance Spectroscopy of Boron Compouds*; Springer-Verlag: New York, 1978.

(28) He, X.; Hartwig, J. F. *Organometallics* **1996**, *15*, 400.

(29) Westcott, S. A.; Blom, H. P.; Marder, T. B.; Baker, R. T.; Calabrese, J. C. *Inorg. Chem.* **1993**, *32*, 2175.

(30) Adhikari, D.; Mossin, S.; Basuli, F.; Dible, B. R.; Chipara, M.; Fan, H.; Huffman, J. C.; Meyer, K.; Mindiola, D. J. *Inorg. Chem.* **2008**, *47*, 10479.

(31) Laitar, D. S.; Mueller, P.; Sadighi, J. P. *J. Am. Chem. Soc.* **2005**, *127*, 17196.

(32) Zhao, H.; Dang, L.; Marder, T. B.; Lin, Z. *J. Am. Chem. Soc.* **2008**, *130*, 5586.

(33) Dang, L.; Zhao, H.; Lin, Z.; Marder, T. B. *Organometallics* **2007**, *26*, 2824.

(34) Ito, H.; Kawakami, C.; Sawamura, M. *J. Am. Chem. Soc.* **2005**, *127*, 16034.

(35) Tran, B. L.; Adhikari, D.; Fan, H.; Pink, M.; Mindiola, D. J. *manuscript in preparation.*

(36) Dickinson, A. A.; Willock, D. J.; Calder, R. J.; Aldridge, S. *Organometallics* **2002**, *21*, 1146.

(37) Braunschweig, H. *Angew. Chem., Int. Ed.* **1998**, *37*, 1786.

(38) Hartwig, J. F.; Muhoro, C. N.; He, X.; Eisenstein, O.; Bosque, R.; Maseres, F. *J. Am. Chem. Soc.* **1996**, *118*, 10936.
(39) Motry, D. H.; M. R. Smith, I. *J. Am. Chem. Soc.* **1995**, *117*, 6615.
(40) Hartwig, J. F.; DeGale, S. R. *J. Am. Chem. Soc.* **1994**, *116*, 3661.
(41) Lam, K. C.; Lam, W. H.; Lin, Z.; Marder, T. B.; Norman, N. C. *Inorg. Chem.* **2004**, *43*, 2541.
(42) Zhu, J.; Lin, Z.; Marder, T. B. *Inorg. Chem.* **2005**, *44*, 9384.
(43) Percec, V.; Bae, J.-Y.; Hill, D. H. *J. Org. Chem.* **1995**, *60*, 1060.
(44) Saito, S.; Oh-tani, S.; Miyaura, N. *J. Org. Chem.* **1997**, *62*, 8024.
(45) Soloway, A. H.; Tjarks, W.; Barnum, B. A.; Rong, F.-G.; Barth, R. F.; Codogni, I. M.; Wilson, J. G. *Chem. Rev.* **1998**, *98*, 2389.
(46) Wulff, G.; Heide, B.; Helfmeier, G. *J. Am. Chem. Soc.* **1986**, *108*, 1089.
(47) James, T. D.; Linnane, P.; Shinkai, S. *Chem. Commun.* **1996**, 281.
(48) Reetz, M. T.; Niemeyer, C. M.; Hermes, M.; Goddard, R. *Angew. Chem., Int. Ed.* **1992**, *31*, 1017.
(49) Ishiyama, T.; Murata, M.; Miyaura, N. *J. Org. Chem.* **1995**, *60*, 7508.
(50) Ishiyama, T.; Itoh, Y.; Kitano, T.; Miyaura, N. *Tetrahedron Lett.* **1997**, *38*, 3447.
(51) Ahiko, T.-a.; Ishiyama, T.; Miyaura, N. *Chem. Lett.* **1997**, 811.
(52) Adams, C. J.; Baber, R. A.; Batsanov, A. S.; Bramham, G.; Charmant, J. P. H.; Haddow, M. F.; Howard, J. A. K.; Lam, W. H.; Lin, Z.; Marder, T. B.; Norman, N. C.; Orpen, A. G. *Dalton Trans.* **2006**, 1370.
(53) Ozerov, O. V.; Guo, C.; Fan, L.; Foxman, B. M. *Organometallics* **2004**, *23*, 5573.
(54) Maennig, D.; Noeth, H. *Dalton Trans.* **1985**, 1689.
(55) Murata, M.; Oyama, T.; Watanabe, S.; Masuda, Y. *J. Org. Chem.* **2000**, *65*, 164.
(56) Patai, S.; Rappoport, Z. *The Chemistry of Organic Silicon Compounds* Chichester, 1989; Vol. Wiley.
(57) *Advances in Chemistry Series* Ziegler, J. M.; Fearon, F. W. G., Eds.; American Chemical Society: Washington DC, 1990; Vol. 224.
(58) Auner, N.; Weis, J. *Organosilicon Chemistry*; VCH: Weinhein, 1994.
(59) Speier, J. l. *Adv. Organomet. Chem.* **1979**, 407.
(60) Ojima, I. In *The Chemistry of Organic Silicon Compounds* Patai, S., Rappoport, Z., Eds.; Wiley: Chichester, 1989, p 1479.
(61) Chalk, A. J.; Harrod, J. H. *J. Am. Chem. Soc.* **1965**, *87*, 16.
(62) Harrod, J. F.; Chalk, A. J. In *Organic Synthesis via Metal Carbonyls*; Wender, I., Pino, P., Eds.; Wiley: New York, 1977, p 673.
(63) Yamashista, H.; Tanaka, M. *Bull. Chem. Soc. Jpn.* **1995**, *68*, 403.
(64) Forsyth, C. M.; Nolan, S. P.; Marks, T. J. *Organometallics* **1991**, *10*, 2543.
(65) Marciniec, B. *Comprehensive Handbook of Hydrosilylation*; Pergamon Press: Oxford, NY, 1992.
(66) Brook, M. A. *Silicon in Organic, Organometallic, and Polymer Chemistry*; Wiley: New York, 2000.

(67) Tamao, K. In *Advances in Silicon Chemistry*; Larson, G. L., Ed.; JAI Press: London, 1996; Vol. 3, p 1.

(68) Hiyama, T. In *Metal Catalyzed Cross-coupling Reactions*; Diederich, F., stang, P. J., Eds.; Wiley: New York, 1998, p 421.

(69) Denmark, S. E.; Choi, J. Y. *J. Am. Chem. Soc.* **1999**, *121*, 5821.

(70) Denmark, S. E.; Tymonko, S. A. *J. Am. Chem. Soc.* **2005**, *127*, 8004.

(71) Lee, J.-Y.; Fu, G. C. *J. Am. Chem. Soc.* **2003**, *125*, 5616.

(72) Murata, M.; Shimazaki, R.; Watanabe, S.; Masuda, Y. *Synthesis* **2001**, 2231.

(73) Sharma, H. K.; Pannell, K. H. *Chem. Rev.* **1995**, *95*, 1351.

(74) Reichl, J. A.; Berry, D. H. *Adv. Organomet. Chem.* **1998**, *43*, 197.

(75) Schneider, N.; Finger, M.; Haferkemper, C.; Bellemin-Laponnaz, S.; Hofmann, P.; Gade, L. H. *Angew. Chem., Int. Ed.* **2009**, *48*, 1609.

(76) Herath, A.; Montgomery, J. *J. Am. Chem. Soc.* **2008**, *130*, 8132.

(77) Baxter, R. D.; Montgomery, J. *J. Am. Chem. Soc.* **2008**, *130*, 9662.

(78) Bierschenk, T. R.; Guerra, M. A.; Juhlke, T. J.; Larson, S. B.; Lagow, R. J. *J. Am. Chem. Soc.* **1987**, *109*, 4855.

(79) Shimada, S.; Rao, M. L. N.; Hayashi, T.; Tanaka, M. *Angew. Chem., Int. Ed.* **2001**, *40*, 213.

(80) Shimada, S.; Rao, M. L. N.; Tanaka, M. *Organometallics* **1999**, *18*, 291.

(81) Avent, A. G.; Gehrhus, B.; Hitchcock, P. B.; Lappert, M. F.; Maciejewski, H. *J. Organomet. Chem.* **2003**, *686*, 321.

(82) Iluc, V. M.; Hillhouse, G. L. *Tetrahedron* **2006**, *62*, 7577.

(83) Nlate, S.; Herdtweek, E.; Fischer, R. A. *Angew. Chem., Int. Ed.* **1996**, *35*, 1861.

(84) Maciejewski, H.; Marciniec, B.; Kownacki, I. *J. Organomet. Chem.* **2000**, *597*, 175.

(85) Gehrhus, B.; Hitchcock, P. B.; Lappert, M. F.; Maciejewski, H. *Organometallics* **1998**, *17*.

(86) Kang, Y.; Lee, J.; Kong, Y. K.; Kang, S. O.; Ko, J. *Chem. Commun.* **1998**, *1998*, 2343.

(87) Schmedake, T. A.; Haaf, M.; Paradise, B. J.; Powell, D.; West, R. *Organometallics* **2000**, *19*, 3263.

(88) Roddick, D. M.; Heyn, R. H.; Tilley, T. D. *Organometallics* **1989**, *8*, 324.

(89) Powell, S. A.; Tenenbaum, J. M.; Woerpel, K. A. *J. Am. Chem. Soc.* **2002**, *124*, 12648.

(90) Arnold, J.; Roddick, D. M.; Tilley, T. D.; Geib, S. J. *Inorg. Chem.* **1988**, *27*, 3510.

(91) Liang, L.; Chien, P.; Huang, Y. *J. Am. Chem. Soc.* **2006**, *128*, 15562.

(92) Shinohara, A.; McBee, J.; Waterman, R. *Organometallics* **2008**, *27*, 5717.

(93) Calimano, E.; Tilley, T. D. *J. Am. Chem. Soc. 130*, 9226.

(94) Gatard, S.; Chen, S.-H.; Foxman, B. M.; Ozerov, O. V. *Organometallics* **2009**, *27*, 6257.

(95) Mitchell, G. P.; Tilley, T. D. *J. Am. Chem. Soc.* **1998**, *120*, 7635.

(96) Mitchell, G.; tilley, T. D. *Angew. Chem., Int. Ed.* **1998**, *37*, 2524.

(97) Glaser, P. B.; Wanandi, P. W.; Tilley, T. D. *Organometallics* **2004**, *23*.

(98) Feldman, J. D.; Peters, J. C.; Tilley, T. D. *Organometallics* **2002**, *21*, 4065.
(99) Peters, J. C.; Feldman, J. D.; Tilley, T. D. *J. Am. Chem. Soc.* **1999**, *121*, 9871.
(100) Chen, W.; Shimada, S.; Tanaka, M.; Kobayashi, Y.; Saigo, K. *J. Am. Chem. Soc.* **2004**, *126*, 8072.
(101) Hermann, W. A.; Eppinger, J.; Spiegler, M.; Runte, O.; Anwander, R. *Organometallics* **1997**, *16*, 1813.
(102) Ohff, A.; Kosse, P.; Baumann, W.; Tillack, A.; Kempe, R.; Gorls, H.; Burlakov, B. B.; Rosenthal, U. *J. Am. Chem. Soc.* **1995**, *117*, 10399.
(103) Schubert, U.; Schwarz, M.; Moller, F. *Organometallics* **1994**, *13*, 1554.
(104) Corey, J. Y.; Braddock-Wilking, J. *Chem. Rev.* **1999**, *99*, 175.
(105) Levy, C. J.; Puddephatt, R. J.; Vittal, J. J. *Organometallics* **1994**, *13*, 1559.
(106) Alcaraz, G.; Sabo-Etienne, S. *Coord. Chem. Rev.* **2008**, *252*, 2395.
(107) Reed, A. E.; Curtiss, L. A.; Weinhold, F. *Chem. Rev.* **1988**, *88*, 899.
(108) Adhikari, D.; Mossin, S.; Basuli, F.; Huffman, J. C.; Szilagyi, R. K.; Meyer, K.; Mindiola, D. J. *J. Am. Chem. Soc.* **2008**, *130*, 3676.
(109) Velde, G. T.; Bickelhaupt, F. M.; Baerends, E. J.; Guerra, C. F.; VanGisbergen, S. J. A.; Snijders, J. G.; Ziegler, T. *J. Comput. Chem.* **2001**, *22*, 931.
(110) Parks, D. J.; Piers, W. E. *J. Am. Chem. Soc.* **1996**, *118*, 9440.
(111) Blackwell, J. M.; Foster, K. L.; Beck, V. H. *J. Org. Chem.* **1999**, *64*, 4887.
(112) Walstrom, A.; Pink, M.; Tsvetkov, N. P.; Fan, H.; Ingleson, M.; Caulton, K. G. *J. Am. Chem. Soc.* **2005**, *127*, 16780.
(113) Burger, B. J.; Barcaw, J. E. In *Experimental Organometallic Chemistry*; Wayda, A. L., Darensbourg, M. Y., Eds.; American Chemical Society: Washinton DC, 1987; Vol. ACS Symposium Series 357, p 79.
(114) Waltz, K. M.; He, X.; Muhoro, C.; Hartwig, J. F. *J. Am. Chem. Soc.* **1995**, *117*, 11357.

Chapter 3

Metal Ligand Covalency: A Tale of Ligand-Based Redox Reactions

3.1 Introduction

3.1.1 Introduction of redox non-innocent ligands

Covalency in the metal-ligand bond has a tremendous impact in the field of electron transfer pathways, reduction potentials and electron delocalization in mixed-valent systems.[1] Moreover, reactivities of transition metal systems are highly dependent on the extent of covalency of a metal-ligand bond. From a material science perspective, the covalency of the metal-ligand bond leads to exchange coupling pathways which often are responsible for the unique magnetic properties of materials. Extreme metal ligand covalency may result in dispersion of the HOMO and LUMO into bands leading to conductivity. Metal-ligand covalency is attractive to organometallic chemists since fundamental understanding of such a covalent system helps in the designing of more efficient catalysts. Due to the different extent of covalency in a metal-ligand bond, assigning the correct oxidation state of the metal is sometimes ambiguous, therefore rendering such an assignment “formal in nature”. In those cases where this dichotomy prevails, the ligand system in question has been referred to as “non-innocent ligands”.[2, 3] These ligand systems are redox active and can stabilize a different effective metal oxidation state than the formal by delocalization of the metal d-electrons or electron holes. Non-innocent ligands are widely used to emphasize the fact that some ligands do not possess a closed shell structure, hence causing a discrepancy between formal and spectroscopic oxidation states.[4, 5]

Recently, complexes bearing organic radicals in interaction with transition metal ions have drawn substantial focus. The interest in such systems derives from the fact that such moieties are ubiquitous in the active sites of metalloproteins. A very well understood example of such a system is the enzyme galactose oxidase, where a tyrosinyl radical, tyrO$^{\bullet}$ radical is coordinated to a Cu$^{(II)}$ center.[6] This enzyme converts primary alcohols into aldehydes chemoselectively, and at a fascinating rate (turnover frequency is 1×10^6 per hour). The key step for the whole process of oxidizing primary alcohols is the abstraction of aliphatic proton adjacent to the alcohol group by the oxygen atom of the tyrosinyl radical, which is a clear example of electronic structure dictating the reactivity. Other examples of such electronic structure contributions to their reactivity are profusely observed in biochemistry. However, few of them may be difficult to detect, for example, in the cases where there are two strongly coupled radical ligands through a metal ion. From this perspective, a detailed understanding of the nature of a transition metal interaction with the ligand, especially if a radical is involved, represents an important paradigm to both chemistry and biochemistry.

Among the several organic type radicals, aminyl radical $NR_2^{\cdot}$, or amine radical cations $NR_3^{\cdot+}$, play an important role in many chemical and biological processes.[7, 8] In usual cases, these radicals are highly reactive, short-lived intermediates, formed thermally or photochemically by homolytic bond cleavage or by N oxidation. However, the electron deficiency at the nitrogen atom can be mitigated by electron donating R-groups such as O, S, phenyl, through resonance (Scheme 1).

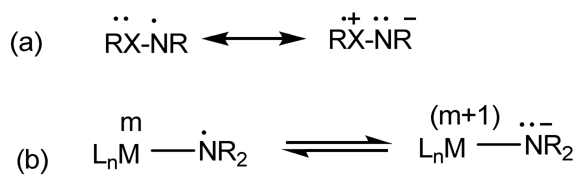

Scheme 1: Resonance forms of stabilized aminyl radicals (a) A heteroatom donor X can stabilize the electron deficient aminyl radical (b) When the aminyl radical is metal coordinated, the metal can donate electron to essentially convert the aminyl to amide.

From this viewpoint, transition metal-coordinated aminyl radicals exhibit a very close resemblance to the metal phenoxyl radical complexes [$ML_n(^{\cdot}OR)$].[3, 9] In few cases, to stabilize an aminyl radical that is short lived and reactive, once must rely on steric protection.[10-12] In general, the unpaired electron of an aminyl radical may be more discretely localized either at N or at the metal, conferring the aminyl and the amide as two distinct electronic states. Alternatively, a resonance could give rise to a more stabilized radical, and an example of such canonical structures is presented in Scheme 1 (1a is heteroatom stabilized and 1b is metal stabilized). Such a bonding scheme should be thought of as limiting resonance structures, with the real structure being a weighted average of the two. Additionally, the possibility of equilibrium between both states (redox isomerism) could also be envisaged.[13] When a radical coordinates to a metal center, the unambiguous assignment of the metal oxidation state poses a problem. In fact, several earlier proposals from different groups have been proved incorrect afterwards through detailed spectroscopic and theoretical investigations.[14, 15] The first controversy concerning the correct assignment of the metal oxidation state was invoked by Holm and Gray.[16, 17] In the reported work of Holm and co-workers, the claim of $Ni^{(III)}$

oxidation state bearing a bis(maleonitriledithiolate) ligand was refuted by Gray. According to Gray and coworkers, the correct oxidation state of the metal to be assigned is $Ni^{(II)}$: a claim clearly substantiated by detailed EPR experiments. In addition to the oxidation prone bis(maleonitriledithiolate), certain amine thiolates and diamines[18-20] display significant amount of ligand-based redox behavior. The close resemblance of transition metal bound dithiolene complexes to the Mo-pterin-dithiolene cofactor in mononuclear oxotransferases[21] prompted Holm *et al.* to systematically investigate the bonding between the metal and the dithiolene ligand in a complete series of non-benzenoid bis(dithiolene) complexes over three oxidation states, $[Ni(S_2C_2Me_2)]^Z$, $Z = -2, -1, 0$.[22] A wide variety of late transition metal chemistry supported by a non-innocent *o*-aminothiophenolates, bis(benzene-1,2,-dithiolates) have also been explored by Wieghardt and co-workers.[23-26] To date, pincer ligands invoking the prototypical PXP (X = C and N) coordination sphere have not been thoroughly investigated in terms of their role as non-innocent ligands. This is surprising given the fact that such ligands are becoming more prominent in the fields of polymerization,[27] cross-coupling,[28, 29] catalysis[30] and group functionalization[31-33]. We present in this chapter compelling evidence of a PNP ($PNP^{-} = [N(2\text{-}P(CHMe_2)_2\text{-}4\text{-}MeC_6H_3)_2$ pincer's redox activity through the combination of spectroscopic experiments and theoretical analyses. During our course of investigations, the redox activity of the ligand engenders a rare example of stabilized aminyl radical when such a ligand is coordinated to $Ni^{(II)}$.

3.1.2 A Prelude to XAS Spectroscopy

Among the traditional methods to experimentally quantify the covalency in the metal-ligand bond, EPR is very popular. However, g-values obtained from EPR experiments do not provide directly the experimental covalency since g-values are effected by mixing of excited states into the ground state, spin orbit coupling, and metal ligand covalency. A more direct ground state probe of covalency, is to supplement g-values with ligand super-hyperfine coupling constants measured by double resonance, ENDOR; and pulsed EPR, ESEEM.[34] For bound excited states, charge transfer transition energies and intensities approximately estimate covalency and delocalization over the ligands by invoking valence bond configuration interaction (VBCI).[35] Given the limitations of the conventional experimental methods, X-ray absorption spectroscopy (XAS), at the ligand K-edge, emerged as a very promising tool.[36] Solomon and co-workers have used the ligand K-edge XAS extensively for the characterization of several metalloproteins,[37-48] determining metal ligand covalency,[49-53] studying Ti-O bond homolysis[54] and probing for the origin of EPR hyperfine splitting.[55] An alternative approach to metal-ligand covalency is to use the multi-edge approach.[56] The X-ray absorption near-edge structure (XANES), which encompasses transitions of core electrons to bound states, is sensitive to the local geometric and electronic environment of the absorbing atom.[57] The edge energy of a transition corresponds to the energy necessary to promote a core electron to the continuum. This is why the edge energies are very element specific, therefore making assignment of a transition more precise or unambiguous. The electric dipole allowed transition for any K-edge spectrum is $1s \rightarrow np$. Due to the intense nature of the transition, mixing of np character into the final state of a forbidden or parity disallowed transition results in gain intensity for that excitation. Sometimes a feature appears at a lower energy than the rising edge which is assigned as a metal based 1s → *n*d transition. These transitions are relatively weak (quadrupole allowed)[58] and gain intensity from symmetry-allowed mixing of metal (*n+1*)p character. Theoretically, quadrupole allowed transitions are two orders of magnitude less intense than the dipole allowed transitions.[59, 60] As a consequence of mixing, formally forbidden electric dipole transitions gain electric dipole intensity from (*n+1*)p mixing into the half-occupied *n*d orbital. Therefore, these spectra serve as a probe of (*n+1*)p mixing into the ground-state orbital. Metal L-edges are at much lower energy, and for *n*d transition metal complexes they fall in 400−1000 eV region. For this same reason, they have an advantage from the resolution perspective (~0.3 eV versus> 1.2 eV for metal K-edges).[61] Since L-edge XAS involves 2p → *n*d excitations, the transitions are dipole allowed and usually very intense. In contrast, 2p → (*n+1*)s transitions are not dipole allowed and only observed if (*n+1*)s orbitals mix with *n*d orbitals. Intensity of a dipole allowed 2p → *n*d transition directly corresponds to the amount of metal d character in a valence molecular orbital.[62] Although this intensity reflects the net effect of the entire ligand environment, it does not probe specific ligand-metal bonds.

Ligand K-edge involves the ligand 1s → *n*p transition. The s → p transitions are electric dipole allowed and thus the intensity of spectral features can be quantitatively analyzed to obtain the experimental ligand *n*p character in the valence molecular orbital. This technique investigates all singly-occupied and unoccupied acceptor orbitals of the transition metal complexes that have a ligand *n*p contribution, and provides a direct probe of the covalency of the ligand-metal bond. Also in ligand K-edge, a pre-edge feature might appear slightly lower in energy than the rising edge, when a 1s → *n*d transition is possible, i.e. a vacant d-orbital is accessible. For example, the compound Cs_2ZnCl_4 does not show any pre-edge feature due to the d^{10} electronic configuration of the $Zn^{(II)}$. In contrast Cs_2CuCl_4 displays a resolved and intense pre-edge feature owing to d^9 electronic configuration with a hole in the d manifold (in the $d_{x^2-y^2}$ orbital for a tetragonal field).[36] Due to the localized nature of the Cl 1s orbital, absorption intensity can only be gained if the Cu $3d_{x^2-y^2}$ orbital contains some Cl 3p orbital character. Scheme 2 depicts how Cu $3d_{x^2-y^2}$ orbital forms covalent bonds with the Cl 3p orbitals, giving rise to a half-occupied antibonding frontier orbital with more prevalent copper d character.

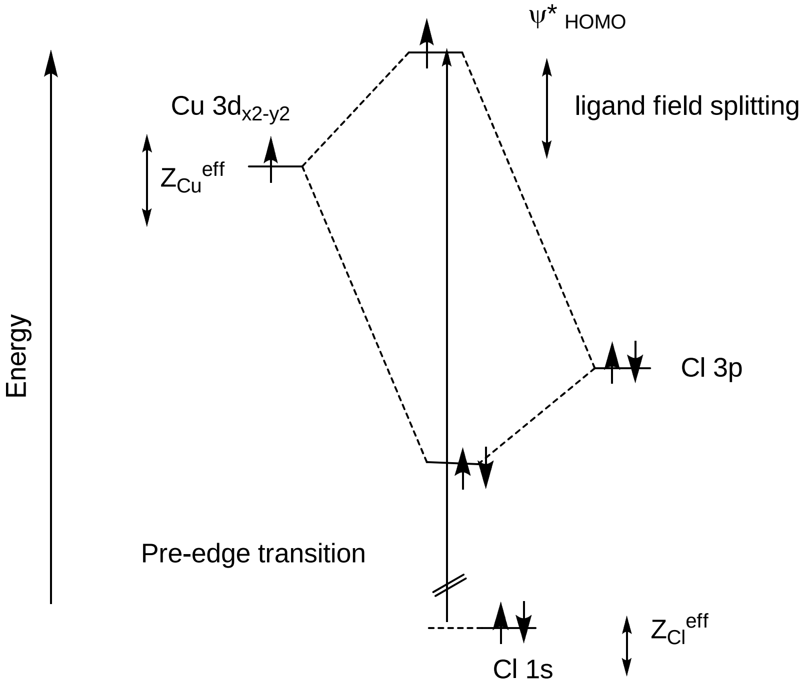

Scheme 2: Schematic orbital energy diagram to characterize ligand pre-edge transition.

The pre-edge transition is ideally recognized as the Cl 1s → ψ* transition gaining intensity from the degree of Cl 3p character in the ψ* wave function. Final state relaxation of ligand orbitals could give rise to differences in the metal-ligand bonding compared to the ground state, which would complicate the analysis of ligand pre-edges. This phenomenon of final state relaxation is frequently observed in metal K- and L-edge XAS, and X-ray photoelectron spectroscopy (XPS) where a metal core hole is created with long lifetime that allows for reorganization of the valence orbitals.[63, 64] The relaxation can lead to shake-up or shake-down transitions which are formally forbidden two-electron transitions.[65]

3.2 Results and Discussion

3.2.2 Single Electron Oxidation of (PNP)NiCl (1)

The synthesis and identity of the complex, (PNP)NiCl (**1**), has been already described in Chapter 1. We were interested to percept whether the ligand scaffold can stabilize multiple oxidation state of nickel (+I to +III). In order to achieve a better understanding about the oxidation potential of **1**, cyclic voltammetry experiment was performed. From the cyclic voltammogram of **1** we found an oxidation potential of the $\mathrm{Ni^{(II)}}$ complex as −0.06 V with respect to the $\mathrm{Fc/Fc^+}$ couple at 0.00 V (shown in Chapter 1). Chemical oxidation of **1** was carried out in THF with Fc[OTf][66] (Scheme 3). During the course of oxidation a rapid color change evinces from green to blue. The byproduct ferrocene is removed by washing the resulting mixture several times with copious amounts of pentane to obtain a paramagnetic product $\mathrm{[(PNP)NiCl]^{\bullet+}[OTf]^{-}}$, $[\mathbf{1}]^{\bullet+}$[OTf] in very good yield (87%). X-ray quality single crystals of $[\mathbf{1}]^{\bullet+}$[OTf] were grown at −35 °C in dichloromethane/ hexane layer.

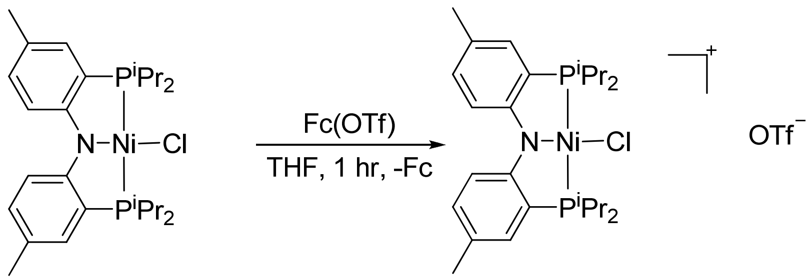

Scheme 3: Synthesis of [**1**]$^{\bullet+}$[OTf] from **1** by single electron oxidation using Fc[OTf].

In order to establish the accurate connectivity and geometry around the Ni-center we collected single crystal X-ray diffraction data (Figure1).

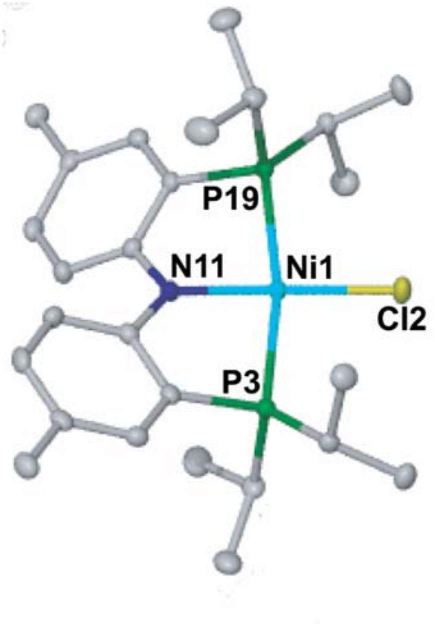

Figure 1: Crystal structures of [**1**]$^{\bullet+}$omitting the non-coordinating anion [OTf$^-$], depicting thermal ellipsoids at the 50% probability level. Hydrogen atoms and methyls of isopropyl groups have been omitted for clarity. Comparison of bond lengths (Å) and angles (degrees) with **1** have been shown in Table 1.

Table 1: Comparison of bond lengths (Å) and bond angles (degree) around the nickel center in **1** and its oxidized form [**1**]$^{\bullet+}$.

Atoms	**1**	**Atoms**	[**1**]$^{\bullet+}$
Ni(1)-Cl(3)	2.1568(8)	Ni(1)-Cl(2)	2.1487(5)
Ni(1)-N(10)	1.8980(15)	Ni(1)-N(11)	1.8547(15)
Ni(1)-P(2)	2.2012(6)	Ni(1)-P(3)	2.2126(6)
Ni(1)-P(18)	2.2025(6)	Ni(1)-P(19)	2.2219(6)
N(10)-Ni(1)-Cl(31)	177.51(6)	N(11)-Ni(1)-Cl(2)	178.01(5)
P(2)-Ni(1)-P(18)	168.88(2)	P(3)-Ni(1)-P(19)	168.42(2)

The molecular structure of the oxidized product reveals a (PNP)NiCl$^{\bullet+}$ cation, [**1**]$^{\bullet+}$ and a non-coordinating OTf^{-} anion in the asymmetric unit. Pierpont and co-workers have exclusively used high quality X-ray structural data to determine specific regions in a non-innocent ligand affected by oxidation. It has been well established that C−O, C−N and C−C distances vary in a systematic fashion in coordinated *o*-catecholate(2^{-}), *o*-benzosemiquinonate(1^{-}), benzoquinone and *o*-diiminobenzoquinone type ligands.[2, 67-69] Similarly, we probed the effect of oxidation in the molecular structure of [**1**]$^{\bullet+}$. Intuitively, if the oxidation takes place solely on the metal center, nickel will be changed to the formal (III) oxidation state and the Ni−N bond distance in [**1**]$^{\bullet+}$ will be significantly shorter when compared to the Ni−N bond distance in **1.** Also we expect change in bond lengths to the whole first coordination sphere of nickel. Surprisingly, we observe little change in Ni−N bond length of 1.8547(15) Å in [**1**]$^{\bullet+}$ when compared to

1.8980(15) Å in **1**. A change of 0.04 Å in bond length can not ensure the change in oxidation state of the metal. On the other hand, if the oxidation takes place mostly on the diarylamine part of the ligand, it is expected that the C−C bond lengths of the aromatic ring will be reflecting this considerable change. Significant elongation of some C−C bonds compared to other C−C bonds in $[Co(L^{ISQ})_2]_2$ (L^{ISQ} = 4,6-di-tert-butyl-2-aminothiosemiquinonate)[70] is a definite clue for a ligand-based oxidation. By DFT calculations on a "$Ni^{(III)}$" complex coordinated with a redox-active ligand, Journaux and co-workers have shown the characteristic quinoid-type short-long-short sequence of C−C bonds within the benzene ring.[71] When our system is scrutinized closely, we observe that all the C−C bond lengths in the aromatic ring are close to 1.39 Å.

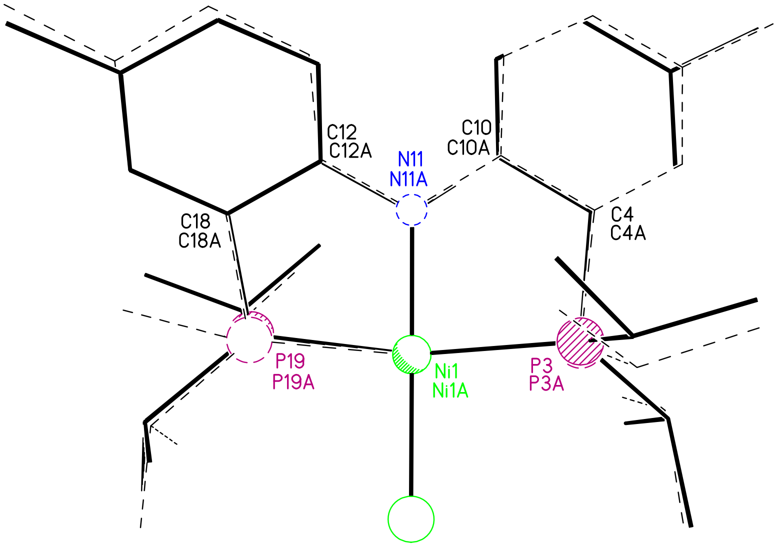

Figure 2: Least squares fit of **1** (solid line) and $[\mathbf{1}]^{\bullet+}$ (dashed line) omitting hydrogen atoms, solvent (in **1**) and anion (in $[\mathbf{1}]^{\bullet+}$[OTf]). The atoms Ni, P, P, N, Cl and bridging phenyl carbons are fitted. Weighted root mean square deviation is 0.0695 Å.

Therefore the absence of any prominent elongation or compression of C−C bonds insinuates the highly delocalized character of the radical, provided the oxidation is ligand based. To establish the change in gross structure of **1** and [**1**]$^{\bullet+}$, both structures are overlapped (Figure 2), which clearly portrays the insignificant change in their geometrical features. The ^{1}H NMR spectrum of [**1**]$^{\bullet+}$ [OTf] reveals several broad peaks consistent with a paramagnetic complex. Solution state magnetic susceptibility of [**1**]$^{\bullet+}$[OTf] in CD_2Cl_2 by Evan's method collected at 25 ^{o}C is in agreement with a system containing a single unpaired electron (μ_{eff} = 2.21(1) μ_B, within the experimental error range. In this context, it is important to mention that the byproduct ferrocene was completely removed from the reaction mixture and amount of that was quantified. Also the slightly higher value in solution state magnetic moment should not arise from paramagnetic impurity present such as ferrocenium triflate since the oxidant was used in 0.99 equivalent.

3.2.3 EPR study of [1]$^{\bullet+}$[OTf]

Since a paramagnetic material was isolated due to the oxidation of **1**, it was important to investigate the nature of the radical present in the complex [**1**]$^{\bullet+}$[OTf]. Accordingly we turned our attention to X-band EPR spectroscopy to understand the characteristics of the radical. If the oxidation is exclusively metal based, it should reveal features of a Ni^{III} (d^7) ion, which would exhibit a g value typically found in the range of 2.15−2.20 due to spin orbit coupling.[72, 73] In contrast, if the oxidation takes place purely on the ligand, it should result in a narrow peak with a g value very close to that for the free electron value, 2.0023. The room temperature solution X-band EPR spectrum of $[\mathbf{1}]^{\bullet+}$ [OTf] in dichloromethane/toluene (Figure 3) revealed an isotropic signal at g_{iso}= 2.0238(3). The g-value is close to the free electron value, suggesting the electron hole to be mainly ligand localized. In addition to this, the spectrum exhibits resolved super-hyperfine patterns originating from interaction of the unpaired spin with the nitrogen, the two phosphorus atoms, and the six aromatic hydrogen atoms composing the pincer ligand. This super-hyperfine features substantiate our claim of a ligand based redox occurring in $[\mathbf{1}]^{\bullet+}$[OTf].

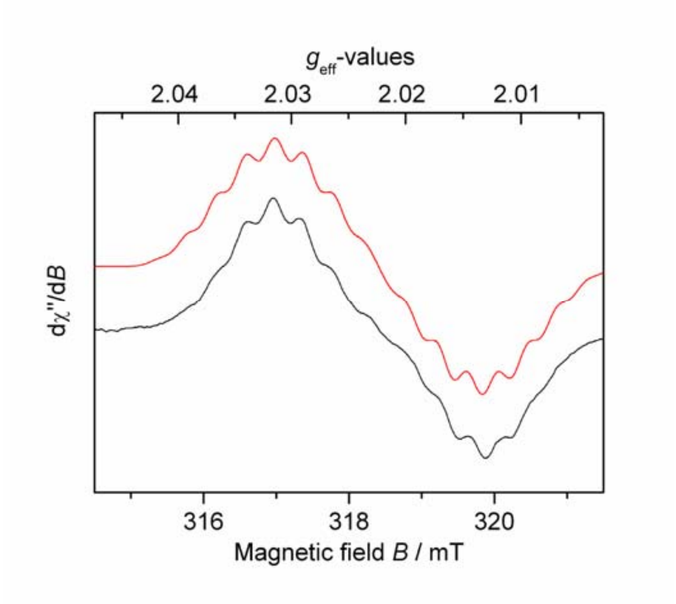

Figure 3: X-band solution EPR spectra of $[\mathbf{1}]^{\bullet+}$[OTf] in dichloromethane/toluene recorded at 292 K with a microwave frequency of 9.0132 GHz, microwave power 8 mW, and modulation width of 0.03 mT.

To assess the contribution of the ligand atoms to the superhyperfine features, a model was constructed taking the X-ray structure of $[\mathbf{1}]^{\bullet+}$[OTf] as our starting point. Intuitively, this model contains the coordinating nitrogen atom and the two aromatic hydrogen atoms on the carbons of the PNP support, which are ortho with respect to the amide, since these can share largest spin density (*vide infra*).To explain the numbers of line appeared in the solution X-band EPR spectrum of [**1**]$^{\bullet+}$[OTf], it was necessary to also include contributions from the two phosphorus atoms as well as the four meta aromatic hydrogen atoms. According to DFT calculations (*vide infra*), the phosphorus atoms have lower percentage of spin density, but in spite of this, there is still some super-hyperfine features which are observable due to higher nuclear g (g_n) value found for phosphorus (2.263). Since the super-hyperfine splitting by some atom depends both on the g_n value of the atom and the unpaired spin density surrounding the atom. In contrast, for the chlorine atom having a nuclear spin of 3/2 for both common isotopes (^{35}Cl, 76%; ^{37}Cl, 24%), super-hyperfine coupling is not commonly observed due to the lower g_n value of ~0.5 for both isotopes (g_n values for different isotopes: ^{35}Cl, 0.548; ^{37}Cl, 0.456).[74] Given the line width of the spectrum, most likely we are unable to observe any super-hyperfine coupling to chloride.[75] An inflection point is observed in the experimental spectrum in accordance with the one N, two P's, two H's, and four H's model outlined here. The isotropic simulation shown in red was performed using: $S = 1/2$, $g_{\text{iso}} = 2.0238(3)$, line width 0.31 mT, Gaussian lineshape; hyperfine coupling to one nitrogen: $I = 1$, 0.97 mT; two hydrogen atoms and two phosphorous: $I = 1/2$, 0.76 mT and $I = 1/2$, 0.50 mT; and four hydrogen atoms: $I = 1/2$, 0.33 mT. At this stage the coupling constants cannot be assigned between the two phosphorous and the two ortho hydrogens, since they both have $I = 1/2$. Due to the line width, uncertainties are large for both H and P coupling constants (0.1 mT), but much less so for the nitrogen super-hyperfine coupling constant which has a direct influence on the overall shape of the derivative signal observed. From the large super-hyperfine coupling constant of nitrogen, it seems reasonable to propose that the lone electron resides mostly on nitrogen. Expectedly, other spectroscopic features of the complex [**1**]$^{\bullet+}$[OTf] will corroborate with the nitrogen centered oxidation.

In order to further verify the nature of the radical in solid state we focused on solid state EPR of [**1**]$^{\bullet+}$[OTf]. Solid state X-band EPR spectrum collected at room temperature, displays a rhombic signal. The simulation shown in red is performed with S = 1/2 and g_1, g_2, g_3 values are observed at 2.040(4), 2.016(4), 2.005(4) respectively (Figure 4). The average of these values matches with the isotropic g-value in solution state, hence proving that the same radical is involved for both the signals in solution and solid state. The anisotropy observed for the g-values in the solid state translates to the non-negligible amount of spin density present on the nickel center. This is also manifested by the significant increase in the isotropic g-value in solution compared to the free electron value; $\Delta g = g_{iso} - g_e = 0.0215(3)$, and is also consistent with the theoretical DFT calculations.

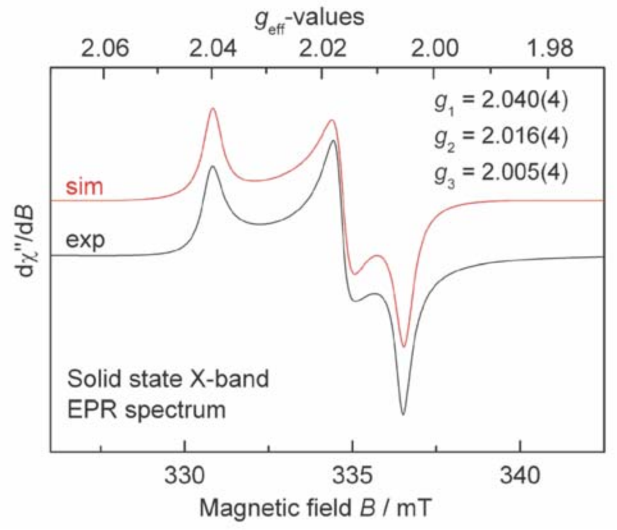

Figure 4: X-band solid state EPR spectra of [**1**]$^{\bullet+}$[OTf] recorded at 292 K with a microwave frequency of 9.4459 GHz, microwave power 1 mW, modulation width of 0.1 mT, modulation frequency of 100 kHz

3.2.4 Comparison of absorption spectra for 1 and [1]$^{\bullet+}$[OTf]

UV-vis spectroscopy sometimes provides very important clues in determining the site of oxidation for the complexes involving redox non-innocent ligands. Accordingly, an absorption spectrum of [**1**][OTf] displays three absorption bands at 872 nm (ε = 1359 M^{-1} cm^{-1}), 589 nm (ε = 4293 M^{-1} cm^{-1}), and 443 nm (ε = 1606 M^{-1} cm^{-1}). These features are strikingly different from the features shown for **1**, which shows a band at 636 nm (ε = 685 M^{-1} cm^{-1}) as well as shoulders at wave lengths below 500 nm. In order to compare the changing features of **1** due to oxidation, UV-vis spectra of **1** and [**1**]$^{\bullet+}$ have been overlaid in Figure 5. Among the three bands for [**1**]$^{\bullet+}$[OTf], the latter two bands can be ascribed to high-intensity charge transfer band (MLCT), whereas the near IR band can be originating from low energy $\pi \rightarrow \pi^*$ transition. The transition observed at 872 nm is consistent with a lower aromatic π/π^* orbitals due to the increase in the effective nuclear charge of the ligand atoms in accord to the oxidation of the scaffold. Near-IR transitions of these types are considered to be valuable spectroscopic markers for non-innocent ligands. Further experiments by XAS will also corroborate with these data analyzed here.

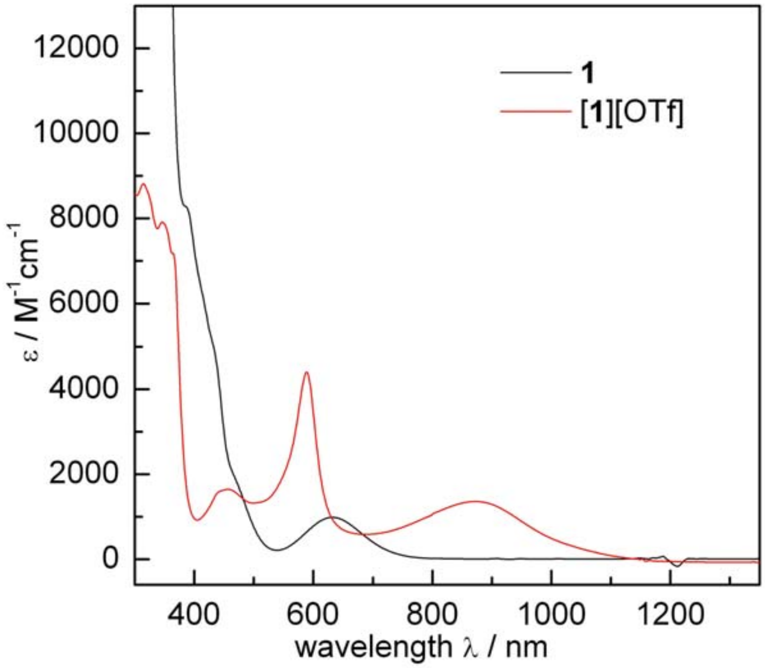

Figure 5: UV-vis spectra of **1** and [**1**]$^{\bullet+}$[OTf], stacked together to show the changing features.

3.2.5 XAS studies

X-ray crystallographic analysis in conjunction with the EPR experiments already revealed some definitive clues about the ligand based redox behavior taking place in [**1**]$^{\bullet+}$. In order to unambiguously assign the Ni oxidation state in complex [**1**]$^{\bullet+}$ we have analyzed the structure by X-ray absorption spectroscopy. Multi-edge XAS techniques become immensely popular as a direct experimental way of probing ligand-based redox chemistry.[56] We therefore performed Ni K- and L-edges, P K- edge, Cl K-edge and N K-edge XAS measurements to decipher the electronic structures of the molecules and to determine changes upon oxidation of **1** to [**1**]$^{\bullet+}$[OTf].

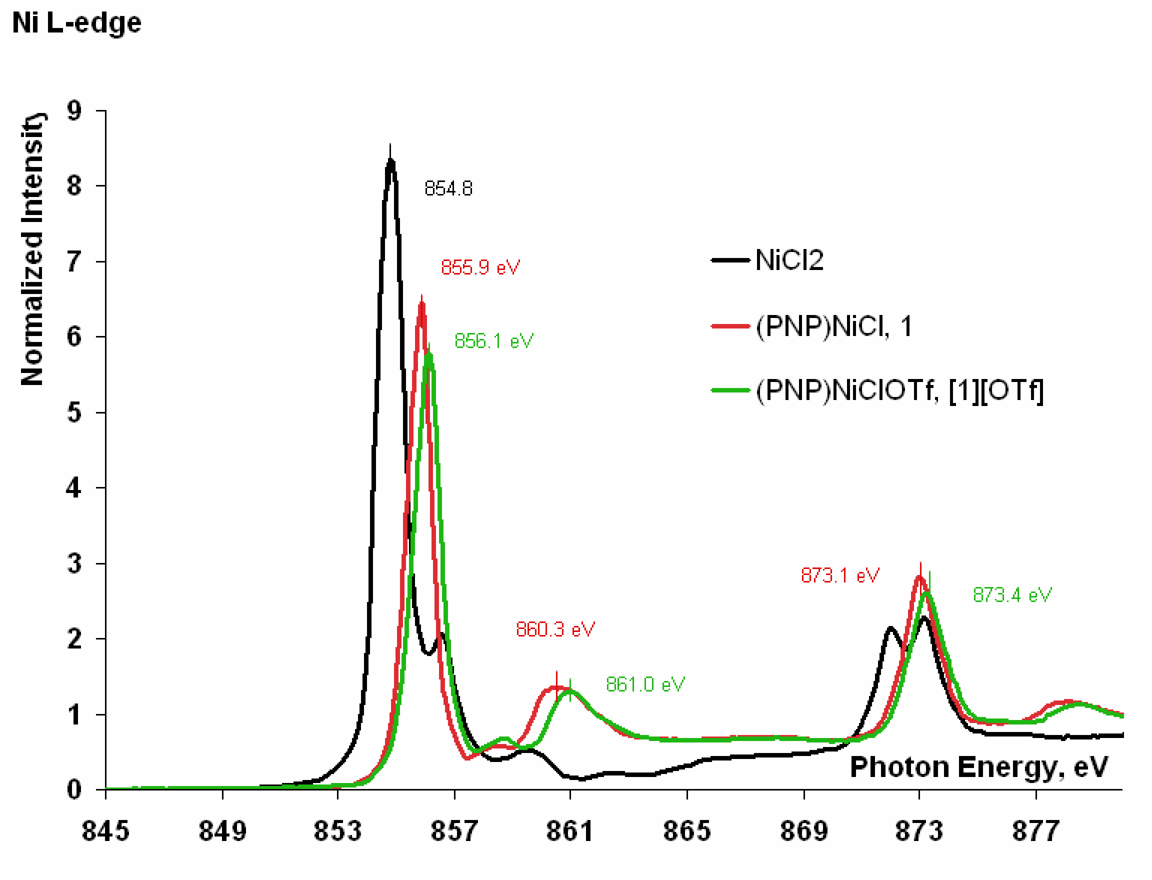

Figure 6: Ni L-edge spectrum of nickel containing complexes along with standard $NiCl_2$ describing the L_3 and L_2 region respectively.

As shown in Figure 6, the Ni L-edge spectra consists of two distinct regions namely L_3 and L_2 (852−875 eV). The L_3 (852−864 eV) and L_2 (870−875 eV) transitions originate from the excitation of an electron to 3d level from $2p_{3/2}$ and $2p_{1/2}$ core-hole states respectively. The Ni L_3-edge spectrum of **1** displays an intense feature at ~855.9 eV with a less intense feature at ~860.3 eV. The latter feature is absent for the $NiCl_2$ spectrum (control reference, black line). When considering the frontier molecular orbitals, the first absorption peak (pre-edge at ~856 eV) can be ascribed to an excitation of the Ni core 2p electrons into the lowest unoccupied orbital (LUMO). Logically, this higher energy separation of ~1.1 eV of **1** compared to $NiCl_2$ relates to the higher energy separation between the donor Ni 2p and acceptor LUMO orbitals. Such a difference may stem from varying ligand field splitting in the $Ni^{(II)}$ ions (i.e. octahedral in $NiCl_2$ and square planar in **1**) which would shift the energy of the acceptor LUMO orbital. Simultaneously, a greater Ni effective nuclear charge in **1** can lower the energy of the Ni 2p orbitals that results in shifting the XAS features to higher energy. To directly address the effect of oxidation of **1** to $[\mathbf{1}]^{\bullet+}$[OTf] we scrutinized the Ni L_3-edge of both complexes. As shown in Figure 6, it indicates a subtle change upon one-electron oxidation which is the conclusive evidence that the redox process only affects the metal to a limited extent. For a single electron redox process involving nickel a shift of 1−2 eV is common whereas in our case the pre-edge feature is shifted only by 0.2 eV.[76] The multi-edge approach plays a pivotal role in dissecting these effects from the experimental data. Cl K-edge pre-edge data (Figure 7) which exhibits features between 2820 and 2824 eV are proportional to the amount of chloride character in the LUMO orbital. Since the intensities and the rising edge positions at ~2826.6 are comparable in both $NiCl_2$ (black trace) and **1** (red trace), it can be concluded that the Cl 3p → Ni 3d electron donation, i.e. Ni−Cl bond covalency should be comparable as well. The higher energy Cl K-edge pre-edge feature at ~2822.4 eV in Figure 7 for $NiCl_2$ and the lower energy Ni L_3-edge pre-edge feature at ~854.8 eV in Figure 6 for $NiCl_2$ indicate a smaller gap between the donor Ni 2p orbital and acceptor Ni 3d orbital in $NiCl_2$ versus **1** (2821.5 and 855.9 eV, respectively).

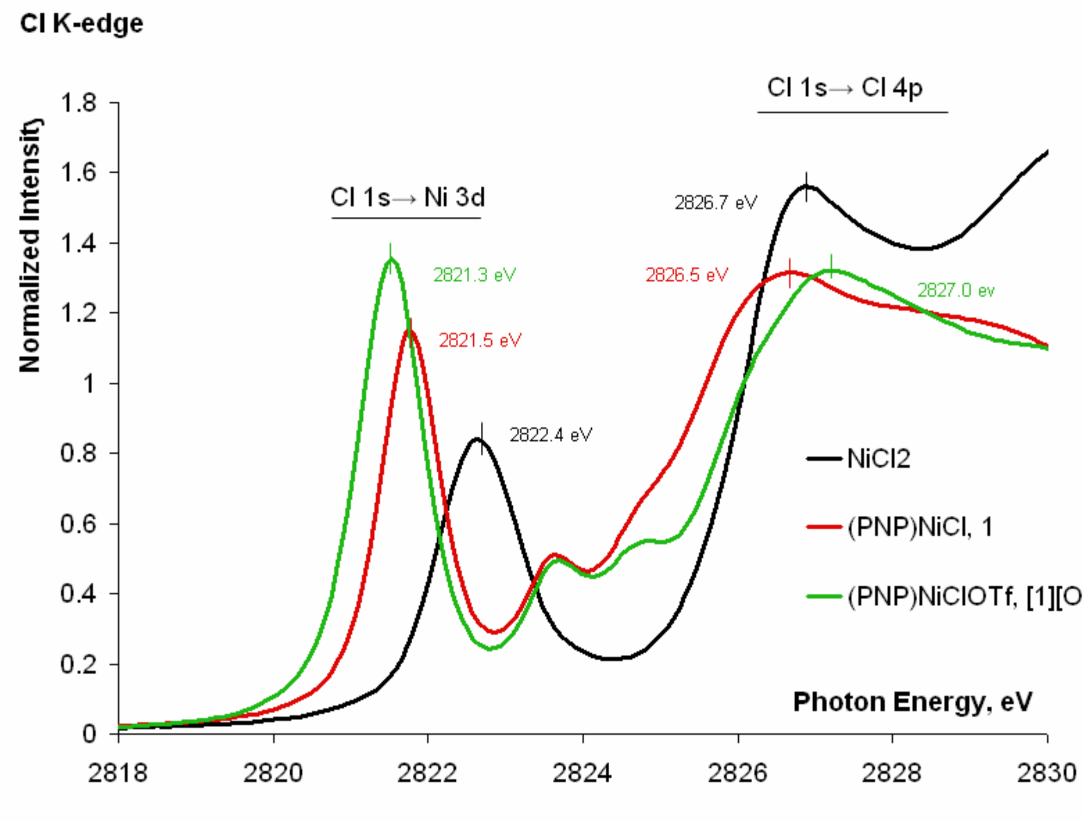

Figure 7: Cl K-edge spectrum of nickel containing complexes along with the standard $NiCl_2$ describing the pre-edge and edge regions. Annotations Cl 1s→Ni 3d and Cl 1s→Cl 4p describe the pre-edge and edge regions respectively.

This low lying Ni 2p orbital in **1** translates into a greater Ni effective nuclear charge in **1** due to back donation from the Ni to the PNP ligand. These features show up as a higher energy feature at the Ni L_3-edge around 860 eV. These similar higher energy features also show up at the Ni L_2-edge for **1** with comparable relative intensities, hence supporting the notion that these excitations are purely Ni-based. Similar intense transitions to higher lying orbitals have been seen by Solomon *et al.* and have been described as the experimental evidence for metal-to-ligand backbonding.[77] When Cl K-edges for **1** and [**1**]$^{•+}$[OTf] are compared, it is observed that pre-edge feature for [**1**]$^{•+}$[OTf] is shifted to lower energy (2821.3 eV for [**1**]$^{•+}$[OTf] versus 2821.5 eV for **1**), but the rising edge is shifted to higher energy (2827.0 eV for [**1**]$^{•+}$[OTf]versus 2826.5 eV for **1**). These features implicate an increased covalency of Cl^{-} in [**1**]$^{•+}$[OTf] compared to **1**. Now, from our earlier spectra as we inferred that the oxidation state of nickel has been changed minimally, it is evident that the chloride ligand must be donating to the ligand based orbitals and not to the metal.

Since the pincer ligand contains phosphines that are generally good donors, we assume a significant role of phosphorus atoms upon oxidation of **1**. In order to assess their involvement, we obtained P K-edge data and compared it to that of the free (PNP)H ligand. The spectrum of the free ligand displays two intense features at 2145.5 eV and 2146.3 eV, which can be ascribed to P core 1s electron transition into the aromatic and two aliphatic P−C σ* orbitals (Figure 8). The number of aliphatic bonds ($P-CHMe_2$) is twice than that of aromatic, and hence the intensity of the transition corresponding to aromatic P−C σ* orbitals is also larger. Since the aliphatic P−C bonds are unaffected by redox changes, we can use these peaks as internal references for estimating the P effective nuclear charge. Ligand complexation to nickel promotes a +0.9 eV shift in these features (2145.5 eV for (PNP)H versus 2147.2 for [**1**]$^{•+}$[OTf], which is due to the electron donation from the P lone pair into the vacant metal 3d/4s/4p orbitals. The slight increase in the difference between aromatic and aliphatic P−C σ* transitions relative to the free ligand (~1.4 eV for **1** and [**1**]$^{•+}$[OTf] compared to 0.8 eV for free (PNP)H) is a marker for the change in electronic structure of the aromatic moiety of the phosphine ligand. The oxidation of the PNP ligand is expected to lower the aromatic π/π* orbitals due to the increase in effective nuclear charge of the ligand atoms, which is consistent with the changes observed for the absorption spectrum for [**1**]$^{\bullet+}$[OTf]. More importantly, a pre-edge feature appears in **1** and [**1**]$^{\bullet+}$[OTf] (2144.8 eV and 2144.4 eV, respectively), that becomes absent for free (PNP)H, corresponds to the P 1s to LUMO (Ni 3d based) transition. Expectedly, the pre-edge feature for [**1**]$^{\bullet+}$[OTf] is shifted to lower energy when compared to **1**, since an increase in the PNP ligand effective nuclear charge will decrease the energy of the LUMO orbital. A similar trend has been documented by Solomon *et al.* in case of chloride[51] and thiolate[47] complexes with first row transition metals. Upon oxidation, a shoulder appears at 2143.3 eV in [**1**]$^{\bullet+}$[OTf], which corresponds to a rather small P 3p character in the SOMO. Compared to the pre-edge transition in (PNP)H, the same transition for **1** and [**1**]$^{\bullet+}$[OTf] is shifted to the lower region which is presumably the effect of back-bonding from phosphorus 3p to the vacant d-orbital of Ni. This feature is also corroborated by the very short Ni−P bond lengths (2.2126(6) and 2.2219(6) Å) in [**1**]$^{\bullet+}$[OTf]. The edge peaks due to 1s → 4p transitions which for **1** and [**1**]$^{\bullet+}$[OTf] (~2147 eV) are again very close in energy, thus proving no significant change in phosphorus oxidation state due to the single electron oxidation.

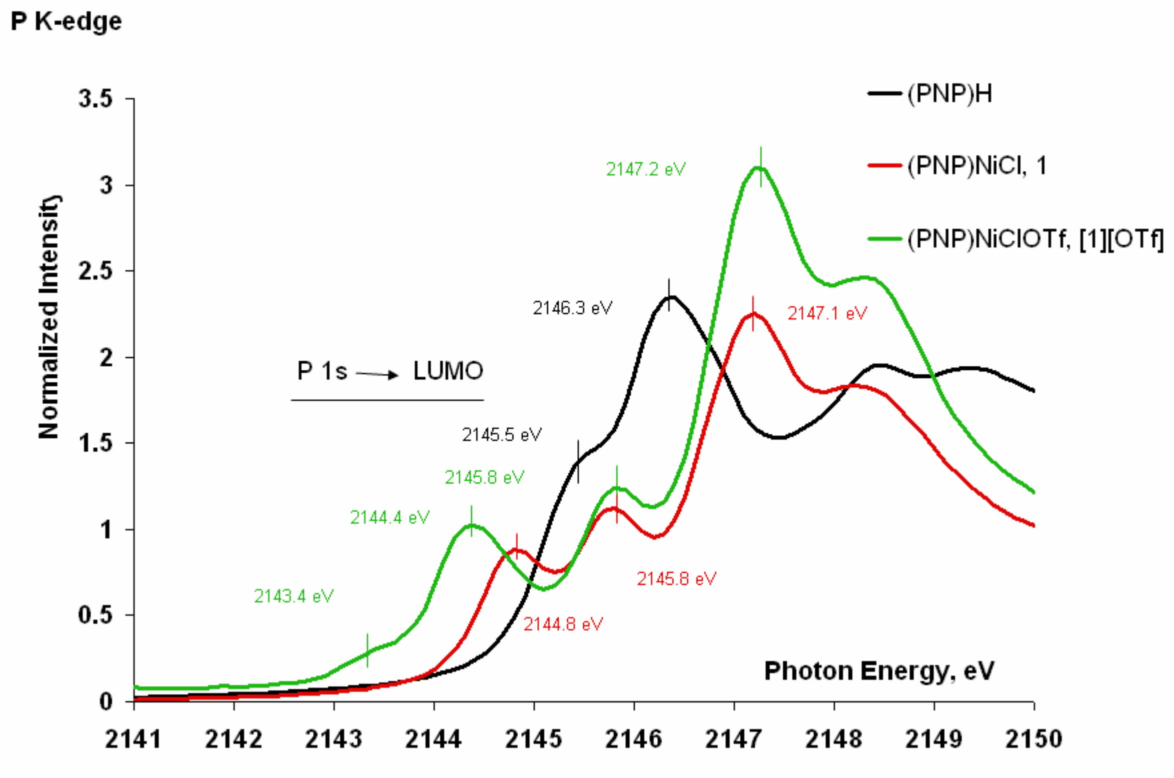

Figure 8: P K-edge spectrum of nickel containing complexes and (PNP)H describing pre-edge and edge transitions.

We also collected Ni K-edge data since K-edge will be instrumental to directly address the oxidation state change of the metal center upon oxidation. A closer inspection in Ni K-edge XAS diagram reveals a very small pre-edge transition for **1**, [**1**]$^{\bullet+}$[OTf] and $NiCl_2$ at 8333.4 eV (Figure 9). Under further examination it is observed that the intensity of the transition corresponding to $NiCl_2$ is less in intensity compared to **1** and [**1**]$^{\bullet+}$[OTf].

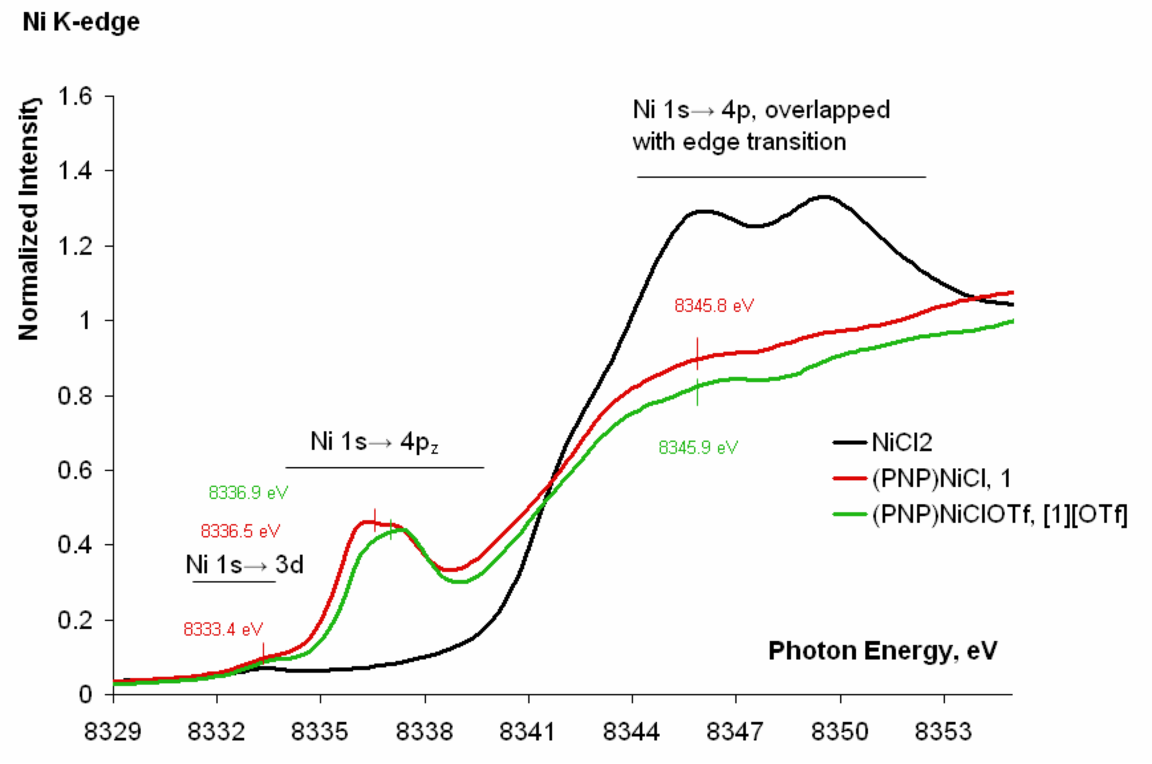

Figure 9: Ni K-edge spectra of nickel containing complexes with standard $NiCl_2$.

This is due to the fact that the first structure is octahedral whereas the latter two are close to square planar. In each case the close to centrosymmetric geometry prohibits d-p mixing, therefore diminishes the intensity of the pre-edge transition. However, **1** and [**1**]$^{\bullet+}$[OTf] are not perfectly square-planar and the ligands are not definitely homoleptic, hence the pre-edge transition is more visible. A broad edge feature for **1** appears at 8336.5 eV and invokes multiple transitions present within the envelope. Similar rising edge transition for [**1**]$^{\bullet+}$[OTf] appears at 8336.9 eV, and are equally broad like the latter one. Since both complexes are square-planar, one of the transitions can be unambiguously assigned to be 1s → $4p_z$, and the transition may be a result of backbonding or a transition from 1s to carbon σ* orbital. Importantly, the rising edge feature in between 8341−8346 eV is unresolved and holds multiple transitions to the Ni

4s/4p and ligand 2p hybrid orbitals. When directly compared the rising edge transitions for **1** and [**1**]$^{\bullet+}$[OTf] are occurring at the energies 8345.8 eV and 8345.9 eV, respectively. Such a small shift in the Ni K-edge rising edge clearly proves that the metal is minimally affected due to the oxidation process.

So far we understood from the XAS data that centers like Ni, P and Cl are not affected or very minimally affected during the course of the oxidation. Our EPR experiments provided definitive clue about the nitrogen to be the major locus of oxidation. We wanted to verify this thought further by performing N K-edge XAS experiments which can provide impeccable evidence for nitrogen oxidation state. Report on N K-edge data is exceptionally rare and we are one of the few groups who were able to successfully collect the data. The major difficulty stems from extremely low energy region (~350−450 eV) of the beamline associated with nitrogen K-edge as well as possible N_2 contamination from the atmosphere even at ultrahigh vacuum condition. In our system, nitrogen, an integral part of the ligand which connects the two aromatic rings of the ligand holds a lone pair, although the lone pair is partially delocalized through the aromatic rings. Interestingly, the lone pair is not interacting with the metal d-orbital as evident from the molecular orbital analysis (*vide infra*). Intuitively, we will observe a vivid change in the spectroscopic pattern once the lone pair is oxidized, if it indeed is oxidized. Indeed that is the case we observe when **1** and [**1**]$^{\bullet+}$[OTf] is assayed under N K-edge XAS. As portrayed in Figure 10, complex **1** displays pre-edge features at 398.6 eV and 401.2 eV, which are assigned to the nitrogen 1s → $3d_{x^2-y^2}$ (Ni) type transition and nitrogen 1s → C−N σ* transition, respectively. These two features are essentially retained although with considerably reduced intensity in case of [**1**]$^{\bullet+}$[OTf]. The most striking change observed in [**1**]$^{\bullet+}$[OTf] is the appearance of a completely new feature at 397.1 eV, which is due to the 1s → SOMO transition. In the SOMO of the molecule [**1**]$^{\bullet+}$ there is a significant contribution of the nitrogen (27%) and lower contribution from nickel (24%) (DFT calculations, *vide infra*). Quite justifiably, the transition at 397.1 eV is very intense due to the p component of the orbital which makes the transition facile. This is direct proof of a hole being created on nitrogen during the oxidation. In the rising edge position of **1** and [**1**]$^{\bullet+}$, a broad feature is observable at 497.4 and 408.9 eV, respectively. These transitions are broad since the transitions could be involving multiple orbitals such as $3p_{x,\,y,\,z}$.

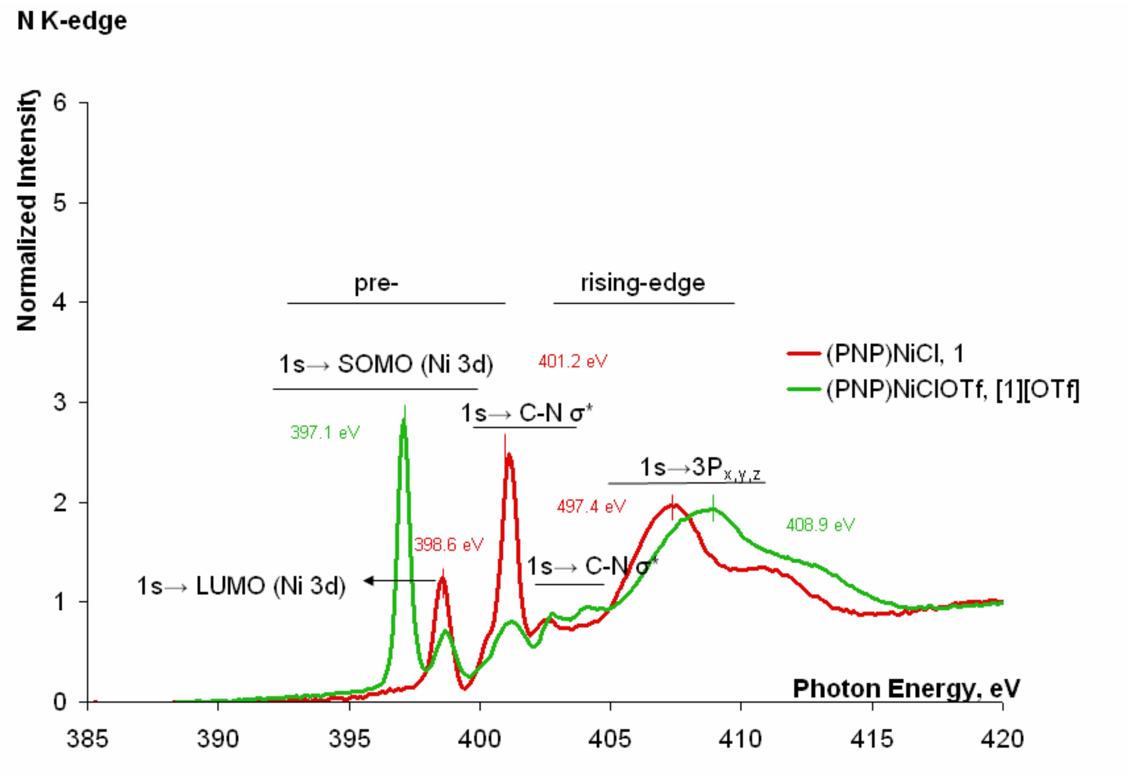

Figure 10: N K-edge spectrum of (PNP)NiCl, **1** and (PNP)NiCl(OTf), [**1**]$^{\bullet+}$[OTf].

A closer analysis reveals that the rising edge position has been shifted 1.5 eV, which also corroborates to the fact that nitrogen is oxidized in the one-electron change from **1** → [**1**]$^{\bullet+}$[OTf]. From this multi-edge XAS experiments it has been unambiguously proved that the complex [**1**]$^{\bullet+}$[OTf] possess an aminyl centered radical that is coordinated to Ni$^{(II)}$. Examples of aminyl radicals are very scarce owing to the highly reactive and short-lived nature of the radical.[78] Grutzmacher *et al.* isolated a trop$_2$N aminyl radical coordinated to a cationic Rh center.[79] (trop = 5-H-dibenzo[a,d]cycloheptene-5-yl). Very recently Peters and Szilagyi reported an aminyl radical supported by a three coordinate copper $^{(I)}$ center.[80]

3.2.6 DFT Calculations

Our claim of a ligand based redox reaction taking place in **1** has been substantiated by EPR and XAS experiments. To justify these arguments further we resorted to high level DFT calculations. The crystal structure geometry for [**1**]$^{\bullet+}$[OTf] was taken as the starting geometry with the simplification of all ^{i}Pr-groups on P to Me-groups and tolyl methyl groups to hydrogen atoms. Spin density calculations using ADF[81] package using a triple-ζ basis set with double polarization function (TZ2P or BSIV in ADF) reveal that the population of electron densities reside around the following centers in Table 2. Scheme 4 depicts the corresponding labeling pattern for radical cation component of complex [**1**]$^{\bullet+}$[OTf].

Table 2: Electron densities around the different atoms for the radical cation component of [**1**]$^{\bullet+}$[OTf].

Atom	Spin density	Atom	Spin density
Ni1	0.256	C19	0.098

P3	0.006	C26	0.083
N22	0.315	C28	0.107
C12	0.095	C32	0.080
C15	0.125	P33	0.005

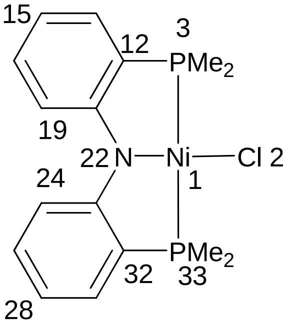

Scheme 4: Labeled scheme of $[\mathbf{1}]^{\bullet+}$ to designate the positions of maximum spin densities calculated by ADF. Simplified model (^{i}Pr and tolyl methyl groups have been replaced by hydrogen atoms) was used for the calculation.

The spin density around the atoms on the ligand backbone suggests that the oxidation has been taken place mostly at the ligand scaffold instead of the Ni metal center, which is supported by the significantly small spin density (0.256) around nickel. Given the fact that the nitrogen is in conjugation with the aromatic rings it is expected that the oxidation of nitrogen will also be translated to the aromatic ring. Expectedly, spin densities are also observed at the carbons of the aromatic ring which are in conjugation with the nitrogen. EPR experiments completely support the spin density obtained from DFT calculations. As seen earlier, there is an insignificant amount of electron density (hyperfine coupling for phosphorus atoms are 0.50 mT) on phosphorus. The probability of significant electron densities on aromatic carbons were not visible in EPR experiments owing to I = 0 for ^{14}C.

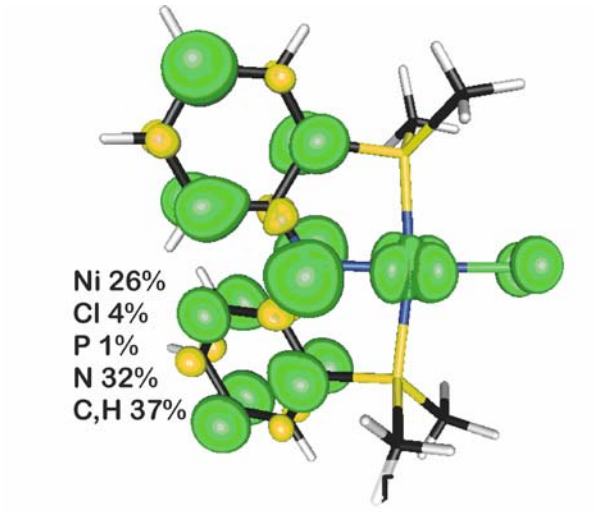

Figure 11: Spin density plot for $[\mathbf{1}]^{\bullet+}$ calculated using BP86 functional and BSV in Amsterdam Density Functional package.

High level DFT calculations were also performed to decipher the electronic structure and to verify the HOMO/LUMO orbital compositions for both **1** and $[\mathbf{1}]^{\bullet+}$. Quite expectedly, the LUMO for **1** is a combination of the Ni $3d_{x^2-y^2}$ orbital with approximately equal contributions from the chloride and each phosphorus 3p orbitals. The atomic compositions (percentile values) are shown in Table 3.

Table 3: HOMO and LUMO orbital composition for **1.**

Atom	LUMO (%)	HOMO (%)
Ni	43	37
Cl	13	5
P	27	1

N	8	23
C, H	9	35

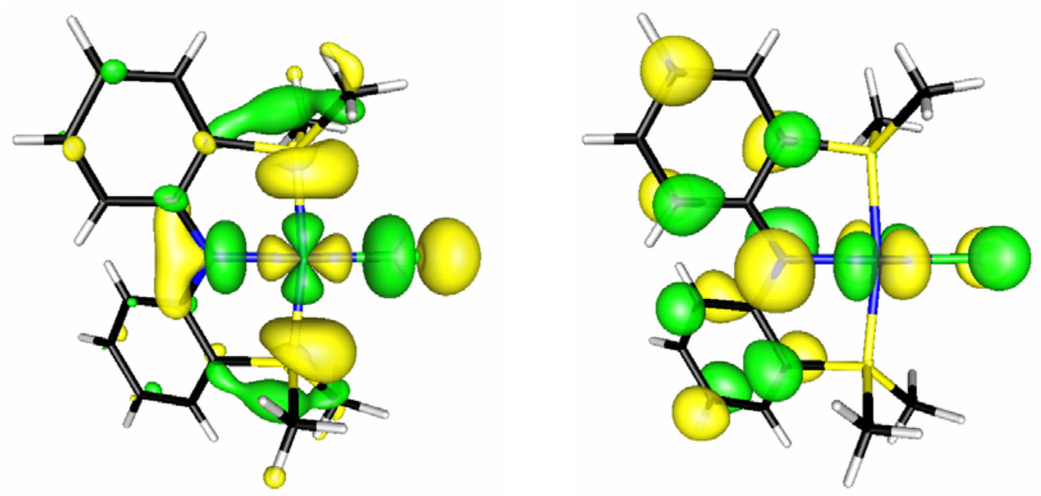

Figure 12: Frontier molecular orbitals of a simplified model of **1** (^{i}Pr groups have been reduced to methyl groups and tolyl groups have been reduced to hydrogen atoms). The figure depicts LUMO (left) and the HOMO of **1**.

In the LUMO orbital of **1**, the PNP ligand's involvement is limited to the in-plane (xy plane) amido lone pair, with only a fractional amount of carbon character due to skewing of the aryl motifs (Figure 12). On the other hand, the HOMO orbital shows considerably greater PNP character (59% versus 44% in LUMO) with the out-of-plane amido N $2p_z$ lone pair and aromatic carbon $2p_z$ contributions. Intuitively, it is easier to apprehend that the oxidation may predominantly affect the out-of-plane amido lone pair. Such a proposal has been already verified from the N K-edge data for [**1**]$^{\bullet+}$. From the pictorial view of the HOMO, it is evident that the metal $3d_{xz}$ and chloride $3p_z$ orbital contribution are reduced relative to the LUMO. Interestingly, the perpendicular nature of the HOMO (along the z direction and considering the molecular plane as xy) forbids the phosphorus atoms to contribute significantly to the overall orbital picture. Not surprisingly, the oxidation process will create a hole in HOMO, and since there is a significant ligand character in the HOMO (59%), oxidation will be more ligand based. However, it is very important to consider that the oxidation will augment significant electron relaxation due to the change in effective nuclear charge of the atoms and such features have been already evident from the XAS edge studies. As a consequence of electron reorganization, the orbital contribution will be changed considerably from **1** to [**1**]$^{\bullet+}$ as evident from their MO pictures.

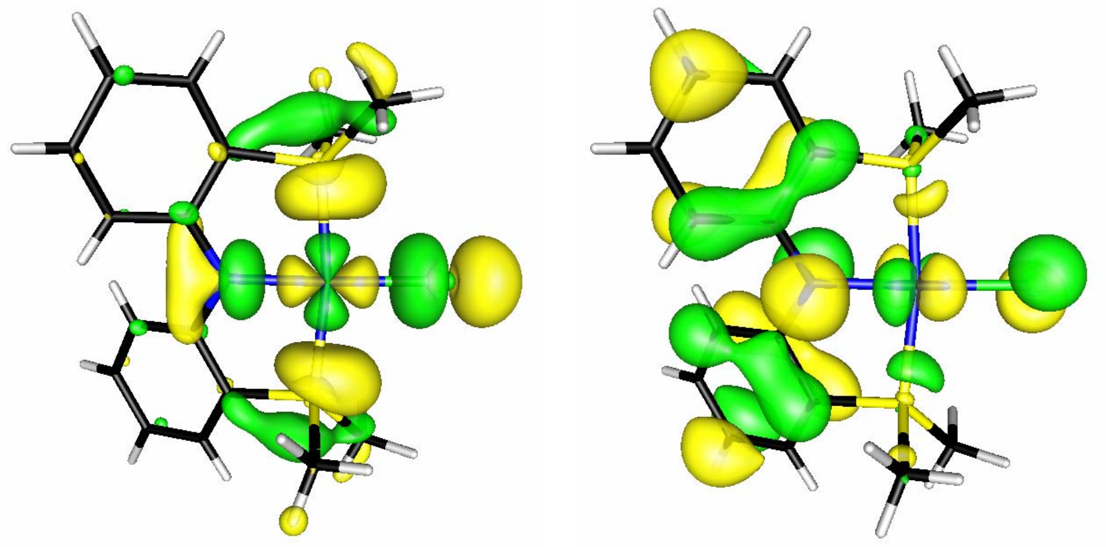

Figure 13: Frontier molecular orbitals of a simplified model of [**1**]$^{\bullet+}$ (^{i}Pr groups have been reduced to methyl groups and tolyl groups have been replaced with hydrogen atoms). The figure depicts LUMO (left) and the SOMO of [**1**]$^{\bullet+}$**.**

As shown in the Table 4 (*vide infra*), the metal character is decreased to 17-24% per electron hole in the SOMO of [**1**]$^{\bullet+}$ versus the 37% contribution in the HOMO of **1**.

Earlier we observed from the Cl K-edge and P K-edge spectra that these two centers have been slightly oxidized. As a consequence, the chlorine and phosphorus character increase by only a few fractions of percent in the SOMO of $[\mathbf{1}]^{\bullet+}$ compared to that of HOMO of **1**.

Table 4: HOMO and LUMO composition of $[\mathbf{1}]^{\bullet+}$.

Atom	LUMO (%)		HOMO (%)	
	α-set	β-set	α-set	β-set
Ni	38	39	17	24
Cl	14	13	7	5
P	28	27	6	3
N	7	7	24	27
C,H	12	14	47	41

Furthermore, the contribution of the aromatic ring of the PNP increases the most by ~15% indirectly indicating that the one electron oxidation in **1** affects this component of the complex the most. Earlier we observed spectroscopically that the Ni L-edge and Cl K-edge pre-edge intensities are very similar in **1** and $[\mathbf{1}]^{\bullet+}$. Since those transitions are directed to the LUMO of the corresponding complexes from nickel 2p and chlorine 1s orbitals respectively, expectedly, the close intensities of these two transitions should translate to the similar LUMO coefficients. Gratifyingly our calculations display the LUMO coefficients to vary within 5% from **1** to the oxidized $[\mathbf{1}]^{\bullet+}$. Similarly, atomic spin densities for $[\mathbf{1}]^{\bullet+}$ indicate small contributions from nickel (26%), chlorine (4%), phosphorus (1%) in contrast to the dominant contribution from amido nitrogen (31%) and carbon residues (38%) of the PNP ligand. Thence, the spin density analysis is fully consistent with the earlier findings in X-band EPR spectrum and multinuclear XAS data.

3.3 Conclusions

This study unequivocally proves the redox non-innocence of a pincer ligand which is profusely used in organometallic chemistry.[82-84] By applying a wide range of characterization methods such as XRD, EPR, UV-Vis, and multi-edge XAS in combination with DFT analysis of the orbitals and spin densities, we have characterized a square-planar $Ni^{(II)}$ radical cation complex. The electron hole is predominantly ligand based and resides mostly at the nitrogen and aryl carbon atoms (ortho and para positions) of the pincer type PNP ligand. Interaction of the unpaired electron with aryl hydrogen and phosphorus atoms has been also established by EPR, but this interaction should be considered very weak on the basis of the coupling constant as well as our computed spin density analysis. Multi-edge XAS has been adopted to unravel the site of oxidation as well as to address some key questions related to bonding scheme. For example, major contribution of the arylamido nitrogen to house the electron hole has been elegantly captured by a novel N K-edge spectroscopic technique. The ability of PNP ligand to house an electron hole may provide very important clue in elucidating the reaction mechanisms where the ligand is involved. Redox processes such as oxidative additions or reductive eliminations involving PNP-supported nickel complexes (e.g. $Ni^{(0)}/Ni^{(II)}$, $Ni^{(II)}/Ni^{(IV)}$ couples) could be occurring in a stepwise manner whereby the ligand peripheral motif might be partially housing a radical along the two-electron sequence (e.g. $Ni^{(I)}$ radical anion and $Ni^{(III)}$ radical cation). From this respect, this category of ligand can be classified as cooperating ligand.[85] Cooperating ligands may be defined as those ligands which take part directly to the bond activation process and undergo reversible chemical transformation.[86] Thus the metal and the ligand cooperate in a synergistic manner and their interplay facilitates the chemical process. The capability of the PNP ligand system to house an electron hole along the bond activation pathway can make the ligand amenable to behave as a cooperating ligand. Given the fascinating role of the tyrosinyl radical in galactose oxidase to oxidize primary alcohols to aldehydes, similar activities may also be expected for the aminyl radicals. For example, Grutzmacher *et al.* reported the use of iridium-aminyl radical complexes that catalyze the dehydrogenation of alcohols to aldehydes, with 1,4-benzoquinone as the H_2 accpetor.[87] They also show that primary non-activated alcohols can be converted to aldehydes with very high activity and selectivity. Furthermore, Vicic *et al.* have proved through elegant spectroscopic studies that the ligand redox effect has a significant influence on alkyl-alkyl cross coupling reactions mediated by a seemingly redox innocent terpy ligand (terpy = 4, 4', 4"-tri-tert-butylpyridine).[29] Having the electronic nature of $[\mathbf{1}]^{\bullet+}$[OTf] unambiguously proved, this is a new entry in the only few examples of stable aminyl radicals.[78] Encouragingly, aminyl radicals are thermodynamically unstable and are able to oxidize organic substrates through hydrogen atom abstraction.[88] Metal complexes comprising aminyl radicals may therefore potentially function as a new oxidation catalyst in organic synthesis. Furthermore, metal coordination complexes of organic radical ligands may inspire the development of new materials.

3.4 Experimental Section

General Procedures: Unless otherwise stated, all operations were performed in a M. Braun Lab Master double-dry box under an atmosphere of purified nitrogen or using high vacuum standard Schlenk techniques under an argon atmosphere.[24] Anhydrous n-hexane, pentane, toluene, and benzene were purchased from Aldrich in sure-sealed reservoirs (18 L) and dried by passage through two columns of activated alumina and a Q-5 column.[25] Diethylether was dried by passage through a column of activated alumina.[25] THF was distilled, under nitrogen, from purple sodium benzophenone ketyl and stored under sodium metal. Distilled THF was transferred under vacuum into thick walled reaction vessel before being transferred into a dry box. C_6D_6 was purchased from Cambridge Isotope Laboratory (CIL), degassed and vacuum transferred to 4 Å molecular sieves. Celite, alumina, and 4 Å molecular sieves were activated under vacuum overnight at 200 ºC. (PNP)Li (PNP = $N[2\text{-}P(CHMe_2)_2\text{-}4\text{-}MeC_6H_4]_2^-$), (PNP)NiCl were prepared according to the literature. [Fc][OTf] was prepared by addition of an equilmolar amount of AgOTf to recrystallize Fc ($FeCp_2$) in CH_2Cl_2. Removal of Ag^0, concentrating and cooling of the filtrate to -35 °C afforded dark blue needles of [Fc][OTf], which were collected, washed with Et_2O and dried under reduced pressure (>90% yield). All other chemical were used as received. CHN analyses were performed by Desert Analytics, Tucson, AZ. ^1H spectrum was recorded on Varian 400 or 300 MHz NMR spectrometers. ^1H is reported with reference to solvent resonances (residual C_6D_5H in C_6D_6, 7.16 ppm). Solution magnetization measurements were determined by the method of Evans. UV-visible spectra were recorded on a Cary 5000 UV-vis-NIR spectrophotometer.

Single Crystal X-ray Diffraction Details. X-ray diffraction data were collected on a SMART6000 (Bruker) system under a stream of N_2 (g) at low temperatures. Single crystals of **1** (THF) and $[\mathbf{1}]^{\bullet+}$[OTf] (CH_2Cl_2 layered with hexane) were grown at −35 °C and room temperature, respectively, from concentrated solutions. Inert-atmosphere techniques were used to place the crystal onto the tip of a diameter glass capillary (0.10 mm) mounted on a SMART6000 (Bruker) at 128−132(2) K. A preliminary set of cell constants was calculated from reflections obtained from three nearly orthogonal sets of 30 frames. The data collection was carried out using graphite-monochromated Mo Kα radiation with a frame time of 5−20 seconds and a detector distance of 5.0 cm. A randomly oriented region of a sphere in reciprocal space was surveyed. In general, three sections of 606 frames were collected with 0.30° steps in ω at different φ settings with the detector set at −43° as 2θ. Final cell constants were calculated from the *xyz* centroids of strong reflections from the actual data collection after integration (SAINT). The structure was solved using SHELXS-97 and refined with SHELXL-97. A direct-methods solution was calculated which provided most non-hydrogen atoms from the E-map. Full-matrix least squares/difference Fourier cycles were performed which located the remaining non-hydrogen atoms. All non-hydrogen atoms were refined with anisotropic displacement parameters. All hydrogen atoms were located in subsequent Fourier maps and included as isotropic contributors in the final cycles of refinement.

Crystal data for **1**·THF: $C_{30}H_{48}ClNNiOP_2$, $M_w = 594.79$, monoclinic, space group $P2(1)/c$, $a = 19.183(6)$, $b = 11.709(4)$, $c = 14.676(3)$ Å, $\beta = 110.738(8)^{\circ}$, $Z = 4$, $\mu = 0.843$ mm^{-1}, Mo-Kα = 0.71073 Å, $V = 3082.8(17)$ Å^3, $T = 128(2)$, $\rho_{\mathrm{calcd}} = 1.282$ mg/mm^3, GoF on $F^2 = 0.820$, $R_1 = 3.34\%$ and $wR_2 = 6.95\%$ (F^2, all data). Out of a total of 11398 reflections collected 6112 were unique and 4205 were observed (R_{int} = 3.75 %) with $I > 2\sigma I$ (dark green cleaved cube, 0.18 x 0.15 x 0.15 mm, 27.49° ≥ θ ≥ 2.08°). A disordered THF solvent is present and was modeled as two distinct molecules. All (non-thf) hydrogen atoms were located in subsequent Fourier maps and included as isotropic contributors in the final cycles of refinement.

Crystal data for $[\mathbf{1}]^{\bullet+}$[OTf]: $C_{27}H_{40}ClF_3NNiO_3P_2S$, M_w = 671.76, monoclinic, space group $P2(1)/n$, a = 10.9057(9), b = 18.8042(15), c = 14.7900(11) Å, β = 92.510(2)°, Z = 4, μ = 0.951 mm^{-1}, Mo-Kα = 0.71073 Å, V = 3030.1(4) Å^3, T = 132(2), ρ_{calcd} = 1.473 mg/mm^3, GoF on F^2 = 0.806, R_1 = 3.38% and wR_2 = 6.80% (F^2, all data). Out of a total of 27480 reflections collected 8843 were unique and 5686 were observed (R_{int} = 5.99 %) with $I > 2\sigma I$ (dark green cleaved cube, 0.25 × 0.12 × 0.10 mm, 30.01° ≥ θ ≥ 2.16°).

X-Band EPR Details. The EPR measurements were performed in quartz tubes with young valves. Solid state X-band EPR spectra were recorded in a Bruker EMX EPR instrument. Anisotropic simulation was performed using the program ESRSIM written by Høgni Weihe, University of Copenhagen, Denmark.[89] Solution EPR spectra were recorded on a JEOL continuous wave spectrometer JES-FA200 equipped with an X-band Gunn oscillator bridge, a cylindrical mode cavity and a helium cryostat. The *g*-value in the solution spectrum was calibrated using the second and fourth line of the Mn^{2+} hyperfine spectrum from an external Mn marker. The marker consists of Mn^{2+} thermally dispersed in MgO placed on the tip of a probe which is inserted slightly into the cavity. The cavity was tuned with both sample and probe inserted. The Mn marker is provided with the JEOL JES-FA200 spectrometer. The isotropic simulation was performed using the JEOL Isotropic Simulation program ISOSimu/FA Version 2.1.0.

XAS Details. The nickel L- and nitrogen K-, phosphorous and chlorine K-edge XAS measurements were carried out at beamlines 10-1 and 6-2 of Stanford Synchrotron Radiation Lightsource respectively under strorage ring (SPEAR 3) conditions of 3 GeV energy and 100-80 mA beam current. BL10-1 has a 30-pole 1.45 Tesla Wiggler insertion device with 6 m spherical grating monochromator. The samples were measured in a vacuum chamber with typical pressures of 10^{-6}−10^{-8} torr. Sample holders for Ni L-edge measurements were mounted in a He purged glove bag tightly wrapped around the vacuum chamber. The energy was scanned between 820-980 eV. The incident beam intensity and beam line optics were optimized at 860 eV. The energy scale was calibrated to the L_{III} and L_{II} edges of NiF_2 at 854.7 and 871.9 eV. Data collection was carried out in electron yield mode by a Channeltron detector with 1.5 kV accelerating potential. BL6-2 is a 56-pole, 0.9 Tesla Wiggler beam line with a liquid nitrogen cooled, Si(111) double crystal monochromator. P and Cl K-edge spectra were collected in the energy range of 2120−2320 and 2720−3050 eV, respectively, using an unfocused beam in a He-purged fly-path at room temperature and a Lytle fluorescence detector. The beam line was optimized at 2320 eV and 3050 eV at the P and Cl K-edges, respectively. The energy scale was calibrated to the most intense feature of $OPPh_3$ at 2147.5 eV and recalibrated for the Cl K-edge at 2820.2 eV using the pre-edge feature of Cs_2CuCl_4. The solid samples were ground and pasted onto a contaminant free Kapton tape from Shercon or carbon tape from Specs CertiPrep in a glove box with sub ppm oxygen and moisture levels. For the P and Cl K-edge measurements samples were protected by a thin polypropylene window (Specs CertiPrep) from exposure to air during sample mounting and change. The incident photon energy was scanned in 0.5 eV steps outside the rising edge region where the step-size was 0.1 eV. At least five scans were averaged to obtain a good signal-to-noise ratio. Further processing of the data has been carried out as described in the literature.[1, 56]

Preparation of [(PNP)NiCl][OTf], [1]$^{\bullet+}$[OTf]. In a vial (PNP)NiCl, **1** (100 mg, 0.191 mmol) was taken in 5 mL THF and the solution cooled to -35 °C. An analogously cold solution/suspension of [Fc][OTf] (62.72 mg, 0.187 mmol) was added dropwise to **1** and the mixture stirred for 1 hour. The solution color changes to deep blue immediately after addition of [Fc][OTf]. After the completion of the reaction, the solution was dried under vacuum and the residue was washed three times (~5 mL each time) with pentane to extract the byproduct, ferrocene (Fc). Pink colored crystals of [**1**]$^{\bullet+}$[OTf] were obtained from the mixture at −35 °C (112 mg, 0.166 mmol, 87% yield) from a CH_2Cl_2 (~ 3 mL) layered solution with hexane (2 full pipettes) over 5 days. ^1H NMR (25 °C, 399.8 MHz, C_6D_6): δ 7.35 (br, $\Delta\nu_{1/2} = 6$ Hz), 7.21 (br, $\Delta\nu_{1/2} = 34$ Hz), 3.68 (br, $\Delta\nu_{1/2} = 21$ Hz), 3.45 (br, $\Delta\nu_{1/2} = 24$ Hz), 2.34 (br, $\Delta\nu_{1/2} = 15$ Hz), 1.15 (br, $\Delta\nu_{1/2} = 20$ Hz). μ_{eff} : 2.21(1) μ_B (CD_2Cl_2, 25 °C, Evans method). UV-vis/NIR (CH_2Cl_2, 25 °C) 443 nm ($\varepsilon = 1606$ $M^{-1}cm^{-1}$), 589 nm ($\varepsilon = 4293$ $M^{-1}cm^{-1}$), 872 nm ($\varepsilon = 1359$ $M^{-1}cm^{-1}$). Anal. Calcd for $C_{27}H_{40}NClF_3NiO_3P_2S$: C, 48.28; H, 6.00; N 2.09. Found: C, 47.90; H, 5.82, N, 2.02. M.p. 220(2) °C.

Electronic Structure Calculations. Density functional calculations were carried out using the Amsterdam Density Functional package.[81] The electronic structures of the computational models **1** and $[\mathbf{1}]^{\bullet+}$[OTf] were calculated by employing a gradient corrected density functional composed Becke non-local and Slater local density functional exchange[90] and Perdew non-local and Vosko-Wilk-Nussair local density functional correlation functions (BP or BP86). Calculations were carried out using triple-ζ basis set with double polarization function (TZ2P or BSIV in ADF). The structures of the computational model were derived from their crystal structures without any modification and provided below. The molecular orbital diagrams and spin density plots were generated using the GOpenMol visualizer program.

3.5 References

1. Solomon, E. I.; Hedman, B.; Hodgson, K. O.; Dey, A.; Szilagyi, R. K., *Coord. Chem. Rev.* **2005,** *249*, 97.
2. Pierpont, C. G.; Lange, C. W., *Prog. Inorg. Chem.* **1994,** *41*, 331.
3. Chaudhuri, P.; Wieghardt, K., *Prog. Inorg. Chem.* **2001,** *50*, 151.
4. Ray, K.; Petrenko, T.; Wieghardt, K.; Neese, F., *Dalton Trans.* **2007,** 1552.
5. Chaudhuri, P.; Verani, C. N.; Bill, E.; Bothe, E.; Weyhermueller, T.; Wieghardt, K., *J. Am. Chem. Soc.* **2001,** *123*, 2213.
6. Whittaker, J. W., *Arch. Biochem. Biophy.* **2005,** *433*, 227.
7. Merenyi, G.; Lind, J., In *N-Centered Radicals*, Alsfassi, Z., Ed. New York, 1998; pp 599-613.
8. Esker, J. L.; Newcomb, M., *Advances in Heterocyclic Chemistry* **1993,** *58*, 1-45.
9. Kaim, W., *Dalton Trans.* **2003,** 761.
10. Williams, D. E., *J. Am. Chem. Soc.* **1966,** *88*, 5665.
11. Miura, Y.; Tomimura, T.; Teki, Y., *J. Org. Chem.* **2000,** *65*, 7889.
12. Miura, Y.; Tomimura, T., *Chem. Commun.* **2001**, 627.
13. Kaim, W.; Wanner, M.; Knodler, A.; Zalis, S., *Inorg. Chim. Acta* **2002,** *337*, 163..
14. Gross, R.; Kaim, W., *Angew. Chem.* **1985,** *97*, 869.
15. Gross, R.; Kaim, W., *Inorg. Chem.* **1987,** *26*, 3596.
16. Maki, A. H.; Edelstein, N.; Davison, A.; Holm, R. H., *J. Am. Chem. Soc.* **1964,** *86*, 4580..

17. Stiefel, E. I.; Waters, J. H.; Billig, E.; Gray, H. B., *J. Am. Chem. Soc.* **1965,** *87*, 3016.
18. Balch, A. L.; Rohrscheid, F.; Holm, R. H., **1965,** *87*, 2301.
19. Balch, A. L.; Holm, R. H., *J. Am. Chem. Soc.* **1966,** *88*, 5201.
20. Weber, J.; Daul, C.; Von Zelewsky, A.; Goursot, A.; Penigault, E., *Chem. Phy. Lett.* **1982,** *88*, 78.
21. Hille, R., *Chem. Rev.* **1996,** *96*, 2757.
22. Lim, B. S.; Fomitchev, D. V.; Holm, R. H., *Inorg. Chem.* **2001,** *40*, 4257.
23. Herebian, D.; Bothe, E.; Bill, E.; Weyhermueller, T.; Wieghardt, K., *J. Am. Chem. Soc.* **2001,** *123*, 10012.
24. Herebian, D.; Bothe, E.; Neese, F.; Weyhermueller, T.; Wieghardt, K., *J. Am. Chem. Soc.***2003,** *125*, 9116.
25. Ray, K.; Bill, E.; Weyhermueller, T.; Wieghardt, K., *J. Am. Chem. Soc.* **2005,** *127*, 5641.
26. Ray, K.; Weyhermueller, T.; Goossens, A.; Craje, M. W. J.; Wieghardt, K., *Inorg. Chem.* **2003,** *42*, 4082.
27. Gossage, R. A.; van de Kuil, L. A.; van Koten, G., *Acc. Chem. Res.* **1998,** *31*, 423.
28. Fan, L.; Ozerov, O. V., *Chem. Commun.* **2005,** 4450.
29. Jones, G. D.; Martin, J. L.; McFarland, C.; Allen, O. R.; Hall, R. E.; Haley, A. D.; Brandon, R. J.; Kanovalova, T.; Desrochers, P. J.; Pulay, P.; Vicic, D. A., *J. Am. Chem. Soc.* **2006,** *128*, 13175.
30. Calimano, E.; Tilley, T. D., *J. Am. Chem. Soc.* **2008,** *130*, 9226.
31. Zhao, J.; Goldman, A. S.; Hartwig, J. F., *Science* **2005,** *307*, 1080.
32. Ghosh, R.; Zhang, X.; Achord, P.; Emge, T. J.; Krogh-Jespersen, K.; Goldman, A. S., *J. Am. Chem. Soc.* **2007,** *129*, 853.
33. Zhang, X.; Emge, T. J.; Ghosh, R.; Goldman, A. S., *J. Am. Chem. Soc.* **2005,** *127*, 8250.
34. Pirbrow, J. R., *Transition Ion Electron Paramagnetic Resonance*. Oxford University Press London, 1990.
35. Tuczek, F.; Solomon, E. I., *Coord. Chem. Rev.* **2001,** *219*, 1075.
36. Hedman, B.; Hodgson, K. O.; Solomon, E. I., *J. Am. Chem. Soc.* **1990,** *112*, 1643.
37. Dey, A.; Chow, M.; Taniguchi, K.; Lugo-Mas, P.; Davin, S.; Maeda, M.; Kovacs, J. A.; Odaka, M.; Hodgson, K. O.; Hedman, B.; Solomon, E. I., *J. Am. Chem. Soc.* **2006,** *128*, 533.
38. Dey, A.; Glaser, T.; Moura, J. J. G.; Holm, R. H.; Hedman, B.; Hodgson, K. O.; Solomon, E. I., *J. Am. Chem. Soc.* **2004,** *126*, 16868.
39. Dey, A.; Okamura, T.; Ueyama, N.; Hedman, B.; Hodgson, K. O.; Solomon, E. I., *J. Am. Chem. Soc.***2005,** *127*, 12046.
40. Dey, A.; Glaser, T.; Couture, M. M. J.; Eltis, L. D.; Holm, R. H.; Hedman, B.; Hodgson, K. O.; Solomon, E. I., *J. Am. Chem. Soc.* **2004,** *126*, 8320.
41. Sarangi, R.; Aboelella, N.; Fujisawa, K.; Tolman, W. B.; Hedman, B.; Hodgson, K. O.; Solomon, E. I., *J. Am. Chem. Soc.* **2006,** *128*, 8286.
42. Wasinger, E. C.; Mitic, N.; Hedman, B.; Caradonna, J.; Solomon, E. I.; Hodgson, K. O., *Biochemistry* **2002,** *41*, 6211.
43. DeBeer, S.; Randall, D. W.; Nersissian, A. M.; Valentine, J. S.; Hedman, B.; Hodgson, K. O.; Solomon, E. I., *J. Phy. Chem. B* **2000,** *104*, 10814.

44. DuBois, J. L.; Mukherjee, P.; Stack, T. D. P.; Hedman, B.; Solomon, E. I.; Hodgson, K. O., *J. Am. Chem. Soc.* **2000,** *122*, 5775.
45. Izumi, Y.; Glaser, T.; Rose, K.; McMaster, J.; Basu, P.; Enemark, J. H.; Hedman, B.; Hodgson, K. O.; Solomon, E. I., *J. Am. Chem. Soc.* **1999,** *121*, 10035..
46. Rose, K.; Shadle, S. E.; Eidsness, M. K.; Kurtz, D. M., Jr.; Scott, R. A.; Hedman, B.; Hodgson, K. O.; Solomon, E. I., *J. Am. Chem. Soc.***1998,** *120*, 10743.
47. Williams, K. R.; Hedman, B.; Hodgson, K. O.; Solomon, E. I., *Inorg. Chim. Acta* **1997,** *263*, 315.
48. Gamelin, D. R.; Williams, K. R.; LaCroix, L. B.; Houser, R. P.; Tolman, W. B.; Mulder, T. C.; de Vries, S.; Hedman, B.; Hodgson, K. O.; Solomon, E. I., *J. Am. Chem. Soc.* **1997,** *119*, 613.
49. Szilagyi, R. K.; Lim, B. S.; Glaser, T.; Holm, R. H.; Hedman, B.; Hodgson, K. O.; Solomon, E. I., *J. Am. Chem. Soc.* **2003,** *125*, 9158.
50. Glaser, T.; Hedman, B.; Hodgson, K. O.; Solomon, E. I., *Acc. Chem. Res.* **2000,** *33*, 859.
51. Shadle, S. E.; Hedman, B.; Hodgson, K. O.; Solomon, E. I., *J. Am. Chem. Soc.* **1 995,** *117*, 2259.
52. Neese, F.; Hedman, B.; Hodgson, K. O.; Solomon, E. I., *Inorg. Chem.* **1999,** *38*, 4854.
53. Shadle, S. E.; Hedman, B.; Hodgson, K. O.; Solomon, E. I., *Inorg. Chem.* **1994,** *33*, 4235-44.
54. George, S. D.; Huang, K.-W.; Waymouth, R. M.; Solomon, E. I., *Inorg. Chem.* **2006,** *45*, 4468.
55. Shadle, S. E.; Penner-Hahn, J. E.; Schugar, H. J.; Hedman, B.; Hodgson, K. O.; Solomon, E. I., *J. Am. Chem. Soc.* **1993,** *115*, 767.
56. Boysen, R. B.; Szilagyi, R. K., *Inorg. Chim. Acta* **2008,** *361*, 1047.
57. Srivastava, U. C.; Nigam, H. L., *Coord. Chem. Rev.* **1973,** *9*, 275.
58. Hahn, J. E.; Scott, R. A.; Hodgson, K. O.; Doniach, S.; Desjardins, S. R.; Solomon, E. I., *Chem. Phy. Lett.* **1982,** *88*, 595.
59. Bair, R. A.; Goddard, W. A., III, *Phys. Rev.* **1980,** *22*, 2767.
60. Brouder, C., *J. Physics: Condens. Matter* **1990,** *2*, 701.
61. Wang, H.; Peng, G.; Miller, L. M.; Scheuring, E. M.; George, S. J.; Chance, M. R.; Cramer, S. P., *J. Am. Chem. Soc.* **1997,** *119*, 4921.
62. George, S. J.; Lowery, M. D.; Solomon, E. I.; Cramer, S. P., *J. Am. Chem. Soc.* **1993,** *115*, 2968.
63. Van der Laan, G.; Westra, C.; Haas, C.; Sawatzky, G. A., *Phy. Rev. B: Condens. Matter and Materials Phy.* **1981,** *23*, 4369.
64. Kau, L. S.; Spira-Solomon, D. J.; Penner-Hahn, J. E.; Hodgson, K. O.; Solomon, E. I., *J. Am. Chem. Soc.* **1987,** *109*, 6433.
65. Agarwal, B. K., *X-ray Spectroscopy*. Springer-Verlag: Berlin, 1979.
66. Bailey, B. C.; Basuli, F.; Huffman, J. C.; Mindiola, D. J., *Organometallics* **2006,** *25*, 2725.
67. Whalen, A. M.; Bhattacharya, S.; Pierpont, C. G., *Inorg. Chem.* **1994,** *33*, 347.
68. Speier, G.; Whalen, A. M.; Csihony, J.; Pierpont, C. G., *Inorg. Chem.* **1995,** *34*, 1355.

69. Mederos, A.; Dominguez, S.; Hernandez-Molina, R.; Sanchiz, J.; Brito, F., *Coord. Chem. Rev.* **1999,** *193-195*, 857.
70. Herebian, D.; Ghosh, P.; Chun, H.; Bothe, E.; Weyhermuller, T.; Wieghardt, K., *Eur. J. Inorg. Chem.* **2002,** 1957.
71. Carrasco, R.; Cano, J.; Ottenwaelder, X.; Aukauloo, A.; Journaux, Y.; Ruiz-Garcia, R., *Dalton Trans.* **2005,** 2527.
72. Shimazaki, Y.; Tani, F.; Fukui, K.; Naruta, Y.; Yamauchi, O., *J. Am. Chem. Soc.* **2003,** *125*, 10512.
73. Lovecchio, F. V.; Gore, E. S.; Busch, D. H., *J. Am. Chem. Soc.* **1974,** *96*, 3109.
74. Nipales, N. S.; Westmoreland, T. D., *Inorg. Chem.* **1995,** *34*, 3374.
75. Barigelletti, F.; Juris, A.; Balzani, V.; Belser, P.; Von Zelewsky, A., *Inorg. Chem.* **1983,** *22*, 3335.
76. Wang, H.; Ge, P.; Riordan, C. G.; Brooker, S.; Woomer, C. G.; Collins, T.; Melendres, C. A.; Graudejus, O.; Bartlett, N.; Cramer, S. P., *J. Phy. Chem. B* **1998,** *102*, 8343.
77. Hocking, R. K.; Wasinger, E. C.; De Groot, F. M. F.; Hodgson, K. O.; Hedman, B.; Solomon, E. I., *J. Am. Chem. Soc.* **2006,** *128*, 10442.
78. Hicks, R. G., *Angew. Chem., Int. Ed.* **2008,** *47*, 7393.
79. Buttner, T.; Geier, J.; Frison, G.; Harmer, J.; Calle, C.; Schweiger, A.; Schonberg, H.; Grutzmacher, H., *Science* **2005,** *307*, 235.
80. Mankad, N. P.; Antholine, W. E.; Szilagyi, R. K.; Peters, J. C., *J. Am. Chem. Soc.* **2009,** *131*, 3878.
81. Te Velde, G.; Bickelhaupt, F. M.; Baerends, E. J.; Fonseca Guerra, C.; Van Gisbergen, S. J. A.; Snijders, J. G.; Ziegler, T., *J. Comput. Chem.* **2001,** *22*, 931.
82. Morales-Morales, D.; Jensen, C., *The Chemistry of Pincer Compounds*. 1 st ed.; Elsevier: Oxford, 2007.
83. van der Boom, M. E.; Milstein, D., *Chem. Rev.* **2003,** *103*, 1759.
84. Milstein, D., *Pure Appl. Chem.* **2003,** *75*, 445.
85. Grutzmacher, H., *Angew. Chem., Int. Ed.* **2008,** *47*, 1814..
86. Walstrom, A.; Pink, M.; Tsvetkov, N. P.; Fan, H.; Ingleson, M.; Caulton, K. G., *J. Am. Chem. Soc.* **2005,** *127*, 16780.
87. Koenigsmann, M.; Donati, N.; Stein, D.; Schoenberg, H.; Harmer, J.; Sreekanth, A.; Gruetzmacher, H., *Angew. Chem., Int. Ed.* **2007,** *46* , 3567.
88. Alfassi, Z., *N-centered Radicals*. Wiley: New York, 1998.
89. Jacobsen, C. J. H.; Pedersen, E.; Villadsen, J.; Weihe, H., *Inorg. Chem.* **1993,** *32*, 1216.
90. Becke, A. D., *Phy. Rev. A: Atomic, Molecular, and Optical Physics* **1988,** *38*, 3098.

Chapter 4

Evaluation of the Non-innocence of PNP ligand as a Function of Metal Centers

4.1 Introduction

Redox non-innocent ligands have garnered considerable attention recently because of their unusual redox properties and their apparent ability to stabilize metals in different oxidation states.[1-3] The interest stems from their wide application in biomimetic chemistry[4] as well as potential application to design smart materials. At this point it is important to define the redox non-innocence. Jorgensen was the first who commented about the innocent or non-innocent character of a ligand in 1966. According to him 'ligands are innocent when they allow oxidation states of the central atom to be well defined', a definition which insinuates to the dependence of the non-innocent behavior both on metal as well as ligand.[5] However, the term non-innocence is often misunderstood as a property of the ligand only, taking dithiolenes and dioxolenes as examples. This is not helpful in complexes where the metal-centered and ligand centered frontier orbitals are at different energies such that their redox potentials are widely separated. For example, $[\mathrm{Ru(bpy)_3}]^{2+}$ (bpy = 2,2'-bipyridine) undergoes metal centered oxidation at +1.26 V (with respect to NHE) and a series of unambiguous ligand-centered reductions because of the substantial energy difference between the d(π) HOMO and the ligand π^* LUMO orbitals where the redox processes take place.[6] On the other hand, in case of $[\mathrm{Cr(bpy)_3}]^{3+}$ a series of one electron reductions are observed whose assignment is more difficult due to the close energy of metal and ligand centric redox orbitals.[7] Whereas the first reduction is metal centric to generate $[\mathrm{Cr^{II}(bpy)_3}]^{2+}$, the next reduction yields in transfer of two electrons to the ligand π^* levels to give a species best described as $[\mathrm{Cr^{III}(bpy)(bpy^{\cdot -})_2}]^{+}$. Further reductions are also delocalized in nature. Hence the bpy is redox active in both $[\mathrm{Ru(bpy)_3}]^{2+}$ and $[\mathrm{Cr(bpy)_3}]^{3+}$, but the description of non-innocence applies far more to the later complex than the former. At this point it is conspicuous that redox non-innocence of a particular ligand is dependent on both the ligand redox active orbital and metal frontier orbitals.[8] In the previous Chapter we evaluated that the pincer PNP-ligand behaves as a redox active ligand when complexed with $\mathrm{Ni^{(II)}}$. Now we focus on the hypothesis that the redox innocence of a given pincer-

PNP is a function of the d-manifold energy of the metal. To solidify the argument we extend our study to a series of metal in the first row transition series ranging from $Fe^{(II)}$ all the way to $Zn^{(II)}$, including their one-electron oxidized forms wherever available. The following exploration indeed proves that the property is a function of frontier metal orbital energy.

4.1.1 Prelude to Mössbauer spectroscopy

The energy levels of a nucleus present in an atom are modified by the environment of the nucleus. These changes in the energy levels can provide valuable information about the atom's local environment within a system and ought to be observed using resonance fluorescence. Mössbauer spectroscopy is a technique which enables the energy levels to be investigated by measuring the energy dependence of the resonant absorption of Mössbauer γ-rays by a nucleus.[9] There are, however, two major obstacles in obtaining the information for atom's local environment: the 'hyperfine' interactions between the nucleus and its environment are extremely small, and the recoil of the nucleus when the γ-ray is emitted or absorbed prevents resonance. Usual experimental arrangement for Mössbauer spectroscopy involves a radioactive source containing the Mössbauer isotope in an excited state and an absorber consisting of the material to be investigated which contains the same isotope in its ground state. For example, radioactive ^{57}Co is often used as the source for ^{57}Fe Mössbauer spectroscopy. ^{57}Co undergoes a spontaneous electron capture transition to give a metastable state of ^{57}Fe which in turn decays to the ground state via a γ-ray cascade. In an usual transmission experiment, the γ-rays emitted by the source pass through the absorber, where they may be partially absorbed and then they pass to a suitable detector. In order to investigate the energy levels of the Mössbauer nucleus in the absorber it is necessary to modify the γ-rays emitted by the source so that they can have the correct energy for resonant absorption. Since resonance only occurs when the transition energy of the emitting and absorbing nucleus match exactly, the effect is isotope specific. The relative number of recoil-free events (strength of the signal is dependent on that) is easily detected in isotopes with very low lying excited states. Additionally, the resolution relies on the lifetime of the excited state. These two factors limit the number of isotopes that can be used for Mössbauer spectroscopy. The most used is ^{57}Fe since it meets both criteria: has very low energy γ-ray and possess a ling-lived excited state.

By this way Mössbauer spectroscopy is a very efficient tool to probe the electron distribution around a particular atom and can give considerable information about the bonds involving that atom (covalency). Two major parameters of a Mössbauer spectrum can be related directly to the populations and changes in population of the valence shell orbitals. The isomer shift (δ, measured in mm sec^{-1}) relates to the total electron density on the atom and the quadrupole splitting reflects any asymmetry in the distribution of electron density. The isomer shift δ is directly proportional to the difference in total electron density at the nucleus between the absorber and the standard, (as shown in equation 1)

$$\delta = \alpha\ [|\psi_A(0)|^2 - |\psi_S(0)|^2]$$

where the proportionality constant α depends principally on the relative change in the nuclear radius between the excited state and the ground state $\delta R/R$. For most of the nuclei the excited state has a larger radius, but for few, especially for ^{57}Fe, the reverse is true. Difference in isomer shifts between compounds therefore reflects with varying sensitivity, differences in electron density at the nucleus which in turn should indicate the differences in population of the valence shell orbitals. The isomer shift responds to any factor which can change the number or distribution of valence shell electrons. It therefore reflects changes such as those in the oxidation state, spin state, hybridization and bond polarity. On the other hand a quadrupole splitting Mössbauer spectrum results from a nucleus with an electric quadrupole moment which experiences an electric field gradient (EFG). Figure 1 pictorially describes the origin of these two important parameters for Mössbauer spectrum. A quadrupole moment exists when the nucleus has spin greater than one-half. All Mössbauer nuclei possess a quadrupole moment in either the ground state or excited state, or both and are liable to exhibit quadrupole splitting. From the structural point of view quadrupole splitting of the signal provides more critical information.

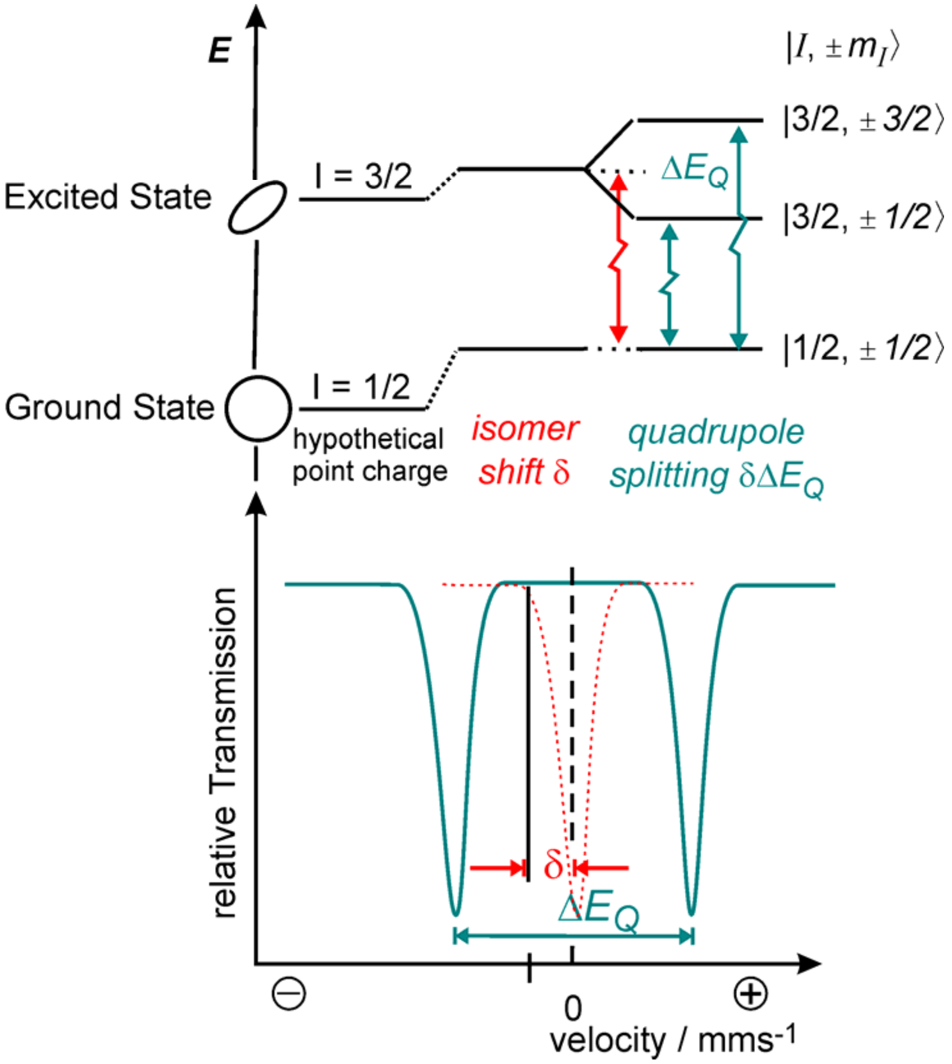

Figure 1: Quadrupole splitting of the ^{57}Fe excited state and shift of the nuclear states by the electric monopole interaction that gives rise to the isomer shift. In a typical Mössbauer spectrum, the absorption lines have Lorentzian shapes in the absence of heterogenities or relaxation effects. The velocity scale is drawn relative to the centroid of Fe metal. The dotted black line represents the isomer shift which is the central point of the spectrum.

After collecting the spectrum a computer fitting program is then used to simulate it. The computer fitting usually provides a width of the absorption peak, which should be close to a theoretically acceptable value to be considered as a good spectrum. If one or more peaks show a value appreciably greater than expected, it is likely that additional signals are present, and a new trial fitting should be made which includes a second subspectrum.

4.2 Results and Discussion

4.2.1 Synthesis of (PNP)FeCl(OTf), 2-OTf and (PNP)FeCl$_2$, 2-Cl

In chapter 3, we reported the single electron oxidation of (PNP)NiCl, (PNP$^-$ = N[2-P(CHMe$_2$)$_2$-4-MeC$_6$H$_3$) takes place mostly in the ligand backbone and affects the metal center very minimally.[10] To investigate whether the site of oxidation changes with differing metals, we focused to study the oxidation behavior of the 3d transition metal complexes from Fe to Zn. Our series begins with PNP complexes of Fe$^{(II)}$ and its one-electron oxidation. (PNP)FeCl, **1** was synthesized by treating FeCl$_2$(THF) with (PNP)Li in toluene solution and stirring the reaction mixture for 12 hours.[11] Removal of the byproduct LiCl, extraction of the product **1** from toluene solution and subsequent crystallization at −35 °C resulted isolation of bright red colored crystals in 89% yield. Previous work in the group reported the oxidation potential of **1** to be −0.56 V.[11] This value clearly conveys that even a weak oxidant may be efficiently oxidize **1**. Accordingly we used a mild oxidant, Fc(OTf), which upon addition to a THF solution of **1**, the color rapidly changes from red to purple. After completion of the reaction (45 minutes), removal of byproduct ferrocene by washing the mixture with copious amounts of pentane offers a paramagnetic product in 87% yield which we speculate to be (PNP)FeClOTf, **2-OTf** (Scheme 1). Several attempts to grow a single crystal of diffraction quality were frustrated by failure, inhibiting our conclusion about the metal center geometry in the complex as well as site of oxidation.

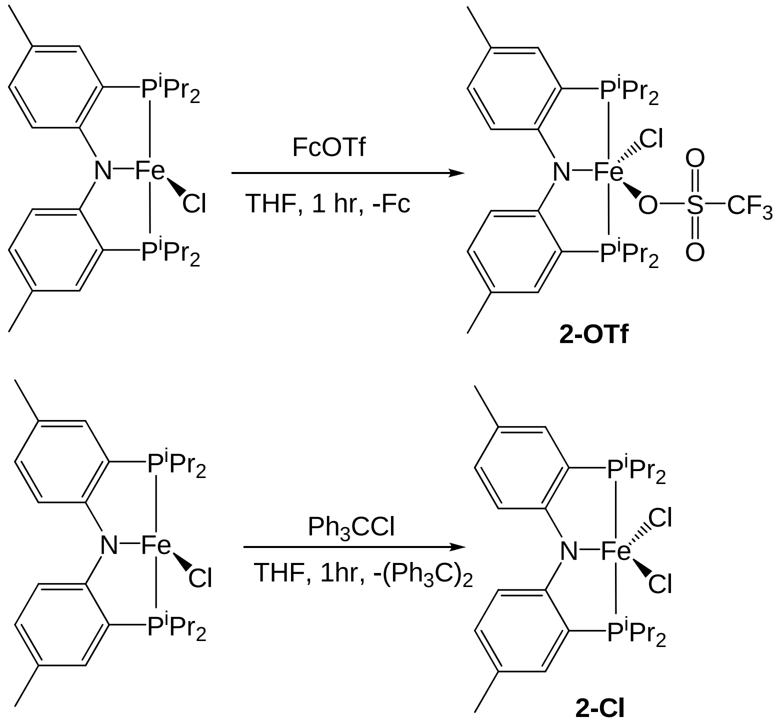

Scheme 1: Oxidation of **1** with different oxidants result in five coordinate iron complexes.

In order to address the metal center geometry and the oxidation state of iron in **2-OTf** we relied to several spectroscopic techniques (*vide infra*). The oxidized product **2-OTf** is paramagnetic and shows resonances in ^{1}H NMR spectrum over a wide range (δ 100 to −60). Solution magnetic moment measured by Evans method provides a value 4.3(2) μ_B that is consistent with three unpaired electrons being present in the oxidized complex. To ascertain the solid state magnetic moment behavior of **2-OTf**, we performed solid state magnetic moment measurement (SQuID) which shows a magnetic moment 4.0 μ_B to 3.8 μ_B over a wide range of temperature (300−25 K), clearly consistent with three unpaired electron (Figure 2). The solid state magnetic moment derives the conclusion that the spin state of complex **2-OTf** remains same both in the solid and the solution state.

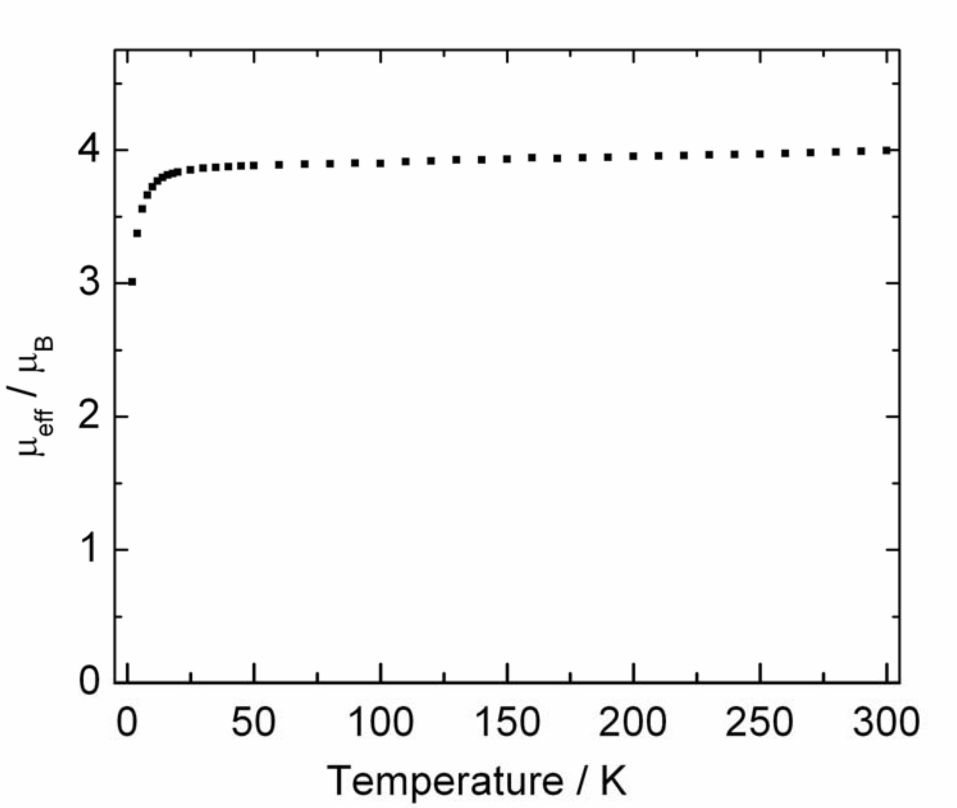

Figure 2: Plot of μ_{eff} as a function of temperature shown for **2-OTf** in the temperature interval 2−300 K.

To evaluate whether the site of oxidation in **1** is influenced by the binding nature of anion, we performed the oxidation with a different oxidant. Accordingly, oxidation was performed with trityl chloride, (reduction potential of Ph_3CCl is −0.11 V in MeCN)[12] and an immediate color change from red to blackish violet ensues upon addition of the oxidant to the THF solution of **1**. After 1.5 hours, the reaction mixture was dried *in vacuo* and the byproduct Gomberg's dimer was washed several times with copious amount of pentane. The violet colored paramagnetic product (PNP)$FeCl_2$, **2-Cl** was isolated in 81% yield with spectroscopic purity. To ascertain the coordination number around the iron center and the geometry of the metal center in the complex we analyzed a single crystal of **2-Cl** by X-ray diffraction analysis (Figure 3). The crystal structure clearly exposes a five coordinate iron center connected to two chloride ligands. From the crystal structure it is obvious to infer that the oxidation has been taken place on the metal center increasing the oxidation state of iron from +II in **1** to +III in **2-Cl**. Mössbauer spectroscopic analysis along with XAS experiments will be fully consistent with the +III oxidation state assignment of the iron center in **2-Cl** (*vide infra*).

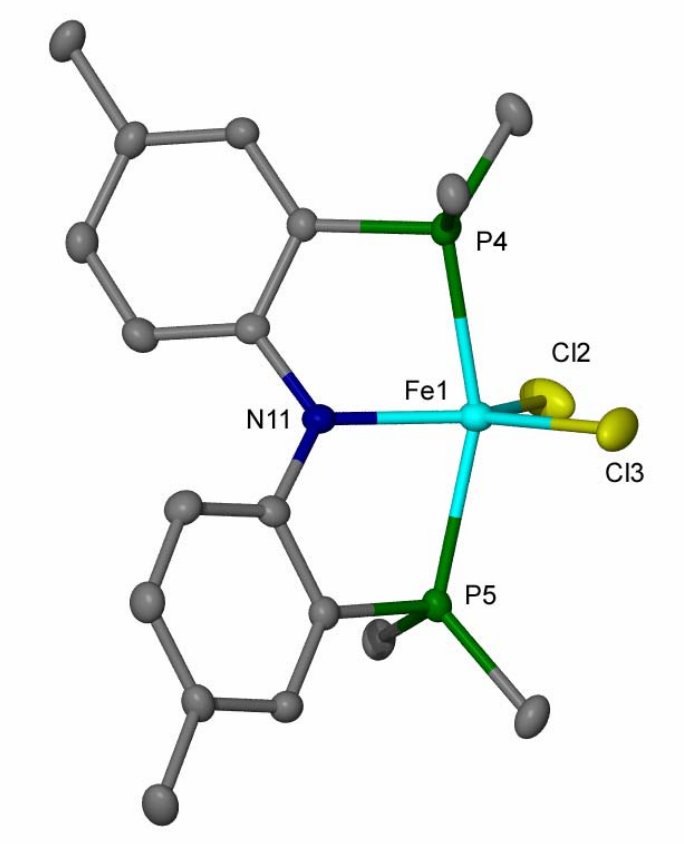

Figure 3: Single crystal X-ray structure of complex **2-Cl** depicting thermal ellipsoids at the 50% probability level. Hydrogen atoms, THF solvent and methyls of the isopropyl groups have been omitted for clarity. Selected bond lengths (Å) and angles (degrees): Fe1-Cl2, 2.2679(6); Fe1-Cl3, 2.2679(6); Fe1-P4, 2.3797(4); Fe1-P5, 2.3797(4); Fe1-N11, 1.972(2); Cl2-Fe1-Cl3, 108.13(4); N11-Fe1-Cl2, 125.935(19); N11-Fe1-Cl3, 125.935(19); N11-Fe1-P4, 79.393(14); N11-Fe1-P5, 79.393(14); P4-Fe1-Cl2, 99.449(18); P4-Fe1-Cl3, 99.449(18).

A close scrutiny of the crystal structure of **2-Cl** describes the geometry around the iron center to be in between square pyramidal and trigonal bipyramidal. Most mononuclear five coordinate structures of $Fe^{(II)}$ adopt similar intermediate geometry depending on the steric and electronic demand around the metal center. We obtained a distortion index (τ) of 0.55 for **2-Cl**. The distortion index is defined by $\tau = (\alpha-\beta)/60$, where β and α are the larger and smaller angle in the basal plane of the square pyramid.[13] Generally, for the square pyramidal structure the metal center is slightly shifted from the basal plane towards the apical ligand. In **2-Cl**, the $Fe^{(III)}$ center is 0.590 Å shifted upwards from the imaginary mean plane composed by the atoms N11, P4, P5, and Cl2, where the mean deviation of the atoms from the plane is 0.355 Å. Both the five membered rings composed of N, Fe, P and two carbons of the corresponding aromatic rings are almost planar (mean deviation of the atoms from the plane is 0.189 Å), and they produce an angle of 28.2 ^{o} between them. Complex **2-Cl** is a very similar structure to the earlier reported example, (PNP'-^{i}pr)$FeCl_2$ where (PNP = 2,6-diaminopyridine) by Kirchner *et al.*[14] In this reported example oxidation state of the iron is +II and the environment around the iron center is perfectly square pyramidal (τ = 0, not reported in the article). Bond lengths in the near vicinity of $Fe^{(II)}$ is clearly elongated compared to the analogous bond lengths in **2-Cl**, as the reported bond lengths are: Fe−N, 2.250(2); Fe−Cl, 2.3708(7) and 2.3040(6); Fe−P, 2.4631(7) and 2.4844(7) respectively. Similar complexes of five coordinate iron adopting square pyramidal geometry are profuse in the literature and sometimes play significant roles as precatalysts for ethylene polymerization, atom transfer radical polymerization, catalytic formation of 3-hydroacrylates from aromatic aldehydes and ethyldiazoacetate.[15-17] In the context of reactivity, square pyramidal complexes should be more reactive compared to their trigonal bipyramidal analogues since the former complexes offer more vacant site. It is safe to speculate at this point the observed catalytic reactivity of the reported complexes stem from their preferable square pyramidal environment around $Fe^{(II)}$ metal center. Solution state magnetic moment for **2-Cl**, measured by Evans method provides a value of 3.3 μ_B which is lower than the expected 3 electron moment. The problem stems from the limited solubility of the complex in $CDCl_3$ which was chosen as a solvent for measurement. Our choice of solvents to solubilize **2-Cl** is very scant. However, within the limit of error, the value hints towards 3 unpaired electrons being present in the system. Gratifyingly, solid state magnetic moment by SQuID magnetometry supports the equal number of unpaired electron. The magnetization of crystalline **2-Cl** was collected in the temperature of 2−300

K at a field of 1 Tesla. Interestingly, the diagram displays a spin transition in the temperature region 80−120 K (Figure 4).

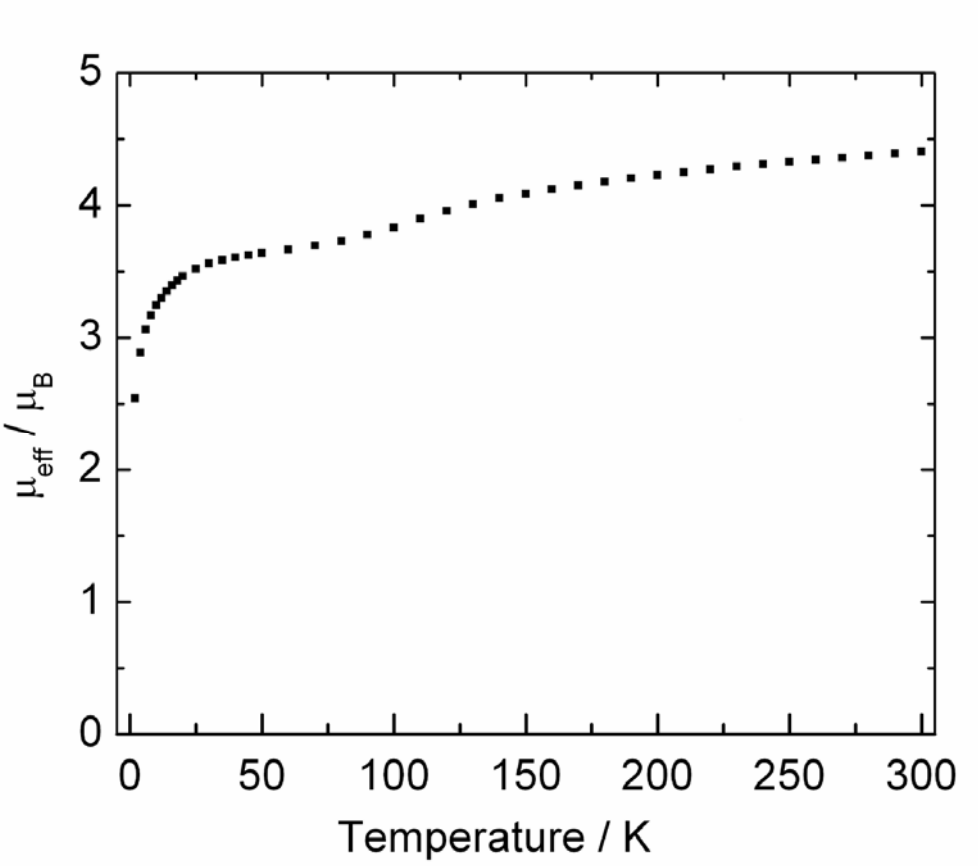

Figure 4: plot of μ_{eff} as a function of temperature shown for **2-Cl** in the temperature interval 2−300 K.

At this point we are uncertain about the reason behind this change in 80−120 K region, but we surmise some temperature dependent geometrical change could be operating behind this spin transition. However the lower temperature region of the diagram depicts clearly the magnetic moment amenable to 3 unpaired electrons being consistent with our prediction from the solution state magnetic moment measurement. We will be verifying shortly by our Mössbauer experiments that two different spin isomers exist at two different (low, 77 K and high, 298 K) temperatures (*vide infra*). Our current focus is to investigate the phenomenon by variable temperature X-ray crystallography.

4.2.2 Synthesis of (PNP)CoCl(OTf), 4-OTf and (PNP)CoCl(BF_4), 4-BF_4 from (PNP)CoCl, 3

After successfully studying the oxidation behavior of **1** we moved to the next close congener of iron. Synthesis of (PNP)CoCl, **3** has been reported earlier by our group.[18] Our initial attempt to oxidize **3** involved AgOTf as the oxidant since the byproduct (metallic Ag^o) separation from the reaction mixture is very convenient. Addition of solid AgOTf to the THF solution of **3** immediately changed the color of the reaction mixture from blue to red. After 45 minutes, the reaction mixture was filtered to get rid of the metallic silver and concentrated THF solution was cooled to −35 °C to obtain a red paramagnetic solid, (PNP)CoClOTf, **4-OTf** in 80% yield (Scheme 2).

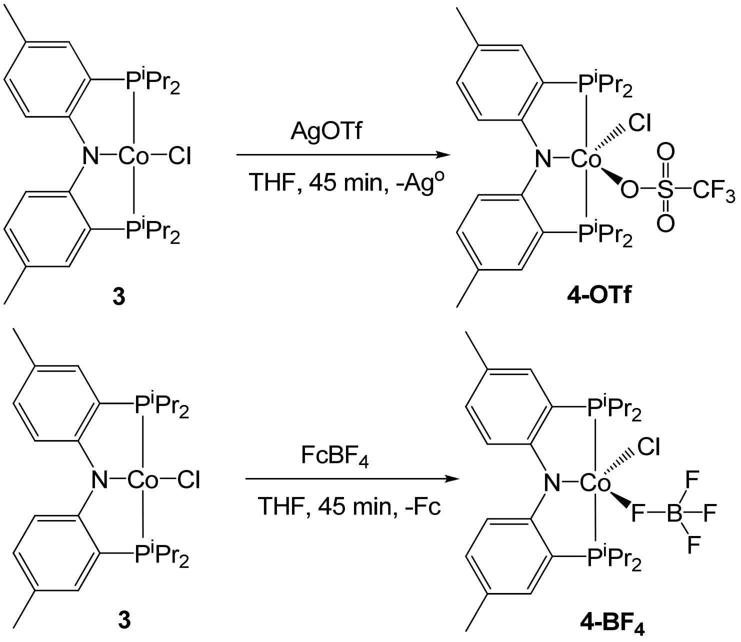

Scheme 2: Oxidation of **3** using different oxidants resulting 5-coordinate cobalt complexes.

To unravel the oxidation state of cobalt in **4-OTf**, we performed single crystal X-ray diffraction analysis. Expectedly, the crystal structure of **4-OTf** displays a five coordinate cobalt center present in a distorted square pyramidal environment as portrayed in Figure 5.

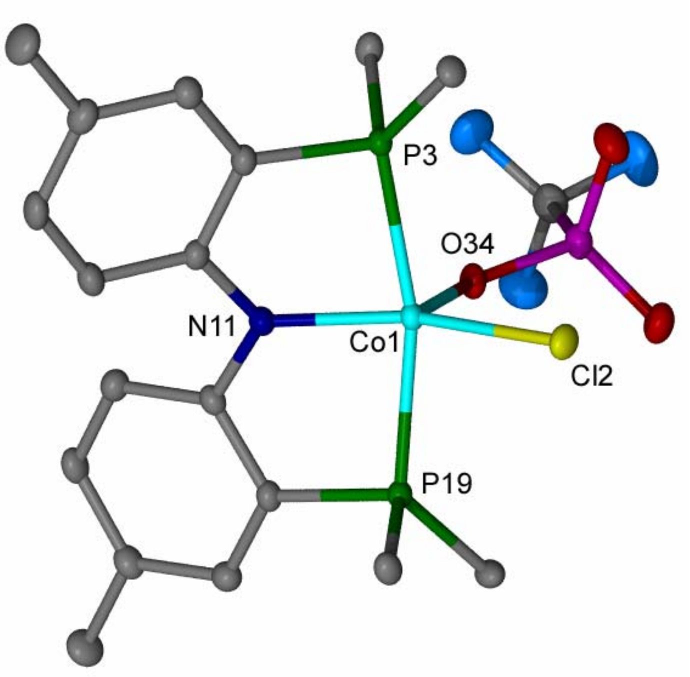

Figure 5: Single crystal X-ray structure of complex **4-OTf** depicting thermal ellipsoids at the 50% probability level. Hydrogen atoms, THF solvent and methyls of the isopropyl groups have been omitted for clarity. Selected bond lengths (Å) and angles (degrees): Co1-Cl2, 2.2255(5); Co1-N11, 1.8755(15); Co1-P3, 2.2601(5); Co1-P19, 2.2819(5); Co1-O34, 2.1286(13); N11-Co1-P3, 83.55(4); N11-Co1-P19, 82.98(4), P19-Co1-Cl2, 98.985(18); P3-Co1-Cl2, 90.208(18); Cl2-Co1-O34, 101.19(4); N11-Co1-O34, 106.34(6), N11-Co1-Cl2, 152.12(5).

The change in coordination number from 4 to 5 during the course of oxidation will change the ligand field splitting pattern dictating magnetic behavior of the complex. A solution state magnetic moment measurement by Evans method reveals a value of 2.97 μ_B clearly indicating two unpaired electrons to be present in the molecule. Intuitively, this magnetic moment is very reasonable with the electronic arrangement of a Co$^{(III)}$, d^6 metal center in a distorted square pyramidal environment. The distortion index in complex **4-OTf** was obtained to be τ = 0.22. Further inspection discloses the cobalt center to be slightly shifted towards the apical triflate group by 0.334 Å from the mean plane consisting of atoms N11, P3, P19, and Cl2. The five membered rings composed of the N, P, Co, and two corresponding carbons are very close to planar (deviation of planarity is only 0.167 Å and 0.145 Å, respectively), and the planes are slightly skewed to each other by an angle of 26.3°. Perhaps this skewing between two five membered chelate rings might translate into the distortion from ideal square pyramidal structure. Examples of five coordinate cobalt centers in a similar geometrical arrangement abound in literature.[19-23] A very close analogues could be the cobalt complexes supported by terpyridine (Tpy) ligands reported by Yasuda and co-workers.[24] In their investigation for cobalt promoted polymerization of norbornene they observed that the $Co^{(II)}$ complexes supported by unsubstituted Tpy ligands adopt a nearly perfect square pyramidal geometry.[24] Interestingly the geometry switches to the distorted trigonal bipyramidal as a function of imposing steric hindrance at the 6,6' positions of the Tpy-ligand. Such an observation was documented when installing two methyl groups at the 6,6' positions of the Tpy ligand converted the geometry of the $Co^{(II)}$ complex to distorted trigonal bipyramdal with τ = 0.516 (calculated). Theopold and coworkers have reported a distorted trigonal bipyramidal $Co^{(III)}$ structure supported by a trispyrazolylborate ligand.[25] Very recently, Caulton and coworkers speculated the presence of a five coordinate $Co^{(III)}$ dihydride, $(PNP)CoH_2$ ($PNP^- = N[^tBu_2PCH_2SiMe_2]$) in a trigonal bipyramidal geometry by DFT calculation.[26] Apparently, from the structure it is easier to infer that the oxidation of **3** has been taken place predominantly on the metal and the current oxidation state of cobalt in **4-OTf** should be assigned as +III. As we will see later other spectroscopic experiments also verify the same metal oxidation state in **4-OTf** as proposed from the crystallographic analysis. To prove the hypothesis, whether coordinating or weakly coordinating anion has any influence on determining the site of oxidation we chose a relatively weakly coordinating anion such as BF_4^-. Consequently, the oxidation of **3** was performed with $FcBF_4$, by the addition of a THF solution of the oxidant to the cold THF solution of **3**, which immediately changed the reaction color from blue to red. After stirring the reaction mixture for 45 minutes, it was dried and the byproduct ferrocene was washed with copious amount of pentane. The solid mass was redissolved in CH_2Cl_2 and layer with pentane at −35 ^oC to isolate a paramagnetic solid, (PNP)CoClBF_4, **4-BF$_4$** in 94% yield as a red colored material. Solid state structure was determined to know whether the anion BF_4^- anion coordinates to the metal center consecutively playing any role in determining the site of oxidation. The solid state structure clearly exposes the cobalt center as five coordinate as the BF_4^- anion binds the metal site through a fluorine atom. The solid structure discloses grossly the same structural features present in the molecule **4-OTf**. Hence the geometrical structure of the molecule barely changes by changing the anion from OTf^- to BF_4^-. As depicted in Figure 6, the cobalt center in the structure is entrapped in a square pyramidal geometry analogous to that in **4-BF$_4$**.

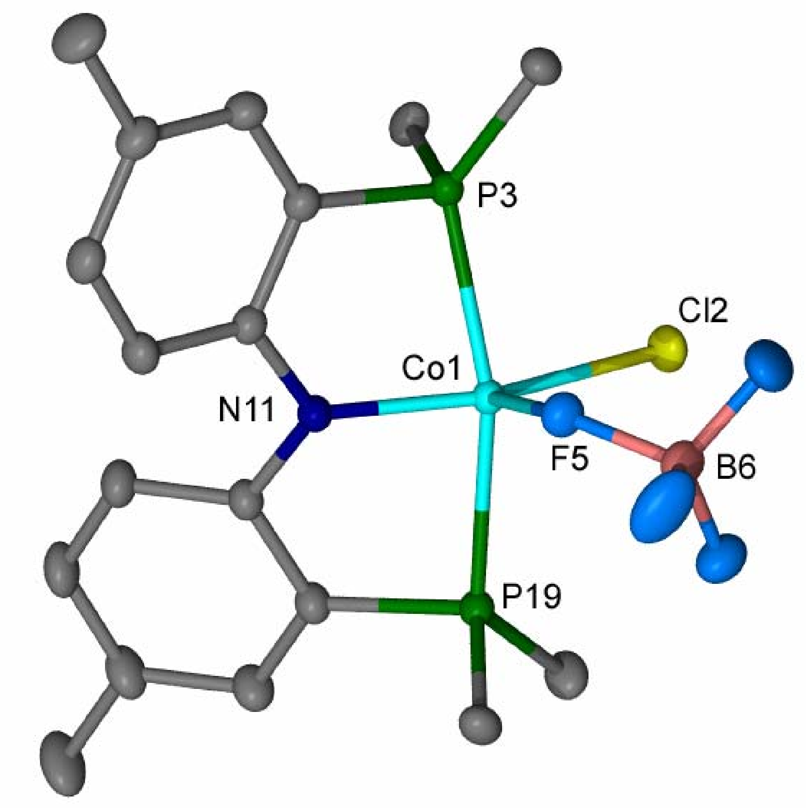

Figure 6: Single crystal X-ray structure of complex **4-BF$_4$** depicting thermal ellipsoids at the 50% probability level. All hydrogen atoms and methyls of the isopropyl groups have been omitted for clarity. Selected bond lengths (Å) and angles (degrees): Co1-Cl2, 2.2168(4); Co1-N11, 1.8678(10); Co1-P3, 2.254(3), Co1-P19, 2.2997(3); Co1-F5, 2.1329(7); F5-B6, 1.4498(15); N11-Co1-P3, 83.36(3); N11-Co1-P19, 93.97(2); N11-Co1-F5, 102.27(4); N11-Co1-Cl2, 159.01(3); F5-Co1-Cl2, 97.82(2).

The structure of **4-BF$_4$** has an extremely small distortion $\tau = 0.078$ from the ideal square pyramidal geometry. The Co−P distances in **4-BF$_4$** are 2.254(3) and 2.2997(3) Å respectively which are comparable with Co−P bond lengths observed in **4-OTf**. Similarly, the Co−N bond length of 1.8678(10) is also very close to what has been observed for **4-OTf** thus further substantiating that the cobalt retains same oxidation state

(+III) in both these. Quite expectedly, the magnetic moment of the complex **4-BF$_4$** in its solution state (μ_{eff} = 2.99 μ_{B}) is consistent with two unpaired electrons as observed in complex **4-OTf**. From X-ray diffraction and solution state magnetic moment measurement experiments it is quite justified to infer the oxidation to be metal centric. Other spectroscopic investigations also insinuates towards a predominantly metal based redox in **3**, completely corroborating this conclusion (*vide infra*).

4.2.3 Synthesis of (PNP)ZnCl, 5 and the oxidation of 5

So far it has been proved that depending on the metal-ligand covalency, the redox active site of a particular complex can be significantly changed. To prove this postulation it was interesting to see what transpires when oxidation of a metal complex is performed, where the metal in question is redox inactive, such as in the case of Zn$^{(II)}$. To test this hypothesis, (PNP)ZnCl, **5**, was synthesized from (PNP)Li and $ZnCl_2$. The yellow colored complex **5** was isolated in moderate yield (66%) from a toluene solution. Zn$^{(II)}$, being a d^{10} element does not have any electronic preference and inclined to adopt tetrahedral geometry due to sp^3 type hybridization.[27] Single crystals were obtained from toluene solution of **5** and structurally analyzed to determine the geometry of the zinc center in the molecule. Figure 7 clearly portrays the molecule to be tetrahedral.

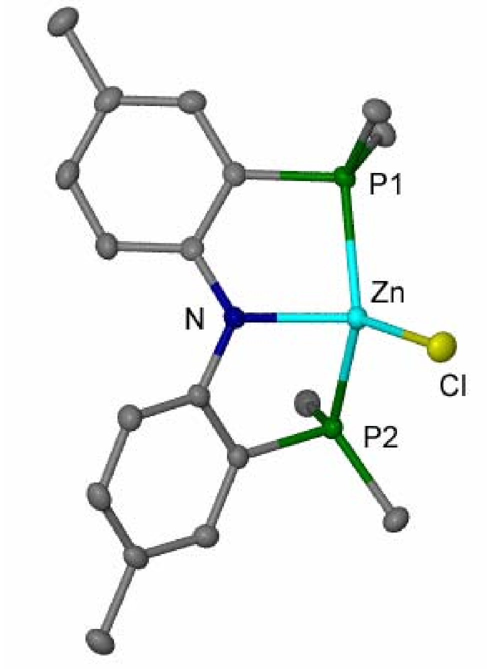

Figure 7: Single crystal X-ray structure of complex **5** depicting thermal ellipsoids at the 50% probability level. All hydrogen atoms and methyls of the isopropyl groups have been omitted for clarity. Selected bond lengths (Å) and angles (degrees): Zn-Cl, 2.2334(5); Zn-N, 2.0179(13); P1-Zn, 2.3514(5); P2-Zn, 2.3826(5); P1-Zn-Cl, 113.518(4); P2-Zn-Cl, 114.631(17); N1-Zn-Cl, 124.81(4); N1-Zn-P1, 85.49(4); N1-Zn-P2, 82.57(4).

It was found that the oxidation of **5** is not very clean and the process undergoes a series of color changes once solid FcOTf is added to the THF solution of **5**. The presence and dissipation of several colors during the course of reaction hint towards a complicated redox process being operational. After completion of the reaction in 2 hours the byproduct ferrocene was removed. One major component of the oxidized product was crystallized from CH_2Cl_2/pentane mixture and the isolated complex was diamagnetic in nature. The identity of the complex was further unveiled by X-ray crystallography analysis. As anticipated from a ligand based oxidation, we observed a significant rearrangement in the geometry of the formal PNP ligand (Scheme 3). Zn$^{(II)}$ being a redox inactive element it is quite expected that the oxidation should take place in the ligand scaffold, and the final structure of the isolated product in (PNHP')ZnCl$_2$(OTf), **6** (PNHP' = NH[2,2'-P^{i}pr$_2$-4,4'-dimethyl-6-P^{i}pr$_2$]) shows how the structure can be modified when the radical generated during the redox procedure is not stabilized. The structure of the final product is presented in Figure 8.

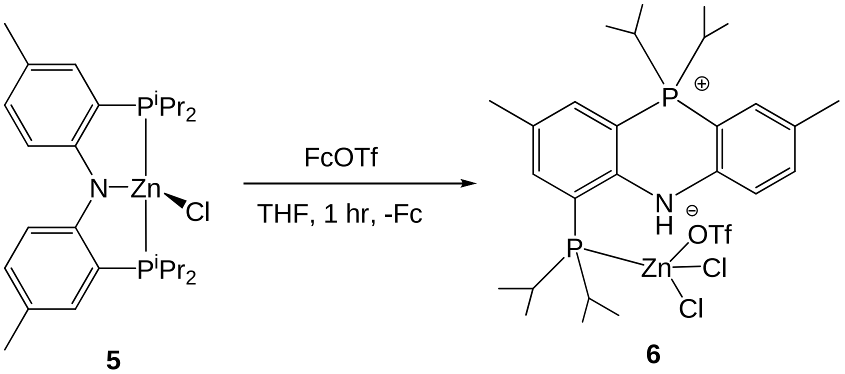

Scheme 3: Oxidation of **5** results in the oxidation of the pincer backbone with significant ligand rearrangement.

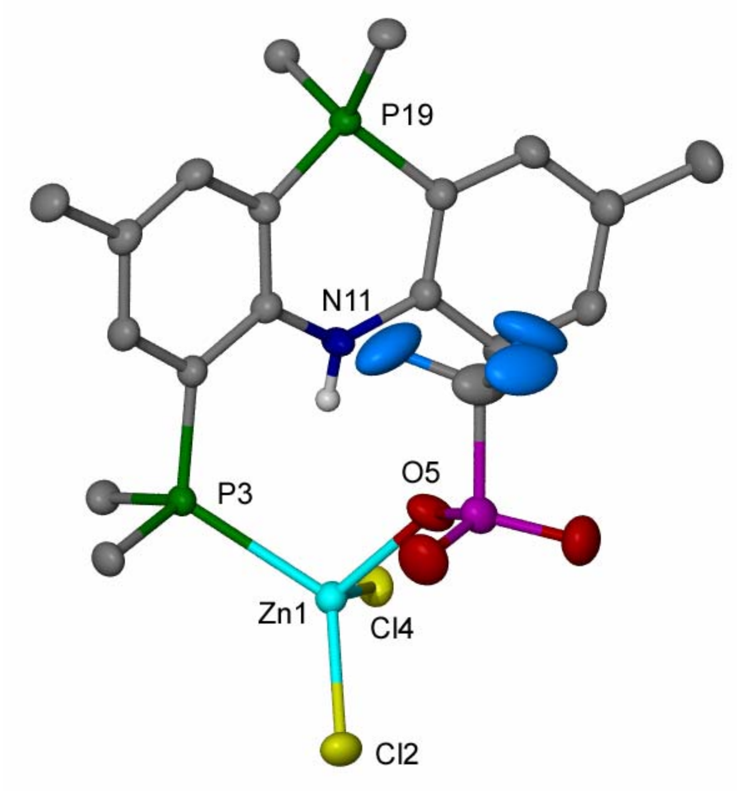

Figure 8: Single crystal X-ray structure of complex **6** depicting thermal ellipsoids at the 50% probability level. All hydrogen atoms and methyls of the isopropyl groups have been omitted for clarity. Selected bond lengths (Å) and angles (degrees): Zn1-Cl2, 2.2176(7); Zn1-Cl4, 2.2435(6); Zn1-P3, 2.4330(6); N11-H, 0.880; Zn1-O5, 2.0388(19); P3-Zn1-O5, 101.80(6), P3-Zn1-Cl4, 105.15(2); P3-Zn1-Cl2, 121.78(3); Cl2-Zn1-Cl4, 113.52(3); C15-P19-C7, 103.68(10).

As evident from Figure 8, it is imperative to tell that one of the phosphine substituents on the aryl ring of the formal PNP has been quaternarized. The oxidation product might be a mixture of intractable materials we have thus far been unable to recognize. The quatenerization of phosphorus may derive from the unstable radical in the ligand backbone which is very reactive to oxidize the phosphine moiety after the aryl ring flips. The original reason for the lack of radical stabilization is due to the metal's inefficiency to form enough covalent bonds with the ligand orbitals. The outcome of this phenomenon is also very evident from the protonated NH-group in the aryl amido fragment. Possibly, the proton migrates from the aryl ring, particularly from the carbon where oxidation of the phosphine has been taken place. Not surprisingly, the $Zn^{(II)}$ metal center in the resulting complex is unaffected by the oxidation and displays four coordinated ligands around it. Zinc prefers to higher coordination number which may rationalize the triflate anion binding to generate a zwitterionic species, despite retaining the zinc oxidation state to +II. Unlike the solid state, OTf^- remains non-coordinated in the solution state as evident from the appearance of ^{19}F NMR resonance at −78 ppm. Further scrutiny shows that Zn−Cl bond lengths (2.2176(7) and 2.2435(6) Å are slightly shorter than the bonds reported by Cotton *et al.* in prototypical $(PMe_3)_2ZnCl_2$ (2.2501(14) and 2.2797(12) Å respectively).[28] The angles Cl2-Zn1-Cl4 (113.52(3)°) and P3-Zn1-Cl2 (121.78(3)°) in **6** are considerably longer than the other two angles, P3-Zn1-Cl4 (105.15(2)°) and P3-Zn1-O5 (101.80(6)°) leading to a distortion along the C_2-axis of the tetrahedron. The distance between N1•••Zn1 is 3.55 Å, which clearly refutes any possibility of σ-donation from nitrogen to zinc. The amido hydrogen was refined and located in crystallographic Fourier map corroborating its presence in proton NMR spectrum at 8.30 ppm as a broad resonance. The presence of the second chloride coordinated to the metal appears most likely from another molecule of **5**, thus implying that this species is not the only species being generated and the process to degradation is intermolecular in nature. It was interesting to probe the origin of amine hydrogen which can be easily traced by executing isotopic labeling studies. The reaction performed in d_8-

THF gave the product with no deuterium incorporation, suggesting the solvent not be the source of the proton. Hence it is very likely that the proton of the amide group stems from ligand degradation and not H atom abstraction from solvent media.

4.2.4 Reduction of $Cu^{(II)}$ by the PNP ligand backbone

As part of the study of the redox non-innocence of PNP over a 3d transition metal center we investigated the behavior of the ligand system with copper. For this purpose synthesis of (PNP)CuCl was attempted. When a cold yellow THF solution of (PNP)Li was added to a brown suspension of $CuCl_2$ the color of the solution mixture was immediately turned to reddish and reddish brown within another few minutes of allowing the mixture to stir. Although the reaction was not very clean, we were able to isolate diamagnetic (PNHP)CuCl, **7** as the major product along with other unidentified impurities. Encouragingly, product **7** can be purified by crystallization from concentrated toluene solution at a temperature of -35 ^{o}C. Protonation of the amido nitrogen is very evident from the emergence of the corresponding broad resonance in ^{1}H NMR spectrum at 10.23 ppm. To understand whether solvent THF became the source of the proton we performed the reaction in d_8-THF. Isolation of the product shows no deuterium incorporation in the arylamido nitrogen, discarding the possibility of solvent being the source of hydrogen atom, analogously to that found for the oxidation of **5**. Most likely, ligand degradation results in protonation of the arylamido nitrogen. The observed rapid color changes during the course of the reaction might be indicative of the degradation of the ligand.

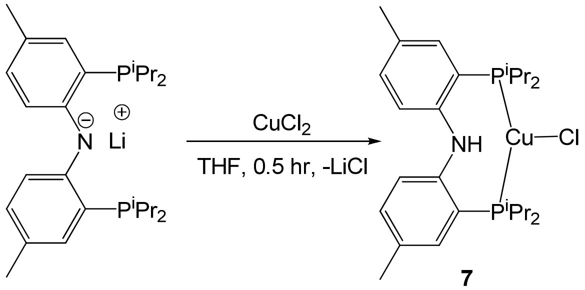

Scheme 4: Spontaneous reduction of Cu$^{(II)}$ to Cu$^{(I)}$ when transmetallation of $CuCl_2$ is attempted with (PNP)Li.

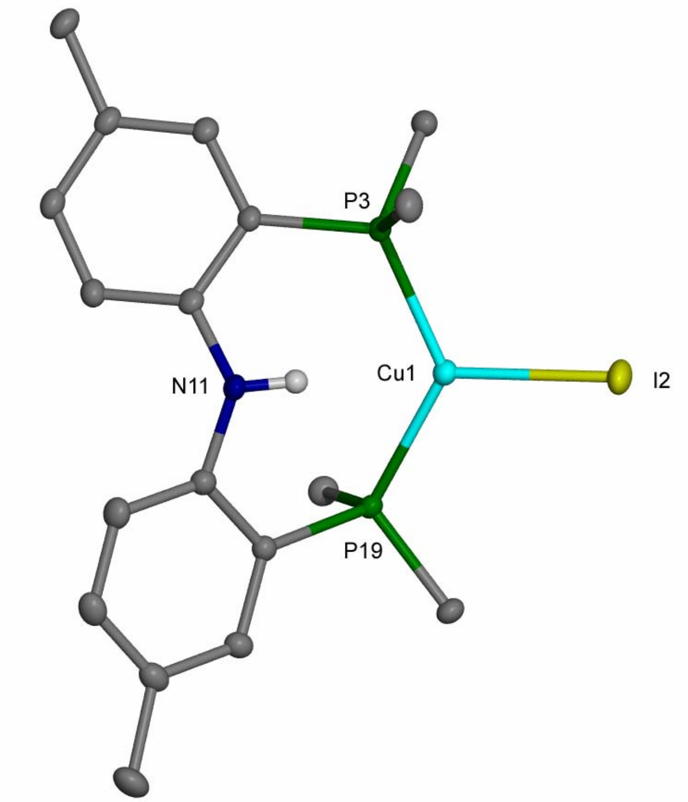

Figure 9: Single crystal X-ray structure of complex **7** depicting thermal ellipsoids at the 50% probability level. All hydrogen atoms and methyls of the isopropyl groups have been omitted for clarity. Selected bond lengths (Å) and angles (degrees): Cu1-I2, 2.5314(3); Cu1-P3, 2.2900(4); Cu1-P19, 2.2976(4), N11-Cu1, 3.094; N11-H, 0.860; P3-Cu1-P19, 129.353 (16); P19-Cu1-I2, 109.571(12); P3-Cu1-I2, 120.371(12).

Such a reduction of the Cu$^{(II)}$ center to Cu$^{(I)}$ is not uncommon when the ligand backbone possesses multiple reducing centers such as phosphine and an amide. Reduction leading to degradation and formation of ill-defined products were documented by Peters and coworkers when Cu$^{(II)}$ sources such as $CuCl_2.0.8THF$, anhydrous $Cu(OAc)_2$, $Cu(OTf)_2$ were treated with bis(phosphino)borate ligand.[29] Our inability to grow a suitable crystal for the X-ray diffraction analysis prompted us to grow a similar crystal possessing another halide. Gratifyingly, we succeeded in obtaining a single crystal of (PNHP)CuI, **7-I** by transmetallation of CuI with (PNP)Li. The salient features from the crystal structure (Figure 9, *vide supra*) involves a trigonal planar Cu$^{(I)}$ center. The observed Cu−I bond length is significantly longer than the Cu−Cl bond length (2.5314(3)Å vs. 2.2183(12) Å) in the close analogue reported by Peters, $[(3,5\text{-}Me_2Ph)B(CH_2P^tBu_2)_2]CuCl$. The Cu−P bond lengths in **7-I** are 2.2976(4) and 2.2900(4) Å respectively, which are slightly elongated compared to the values reported by them, 2.2433(11) and 2.2481(12) Å. This hints to the more back-donation present in Peters' complex compared to ours.[29] Cu$^{(I)}$ is minimally deviated by 0.114 Å from the mean imaginary plane drawn by the atoms P3, P19, and I2. This fact is also corroborated by the sum of angle around the copper center which is 359.30^{o}. Cu$^{(I)}$ examples are abundant in literature and have widespread use in diverse fields such as catalytic hydrocarbon functionalization,[30, 31] catalytic oxidation reactions[32-35] and biomimetic dioxygen activation.[35-37] XAS spectroscopic analysis unequivocally affirms the oxidation state of copper in **7-I** as Cu$^{(I)}$ (*vide infra*). In conclusion, the attempt towards complexation of Cu$^{(II)}$ to PNP leads to the reduction of the metal center to Cu$^{(I)}$.

4.3 Mössbauer spectroscopic studies of complexes 1, 2-OTf and 2-Cl

As discussed in our introduction, Mössbauer is a suitable method to explain changes in oxidation states and the degree of covalency in a complex as the isomer shift (δ) in conjunction with quadrupole splitting (ΔE_Q) can provide definitive evidences. The zero-field Mössbauer spectrum recorded for **1**, at 77 K produced an isomer shift of 0.72 mm sec^{-1} and a quadrupolar splitting of 1.59 mm sec^{-1}, consistent with high spin Fe$^{(II)}$ ion (Figure 9).[9] The isomer shift is typical for four coordinate ferrous ions and resembles that of a pseudo-tetrahedral Fe$^{(II)}$-S_4 sites in iron-sulfur clusters (δ = 0.72 mm sec^{-1}).[38] A similar experiment performed at 77 K on a sample of **2-OTf** produced an isomer shift value, 0.46 mm sec^{-1}and quadrupole splitting, 1.98 mm sec^{-1} (Figure 10). The significant shift in δ-value invokes an increase in oxidation state of the metal in question. As a consequence of oxidation, one d-electron is lost from Fe$^{(II)}$ which increases the s electron density around the iron nucleus and the δ-value shifts negatively due to δR/R being negative for ^{57}Fe nucleus. These values are also consistent to an intermediate spin ferric center in complex **2-OTf**. The quadrupole splitting is influenced by the departure from cubic symmetry around the nuclei. After obtaining a definitive clue about the metal-centric oxidation of iron in **2-OTf**, we attempted to justify it for the other oxidized complex, **2-Cl**, since we had obtained structural information of the latter. Gratifyingly, the isomer shift observed for the complex appears identical (δ = 0.46 mm sec^{-1}) to the value found in **2-OTf** with slight shifting in quadrupole splitting value (ΔE_Q = 1.56 mm sec^{-1}) (Figure 12, top). This values conclusively proves the metal-centric oxidation is also occurring in case of **2-Cl**. The deviation of ΔE_Q value possibly stems from the different electric field gradient created around the iron center in **2-Cl** due to the changed ligand environment from **2-OTf**. All the Mössbauer parameters are summarized for **1**, **2-OTf**, **2-Cl** for direct comparison in Table 1.

Table 1: Tabulation of the Mössbauer parameters of iron containing complexes

Complex	δ / mm s^{-1}	ΔE_Q / mm s^{-1}	Γ_{FWHM} / mm s^{-1}
1	0.72(1)	1.59(1)	0.28(1)
2-OTf	0.46(1)	1.98(1)	0.44(1)
2-Cl	0.47(1)	1.57(1)	0.40(3)
2-Cl (at 298 K)	0.36(1)	0.53(1)	0.26(1)

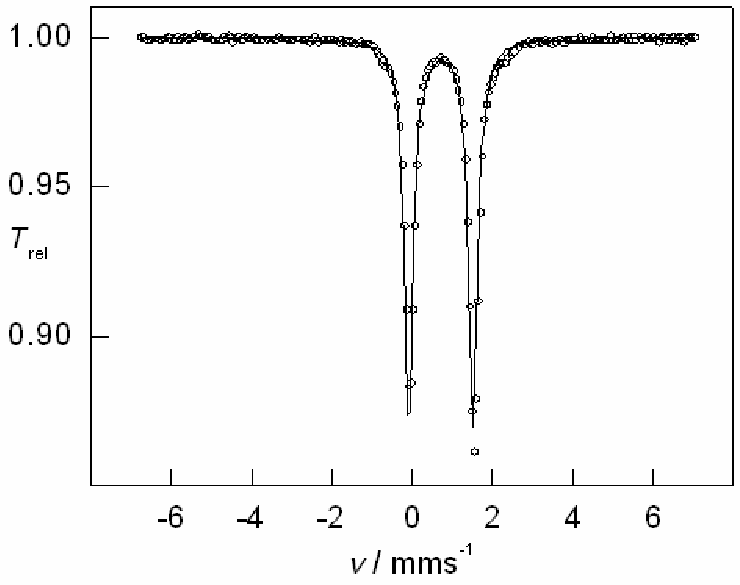

Figure 10: Zero-field Mössbauer spectrum for **1** recorded at 77 K. The ordinate shows relative transmission, and the solid lines are the fits by using Lorentzian doublets.

To authenticate our solid state magnetic moment data we collected the Mössbauer data for **2-Cl** at 77 K as well as 298 K. If we compare the Mössbauer parameters for **2-Cl** at those two temperatures we observe distinctly distinguishable values. The quadrupole splitting value observed at 298 K is consistent with a high spin (S = 5/2) $Fe^{(III)}$. This validates our SQuID experimental data which displays a spin transition occurring at the temperature range of 80−120 K. Different Mössbauer parameters collected at different temperatures unambiguously proves that two separate spin isomers to be present at those specified temperatures.

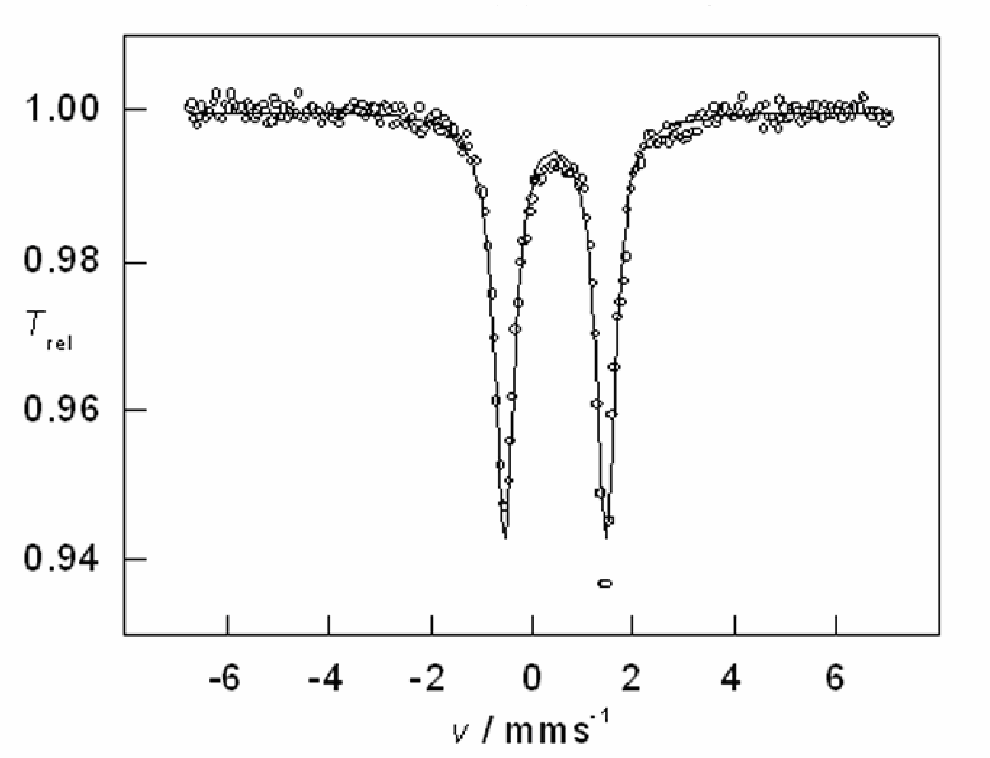

Figure 11: Zero-field Mössbauer spectrum for **2-OTf** recorded at 77 K. The ordinate shows relative transmission, and the solid lines are the fits by using Lorentzian doublets.

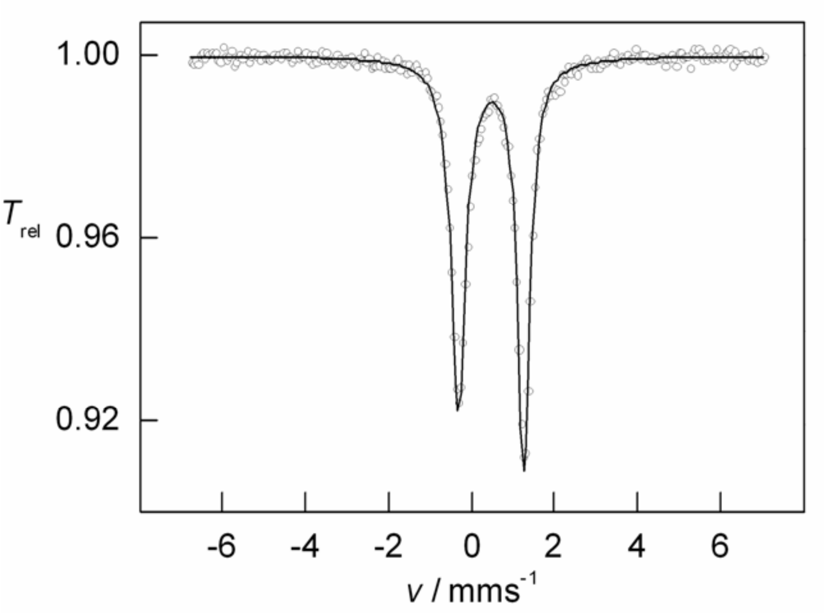

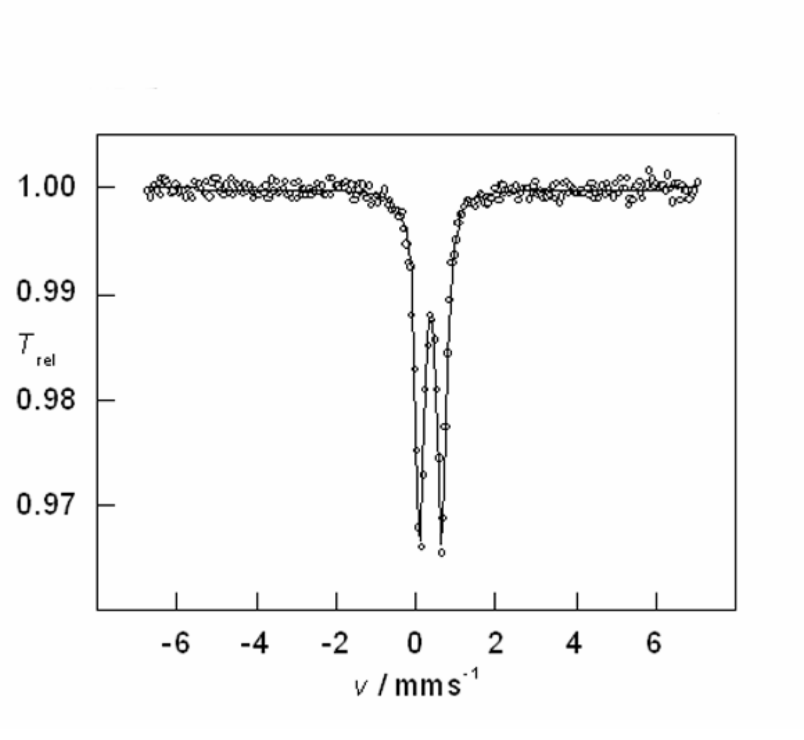

Figure 12: Zero-field Mössbauer spectra for **2-Cl** recorded at 77 K (top) and at 298 K. The ordinate shows relative transmission, and the solid lines are the fits by using Lorentzian doublets.

4.4 DFT calculations

The phenomenon of spin transition between intermediate spin state(S =3/2) and high spin state (S = 5/2) for Fe$^{(III)}$ is extremely rare.[39] To understand the phenomenon in depth we resorted on high level DFT calculations. **2-Cl** was simplified structurally by replacing the methyl groups of the aryl backbone by hydrogen atoms and isopropyl groups with methyl groups. Geometry optimizations were performed at the B3LYP*/6-31G** level of theory[40-43] with transition metals represented using the Los Almos LACVP basis.[44-46] The calculations favor the high spin state over the intermediate spin state by 2.42 Kcal mol^{-1}. Given the extremely low energy difference between two states, the spin transition between these two states is highly probable. Arguably, concomitant geometry change of **2-Cl** will take place along the spin change phenomenon. Indeed notable changes are noticed in Fe−P and Fe−N bond lengths and Cl−Fe−Cl angle. The observed changes are summarized in Table 2

Table 2: Important geometric parameters (bond lengths in Å and angles in degrees) during the spin crossover phenomenon.

	Fe–N	Fe–P	Fe–P	Fe–Cl	Fe–Cl	Cl–Fe–Cl
$S = 3/2$	1.971	2.330	2.330	2.311	2.302	112.5
$S = 5/2$	2.006	2.582	2.583	2.281	2.282	128.1

Intuitively the elongation of the Fe−P and Fe−N bonds can be followed since in high spin state, additional antibonding orbital d_{z^2} will be occupied. In contrary, change in Cl−Fe−Cl angle is not along our line of expectation as the angle is less than 120° in the intermediate spin state where an angle greater than 120° is expected due to chloride ligand repulsion. This discrepancy can be understood by detail analysis of the molecular orbital diagram of **2-Cl** in S = 3/2 state (Figure 13).

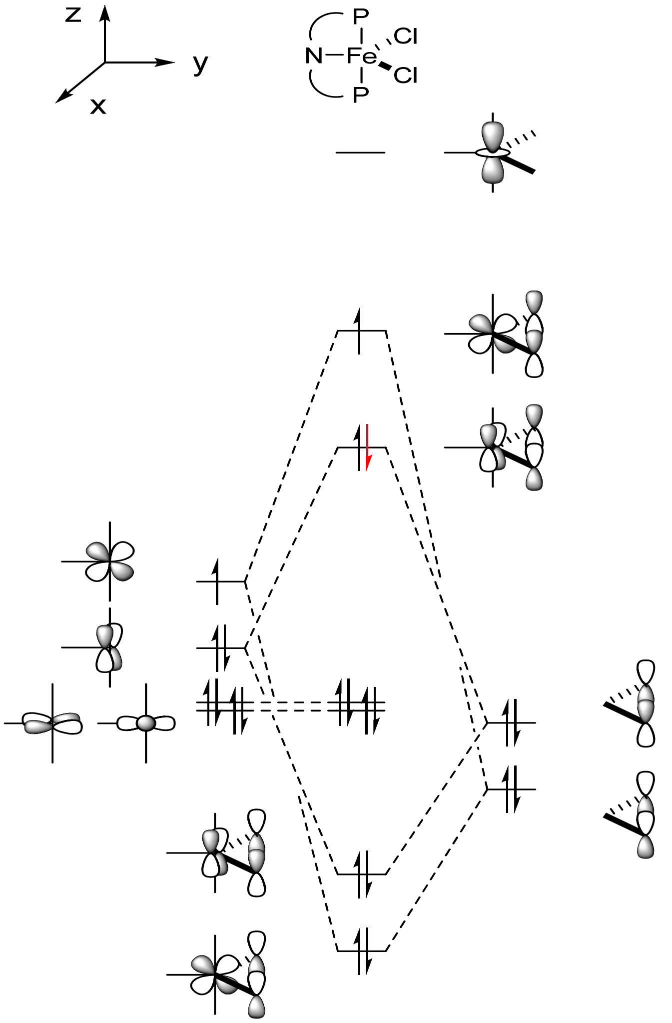

Figure 13: Frontier orbital diagram of **2-Cl** in the intermediate spin state.

The most important interaction to understand is that of the d_{xz}/d_{yz} orbitals and the filled p-orbitals on the chloride ligands. Of these two d orbitals it is expected that the d_{yz} orbital to be more hybridized toward the chlorides which provides the impetus for an angle smaller than 120^{o} in the *S* = 3/2 state. The better overlap causes the bonding/antibonding combinations to be below and above those of the d_{xz} based interactions, respectively. Because one will be filled/filled and one will be filled/half-filled, the stronger interactions for the d_{yz} orbital cause it to have only one electron in the antibonding combination. Consequently it will retain some of its bonding character, leading to the Cl–Fe–Cl angle being more acute than 120°. This proposed model also explains why the Cl–Fe–Cl angle changes concomitant with spin crossover. The spin active electron is highlighted in red (Figure 13). In spin crossover compounds like Fe^{II} (d^6 electronic configuration), electrons are removed from non-bonding t_{2g} orbitals and placed into antibonding e_g orbitals. Thus, the electronic character of the orbital from which the electron originates is neglected, which can predict the structural change based on the character of the antibonding e_g orbital alone. Here, however, the combination of an intermediate spin state and π-basic ligands makes the character of the orbital from which the electron originates important. Removal of an electron from this orbital which is antibonding with respect to the Fe–Cl bonds should result in bond contraction and an increase in the Cl–Fe–Cl angle (out-of-phase p_z orbitals). Indeed when the interactions of the two d-π orbitals are equal, we find Cl–Fe–Cl is greater than 120° since chlorides repel one another more than the PNP nitrogen.

4.5 XAS studies

X-ray absorption spectroscopic technique has emerged recently as an efficient probe for the effective oxidation state of a metal center and consequently locating the site of oxidation and the extent of metal-ligand covalency.[47, 48] We have demonstrated in Chapter 3 how multi-edge XAS approach can assess the role of each ligand, and provide complementary information in determining the composition of the redox active molecular orbitals.[10] Here we use this powerful technique to unambiguously locate the site of oxidation in a series of 3d transition metal complexes. Due to already conclusive Mössbauer data, we start our exploration with the iron complexes.

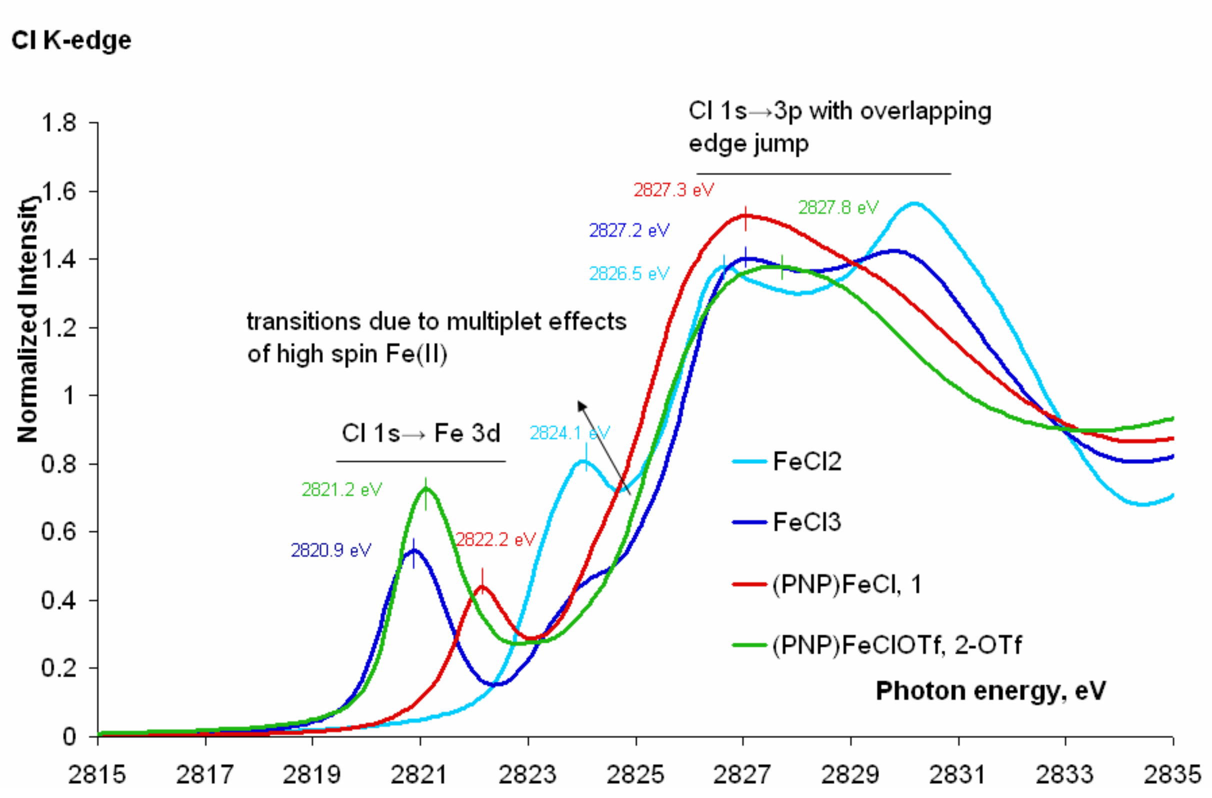

Figure 14: Cl K-edge spectra for various iron containing complexes.

In Figure 14, the Cl K-edge spectrum is shown for a series of iron containing complexes including **1** and **2-OTf**. The other complexes such as $FeCl_2$ and $FeCl_3$ have been chosen as reference for the oxidation state as well as to evaluate the influence of the ligand field in determining metal-ligand covalency. $FeCl_2$ displays a distinct pre-edge feature at 2824.1 eV and a rising edge at ~ 2826.5 eV. The features become strikingly different when compared to a complex of different iron oxidation state, i.e. $FeCl_3$ (blue trace). In that case the pre-edge energy has been enormously shifted to 2820.9 eV (a difference of 3.2 eV in pre-edge) and the rising edge has been shifted to higher energy at 2827.2 eV. This shift of the pre-edge energy position to lower energy is a characteristic feature of increased effective nuclear charge on the iron, which stabilizes the d-manifold. Simultaneously, the rising edge for the $FeCl_3$ shifts by 0.7 eV from the $FeCl_2$ to the higher energy side due to the increased Cl→Fe donation to the more oxidized metal center and hence the increasing effective nuclear charge (Z_{eff}) stabilizes Cl 1s orbital. Further analysis of the spectrum reveals a shoulder appears at 2823.9 eV which is likely due to multiplet effects of a high-spin iron center.[49] When **1** is compared to the reference spectra of $FeCl_2$ and $FeCl_3$, the pre-edge feature emerges at 2822.2 eV and the rising edge shows up at 2827.3 eV. The lower energy pre-edge feature along with the about similarly shifted rising-edge in comparison to the reference $FeCl_2$ indicate less covalent Fe–Cl bond in **1**. This lowered Fe−Cl bond covalency in **1** results in less electron donation from the chloride to the iron. Hence Z_{eff} for chloride will be less which causes the transition to take place at lower energy. In comparison to **1**, the oxidized product **2-OTf** (green trace) shows a pre-edge feature at 2821.2 eV, which is 1 eV shifted in the lower energy direction. This feature clearly tells us that the iron center has been oxidized for which the d-manifold of the oxidized species is more stabilized causing the pre-edge transition to shift at lower energy. This conclusion is further supported when the rising edge of **2-OTf** (2827.8 eV) is compared to **1** (2827.3 eV). The 0.5 eV shift in the rising edge towards the higher energy region proves that the chlorine atom donates more electron in the oxidized form than in the reduced. Since the pre-edge for **2-OTf** is shifted by 1 eV towards lower energy, and the edge becomes shifted by 0.5 eV in higher energy direction, altogether the d-manifold of **2-OTf** is stabilized by 1.5 eV when compared to **1**. Furthermore, the intensity of the pre-edge transition is increased due to the increased chlorine character of an electron hole opening up due to oxidation (statistical probability of the transition increases with increased number of absorbers/holes). After successfully analyzing the Cl K-edge we turned our attention to the Fe L-edge data which complements the observation we have already assessed from the Cl K-edge spectrum. Accordingly, we collected Fe L-edge data for the series of complexes which are shown in Figure 15.

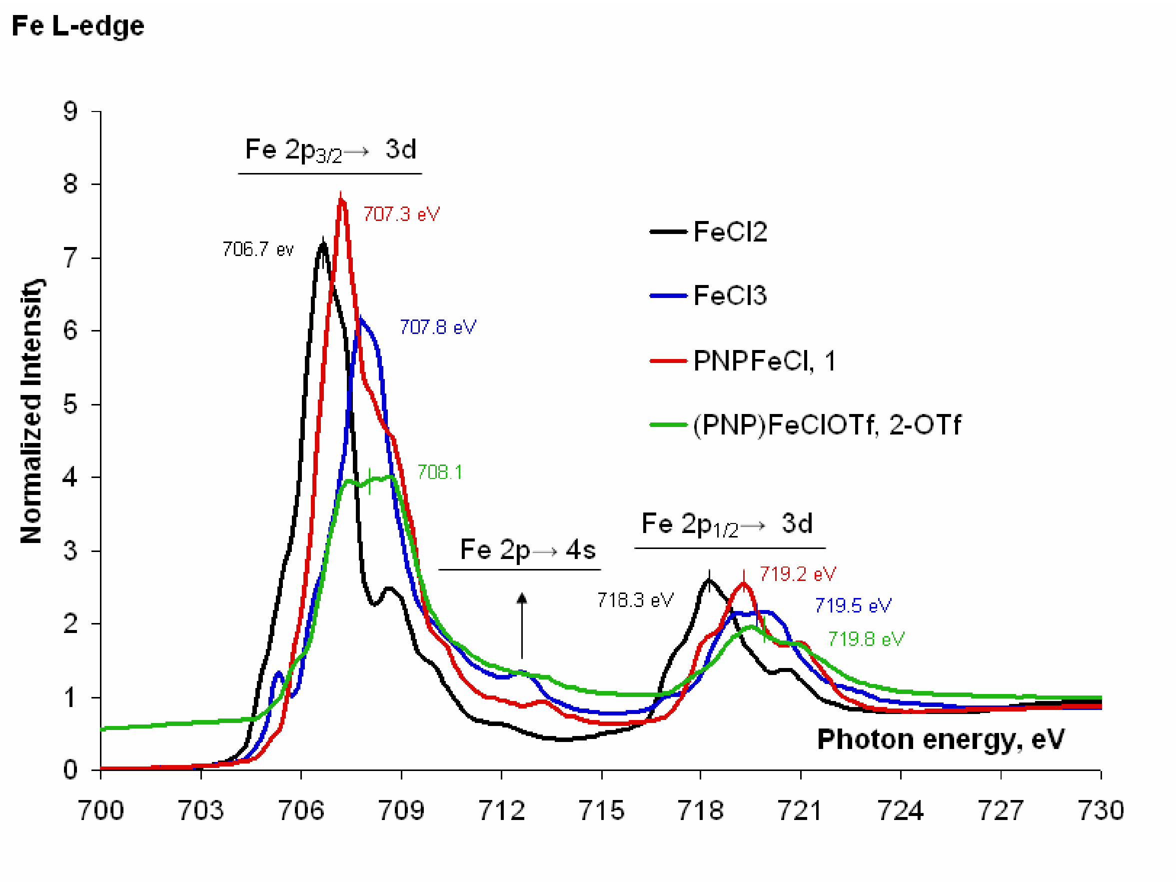

Figure 15: Fe L-edge for a series of iron containing complexes.

As depicted in Figure 15, the oxidation state of Fe in **2-OTf** was compared with the parent complex, **1**, as well as the other references such as $FeCl_2$ and $FeCl_3$. The spectra display two clear groups of transitions which are designated as L_3 (~704−712 eV) and L_2

(~717−724 eV). Reference spectrum of $FeCl_2$ displays L_3 transition feature at 706.7 eV and L_2 transition feature at 718.3 eV. In comparison, the reference $FeCl_3$ features the L_3 edge at 707.8 eV and L_2 edge at 719.5 eV. Both the L_3 and L_2 edges shift towards the higher energy as expected for the increasing oxidation state in $FeCl_3$. The intensity of the transition in case of $FeCl_3$ slightly decreases as increasing ligand covalency will augment mixing of more ligand 3p character in the metal d-orbital, consequently decreasing the intensity of the Fe 2p → 3d transition. However, increasing the number of holes as a consequence of oxidation should not be overlooked, which should theoretically increase the intensity of the transition in question. Hence the increase or decrease in intensity is a balance between two opposing factors of changing the amount of covalency and the number of radical holes. Complex **1** (red trace) shows an intense transition at 707.3 eV as L_3 edge and a broad feature at 719.2 eV as L_2 edge. In the case of **2-OTf** (green trace), L_3 and L_2 edges emerge at 708.1 eV and 719.8 eV respectively. Both edges shift slightly (0.6−0.7 eV) towards higher energy when compared to **1**, suggesting a metal centric oxidation is occurring in this case. More importantly, the pattern of the spectrum changes quite significantly from that of **1**. The shape of the spectrum permits determining the ligand field strength but is convoluted by multiplet contributions similar to the effects describe by the Tanabe-Sugano diagram[50] for a d^n metal complexes but for the core hole-reduced metal d-manifold ($2p^5 3d^{n+1}$) final states.[49] Thus the Fe L-edge studies consolidate the earlier view of metal centric oxidation derived from the Cl K-edge.

The direct proof of metal centric oxidation comes from reviewing the Fe K-edge spectra, which can directly reflect the iron oxidation state of the complex in question[51] (Figure 16). In the case of $FeCl_2$ there is a very weak pre-edge feature at 7111.6 eV as the complex retains octahedral symmetry. This weak pre-edge character could include multiple transitions upon closer inspection. Solomon and coworkers have analyzed the pre-edge region of iron complexes to distinctly assign those transitions as well as to separate out the dipolar and quadrupolar component of the transition.[49] The rising-edge feature is apparently broad but closer inspection reveals resolved features at 7120.7 and 7123.2 eV. These transitions are directed to different orbitals originated from mixing in 4p/4s of the metal and 3p/4p of the ligand. The energy gap between these metal based orbitals is a function of Z_{eff} of metal and the value increases with increasing Z_{eff}. Consequently, the extent of mixing of these orbitals with 3p/4p orbitals of ligands will vary from metal to metal depending on their Z_{eff}. $FeCl_3$ shows a pre-edge feature at 7113.4 eV and two shoulders like transitions at 7124.7 eV and 7130.8 eV. As expected, there is a clear shift both in pre-edge and edge transitions when $FeCl_3$ is compared to $FeCl_2$ towards the higher energy direction.

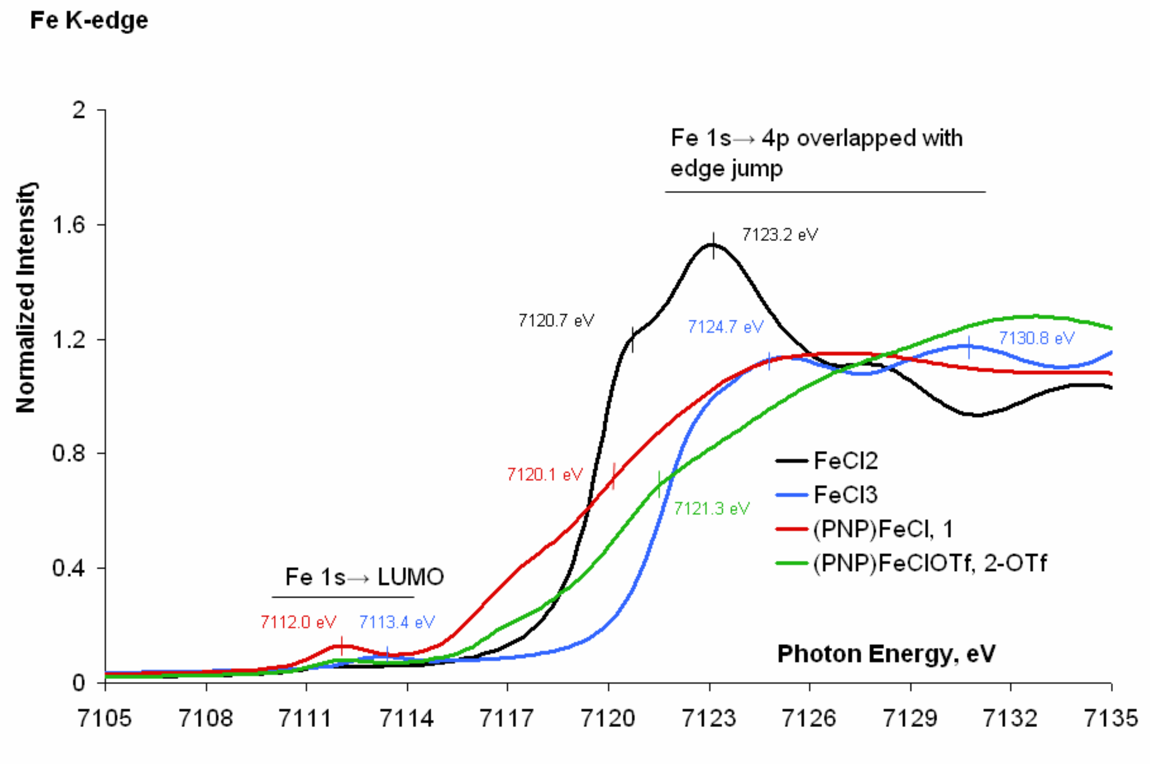

Figure 16: Fe K-edge spectrum for various iron containing complexes

Increasing effective nuclear charge on the metal stabilizes the metal 1s orbital energy therefore shifting the rising-edge and pre-edge transition (1s → 3d) to higher energy. Importantly, the analysis of 1s → 3d pre-edge features has been proven very useful in determination of the coordination number of the iron center in several enzymes,[52-54] the energy position of the pre-edge feature is further affected by ligand-field splitting parameters. Complex **1** evinces a pre-edge feature at 7112.0 eV and edge at ~ 7120.1 eV although the edge is not well resolved. Similarly, complex **2-OTf** exhibits a pre-edge feature at 7112.2 eV and an unresolved edge feature at 7121.3 eV. At this point it is evident that the edge shifts considerably (1.2 eV), which is a direct proof of metal-centric oxidation. Taken together, the multi-edge approach reveals the oxidation taking place predominantly at the metal.

4.5.1 XAS studies on Co complexes

In an attempt to study the non-innocence of the PNP-ligand as a function of metal centers the oxidation behavior of cobalt complexes with the ligand was also investigated. Earlier assumption from the crystallographic data was the oxidation of **3** would be metal centered. We wish to justify this assumption by the use of XAS methodology. Accordingly, complex **3** and **4-OTf** were scrutinized by multi-edge XAS along with $CoCl_2$ as a reference.

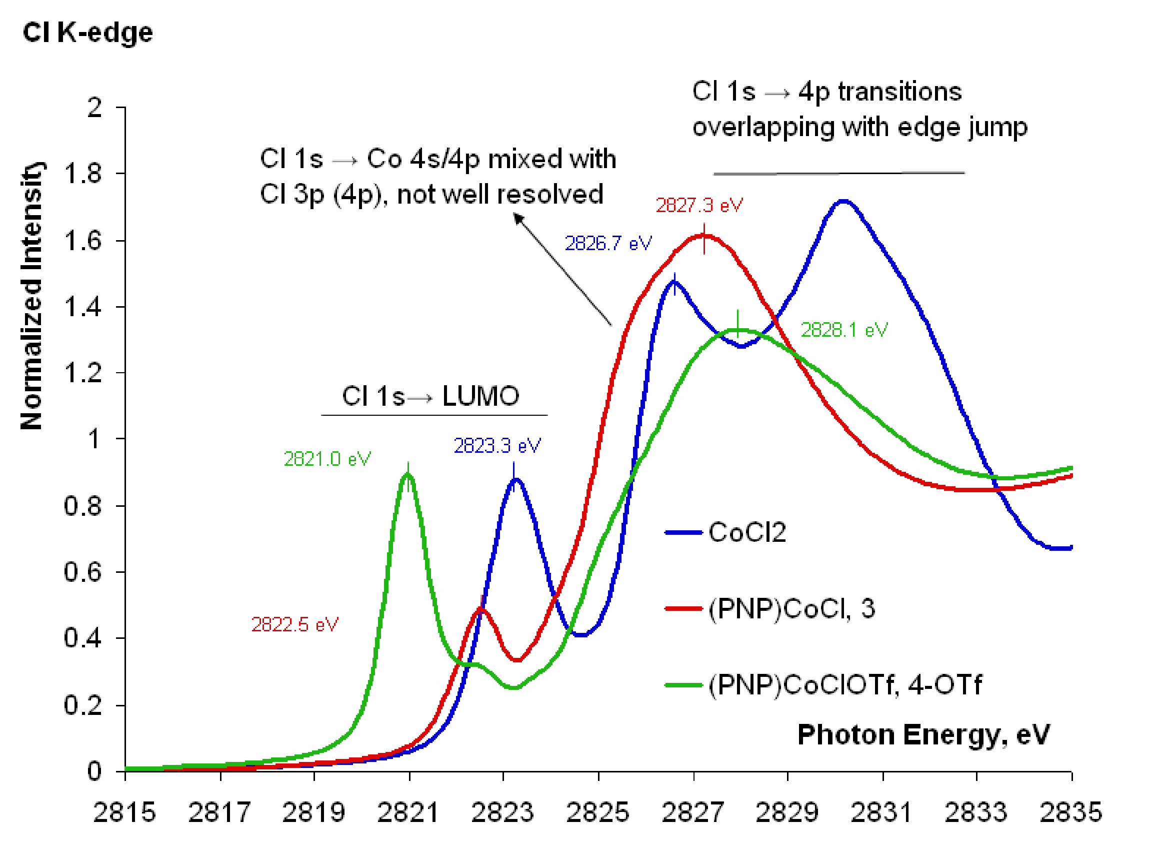

Figure 17: Cl K-edge spectra for various cobalt containing complexes.

In Figure 17, $CoCl_2$ displays a distinct pre-edge peak at 2823.3 eV and an edge at ~2826.7 eV. In comparison, complex **3** exhibits a pre-edge feature at 2822.5 eV, and an edge at 2827.3 eV. The difference in pre-edge and edge transition value stems from different ligand splitting environment (square planar in **3** compared to octahedral in $CoCl_2$). Upon closer look, **4-OTf** exhibits further lower energy shifted pre-edge feature at 2821.0 eV (green trace) and an edge at 2828.1 eV. The intensity of the pre-edge is considerably increased from that of **3** which hints towards more d-p mixing. This may stem from a distorted square pyramidal geometry of cobalt in **4-OTf** where the lack of centro-symmetry facilitates more mixing of the d and p-orbitals. The lower energy pre-edge and higher energy edge of **4-OTf** compared to **3** is fully consistent with the Co$^{(III)}$ oxidation state in **4-OTf**. Moreover, the increasing effective nuclear charge in **4-OTf** causes the overlapping features in the edge region (green trace) more well resolved than the virtually unresolved features in **3** (red trace). Expectedly our multi-edge XAS approach will also manifest features in agreement with the metal-centric oxidation in **3**. The Co L-edge spectrum has been displayed in Figure 18 which projects both the L_3 and L_2 region within an energy range of 770−801 eV.

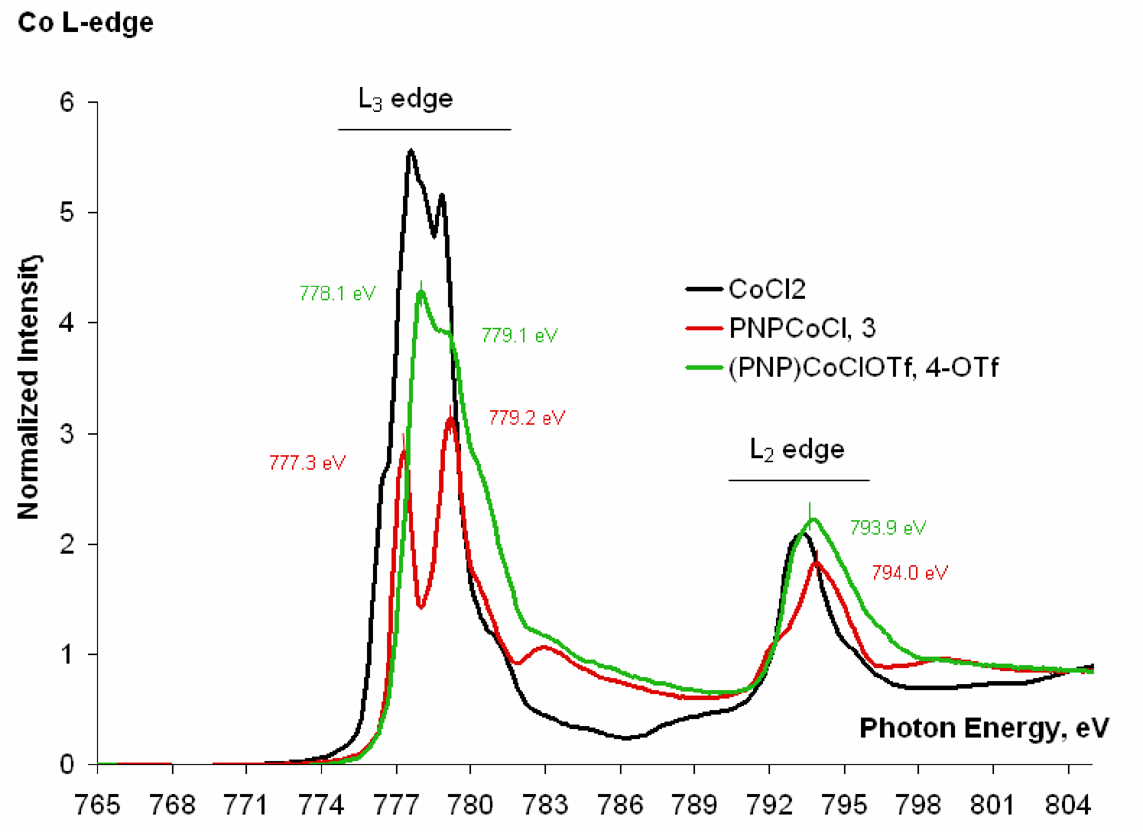

Figure 18: Co L-edge spectrum for cobalt complexes.

When **3** is analyzed, well resolved transition features are observed in L_3 edge at 777.3 eV and 779.2 eV and L_2 edge is observed at 794.0 eV. In comparison **4-OTf** exposes two relatively broad L_3 edge features at 778.1 eV and 779.1 eV respectively. On the other hand L_2 edge for **4-OTf** appears as a broad feature at 793.9 eV. The slight shift in energy for both the L_3 and L_2 edges and more importantly the change in nature of the curve from **3** to **4-OTf** clearly verifies the different oxidation state of metal in **4-OTf** from that of **3**. So far, analysis of Cl K-edge and Co L-edge confirmed that the oxidation took place predominantly on metal. Now we will like to directly verify this hypothesis by metal K-edge. Accordingly, spectrum for **3, 4-OTf** and **4-BF$_4$** were collected.

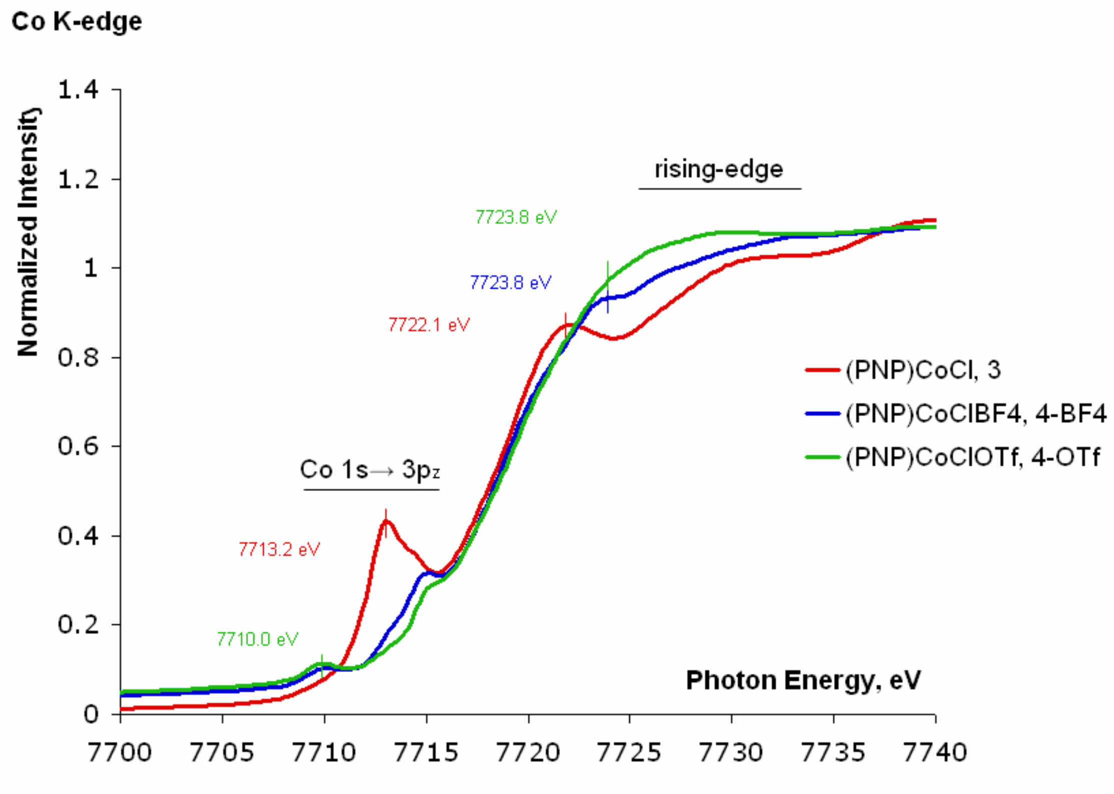

Figure 19: K-edge spectrum for cobalt complexes.

When **3** is analyzed in Co K-edge spectrum, it shows a resolved edge at 7713.2 eV (Co 1s→ $3p_z$) and a rising-edge at 7722.1 eV. The edge region displays overlapped features from multiple transitions. On the other hand both **4-OTf** and **4-BF$_4$** show a pre-edge at 7710.0 eV and rising-edge at 7723.8 eV. Hence a direct comparison reveals 1.7 eV shift in the rising-edge due to the oxidation. This amount of shift conclusively proves the metal centered oxidation taking place in **3**. To summarize the results of iron and cobalt oxidation the edges values have been presented in Table 2.

Table 2: Salient edge transition energies in iron and cobalt complexes.

	Cl K-edge		Metal K-edge	
Complex	Pre-edge (eV)	Edge (eV)	Pre-edge (eV)	Edge (eV)
1	2822.2	2827.3	7112.0	7120.1
2-OTf	2821.2	2827.8	7112.2	7121.3
3	2822.5	2827.3	7712.7	7722.1
4-OTf	2821.0	2828.1	7710.0	7723.8

During evaluating the redox behavior of the pincer for a series of 3d metal centers we also studied the behavior of nickel-pincer complex. Already, through spectroscopic investigations in conjunction with high level DFT calculations it has been unanimously proved that the oxidation is predominantly ligand based (Chapter 3). Strikingly, for (PNP)NiCl oxidation is ligand–centered which is switched from metal-centric iron and cobalt oxidation.

4.5.2 XAS performed on Zinc complexes

We were interested to observe how the oxidation locus changed when the metal center in question was redox innocent by studying (PNP)ZnCl, **5** with mulit-edge XAS approach. As discussed in the previous section of this chapter that the oxidation is not clean and one of the products isolated from the product mixture shows the ligand backbone to be oxidized and fused to the other aromatic ring through the phosphorus atom (*vide supra*). We analyzed **5** by XAS and the results have been compared with a reference $ZnCl_2$.

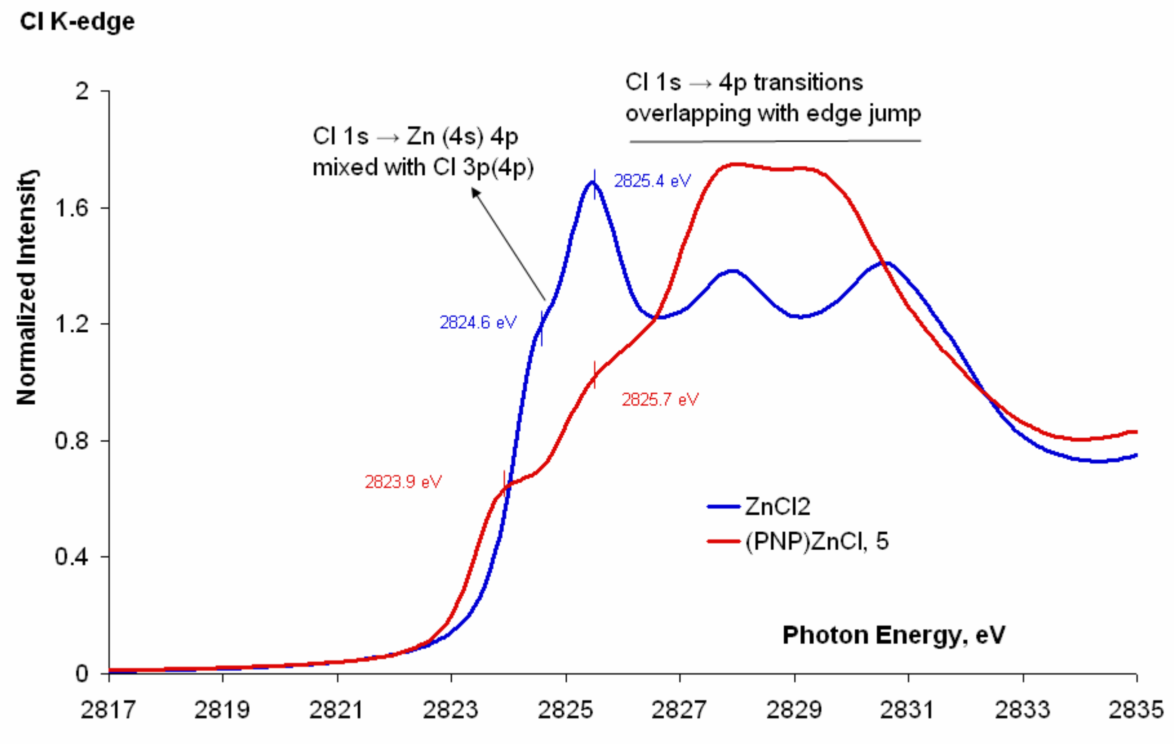

Figure 20: Cl K-edge spectra for zinc containing complexes

The Cl K-edge spectrum of $ZnCl_2$ appears very similar to the reported spectrum of Cs_2ZnCl_4 by Hodgson *et al.*[55] Upon analysis of **5** two resolved transitions are found at

2823.9 eV and 2825.7 eV, which correspond transitions from Cl 1s orbital to two orbitals originated from Zn 4s/4p and Cl 3p/4p mixing. Since the effective nuclear charge for Zn is higher than the other metals studied in the series (Fe, Co, etc), the energy separation between these orbitals is large. Well resolved features due to the transitions directed to the discussed orbitals in **5** further supports the argument. As expected, no distinct pre-edge features are observed for the d^{10} metal center. Reference $ZnCl_2$ spectrum also shows similar well resolved features in the edge region.

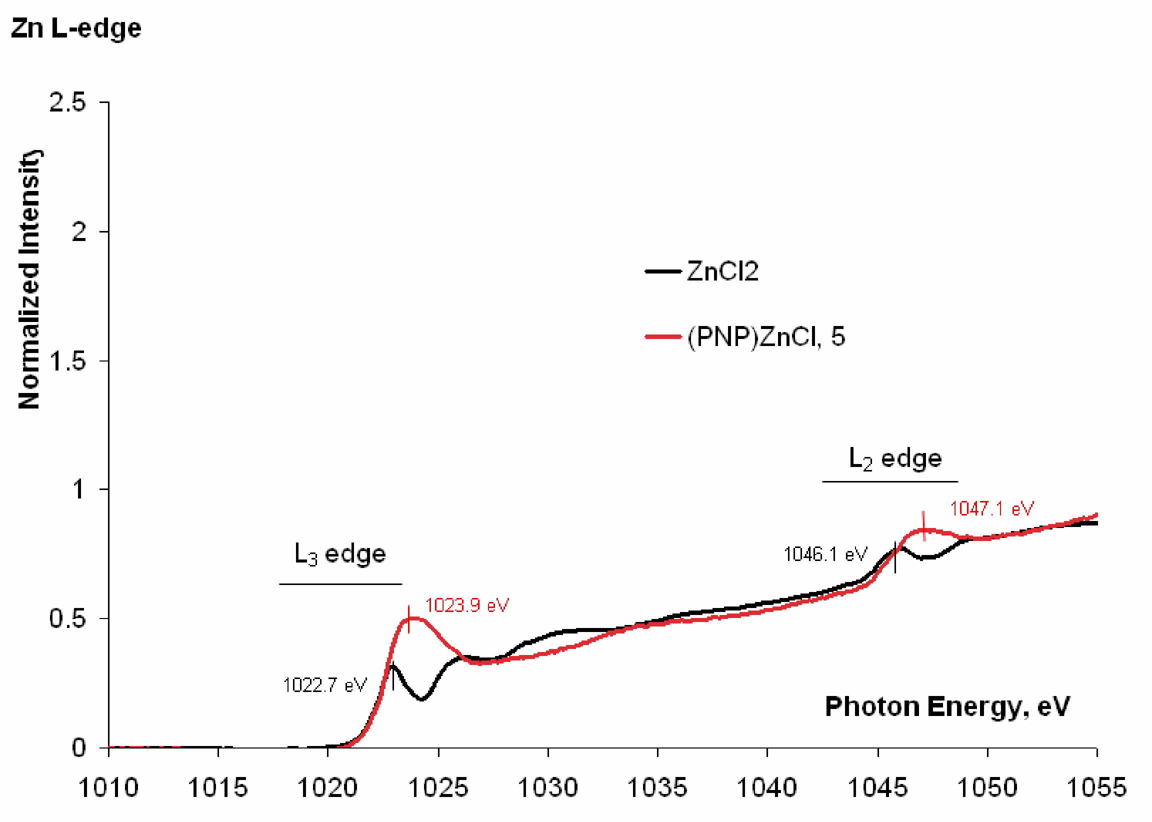

Figure 21: L-edge spectrum for zinc containing complexes.

In Figure 21, L_3 and L_2 edges have been depicted for both $ZnCl_2$ and **5**. $ZnCl_2$ shows an L_3 edge at 1022.7 eV and L_2 edge at 1046.1, respectively. When compared to **5**, it is evident that the features remain similar and appear at 1023.9 and 1047.1 eV respectively. The about 1 eV shift can be attributed to the different energy position of the Zn 4s orbital in an octahedrally zinc$^{(II)}$ chloride *versus* the tetrahedral complex **5**. Expectedly, no considerable change in the oxidation state of Zn is directly observed during complexation with PNP upon analysis of Zn K-edge XAS.

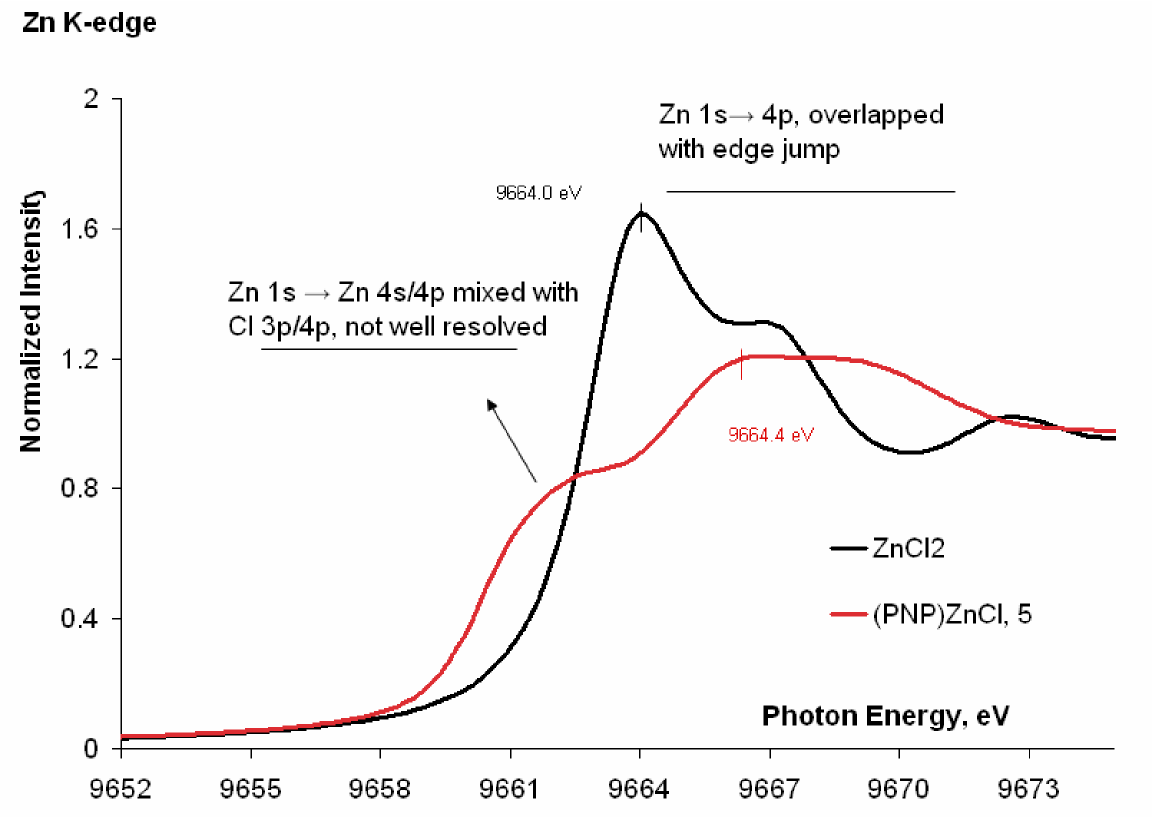

Figure 22: K-edge spectrum for zinc containing complexes.

From Zn K-edge measurements, the different 4s/4p mixing of the Zn with the ligand 3p orbitals are distinctly observed for the octahedral *versus* tetrahedral environment. This is in agreement with the fact that with increasing effective nuclear charge of the metal, the energy gap between 4s and 4p orbital increases, thus making a good resolution possible between the transitions.

4.5.3 XAS performed on Cu samples

In order to compare the redox behavior of the ligand in a series of 3d transition metals, we also studied copper. Preparation of Cu$^{(II)}$ complex of the pincer PNP is not clean and mostly results in reduction of the Cu$^{(II)}$ center to Cu$^{(I)}$. However, inclusion of complex **7** helps in understanding the ligand's behavior as function of varying metal d-orbital energies. Hence **7** was analyzed by XAS and the following features clearly provide clues about the undergoing redox process during complexation of CuCl$_2$ with (PNP)Li (Figure 23). The XAS investigation will also validate our assignment of Cu$^{(I)}$ in **7**.

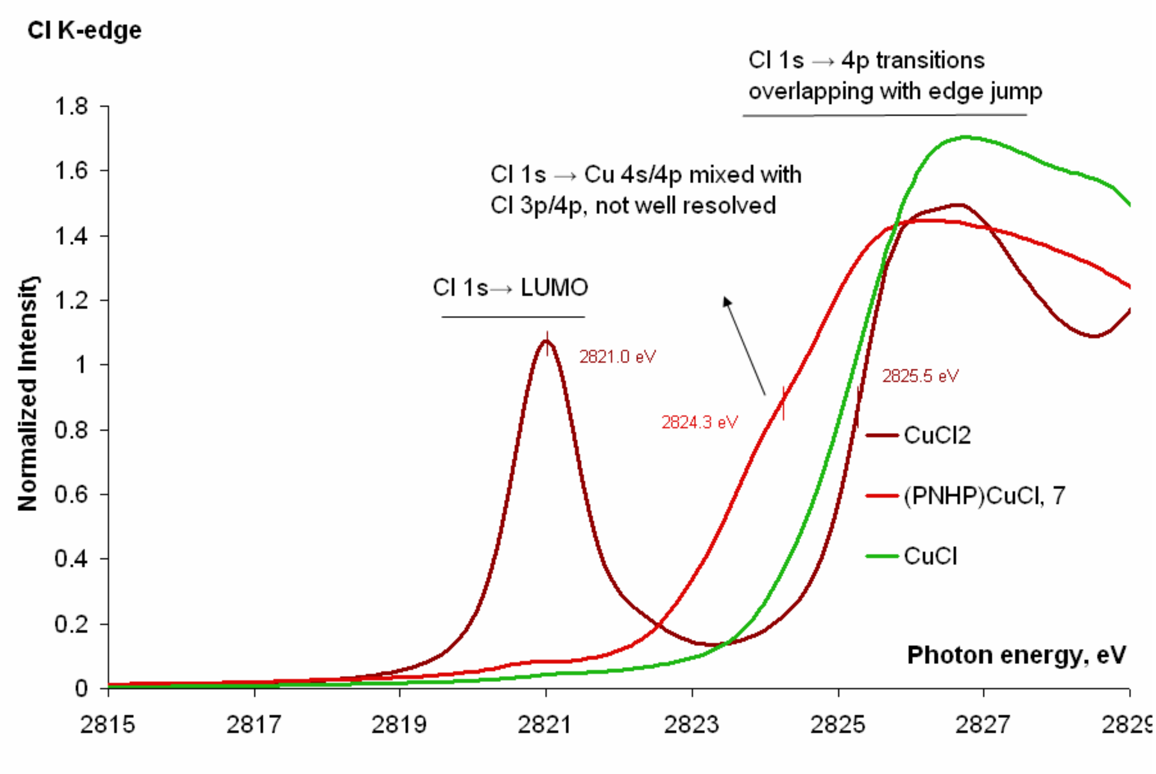

Figure 23: Cl K-edge of the copper containing complexes.

Reference anhydrous $CuCl_2$ shows a sharp pre-edge feature at 2821.0 eV due to the d^9 electronic configuration of the metal center in the complex. The reference CuCl exhibits remarkably different transitions since d^{10} electronic configuration of $Cu^{(I)}$ prevents any pre-edge transition similarly to $ZnCl_2$ (d^{10}) sample. The Cu K-edge pre-edge data (1s→3d transition) is a spectroscopic marker[56] for copper$^{(II)}$ oxidation state and the absence of any pre-edge feature in **7** unequivocally proves the copper oxidation state to be +I in **7**. Only a broad edge feature is evolved at 2824.3 eV which is shifted to the lower energy side compared to anhydrous $CuCl_2$ at 2825.5 eV. This shift in Cl K-edge is also consistent with a single electron reduction from $Cu^{(II)}$ to $Cu^{(I)}$. Moreover similarity in the nature of the spectra for **7** and the reference CuCl further consolidates the claim. Other multi-edge analysis will also be supporting this conclusion (*vide infra*).

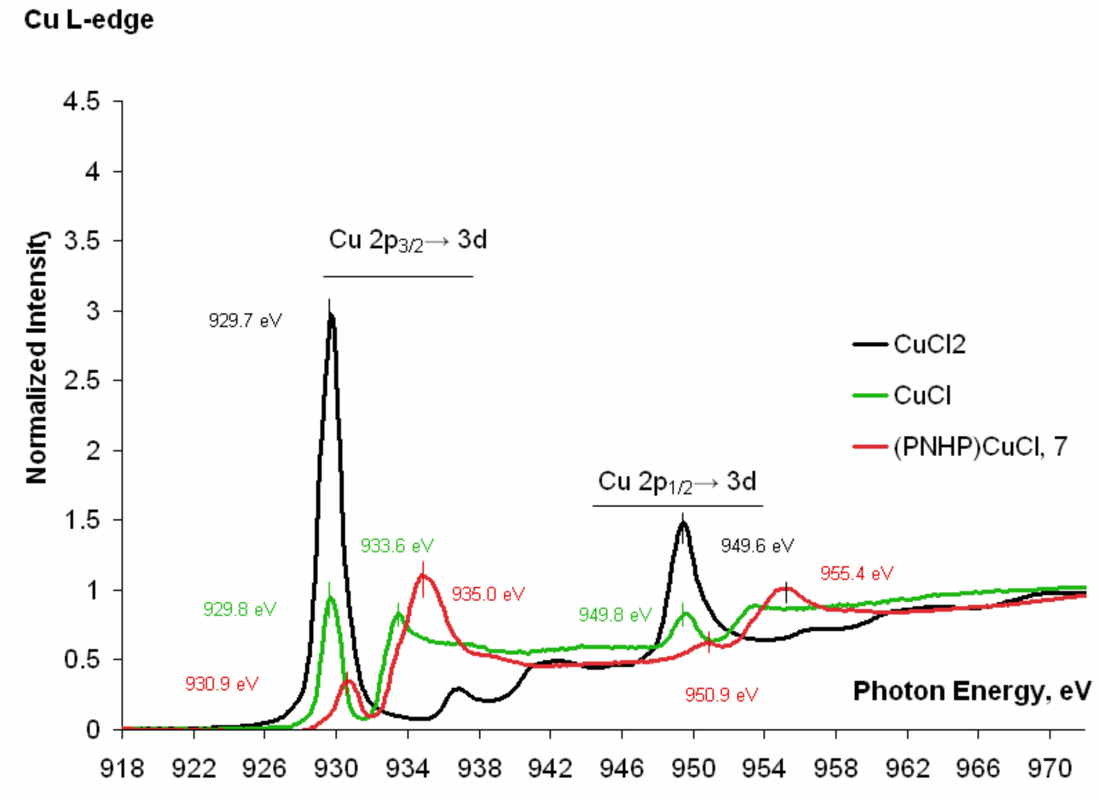

Figure 24: L-edge spectrum for copper containing complexes.

Further support for the above conclusion comes from the analysis of the Cu L-edge for the same set of complex. Anhydrous $CuCl_2$ shows an intense L_3 transition at 929.7 eV which is assigned as the 2p → $3d_{x2-y2}$ transition, a process electric dipole allowed for a d^9 metal system. The L_2 edge appears at 949.6 eV maintaining an approximately 1:2 ratio with L_3 edge.[57] The current limitation of normalization methods for L-edges deprived us to obtain a properly normalized spectrum, although the well resolved L_3 and L_2 features are eminent.[58-60] When $Cu^{(I)}$ in CuCl is compared to $CuCl_2$ an edge transition (2p → 3s) is observed at 933.6 eV. Nearly identical features are observed in the L_2 edge at 949.8 eV with reduced intensity. A direct comparison to complex **7**, provides a very low intensity L_3-edge pre-edge transition centered at 930.9 eV and an edge transition at 935.0 eV, consistent with $Cu^{(I)}$ assignment of the oxidation state. Corresponding transitions in the L_2 edge also appear at 950.9 eV and 955.4 eV respectively. Hence L-edge analysis of the Cu containing complexes unambiguously prove the metal oxidation state to be $Cu^{(I)}$ in **7**. Additionally, the reference CuCl sample shows similar features to **7** further substantiating our conclusion.

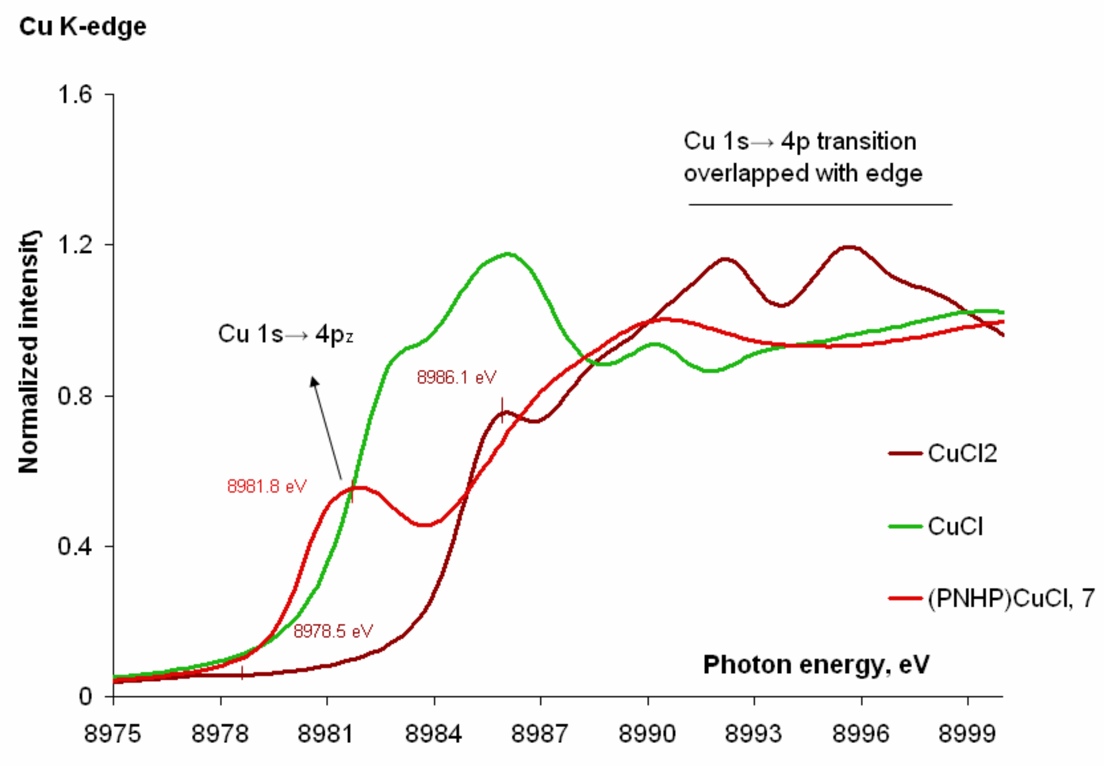

Figure 25: K-edge spectrum for copper containing complexes.

The Cu K-edge spectrum reveals more interesting features as well as sheds more insight into the electronic structure of the complex **7**. In the Cu K-edge, the pre-edge features are almost overlapping with the rising edge features for the reference anhydrous $CuCl_2$. The feature at 8986.1 eV can be assigned to 1s → 4p along with shakedown transition.[61] A salient feature for **7** revealed a transition at 8981.8 eV, which can be tentatively assigned to 1s → $4p_z$. Solomon *et al.* did a thorough study of analyzing 40 copper containing complexes to infer that $Cu^{(II)}$ peak emerges at energies greater than 8985.0 eV. Hence the peak at 8981.8 eV can be conveniently assigned to a $Cu^{(I)}$ signature. For $CuCl_2$, a very weak feature is observed at lower energy (8978.5 eV) and has been proposed to be the 1s → 3d transition[51] as confirmed by single-crystal studies.[62] Moreover Solomon *et al.* have shown that the pre-edge peaks for $Cu^{(I)}$ complexes can be reasonably correlated to the coordination number. For a 3-coordinate trigonal planar system the degeneracy of the $p_{x,y,z}$ will be lifted, and $p_{x,y}$ orbitals will form a degenerate set above p_z (considering xy as the molecular plane). Thus the transition at 8981.8 eV should correspond to 1s → $4p_z$ and is predicted to be polarized along C_3, which is the Z-axis in our case. A broad rising-edge feature also proves the overlapping transition of the metal based 4s/4p to ligand based orbitals. All the assigned transitions perfectly match the trigonal planar geometry of **7** evaluated from single crystal X-ray diffraction studies. Taken all these evidences together, we unequivocally confirm the oxidation state of copper in **7** to be +I.

4.6 Conclusion

The above study describes a thorough analysis of the redox non-innocence of the pincer PNP manifested as a function of metal centers, or precisely the energy of the metal d-manifold (or the frontier orbitals). In our analysis over a series 3d transition metals we explored complexes ranging from iron to copper, and found that the effective nuclear charge increases, therefore attaining the stabilization of the metal d-manifold. Usually, ligand frontier orbitals are lower in energy compared to unoccupied metal frontier d-orbitals, which makes the antibonding combination of metal-ligand orbitals to be mainly metal-based. This results in oxidation processes that are mainly metal-centered. This classical behavior is observed for **1** and **3** where predominantly metal based oxidation is detected. Moving to nickel, due to the increased effective nuclear charge (Z_{eff}), the d-orbitals are stabilized in energy to such an extent that the metal d-orbital energy is comparable to ligand orbital energy. As a consequence, metal ligand covalency in Ni−Cl bond increases significantly so the oxidation process takes place in the ligand backbone. In the case of diarylamido ligands, the out of plane nitrogen lone pair (out of plane from the molecular plane) may play a significant role in the energy of the ligand based orbitals. It might happen that for the other ligands where no such amido moiety is present the oxidation process could have been distinctly metal based. Overall, the redox behavior switches predominantly from metal to the ligand when we move from iron and cobalt to nickel. When the series is further moved to copper, we end up with an inverted scheme of metal and ligand based orbitals. The d-manifold is so stabilized in the case of $Cu^{(II)}$, due to increased Z_{eff}, such that the energy decreases far below the ligand orbitals. This fact is vividly corroborated by the spontaneous reduction of the $Cu^{(II)}$ center when complexation of $Cu^{(II)}$ is attempted with PNP-lithium salt. Although the reaction is not clean and the final product is marred with some other uncharacterized products, we are certain about the major product to retain $Cu^{(I)}$ oxidation state. Numerous studies have focused earlier on determining the factors that control the locus of oxidation in salen (salen = N,N'-bis(3,5-di-tert-butylsalicylidene)-1,2-cyclohexane-(1R,2R)-diamine) based complexes.[63-67]Along these studies, Stack *et al.* have shown that the locus of oxidation switches from ligand to metal when moving form $[Ni(salen)]^+$ to $[Cu(salen)]^+$.[68] Our study is unique since the redox non-innocence of the PNP ligand is very implicit and only manifests under a special circumstance, as qualitatively depicted in Figure 26.

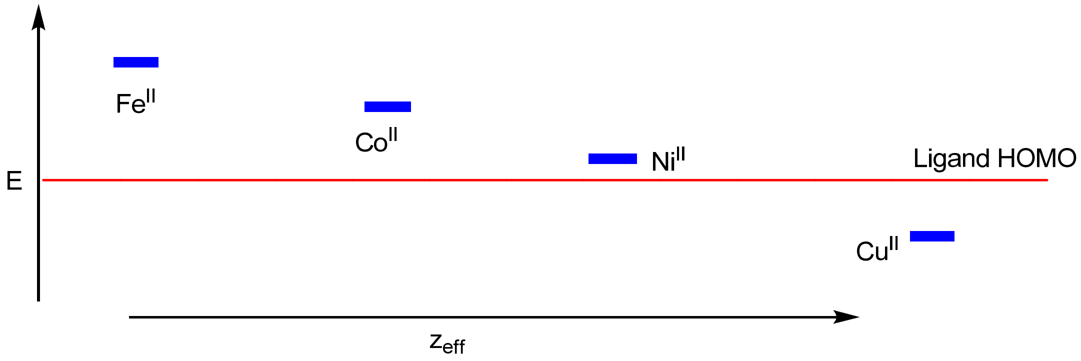

Figure 26: Qualitative diagram to show how the energy of the d-manifold for a metal ion decreases with increasing Z_{eff}. Ligand frontier orbitals, engaged in forming molecular orbitals are assumed to remain same in relative energy. The figure also shows how in case of nickel, metal orbitals and ligand frontier orbitals are very close in energy, thus the oxidation behavior switches from metal to ligand. In case of copper, metal d-orbitals are even more stabilized than ligand orbitals, forming an inverted pattern which explains the reduction of the metal center during complexation with PNP-ligand.

Given the widespread use of pincers in organometallic chemistry this study may provide clear clues about how a reaction follows some specific pathway involving the ligand. Very recently, Heyduk *et al.* showed how the usage of redox active ligands may facilitate important chemical transformations such as C−C bond formation, especially in the context of early transition metals such as Zr.[69] Even the role of the redox active ligand has been described in activation of dihydrogen by Rauchfuss *et al.*[70] A similar study by Fujii *et al.* elucidated how interconversion between Mn^{IV}-phenolate and Mn^{III}-phenoxyl radicals can offer unique reactivity.[66] Judicious choice of ligands which can behave as an electron reservoir may lead to unprecedented reactivity of the complexes which is not possible for strictly metal centric chemistry. Taken together, our current study on redox non-innocence of the pincer may help understanding and designing novel catalytic systems by unraveling the structure-reactivity relationship.

4.7 Experimental Data

General procedures: Unless otherwise stated, all operations were performed in a M. Braun Lab Master double-dry box under an atmosphere of purified nitrogen or using high vacuum standard Schlenk techniques under an argon or dinitrogen atmosphere. Anhydrous *n*-hexane, pentane, toluene, and benzene were purchased from Aldrich in sure-sealed reservoirs (18 L) and dried by passage through two columns of activated alumina and a Q-5 column. Diethylether was dried by passage through a column of activated alumina. THF was distilled, under nitrogen, from purple sodium benzophenone ketyl and stored under sodium metal. Distilled THF was transferred under vacuum into thick walled reaction vessels before being carried into a dry box. Deuterobenzene was purchased from Cambridge Isotope Laboratory (CIL), degassed and vacuum transferred to 4 Å molecular sieves. All other deuteron solvents were stored under sodium metal. Celite, alumina, and 4 Å molecular sieves were activated under vacuum overnight at 200 ºC. **1** and **3** were prepared following the literature procedure.[11, 18] All other chemicals were purchased from Strem Chemicals or Aldrich and used as received. CHN analyses were performed by Midwest microlab, Indianapolis, IN. ^{1}H, ^{13}C and ^{31}P NMR spectra were recorded on Varian 400 or 300 MHz NMR spectrometers. ^{1}H and ^{13}C NMR are reported with reference to residual solvent resonances. ^{31}P NMR chemical shifts are reported with respect to external H_3PO_4 (0.0 ppm). Magnetic moments were obtained by the method of Evans.[71, 72] UV-visible spectra were recorded on a Cary 5000 UV-vis-NIR spectrophotometer. Magnetization measurements were performed on a Quantum Design SQuID susceptometer 0–5 T, 2–300 K. ^{57}Fe Mössbauer spectra were recorded on a Wissel Mössbauer spectrometer (MRG-500) at 77 K in constant acceleration mode. ^{57}Co/Rh was used as the radiation source. WinNormos for Igor Pro software has been used for the quantitative evaluation of the spectral parameters (least-squares fitting to Lorentzian peaks). The minimum experimental line widths were 0.20 mm sec^{-1}. The temperature of the samples was controlled by an MBBC-HE0106 Mössbauer He/N_2 cryostat within an accuracy of ±0.3 K. Isomer shifts were determined relative to α-iron at 298 K. X-ray diffraction data were collected on a SMART6000 (Bruker) system under a stream of N_2 (g) at low temperatures.

XAS Details: The metal L-, K-, and chlorine K-edge XAS measurements were carried out at beamlines 10-1, 7-3 and 6-2 of Stanford Synchrotron Radiation Laboratory under strorage ring (SPEAR 3) conditions of 3 GeV energy and 100-80 mA beam current. BL10-1 has a 30-pole 1.45 Tesla Wiggler insertion device with 6 m spherical grating monochromator. The samples were measured in a vacuum chamber with typical pressures of 10^{-6}–10^{-8} torr. Data collection was carried out in electron yield mode by a Channeltron detector with 1.5kV accelerating potential.BL7-3 is a 20-pole, 2T Wiggler beamline equipped with a Si(220) downward reflecting, double-crystal monochromator. Data were collected using an unfocused beam in transmission mode using ground samples that were diluted in BN for minimal absorption effects. BL6-2 is a 56-pole, 0.9 Tesla Wiggler beam line with a liquid nitrogen cooled, Si(111) double crystal monochromator. Cl K-edge spectra were collected in the energy range of 2720−3050 eV, respectively, using an unfocused beam in a He-purged fly-path at room temperature and a Lytle fluorescence detector. The beam line was optimized at 3050 eV for Cl K-edge. The energy scale was calibrated for the Cl K-edge at 2820.2 eV using the pre-edge feature of Cs_2CuCl_4. The solid samples were ground and pasted onto a contaminant free Kapton tape from Shercon or carbon tape from Specs CertiPrep in a glove box with sub ppm oxygen and moisture levels. For Cl K-edge measurements samples were protected by a thin polypropylene window (Specs CertiPrep) from exposure to air during sample mounting and change. Sample holders for metal L-edge measurements were mounted in a He purged glove bag tightly wrapped around the vacuum chamber. At least five scans were averaged to obtain a good signal-to-noise ratio. Further processing of the data has been carried out as described in the literature.[47] Calibration points used during the data normalization for different edges is summarized below.

Metal K-edge series

Fe calib. 7111.2 eV, norm. 7130 eV

Mn calib. 6539 eV , norm. 6570 eV

Zn calib. 9659 eV, norm. 9690 eV

Cu calib. 8979 eV, norm. 9100 eV

Ni calib, 8333 eV, norm. 8360 eV

Co calib. 7709 eV, norm. 7740 eV

Two point calibration for L-edges

Fe calib. 708.5 eV (2 nd intense peak), L2 720.5 ev(2 nd peak) of hematite,

Mn calib. 640.7 eV , L2 654.9 eV, Zn calib. 9659 eV,

Cu calib. 930.5 eV, L2 950.5 eV,

Ni calib, 854.7 eV, L2, 871.9 eV,

Co$^{(II)}$ calib. 780.0 eV, L2, 795.2 eV,

Co$^{(III)}$ calib. 781.0 eV, L2, 796.2 eV,

Zn calib. 1021.8 ev, L2 1044.9 eV.

Computational Details

All calculations were carried out using density functional theory (DFT) as implemented in the Jaguar 7.0 suite of quantum chemistry programs. Geometry optimizations were performed at the B3LYP*/6-31G** level of theory[40-43] with transition metals represented using the Los Almos LACVP basis.[44-46] Energies computed with double-ζ basis set are not reliable for redox phenomenon, as we previously reported. Subsequent single-point energies were conducted with Dunning's correlation consistent triple-ζ basis set, cc-pVTZ(-f),[73] with transition metals represented using LACVP3P, a decontracted version of LACVP to match the effective core potential with a triple-ζ quality basis.analytical vibrational frequencies within the harmonic approximation were computed with the double-ζ basis for thermodynamics analysis and to ensure all stationary points were well-defined minima.

Synthesis of (PNP)FeCl(OTf), 2-OTf

In a vial **1** (100 mg, 0.192 mmol) was dissolved in 5 mL of THF and cooled to −35 °C. Solid FcOTf (63.81 mg, 0.190 mmol) was added slowly to that precooled solution of **1**. Immediate after the addition the reddish color of the solution was changed to purple. The reaction mixture was stirred for 45 minutes after which it was dried in vacuo. The solid mass was washed with pentane (4 times, 5 mL each time) and dried again. The solid was isolated in spectroscopic purity (112 mg, 0.167 mmol, 87% yield).^{1}H NMR (25 °C, 399.8 MHz, THF): δ 79.9 (br, $\nu_{1/2}$ = 156 Hz), 66.0 (br, $\nu_{1/2}$ = 143 Hz), 62.3 (br, $\nu_{1/2}$ = 156 Hz), 51.3 (br, $\nu_{1/2}$ = 616 Hz), 44.1 (br, $\nu_{1/2}$ = 524 Hz), 10.2(br, $\nu_{1/2}$ = 1830 Hz), 1.13 (br, $\nu_{1/2}$ = 110 Hz), 0.86 ($\nu_{1/2}$ = 49 Hz), −89.2 (br, $\nu_{1/2}$ = 485 Hz), −110.7 (br, $\nu_{1/2}$ = 93 Hz), −113 (br, $\nu_{1/2}$ = 95 Hz). μ_{eff} : 4.3 μ_B (CD_2Cl_2), 25 °C, Evan's method). Anal. Calcd for $C_{26}H_{40}NP_2O_3SF_3ClFe$: C, 48.48; H, 6.03; N 2.09. Found: C, 48.45; H, 5.98, N, 2.05. UV-vis (THF, 25 °C): 854 nm (ε = 456 M^{-1} cm^{-1}), 518 nm (ε = 418 M^{-1} cm^{-1}), 306 nm (ε = 7156 M^{-1} cm^{-1}) M.P. 169 °C

Synthesis of (PNP)FeCl$_2$, 2-Cl

In a vial **1** (200 mg, 0.384 mmol) was dissolved in 5 mL of THF and cooled to −35 °C. In another vial Ph_3CCl (107.24 mg, 0.384 mmol) was dissolved in 2 mL of THF, cooled to −35 °C and added slowly to the pre-cooled solution of **1**. Immediate after the addition the reddish color of the solution was changed to blackish purple. The reaction mixture was stirred for 1.5 hours after which it was dried in vacuo. The solid mass was washed with pentane (5 times, 5 mL each time) and dried again. The solid was isolated in spectroscopic purity (174 mg, 0.312 mmol, 81% yield). ^{1}H NMR (25 °C, 399.8 MHz, CdCl$_3$) δ 108.9 (br, $\nu_{1/2}$ = 309 Hz), 67.76 (br, $\nu_{1/2}$ = 44 Hz), 62.10 (br, $\nu_{1/2}$ = 91 Hz), 36.95 (br, $\nu_{1/2}$ = 982 Hz), 13.48 (br, $\nu_{1/2}$ = 859 Hz), 6.97, 1.30, −103.0 (br, $\nu_{1/2}$ = 190 Hz). μ_{eff} : 3.3 μ_B (CDCl$_3$, 25 °C, Evan's method). UV-vis (CH$_2$Cl$_2$, 25 °C): 902 nm (ε = 2908 M^{-1} cm^{-1}), 536 nm (ε = 4105 M^{-1} cm^{-1}), 386 nm (ε = 4094 M^{-1} cm^{-1}). MS-CI, [M-Cl]$^+$: calcd, 519.867; found, 519.168. M.P. 184 °C

Synthesis of (PNP)CoCl(BF$_4$), 4-BF$_4$

In a vial was dissolved **3** (150 mg, 0.286 mmol) in 5 mL of THF and in another vial a suspension was made of FcBF$_4$ (78.26 mg, 0.287 mmol) in 3 ml of THF. The ferrocenium tetrafluoroborate suspension was added to the cobalt complex solution slowly and within 3 minutes of the addition solution color changed to purple. The reaction mixture was stirred for 45 minutes and dried in vacuo. The solid mass was washed with pentane portion wise (5ml each, 4 times) to remove the byproduct ferrocene. Red colored crystals were obtained by dissolving the complex in dichloromethane and layering the solution with pentane. (165 mg, 0.271 mmol, 94 % yield).

^{1}H NMR (25 °C, 399.8 MHz, CdCl$_3$): δ 77.4 (br, $\nu_{1/2}$ = 469 Hz), 63.5 (br, $\nu_{1/2}$ = 412 Hz), 3.13 ($\nu_{1/2}$ = 31 Hz), 2.46 ($\nu_{1/2}$ = 56 Hz), 1.23 (br, $\nu_{1/2}$ = 751 Hz), 3.46 ($\nu_{1/2}$ = 39 Hz), −26.9 (br, $\nu_{1/2}$ = 337 Hz), −69.0 (br, $\nu_{1/2}$ = 850 Hz). μ_{eff} : 2.99 μ_B (CDCl$_3$, 25 °C, Evan's method). Anal. Calcd for $C_{26}H_{40}NP_2BF_4ClCo$: C, 51.25; H, 6.62; N 2.29. Found: C, 51.16; H, 6.70, N, 2.23. UV-vis (CH$_2$Cl$_2$, 25 °C): 942 nm (ε = 1272 M^{-1} cm^{-1}), 593 nm (shoulder peak) (ε = 1864 M^{-1} cm^{-1}), 506 nm (ε = 3914 M^{-1} cm^{-1}), M.P. 154 °C

Synthesis of (PNP)CoCl(OTf), 4-OTf

In a vial was dissolved **3** (150 mg, 0.286 mmol) in 5 mL of THF. Solid AgOTf (77.43 mg, 0.301 mmol) was added to the cobalt complex solution slowly and within 3 minutes of the addition solution color changed to red. The reaction mixture was stirred for 45 minutes and dried in vacuo. The reaction mixture was filtered to get rid of the silver metal. The filtrate was concentrated and kept at – 35 °C for 2 days to yield red crystals of (PNP)CoCl(OTf) (142.6 mg, 0.212 mmol, 74 % yield).

^{1}H NMR (25 °C, 399.8 MHz, $CdCl_3$): δ 95.5 (br, $\nu_{1/2}$ = 547Hz), 76.2 (br, $\nu_{1/2}$ = 90 Hz), 59.8 ($\nu_{1/2}$ = 93 Hz), 3.78 ($\nu_{1/2}$ = 112 Hz), 2.30 (br, $\nu_{1/2}$ = 17 Hz), 1.94 ($\nu_{1/2}$ = 27 Hz), 1.22 ($\nu_{1/2}$ = 35 Hz), 1.05 ($\nu_{1/2}$ = 36 Hz), 0.83 ($\nu_{1/2}$ = 190 Hz), 0.59 ($\nu_{1/2}$ = 94 Hz), −4.00 ($\nu_{1/2}$ = 880 Hz), −5.28 ($\nu_{1/2}$ = 863 Hz), −25.1 (br, $\nu_{1/2}$ = 533 Hz). μ_{eff} : 2.97 μ_B ($CdCl_3$, 25 °C, Evan's method). Anal. Calcd for $C_{26}H_{40}NP_2O_3SF_3ClCo$: C, 48.29; H, 6.00; N 2.09. Found: C, 48.55; H, 5.52, N, 1.78. UV-vis (CH_2Cl_2, 25 °C): 984 nm (ε = 1344 M^{-1} cm^{-1}), 596 nm (shoulder peak) (ε = 902 M^{-1} cm^{-1}), 494 nm (ε = 2610 M^{-1} cm^{-1}). M.P. 142 °C.

Synthesis of (PNP)ZnCl, 5

In a round bottom flask anhydrous $ZnCl_2$ was taken (262 mg, 1.92 mmol) in 5 mL THF and LiPNP (837 mg, 1.92 mmol) in 10 mL of THF was added dropwise to that solution. The solution color changed to yellow within 5 minutes. The reaction mixture was stirred for 12 hours and dried in vacuo. The dried mass was extracted with toluene, filtered, concentrated and kept at − 35 °C to obtain yellow crystals of **5** (631 mg, 1.28 mmol, 66 % yield). ^{1}H NMR (25 °C, 399.8 MHz, C_6D_6): δ 7.51 (m, C_6H_3, 2H), 6.94 (m, C_6H_3, 4H), 2.17(s, *Me*Ar, 6H), 2.02(septet, C*H*Me$_2$, 4H), 1.11-0.99 (m, overlapping CH*Me*$_2$, 24H). ^{13}C NMR (25 °C, 100.6 MHz, C_6D_6): δ 156.91 (aryl), 133.18 (aryl), 129.33 (aryl), 125.69 (aryl), 124.89 (aryl), 117.78 (aryl), 22.35 (*C*HMe$_2$), 20.77 (*Me*Ar), 19.30 (CH*Me*$_2$), 18.43 (CH*Me*$_2$). ^{31}P NMR (25 °C, 121.5 MHz, C_6D_6) δ − 8.53. Anal. Calcd for $C_{26}H_{40}NP_2ZnCl$: C, 59.99; H, 7.62; N 2.65. Found: C, 59.64; H, 7.29; N, 2.20.

Synthesis of (PNHP')ZnCl$_2$(OTf), 6

In a vial **5** (51mg, 0.103 mmol) was dissolved in 5 mL of THF and FcOTf suspension (36.33 mg, 0.108 mmol) in 2 mL of THF was added to that solution. Immediate after the addition the color of the reaction mixture changed to yellow within 5 minutes with a transient reddish and greenish color in between. The yellow reaction mixture was stirred for 2 hours and then dried in vacuo. Dried mass was washed with pentane portionwise (4 times, 5 mL each) and the byproduct ferrocene was discarded. Yellow colored crystals were obtained from THF solution of the product layered with pentane and keeping the solution at − 35 °C.

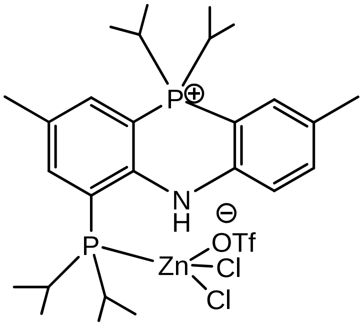

^{1}H NMR (25 °C, 399.8 MHz, C_6D_6), δ 8.30 (br, Ar$_2$N*H*), 7.75 (d, aryl), 7.60 (s, aryl), 7.41 (t, aryl), 7.26 (br, aryl), 7.10 (br, aryl), 4.19 (s, C*H*$_3$), 3.81 (THF), 3.32 (septet, C*H*Me$_2$), 2.85 (overlapping septets, C*H*Me$_2$), 2.50 (m, C*H*Me$_2$ and CH*Me*$_2$ overlapped), 2.40 (overlapping singlets, Ar*Me* and CH*Me*$_2$ overlapped), 2.41 (s, CH*Me*$_2$), 2.31 (s, CH*Me*$_2$),

1.88 (THF), 1.37-1.21 (br, overlapping CH*Me*$_2$). ^{13}C NMR (25 ^{o}C, 100.6 MHz, C_6D_6): δ 154.9 (aryl), 150.27 (aryl), 145.48 (aryl), 139.96 (aryl), 136.74 (aryl), 136.00 (aryl), 133.56 (aryl), 132.45 (aryl), 129.41 (aryl), 129.03 (aryl), 126.21 (aryl), 124.21 (aryl), 119.80 (aryl), 119.05 (aryl), 67.94 (*C*F_3SO_3), 26. 34 (CHMe$_2$), 25.84 (CHMe$_2$), 25.51 (THF), 23.96 (CHMe$_2$), 23.14 (CHMe$_2$), 23.04 (Me), 22.87 (Me), 20.58 (Me), 20.44 (Me), 18.82 (Me), 18.74 (Me), 17.85 (THF), 16.56 (Me), 16.45 (Me). ^{31}P NMR (25 ^{o}C, 121.5 MHz, C_6D_6) δ 19.04, −18.66. Mass spectroscopic analysis, ESI, [M-Cl]$^+$ calcd, 528.1694 obtained, 528.1718.

Synthesis of (PNHP)CuCl, 7

In a vial $CuCl_2$ (75 mg, 0.558 mmol) was dissolved in 2 mL of THF to form a suspension. In another vial (PNP)Li (242.95 mg, 0.558 mmol) was dissolved in 4 mL of THF and cooled to −35 ^{o}C. The cold THF solution of (PNP)Li was added to the suspension of $CuCl_2$ which displays an immediate color change to red. Within 5 minutes the color of the reaction mixture was turned to yellowish green. The reaction mixture was stirred for 2 hours after which it was dried in vacuo. The product was extracted from toluene and the concentrated toluene solution was stored at −35 ^{o}C. Within 24 hours the cold toluene extract provides yellowish crystals of (PNHP)CuCl**, 7.** ^{1}H NMR (25 ^{o}C, 399.8 MHz, C_6D_6): δ 10.23 (br, 1H, ArN*H*Ar), 7.33 (d, 2H, C_6*H*$_3$), 7.07 (s, 2H, C_6*H*$_3$), 6.96 (d, 2H, C_6*H*$_3$), 2.32 (septet, 4H, C*H*Me$_2$), 2.12 (s, 6H, *Me*Ar), 1.37 (dd, 12H, CH*Me*$_2$), 1.03 (dd, 12H, CH*Me*$_2$). ^{13}C NMR (25 ^{o}C, 100.6 MHz, C_6D_6): δ 147.38 (aryl), 133.73 (aryl), 131.87 (aryl), 129.33 (aryl), 125.70 (aryl), 118.03 (aryl), 24.18 (*C*HMe$_2$), 20.87 (*Me*Ar), 19.48 (CH*Me*$_2$), 18.22 (CHMe$_2$). ^{31}P NMR (25 ^{o}C, 121.5 MHz, C_6D_6): δ −10.28. MS-CI, [M-Cl]$^+$: calcd, 492.1127; found, 492.1982.

Synthesis of (PNHP)CuI, 7-I

In a vial CuI (40 mg, 0.210 mmol) was dissolved in 2 mL of THF to form a suspension. In another vial (PNP)Li (91.47 mg, 0.210 mmol) was dissolved in 4 mL of THF and cooled to −35 ^{o}C. The cold THF solution of (PNP)Li was added to the suspension of CuI which displays an immediate color change to yellow. The reaction mixture was stirred for 1 hour after which it was dried in vacuo. The product was extracted from toluene and the concentrated toluene solution was stored at −35 ^{o}C. Within 24 hours the cold toluene extract provides yellowish crystals of (PNHP)CuI**, 7-I.** ^{1}H NMR (25 ^{o}C, 399.8 MHz, C_6D_6): δ 9.64 (br, 1H, ArN*H*Ar), 7.30 (d, 2H, C_6H_3), 7.04 (s, 2H, C_6H_3), 6.93 (d, 2H, C_6H_3), 2.35 (septet, 4H, C*H*Me$_2$), 2.121 (s, 6H, *Me*Ar), 1.33 (dd, 12H, CH*Me*$_2$), 0.96 (dd, 12H, CH*Me*$_2$). ^{13}C NMR (25 ^{o}C, 100.6 MHz, C_6D_6): δ 169.36 (aryl), 132.70 (aryl), 131.73 (aryl), 127.83 (aryl), 126.35 (aryl), 125.02 (aryl), 25.85 (*C*HMe$_2$), 20.84 (*Me*Ar), 19.51 (CH*Me*$_2$), 18.13 (CH*Me*$_2$). ^{31}P NMR (25 ^{o}C, 121.5 MHz, C_6D_6): δ −9.34

4.8 References

1. Kaim, W.; Schwederski, B., *Pure Appl. Chem.* **2004,** *76*, 351.
2. Allgeier, A. M.; Mirkin, C. A., *Angew. Chem., Int. Ed.* **1998,** *37*, 895.
3. Ward, M. D.; McCleverty, J. A., *Dalton Trans.* **2002,** 275.
4. Stubbe, J.; Van der Donk, W. A., *Chem. Rev.* **1998,** *98*, 2661.
5. Jorgensen, C. K., *Coord. Chem. Rev.* **1966,** *1*, 164.
6. Juris, A.; Balzani, V.; Barigelletti, F.; Campagna, S.; Belser, P.; Von Zelewsky, A., *Coord. Chem. Rev.* **1988,** *84*, 85.
7. Hughes, M. C.; Macero, D. J., *Inorg. Chem.* **1976,** *15*, 2040.

8. Hanazaki, I.; Nagakura, S., *Bull. Chem. Soc. Jan.* **1971,** *44*, 2312.
9. Greenwood, N. N.; Gibb, T. C., *Mossbauer Spectroscopy*. Chapman and Hall Ltd.: London, 1971.
10. Adhikari, D.; Mossin, S.; Basuli, F.; Huffman, J. C.; Szilagyi, R. K.; Meyer, K.; Mindiola, D. J., *J. Am. Chem. Soc.* **2008,** *130*, 3676.
11. Adhikari, D.; Basuli, F.; Fan, H.; Huffman, J. C.; Pink, M.; Mindiola, D. J., *Inorg. Chem.* **2008,** *47*, 4439.
12. Connelly, N. G.; Geiger, W. E., *Chem. Rev.* **1996,** *96*, 877.
13. Addison, A. W.; Rao, T. N.; Reedijk, J.; Van Rijn, J.; Verschoor, G. C., *Dalton Trans.* **1984,** 1349.
14. Benito-Garagorri, D.; Wiedermann, J.; Pollak, M.; Mereiter, K.; Kirchner, K., *Organometallics* **2007,** *26*, 217.
15. Zhang, J.; Gandelman, M.; Herrman, D.; Leitus, G.; Shimon, L. J. W.; Ben-David, Y.; Milstein, D., *Inorg. Chim. Acta* **2006,** *359*, 1955.
16. O'Reilly, R. K.; Gibson, V. C.; White, A. J. P.; Williams, D. J., *Polyhedron* **2004,** *23*, 2921.
17. Britovsek, G. J. P.; Gibson, V. C.; Mastroianni, S.; Oakes, D. C. H.; Redshaw, C.; Solan, G. A.; White, A. J. P.; Williams, D. J., *Eur. J. Inorg. Chem.* **2001,** 431.
18. Fout, A. R.; Basuli, F.; Fan, H.; Tomaszewski, J.; Huffman, J. C.; Baik, M.-H.; Mindiola, D. J., *Angew. Chem., Int. Ed.* **2006,** *45*, 3291.
19. Zhang, M.; Hao, P.; Zuo, W.; Jie, S.; Sun, W.-H., *J. Organomet. Chem.* **2008,** *693*, 483.
20. Cowdell, R.; Davies, C. J.; Hilton, S. J.; Marechal, J.-D.; Solan, G. A.; Thomas, O.; Fawcett, J., *Dalton Trans.* **2004,** 3231.
21. Chen, Y.; Qian, C.; Sun, J., *Organometallics* **2003,** *22*, 1231.
22. Chen, Y.; Chen, R.; Qian, C.; Dong, X.; Sun, J., *Organometallics* **2003,** *22*, 4312.
23. Sun, W.-H.; Hao, P.; Zhang, S.; Shi, Q.; Zuo, W.; Tang, X.; Lu, X., *Organometallics* **2007,** *26*, 2720.
24. Sato, Y.; Nakayama, Y.; Yasuda, H., *J. Organomet. Chem.* **2004,** *689*, 744.
25. Thyagarajan, S.; Shay, D. T.; Incarvito, C. D.; Rheingold, A. L.; Theopold, K. H., *J. Am. Chem. Soc.* **2003,** *125*, 4440.
26. Ingleson, M.; Fan, H.; Pink, M.; Tomaszewski, J.; Caulton, K. G., *J. Am. Chem. Soc.* **2006,** *128*, 1804.
27. Lippard, S. J.; Berg, J. M., *Bioinorganic Chemistry*. Akad Verlag: Berlin, Germany, 1995.
28. Cotton, F. A.; Schmid, G., *Polyhedron* **1996,** *15*, 4053.
29. Thomas, J. C.; Peters, J. C., *Polyhedron* **2004,** *23*, 2901.
30. Schneider, J. L.; Young, V. G., Jr.; Tolman, W. B., *Inorg. Chem.* **2001,** *40*, 165.
31. Diaz-Requejo, M. M.; Belderrain, T. R.; Nicasio, M. C.; Trofimenko, S.; Perez, P. J., *J. Am. Chem. Soc.***2003,** *125*, 12078.
32. Dai, X.; Warren, T. H., *Chem. Commun.* **2001,** 1998.
33. Spencer, D. J. E.; Aboelella, N. W.; Reynolds, A. M.; Holland, P. L.; Tolman, W. B., *J. Am. Chem. Soc.* **2002,** *124*, 2108.
34. Laitar, D. S.; Mathison, C. J. N.; Davis, W. M.; Sadighi, J. P., *Inorg. Chem.* **2003,** *42*, 7354.
35. Hu, X.; Castro-Rodriguez, I.; Meyer, K., *J. Am. Chem. Soc.* **2003,** *125*, 12237.

36. Kaur, H.; Zinn, F. K.; Stevens, E. D.; Nolan, S. P., *Organometallics* **2004,** *23*, 1157.
37. Mankad, N. P.; Gray, T. G.; Laitar, D. S.; Sadighi, J. P., *Organometallics* **2004,** *23*, 1191.
38. Beinert, H.; Holm, R. H.; Munck, E., *Science* **1997,** *277*, 653.
39. Djukic, B.; Dube, P. A.; Razavi, F.; Seda, T.; Jenkins, H. A.; Britten, J. F.; Lemaire, M. T., *Inorg. Chem.* **2009,** *48* (2), 699.
40. Becke, A. D., *Phy. Rev. A: Atomic, Molecular, and Optical Physics* **1988,** *38*, 3098.
41. Lee, C.; Yang, W.; Parr, R. G., *Phy. Rev. B: Condensed Matter and Materials Physics* **1988,** *37*, 785.
42. Stephens, P. J.; Devlin, F. J.; Chabalowski, C. F.; Frisch, M. J., *J. Phy. Chem.* **1994,** *98*, 11623.
43. Reiher, M.; Salomon, O.; Hess, B. A., *Theo. Chem. Acc.* **2001,** *107*, 48.
44. Hay, P. J.; Wadt, W. R., *J. Chem. Phy.* **1985,** *82*, 270.
45. Wadt, W. R.; Hay, P. J., *J. Chem. Phy.* **1985,** *82*, 284.
46. Hay, P. J.; Wadt, W. R., *J. Chem. Phy.* **1985,** *82*, 299.
47. Solomon, E. I.; Hedman, B.; Hodgson, K. O.; Dey, A.; Szilagyi, R. K., *Coord. Chem. Rev.* **2005,** *249*, 97.
48. Glaser, T.; Hedman, B.; Hodgson, K. O.; Solomon, E. I., *Acc. Chem. Res.* **2000,** *33*, 859.
49. Westre, T. E.; Kennepohl, P.; DeWitt, J. G.; Hedman, B.; Hodgson, K. O.; Solomon, E. I., *J. Am. Chem. Soc.* **1997,** *119*, 6297.
50. Sugano, S.; tanabe, Y., *Multiplates of Transition-metal Ions in Crystals*. Academic press: New York, 1970.
51. Shulman, R. G.; Yafet, Y.; Eisenberger, P.; Blumberg, W. E., *Proc. Natl. Acad. Sci.* **1976,** *73*, 138.
52. Roe, A. L.; Schneider, D. J.; Mayer, R. J.; Pyrz, J. W.; Widom, J.; Que, L., Jr., *J. Am. Chem. Soc.* **1984,** *106*, 1676.
53. True, A. E.; Scarrow, R. C.; Randall, C. R.; Holz, R. C.; Que, L., Jr., *J. Am. Chem. Soc.* **1993,** *115*, 4246.
54. Pavlosky, M. A.; Zhang, Y.; Westre, T. E.; Gan, Q.-F.; Pavel, E. G.; Campochiaro, C.; Hedman, B.; Hodgson, K. O.; Solomon, E. I., *J. Am. Chem. Soc.* **1995,** *117*, 4316.
55. Hedman, B.; Hodgson, K. O.; Solomon, E. I., *J. Am. Chem. Soc.* **1990,** *112*, 1643.
56. DuBois, J. L.; Mukherjee, P.; Stack, T. D. P.; Hedman, B.; Solomon, E. I.; Hodgson, K. O., *J. Am. Chem. Soc.* **2000,** *122*, 5775.
57. Sarangi, R.; Aboelella, N.; Fujisawa, K.; Tolman, W. B.; Hedman, B.; Hodgson, K. O.; Solomon, E. I., *J. Am. Chem. Soc.* **2006,** *128*, 8286.
58. de Groot, F., *Chem. Rev.* **2001,** *101*, 1779.
59. de Groot, F., *Coord. Chem. Rev.* **2005,** *249*, 31.
60. George, S. J.; Lowery, M. D.; Solomon, E. I.; Cramer, S. P., *J. Am. Chem. Soc.* **1993,** *115*, 2968.
61. Shadle, S. E.; Penner-Hahn, J. E.; Schugar, H. J.; Hedman, B.; Hodgson, K. O.; Solomon, E. I., *J. Am. Chem. Soc.* **1993,** *115*, 767.

62. Hahn, J. E.; Scott, R. A.; Hodgson, K. O.; Doniach, S.; Desjardins, S. R.; Solomon, E. I., *Chem. Phy. Lett.* **1982,** *88*, 595.
63. Thomas, F.; Jarjayes, O.; Duboc, C.; Philouze, C.; Saint-Aman, E.; Pierre, J.-L., *Dalton Trans.* **2004,** 2662.
64. Shimazaki, Y.; Yajima, T.; Tani, F.; Karasawa, S.; Fukui, K.; Naruta, Y.; Yamauchi, O., *J. Am. Chem. Soc.* **2007,** *129*, 2559.
65. Storr, T.; Wasinger, E. C.; Pratt, R. C.; Stack, T. D. P., *Angew. Chem., Int. Ed.* **2007,** *46*, 5198.
66. Kurahashi, T.; Kikuchi, A.; Tosha, T.; Shiro, Y.; Kitagawa, T.; Fujii, H., *Inorg. Chem.* **2008,** *47*, 1674.
67. Rotthaus, O.; Thomas, F.; Jarjayes, O.; Philouze, C.; Saint-Aman, E.; Pierre, J.-L., *Chem.- Eur. J.* **2006,** *12*, 6953.
68. Storr, T.; Verma, P.; Pratt, R. C.; Wasinger, E. C.; Shimazaki, Y.; Stack, T. D. P., *J. Am. Chem. Soc.* **2008,** *130*, 15448.
69. Haneline, M. R.; Heyduk, A. F., *J. Am. Chem. Soc.* **2006,** *128*, 8410.
70. Ringenberg, M. R.; Kokatam, S. L.; Heiden, Z. M.; Rauchfuss, T. B., *J. Am. Chem. Soc.* **2008,** *130*, 788.
71. Sur, S. K., *J. Magn. Reson.* **1989,** *82*, 169.
72. Evans, D. F., *J. Chem. Soc.* **1959**, 2003.
73. Dunning, T. H., Jr., *J. Chem. Phy.* **1989,** *90*, 1007.

Appendix of Molecules

The appendix of molecules is a composition of compounds that are not completely characterized, but the molecules are interesting and worth pursuing.

Synthesis of (PNP)FeMe

In a vial (PNP)FeCl (75 mg, 0.144 mmol) was dissolved in 5 mL of ether and cooled to −35 ^{o}C. In an another vial $MeLi(Et_2O)_{0.2}$ (5.31 mg, 0.144 mmol) was added in 1 mL of ether and cooled analogously. Both the solution was mixed in cold condition upon which an immediate color change to orange took place. The reaction mixture was stirred for an hour. After the completion of the reaction, the mixture was filtered and the ethereal filtrate was dried to isolate (PNP)FeMe as an orange colored solid (62 mg, 0.124 mmol, 83% yield). ^{1}H NMR (25 ^{o}C, 399.8 MHz, C_6D_6): δ 36.76 (br, $\nu_{1/2}$ = 205 Hz), 21.50 (br, $\nu_{1/2}$ = 210 Hz), 2.21 (br, $\nu_{1/2}$ = 728 Hz), 1.35 (br, $\nu_{1/2}$ = 286 Hz), −1.52 (br, $\nu_{1/2}$ = 212 Hz), −10.02 (br, $\nu_{1/2}$ = 250 Hz), −19.74 (br, $\nu_{1/2}$ = 227 Hz), −67.79 (br, $\nu_{1/2}$ = 361 Hz).

Synthesis of (PNP)FePh

In a vial (PNP)FeCl (60 mg, 0.115 mmol) was dissolved in 3 mL of ether and cooled to −35 ^{o}C. In another vial PhLi (9.70 mg, 0.115 mmol) was added in 1 mL of ether and cooled analogously. Both the solution was mixed in cold condition upon which an immediate color change to reddish orange took place. The reaction mixture was stirred for an hour. After the completion of the reaction, the mixture was filtered and the ethereal filtrate was dried to isolate (PNP)FePh as an orange colored solid (57 mg, 0.102 mmol, 88% yield). ^{1}H NMR (25 ^{o}C, 399.8 MHz, C_6D_6): δ 63.70 (br, $\nu_{1/2}$ = 240 Hz), 51.41 (br, $\nu_{1/2}$ = 47 Hz), 32.76 (br, $\nu_{1/2}$ = 70

Hz), 23.78 (br, $\nu_{1/2}$ = 41 Hz), 22.45 (br, $\nu_{1/2}$ = 41 Hz), 13.82 (br, $\nu_{1/2}$ = 53 Hz), 1.11 (br, $\nu_{1/2}$ = 66 Hz), −0.57 (br, $\nu_{1/2}$ = 51 Hz), −8.65 (br, $\nu_{1/2}$ = 137 Hz), −19.96 (br, $\nu_{1/2}$ = 67 Hz).

Synthesis of (PNP)Fe(μ-H)$_2$BH$_2$

In a vial (PNP)FeCl (300 mg, 0.575 mmol) was dissolved in 6 mL of THF and cooled to −35 ^{o}C. NaBH$_4$ as solid (108.76 mg, 2.875 mmol) was added to the cold solution of (PNP)FeCl. During the reaction the color of the solution changes from red to brown. After two hours of stirring, the reaction mixture was dried and extracted with hexane. Brown colored crystals of (PNP)Fe(μ-H)$_2$BH$_2$ (233 mg, 0.467 mmol, 81% yield) appear from hexane solution at room temperature within 24 hours. X-ray crystal structure was determined for the molecule (IUMSC number **08001**). ^{1}H NMR (25 ^{o}C, 300.1 MHz, C$_6$D$_6$): δ 30.24 (br, $\nu_{1/2}$ = 27 Hz), 26.32 (br, $\nu_{1/2}$ = 36 Hz), 21.54 (br, $\nu_{1/2}$ = 29 Hz), 2.75 (br, $\nu_{1/2}$ = 28 Hz), 1.09 (br, $\nu_{1/2}$ = 137 Hz), −9.37 (br, $\nu_{1/2}$ = 41 Hz), −16.09 (br, $\nu_{1/2}$ = 35 Hz). ^{11}B NMR (25 ^{o}C, 160.6 MHz, C$_6$D$_6$): δ −39.8 (br, $\nu_{1/2}$ = 161 Hz). Following figure depicts the molecule where PNP cartoon is [N(2-P(CHMe$_2$)$_2$-4-MeC$_6$H$_3$)$_2$]$^-$.

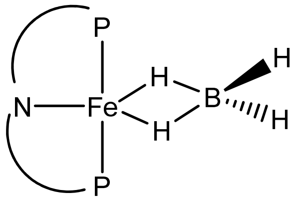

Synthesis of (PNP)Fe(N$_2$)(μ-H)MgCl(THF)$_2$

In a vial was taken (PNP)FeCl (56 mg, 0.115 mmol) in 3 mL of ether and cooled to −35 ^{o}C. Etyl magnesium chloride (2 M solution in ether, commercial source-Aldrich) (0.06

mL, 0.115 mmol) was taken in a syringe and added dropwise to the cold solution of (PNP)FeCl. Immediate after the addition the color of the solution changed to brown. The solution was stirred for two hours during which a white solid accumulated at the bottom of the vial. After completion the reaction mixture was filtered and the ethereal filtrate was dried in vacuo. The product was isolated in 68% crude yield. X-ray diffraction quality crystal was grown from THF/pentane mixture after keeping the solution at −35 °C overnight. X-ray crystal structure was determined for the molecule (IUMSC number **08023**). ^{1}H NMR (25 °C, 300.1 MHz, C_6D_6): δ 38.5 (br), 21.9 (br), 19.9 (br), 2.18 (br), 1.07 (br), −1.86 (br), −9.70 (br), −20.40 (br). μ_{eff} : 2.40(2) μ_B . IR (KBR plate, nujol) 2084 cm^{-1} for N_2 stretch. Isotope labeling with $^{15}N_2$ showed the stretch at 2013 cm^{-1} (weak stretch). Following figure depicts the molecule where PNP cartoon is [N(2-P(CHMe$_2$)$_2$-4-MeC$_6$H$_3$)$_2$]$^-$.

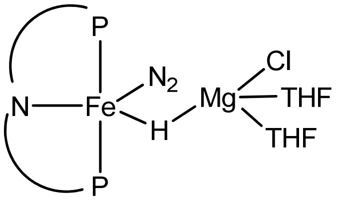

Synthesis of (PNP)CoEt

In a vial was taken (PNP)CoCl (100 mg, 0.191 mmol) in 3 mL of ether and cooled to −35 °C. Etyl magnesium chloride (2 M solution in ether, commercial source-Aldrich) (0.10 mL, 0.191 mmol) was taken in a syringe and added dropwise to the cold solution of (PNP)CoCl. Immediate after the addition the color of the solution changed to reddish brown. The solution was stirred for 20 minutes during which a white solid accumulated at the bottom of the vial. After the completion of the reaction the reaction mixture was dried in vacuo and extracted with benzene. The benzene extract was dried in vacuo and redissolved in 1 mL of THF. 3 drops of pentane was added to the THF solution and kept the solution overnight at −35 °C. Red crystals appeared from the solvent mixture and collected. X-ray crystal structure was determined for the molecule (IUMSC number **08099**). ^{1}H NMR (25 °C, 300.1 MHz, C_6D_6): δ 31.79 (br, $\nu_{1/2}$ = 262 Hz), 29.36 (br, $\nu_{1/2}$ = 706 Hz), 21.41 (br, $\nu_{1/2}$ = 97 Hz), 10.49 (br, $\nu_{1/2}$ = 318 Hz), 31.79 (br, $\nu_{1/2}$ = 262 Hz), 8.21 (br, $\nu_{1/2}$ = 27 Hz), 2.17 (br, $\nu_{1/2}$ = 373 Hz), −23.19 (br, $\nu_{1/2}$ = 218 Hz), −70.34 (br, $\nu_{1/2}$ = 686 Hz).

Debashis Adhikari

Department of Chemistry
Indiana University
800 E. Kirkwood Ave.
Bloomington, IN 47405
Tel: (812) 856-0670
Fax: (812) 855-8300
dadhikar@indiana.edu

Home Address:
407 S Grant St. Apt 08
Bloomington, IN 47401
Tel: (812) 345-5690

Education

Fall 2004-Spring 2009 — **Indiana University** — **Bloomington, IN**
Ph. D. Studies under Professor Daniel J. Mindiola
Thesis: Synthesis, Structure and Reactivity Studies of Nickel Pincer Complexes and Evaluating the Redox Non-innocence of the Ligand

Fall 2002-Spring 2004 — **IIT, Kanpur** — **Kanpur, India**
M.S. Studies under Professor V. K. Singh
Thesis: Development of Ti-based Asymmetric Catalyst

Fall 1999-Spring 2002 — **Calcutta University** — **Calcutta, India**
B.S. in Chemistry

Teaching Experience

Spring 2006 — *Associate Instructor*
Instructor for General Chemistry, C121

Fall 2005 — *Associate Instructor*
Instructor for General Chemistry, C121

Spring 2005 — *Associate Instructor*
Instructor for General Chemistry, C118

Research Expertise

Inorganic and organometallic synthesis. Manipulation of highly reactive metal complexes. Used Glove box and Schlenk line techniques. Elucidation of reaction mechanisms. Characterization of products with NMR, FTIR, X-ray crystallography and cyclic voltammetry. Analysis of paramagnetic material by EPR spectroscopy. Used X-ray absorption spectroscopic techniques. Productive in collaborative research.

Honors and Awards

2009 — William H. Nebergall Memorial Award for Excellence in Research, Indiana University
2007 — Indiana University College of Arts and Sciences Travel Award
2004 — Junior Research Fellowship, India.
2003 — Summer Research Fellowship, Indian Academy of Sciences.

Publications

[11] **Adhikari, D**.; Basuli, F.; Orlando, J. H.; Gao, X.; Huffman, J. C.; Pink, M.; Mindiola, D. J.; Zwitterionic and Cationic Titanium and Vanadium Complexes Having Terminal M−C Multiple Bonds. The Role of β−Diketiminate Framework in Formation of Charge Separated Species. *Organometallics,* **2009**, *28*, 4115-4125.

[10] **Adhikari, D**.; Pink, M.; Mindiola, D. J.; A Mild Protocol Toward the Synthesis of Stable Nickel Complexes Having Primary and Secondary

Silyl ligands. *Organometallics,* **2009**, *28*, 2072-2077.

[9] **Adhikari, D**.; Tran, L. B.; Zuno-Cruz, F. J.; Cabrera, G. S.; Mindiola, D. J. Complexes of Bulky β-Diketiminate Ligands. *Inorg. Synth*., **2009**, *35*, in press.

[8] **Adhikari, D**.; Mossin, S.; Basuli, F.; Dible, B. R.; Chipara, M.; Fan, H.; Huffman, J. C.; Meyer, K.; Mindiola, D. J. A Dinuclear Ni(I) System Having a Diradical Ni_2N_2 Diamond Core Resting State: Synthetic, Structural and Spectroscopic Elucidation and Reductive Bond Splitting Reactions. *Inorg. Chem*., **2008**, *47*, 10479-10490.

[7] Fan, H.; **Adhikari, D**.; Saleh, A. A.; Clark, R. L.; Zuno-Cruz, F. J.; Cabrera, G. S.; Huffman, J. C.; Pink, M.; Mindiola, D. J.; Baik, M-H. Understanding and Predicting Distorted T- vs. Y-Geometries for Neutral Chromous Complexes Supported by a Sterically Encumbering β-Diketiminate Ligand. *J. Am. Chem. Soc*., **2008**, *130*, 17351-17361.

[6] **Adhikari, D**.; Basuli, F.; Fan, H.; Huffman, J. C.; Pink, M.; Mindiola, D. J. P=N Bond Formation Via Incomplete N-Atom Transfer from a Ferrous Amide Complex. *Inorg. Chem*., **2008**, *47*, 4439-4441.

[5] **Adhikari, D**.; Mossin, S.; Basuli, F.; Huffman, J. C.; Szilagyi, R. K.; Meyer, K.; Mindiola, D. J. Structural, Spectroscopic and Theoretical Elucidation of a Redox Active Pincer-Type Ancillary Applied in Catalysis. *J. Am. Chem. Soc*., **2008**, *130*, 3676-3682.

[4] **Adhikari, D**.; Huffman, J. C.; Mindiola, D. J. Structural Elucidation of a Nickel Boryl Complex. A Recyclable Borylation Ni(II) Reagent of Bromobenzene. *Chem. Commun*., **2007**, *43*, 4489-4491.

[3] Fafard, C. M.; **Adhikari, D**.; Foxman, B. M.; Mindiola, D. J.; Ozerov, O. V. Addition of Ammonia, Water, and Dihydrogen Across a Single Pd-Pd Bond. *J. Am. Chem. Soc*., **2007**, *129*, 10318-10319.

[2] Basuli, F.; **Adhikari, D**.; Huffman, J. C.; Mindiola, D. J. Organometallic Consequences of a Redox Reaction. Terminal Trimethylsilylmethylidene Titanium Complexes Prepared by a One-Electron Oxidation Step. *J. Organomet. Chem*., **2007**, *692*, 3315-3320.

[1] **Adhikari, D**.; Zhao, G.; Basuli, F.; Tomaszewski, J.; Huffman, J. C.; Mindiola, D. J. Tl(I), Fe(II) and Co(II) Complexes Supported by a Monoanionic N,N,N'-Heteroscorpionate Ligand Bis(3,5-di-tertbutylpyrazol-1-yl)-1-CH_2NAr (Ar = 2,6-$^iPr_2C_6H_3$). *Inorg. Chem*., **2006**, *45*, 1604-1610.

Presentations

[4] **Adhikari, D**.; Huffman, J. C.; Mindiola, D. J. Structural Elucidation of a Nickel Boryl Complex. 235 th ACS National Meeting, New Orleans, LA, United States, April 6-10, 2008.

[3] **Adhikari, D**.; Basuli, F.; Huffman, J. C.; Mindiola, D. J. Late Transition Metal Chemistry Supported by a Rigid PNP Pincer-type Ligand. 233 th

ACS National Meeting, Chicago, IL, United States, March 25-29, 2007.

[2] **Adhikari, D**.; Basuli, F.; Huffman, J. C.; Mindiola, D. J. Redox Chemistry of a Ni_2N_2 Diamond Core: A Masked Three Coordinate Ni(I) Synthon. 232 th ACS National Meeting, San Francisco, CA, United States, Sept 10-14, 2006.

[1] **Adhikari, D**.; Zhao, G.; Basuli, F.; Tomaszewski, J.; Huffman, J. C.; Mindiola, D. J. Exploring Functional Groups with a Tripodal Heteroscorpionate Ligand. 230 th ACS National Meeting, Washington DC, United States, Aug 28-Sep1, 2005.

References

Prof. Daniel J. Mindiola (mindiola@indiana.edu)
Department of Chemistry, Indiana University, 800 E. Kirkwood Ave,
Bloomington, IN 47405.
(812) 855-2399

Prof. Kenneth G. Caulton (caulton@indiana.edu)
Department of Chemistry, Indiana University, 800 E. Kirkwood Ave,
Bloomington, IN 47405.
(812) 855-4798

Prof. Dongwhan Lee (dongwhan@indiana.edu)
Department of Chemistry, Indiana University, 800 E. Kirkwood Ave,
Bloomington, IN 47405.
(812) 855-9364

Prof. Mu-Hyun Baik (mbaik@indiana.edu)
Department of Chemistry, Indiana University, 800 E. Kirkwood Ave,
Bloomington, IN 47405.
(812) 856-0454